Heavy Vehicle Systems Optimization

2003 Annual Progress Report

Less dependence on foreign oil, and eventual transition to an emissions-free, petroleum-free vehicle

freedomCAR & vehicle technologies program

U.S. Department of Energy
Energy Efficiency and Renewable Energy
Bringing you a prosperous future where energy is clean, abundant, reliable and affordable

U.S. Department of Energy
FreedomCAR and Vehicle Technologies Program
1000 Independence Avenue, S.W.
Washington, D.C. 20585-0121

FY 2003

Annual Progress Report for Heavy Vehicle Systems Optimization

Energy Efficiency and Renewable Energy
FreedomCAR and Vehicle Technologies Program

Approved by Dr. Sidney Diamond **Technology Area Development Specialist**

February 2004

Contents

Contents (Cont.)

Contents (Cont.)

Forward

We are pleased to provide the annual report for FY 2003 for the Heavy Vehicle Systems Optimization Program. As emission regulations became more stringent, it is clear that improvements in the diesel engine efficiency could be limited. Therefore, Heavy Vehicle Optimization addresses the very important area of non-engine losses that is fertile for large fuel efficiency improvements. These parasitic energy losses are divided into aerodynamic drag, which accounts for about 53% of the non-engine losses of a fully loaded class 8 tractor-trailer traveling at 65 mph on a level highway; rolling resistance (32% of non-engine losses); drivetrain (6%); and auxiliary losses (9%). As aerodynamic drag is reduced, brakes that already operate at capacity can be seriously overloaded. Therefore, the program also includes a safety line item that concentrates on improvement of brake systems. Funds in FY 2003 were approximately $10.3 M. Projects are selected on the basis of proposals addressing open solicitations issued by the Office of FreedomCAR and Vehicle Technologies, or proposals from national laboratories. All contracts with our industrial partners are cost-shared at least 50%.

The primary goal of the program is to develop cost-effective technologies that will vastly improve the fuel efficiency of heavy vehicles and will eventually devolve into all vehicles. The ultimate goals are consistent with the goals of the 21st Century Truck Initiative: a 10-mpg, fully loaded class 8 tractor/trailer at highway speeds.

The individual goals are to reduce the aerodynamic drag coefficient by 25%, resulting in about a 12.5% increase in fuel efficiency at 65 mph (and larger at higher velocities); a 40% decrease in rolling resistance; a 30% decrease in drivetrain losses; a 50% decrease in auxiliary loads; and an 8% decrease in the size of the radiator despite the higher cooling demands of higher-power engines and exhaust gas recirculation.

The individual sections contained in this annual report indicate that excellent, steady progress is being made toward these 2010 goals. Highlights include, but are not restricted to, a demonstration of the “more electric truck,” in which many of the belt-driven devices were replaced by electrically driven ones, an integral starter-generator, a high-efficiency air conditioner, and installation of a system to avoid long idling that included an invertor and an auxiliary power unit. Advanced state-of-the-art computational fluid dynamics is leading to the exploration of novel devices to reduce aerodynamic drag. Nanofluids (fluids containing either small copper particles or carbon nanotubes) are being developed that have a 250% higher thermal conductivity than conventional cooling fluids. A theory of scuffing, the catastrophic failure of material under rubbing conditions, has been developed that allows some predictive capabilities. A device that converts any hydrocarbon into hydrogen has been advanced to the point where a major supplier has taken over the commercial development, contributing a major portion of the funding for continued development of the device. Computer modeling of a diesel engine has shown critical areas where fuel efficiencies can be gained if friction can be reduced by coatings, surface treatments, and/or the use of tailored lubricants. Dimples produced on the surface by means of a laser can reduce friction in the boundary layer lubrication region.

Finally, it is my pleasure to thank the dedicated scientists and engineers who are working with the Office of FreedomCar and Vehicle Technologies. It is their expertise, drive, and initiative that have made great strides in their technologies; their innovations will continue to contribute to advances in the reduction of parasitic energy losses for heavy vehicles. A special note of recognition is due to Dr. Jules Routbort, the technical program manager for Heavy Vehicle Systems Optimization. His zeal, knowledge, insight, and organizing

skills have energized all our colleagues, who are striving to accomplish the goals presented above in the best technical interest of our nation.

Dr. Sidney Diamond, Technology Area Development Specialist
Heavy Vehicle Systems Optimization
Office of FreedomCar and Vehicle Technologies
Energy Efficiency and Renewable Energy
U.S. Department of Energy

I. Aerodynamic Drag Reduction

A. DOE Project on Heavy Vehicle Aerodynamic Drag

Project Principal Investigator: R.C. McCallen
Lawrence Livermore National Laboratory
P.O. Box 808, Livermore, CA 94551-0808
(925) 423-0958; mccallen1@llnl.gov

Principal Investigator: K. Salari
Co-Investigator: J. Ortega
Lawrence Livermore National Laboratory
P.O. Box 808, Livermore, CA 94551-0808
(925) 424-4635; salari1@llnl.gov

Principal Investigator: L.J. DeChant
Co-Investigators: C.J. Roy, J.L. Payne, and B. Hassan
Sandia National Laboratories
P.O. Box 5800, MS 0825, Albuquerque, NM 87185-0825
(505) 844-4250; ljdecha@sandia.gov

Principal Investigator: W.D. Pointer
Argonne National Laboratory
9700 S. Cass Avenue, NE-208, Argonne, IL 60439
(630) 252-1052; dpointer@anl.gov

Principal Investigator: F. Browand
Co-Investigators: M. Hammache and T.-Y. Hsu
Aerospace & Mechanical Engineering, University of Southern California
RRB 203, Los Angeles CA 90089-1191
(213) 740-5359; browand@spock.usc.edu

Principal Investigator: J. Ross
Co-Investigators: D. Satran, J.T. Heineck, S. Walker, and D. Yaste
NASA Ames Research Center
MS 260-1, Moffett Field, CA 94035
(650) 604-6722; jcross@mail.arc.nasa.gov

Principal Investigator: R. Englar
Georgia Tech Research Institute
ATASL, CCRF, Atlanta, GA 30332-0844
(770) 528-3222; bob.englar@gtri.gatech.edu

Principal Investigator: A. Leonard
Co-Investigators: M. Rubel and P. Chatelain
California Institute of Technology
1200 East California Blvd. MC 301-46, Pasadena, CA 91125
(626) 395-4465; tony@galcit.caltech.edu

Technology Development Manager: Sid Diamond
(202) 586-803; sid.diamond@ee.doe.gov
Technical Program Manager: Jules Routbort
(630) 252-5065; routbort@anl.gov

Contractors: Lawrence Livermore National Laboratory, Sandia National Laboratories, Argonne National Laboratory, NASA Ames Research Center, Georgia Tech Research Institute, University of Southern California, California Institute of California
Contract Nos.: W-7405-ENG-48, DE-AC04-94AL85000, W-31-109-ENG-38, DE-AI01-99EE50559, DE-AC03-02EE5069, DE-AC03-98EE50512, DE-AC03-98EE50506

Consortium members in NASA Ames Research Center 12-foot pressure wind tunnel.

Objective

- Provide guidance to industry in the reduction of aerodynamic drag of heavy truck vehicles.
- Establish a database of experimental, computational, and conceptual design information, and demonstrate potential of new drag-reduction devices.

Approach

- Develop and demonstrate the ability to simulate and analyze aerodynamic flow around heavy truck vehicles using existing and advanced computational fluid dynamics (CFD) tools.
- Through an extensive experimental effort, generate an experimental data base for code validation.
- Using experimental data base, validate computations.
- Provide industry with design guidance and insight into flow phenomena from experiments and computations.

- Investigate aero devices (e.g., boattail plates, side extenders, blowing and acoustic devices) and provide industry with conceptual designs of drag reducing devices. Demonstrate the full-scale fuel economy potential of these devices.

Accomplishments

- Drag reduction devices met project goals:
  - Angled plates provide 50% more drag reduction than boattail plates
  - Use of angled plates (~15%) with skirts or lowboy trailers (~10%) provides over 20% reduction in drag which corresponds to more than 10% reduction in fuel use at highway speeds.
  - Track tests of the pneumatic blowing device demonstrated a maximum reduction of 5-6% in fuel use (not accounting for fuel use for blowing). Recent wind-tunnel tests have identified configuration/blowing improvements indicating potential fuel economy of 7% from blowing (without consideration of the energy required for the air) and a drag reduction of 10-12% due to configuration changes.
  - Full-scale test results on an SUV indicate the potential for blowing to reduce drag (increase fuel economy), increase drag for braking, reduce drag due to side winds, and provide directional stability, without moving parts.
  - Computationally showed that use of a "splitter plate" in the tractor-trailer gap may be one way to maintain a symmetrical, low drag condition.
- Insight from experiments and experimental data base provided clear guidance to industry on reliable, predictable experimental techniques:
  - Reynolds number (Re) effects on the vehicle drag coefficient (C_D) are in general minimal for experiments with Re above 1 million. This finding supports the common use of scaled down vehicles and Re below typical highway Re for experimentation.
  - Experiments indicate that inaccuracies should be considered when evaluating gap and wake drag reduction devices at lower than highway Re. Low Re experiments should provide ball park estimates, but accurate optimization of devices may require road testing.
  - Edge radius effects and/or the cleanliness of the vehicle upstream flow are critical to achieving accurate predictions.
  - Drag measurements alone are not sufficient to provide an understanding of the impact of geometry modifications and direction for design improvements and advanced measurement techniques (e.g., particle-image velocimetry, unsteady pressure taps, oil film interferometry) should be included to provide important information on the global and local structure of the flow and clear design direction.
- Computational results provided the following clear guidance and caution warnings on the use of steady Reynolds-averaged Navier Stokes (RANS) models for CFD simulations:
  - Conclusions on predictive capability of a turbulence model can only be determined with grid converged solutions.
  - When using wall functions, the first wall point should be held fixed while refining the grid.
  - The computed overall vehicle drag is highly dependent on the choice of turbulent steady RANS model. Solutions may disagree with measurements by 0.5 to 50% for 0 degree yaw and by even higher percentages at yaw angles.
  - Steady RANS models generally do a good job predicting the flow on the front and sides of the vehicle, where the flow stays attached and does not exhibit separation and recirculation zones.
  - The flow structure in the trailer wake presented by the time-averaged experimental data does not compare with that computed with the steady RANS models. Thus, use of steady RANS to evaluate drag reduction devices in the trailer wake and tractor-trailer gap may provide inaccurate design guidance.

Future Direction

- Continue to develop and evaluate drag reducing conceptual designs and encourage and work with industry to road test the most promising drag reducing devices. Road tests with angled plates and SAE track tests with the pneumatic device are planned for FY04.
- Continue experimental data reduction and analysis for the generic conventional model (GCM).

- Continue computations of flow around GCM, compare to experimental data, perform analyses, and provide guidance to industry on use of unsteady RANS and hybrid RANS/Large-Eddy Simulation methods.
- Develop and use an apparatus for studying wheel and tire splash and spray, pursuing ways to minimize this road safety hazard.
- Investigate air flow around rotating tires for improved brake cooling, as well as drag reduction.
- Investigate aerodynamics of filled and empty coal cars to determine effective concepts for drag reduction.
- Collaborate with DOE Industrial Consortium, which will be conducting fleet tests of advanced aerodynamic drag reduction devices. Schedule industry site visits and meetings to share findings and encourage consideration of effective design concepts for road testing.

Introduction

A modern Class 8 tractor-trailer can weigh up to 80,000 pounds and has a wind-averaged drag coefficient around $C_D = 0.6$. The drag coefficient is defined as the drag/(dynamic pressure × projected area). The higher the speed the more energy consumed in overcoming aerodynamic drag. At 70 miles per hour, a common highway speed today, overcoming aerodynamic drag represents about 65% of the total energy expenditure for a typical heavy truck vehicle. Reduced fuel consumption for heavy vehicles can be achieved by altering truck shapes to decrease the aerodynamic resistance (drag). It is conceivable that present day truck drag coefficients might be reduced by as much as 50%. This reduction in drag would represent approximately a 25% reduction in fuel use at highway speeds. An estimated total savings of $1.5 billion per year can be recognized in the United States alone for just a 6% reduction in fuel use. This reduction represents 1% of all fuel use in the United States.

The project goal is to develop and demonstrate the ability to simulate and analyze aerodynamic flow around heavy truck vehicles using existing and advanced computational fluid dynamics (CFD) tools. Activities also include an extensive experimental effort to generate data for code validation and a design effort for developing drag reducing devices. The final products are specific device concepts that can significantly reduce aerodynamic drag, and thus improve fuel efficiency, in addition to an experimental data base and validated CFD tools. The objective is to provide industry with clear guidance on methods of computational simulation and experimental modeling techniques that work for predicting the flow phenomena around a heavy vehicle and add-on drag reducing devices. Development of effective drag reducing devices is also a major goal.

The following reports on the findings and accomplishments for fiscal year 2003 in the project's three focus areas

- Drag reduction devices
- Experimental testing
- Computational modeling

A summary is given in the introduction portion of this report and detailed reports from each participating organization are provided in the appendices. Included are experimental results and plans by NASA, USC, GTRI, and LLNL in Appendices A through D. The computational results from LLNL and SNL for the integrated tractor-trailer benchmark geometry called the Ground Transportation System (GTS) model are in Appendices D and E, from ANL for the Generic Conventional Model (GCM, a.k.a. SLRT) in Appendix F, by LLNL for the tractor-trailer gap and trailer wake flow investigations in Appendix D, and turbulence model development and benchmark simulations being investigated by Caltech in Appendix G. USC is also investigating an acoustic drag reduction device that has been named 'Mozart' (Appendix B), GTRI continues their investigation of a blowing device (Appendix C), and LLNL presents their idea for a gap drag reduction device (Appendix D).

Drag Reduction Devices

There are three areas identified for aero drag reduction and several drag reduction devices have been investigated

- **Tractor-Trailer Gap**
  Stabilizing devices, cab extenders
- **Wheels/Underbody**
  Skirts/lowboy trailer ($\Delta C_D \sim 0.05$), splitter plate
- **Trailer Base**
  Boattail plates ($\Delta C_D \sim 0.05$), base flaps ($\Delta C_D \sim 0.08$), rounded edges, and pneumatics

The drag reduction for various device add-ons is shown in Figure 1, as a function of yaw angle. These results were obtained in the NASA Ames 12-ft Pressure Wind Tunnel (PWT) using the realistic GCM geometry, tested at realistic highway Reynolds numbers. Side and roof extenders are shown to significantly reduce the drag and high yaw. Base flaps, as shown in a close-up in Figure 2, are expected to provide 50% more drag reduction than boattails. For a tractor-trailer with a $C_D = 0.55$ the percent drag reduction ($\Delta C_D/C_D$) utilizing base flaps (~15%) and side skirts and/or a low boy (~10%) is estimated at 22 to 25%. Thus, the use of base flaps and skirts would provide an 11 to 12% fuel savings which should result in a $3 billion per year fuel cost savings in the US. (Note that the cost of the device and possible maintenance over the year should also be considered for determining the overall cost savings to the fleet owner.)

The base flaps are simple flat plates mounted on the edges of the back end of a trailer. The lengths of the plates match the dimensions of the trailer base (two 11.5-ft-long plates on the sides and two 8.5-ft-long plates on the top and bottom). The width of the plates or how much they protrude from the trailer is about 1/4 the width of the trailer or about 2 feet. Tilting the flaps about 20° inward away from being flush with the trailer sides appears to provide the optimum drag reduction. The optimum flap angle for an on road vehicle is yet to be determined, but we expect it to be near 20°.

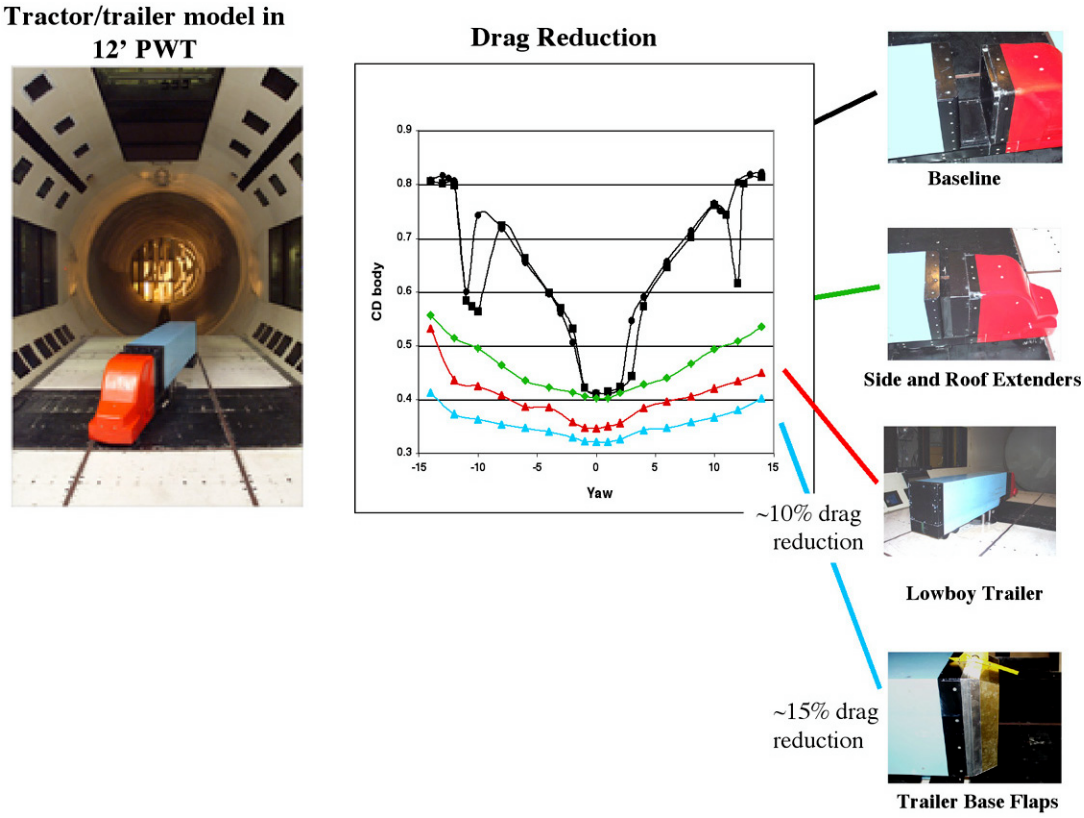

Figure 1. GCM in tunnel, variation in body drag coefficient with yaw angle for various configurations and device add-ons, and PIV and pressure sensitive paint results for baseline and with side extenders

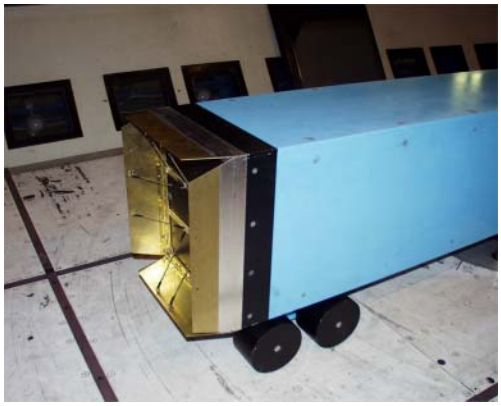

Figure 2. Base flaps (gold colored) mounted on back end of trailer (blue) in NASA's 12-ft pressure wind tunnel

Development has continued on tangential blowing aircraft-based technology to reduce HV drag by eliminating aft separation on the trailer and recovering base pressure on the back doors. Smaller-scale tunnel results have shown measured drag reductions as high as 15-18% due to blowing (without consideration of the energy required to blow) and 10-12% due to the device's corner rounding, for a total of 25 to 30%. Blowing also has the potential to increase drag for use in braking, to reduce drag due to side winds, and to overcome directional instabilities due to side gusts. A maximum of 5-6% fuel economy increase (not accounting for energy use for blowing) resulted during on-track HV fuel economy tests, and full-scale testing of a Pneumatic Sports Utility Vehicle is ongoing.

Road testing the drag reduction devices is needed to determine

- On road fuel savings,
- Optimal flap deflection angle for various tractor-trailer geometries,
- Optimal flap shape,
- Optimum skirt height,
- Durability, practicality, safety, ease of operation of proposed devices, and
- Impact on truck braking capability.

It is recommended that road testing include

- Instantaneous broadcast fuel rate (1/2 second updates),
- Repeated forward and back trip runs over known, instrumented highways (e.g., South-to-North and North-to-South runs over a portion of California I-15), and
- Base flap device evaluated in close-following combinations of 1 to 3 trucks.

To recognize these levels of fuel savings by the most effective use of drag reduction devices, the involvement and acceptance by tractor manufacturers, trucking associations, fleet owners, and drivers is critical. It is thus important to

- Solicit input and feedback from these organizations for design of base flaps and low boy and/or skirt construction,
- Demonstrate "actual" fuel savings from road tests and interest OEMs in doing testing, and
- Make site visits or attend DOE's Industry Consortium's Working Group meetings to encourage input and feedback.

Suggestions included encouraging the DOE Industry Consortium to road test base flaps and skirts or low boys as part of their DOE funded effort. Another suggestion is to contract with California Partners for Advanced Transit and Highways (PATH) to perform the proposed road tests as part of their 3-truck demonstration platoon.

Experimental Findings and Suggested Guidance

Experiments have been conducted on a Generic Conventional Model (GCM) in the NASA Ames 7-ft × 10-ft wind tunnel for Reynolds numbers (Re) of 1 million based on the width of the trailer, which corresponds to a full-scale vehicle traveling at roughly 15-mph. Experiments have also been performed on the GCM geometry in the NASA Ames 12-ft pressure wind tunnel (PWT) for Re of 1 and 6 million, where the later corresponds to a full-scale vehicle traveling at 80-mph. Geometry configurations included the addition of tractor side extenders, a low boy trailer, and boattails and angled flaps on the trailer's trailing edge. The results in the PWT are obtained for a constant Mach number (Ma = 0.15) by pressurizing the tunnel. This allows for the determination of Re and geometry effects. Yaw angles were varied from +14 to -14° measured from the vehicle length axis and wind direction so that

accurate wind-averaged drag could be determined, in addition to determining the effect of yaw angle. The following is a list of experimental techniques and measurements:

- Internal balance measured the vehicle forces and moments
- Load cells measured the drag for the body axis and yawing moment of the tractor
- Static pressure taps on the model (476) and taps on the walls and floor (368) measured static pressure conditions
- Unsteady pressure transducers (14) provide a pressure time history on the surface of the vehicle
- Three-dimensional particle image velocimetry (PIV) provided a time history of the velocity field on planes in the wake of the vehicle and in the tractor-trailer gap.

Drag measurements alone are not sufficient to provide an understanding of the impact of geometry modifications and direction for design improvements. It is recommended that advanced measurement techniques like PIV and pressure sensitive paint (PSP) be included. These advanced techniques provide important information on the global and local structure of the flow and can provide clear design direction.

The following are the determined Re effects (note: Re is based on the width of the trailer and freestream velocity):

- Re effects on C_D are in general minimal for experiments with Re above 1 million. This finding supports the common use of scaled down vehicles and Re below typical highway Re for experimentation.
- It should be noted that some Re influence was apparent on the flow structure in the tractor-trailer gap and the back end of the trailer. It was most apparent in the upper portion of the flow region in the gap and in the wake. Thus, some inaccuracies should be considered when evaluating gap and wake drag reduction devices at lower than highway Re. Low Re experiments should provide ball park estimates, but accurate optimization of devices may require road testing.
- Edge radius effects and/or the cleanliness of the vehicle upstream flow are critical to achieving accurate predictions. Corner radii on the leading edge of the vehicle should provide Re > 50,000, based on corner radius and tunnel freestream velocity. Tripping the flow at the vehicle leading edge may also be required to avoid flow separation.

Computational Findings and Suggested Guidelines

Team members from LLNL, SNL, ANL, and Caltech are investigating a wide range of turbulence models including steady and unsteady Reynolds-averaged Navier-Stokes (RANS and URANS, respectively), large-eddy simulation (LES), and hybrid methods that use a combination RANS and LES models in the simulation. In addition, various numerical approaches are being considered including finite volume, finite element, and vortex methods. The focus of the focus of this years effort was steady RANS with and without the use of wall functions. Wall functions provide an approximation to the flow field in the wall region and the flow field is not resolved.

The following are the general observations and guidelines for steady RANS modeling:

- Conclusions on predictive capability of a turbulence model can only be determined with grid converged solutions. Predicted flow structures in separated regions, like the trailer wake, vary significantly with grid refinement. Variation in overall drag is not substantial but still apparent with grid refinement.
- When using wall functions, the first wall point should be held fixed while refining the grid (i.e., the distance from this grid point to the wall should not change), but it is appropriate to decrease the width of the wall elements while refining the grid (i.e., refinement in direction tangent to walls).
- The computed overall vehicle drag is highly dependent on the choice of turbulent steady RANS model. Solutions may disagree with measurements by 0.5 to 50% for 0 degree yaw and by even higher percentages at yaw angles. Thus, the performance of steady RANS models for a given geometry is not predictable and experimental results to determine ball park

accuracy is critical when relying on steady RANS for design guidance.
- Steady RANS models generally do a good job predicting the flow on the front and sides of the vehicle, where the flow stays attached and does not exhibit separation and recirculation zones.
- The flow structure in the trailer wake presented by the time-averaged experimental data does not compare with that computed with the steady RANS models. The trailer wake is a region of transient full flow separation and large recirculation zones. Thus, use of steady RANS to evaluate drag reduction devices in the trailer wake and tractor-trailer gap may provide inaccurate design guidance.

Near term plans are to organize similar types of guidelines related to the performance of unsteady RANS, LES, and hybrid models.

Conclusions

The DOE Heavy Vehicle Aero Drag Team has successfully modeled the flow field around a generic conventional model both experimentally and computationally. This effort has provided detailed insight into the flow phenomena, which has lead to the successful development of drag reduction devices. Evaluation of an angled plate base drag device (15%) with the use of a low boy trailer and/or side skirts (10%) indicates an expected drag reduction of 22 to 25%. Use of these devices should provide an 11 to 12% fuel savings which is estimated to result in a $3 billion per year fuel cost savings in the US. Efforts continue on investigation of acoustic and pneumatic devices to reduce base and separation drag, and some new ideas for reducing tractor-trailer gap drag. Future new areas being investigated are wheel and wheel well aerodynamics related to brake cooling, tire splash and spray, and an entire new related area of investigation involving the evaluation of coal car aerodynamics with the objective of identifying drag reduction devices for filled and empty cars.

B. Experimental Modeling of Generic Conventional Model

Principal Investigator: J. Ross
Co-Investigators: D. Satran, J.T. Heineck, S. Walker, and D. Yaste
NASA Ames Research Center
MS 260-1, Moffett Field, CA 94035
(650) 604-6722; jcross@mail.arc.nasa.gov

Technology Development Manager: Sid Diamond
(202) 586-8032; sid.diamond@ee.doe.gov
Technical Program Manager: Jules Routbort
(630) 252-5065; routbort@anl.gov

Contractor: NASA Ames Research Center
Contract No.: DE-AI01-99EE50559

Objective

- Acquire data for calibrating CFD codes used to predict the performance of generic vehicles representing Class 8 tractor-trailers.
- Evaluate drag reduction devices.

Approach

- Perform experiments utilizing standard and advanced measurement techniques in the NASA Ames 7-ft × 10-ft wind tunnel and 12-ft pressure wind tunnel on the Generic Conventional Model (GCM).
- Include evaluation of side and roof extenders, boattail plates, base flaps, trailer skirts, and lowboy trailer configurations.

Accomplishments

- Two test entries were completed in the 12-foot pressure wind tunnel to obtain the aerodynamic data on the GCM.
- Limited Reynolds number effects were found for the GCM.
- Base flaps were the most effective drag reduction device for trailers.
- Trailer skirts produced some drag reduction but the lowboy trailer configuration was more effective.
- Side and roof extenders were effective for the tractor.

Future Direction

- Document the test results and publish the database for computational code validation support.
- Begin experimental efforts for the evaluation of wheel and wheel well aerodynamics for brake cooling and reduction of splash and spray.
- Begin experimental efforts for the evaluation of coal car aerodynamics.

Introduction

In cooperation with the U.S. Department of Energy, a series of wind tunnel tests have been conducted by the Experimental Aerophysics Group at NASA Ames Research Center on generic vehicles representing Class 8 tractor-trailers. The primary goal for these wind tunnel tests was to produce high quality data for validating Computational Fluid Dynamics (CFD) codes. The final test was conducted in the NASA Ames Research Center's 12-foot pressure wind tunnel generating data at a variety of Reynolds Numbers, from 1/8 to full-scale road values, on the same 1/8th-scale model.

Current CFD codes have a difficult time accurately predicting the drag levels for tractor-trailer configurations. Enhanced CFD codes that can reliably produce accurate results will enable industry to better understand all aspects of the flow around trucks, leading to better integrated tractor/trailer designs. To properly validate the CFD codes, the aerodynamic databases include vehicle forces and moments, surface pressures, fluctuating pressures on the rear of the tractor and front and rear of the trailer, skin friction measurements, and 3D Particle Image Velocimetry (PIV) off-body flow field measurements in the gap between the tractor and trailer and in the wake behind the trailer.

Besides generating a database for validating CFD codes, the Experimental Aerophysics Group has investigated numerous drag reduction devices. Some examples of the devices include the side and roof extenders which reduce the gap between the tractor and trailer, the lowboy trailer configuration where the ground clearance is reduced to a minimum and the wheels are covered by fairings, and base flaps which help turn the flow inward as it leaves the back of the trailer reducing the size of the wake and providing increased base pressure. Additional drag reduction concepts included boattail plates, gap fairings, and trailer skirts.

Results

As can be seen in Figures 1 through 5, significant drag reduction is produced with the different

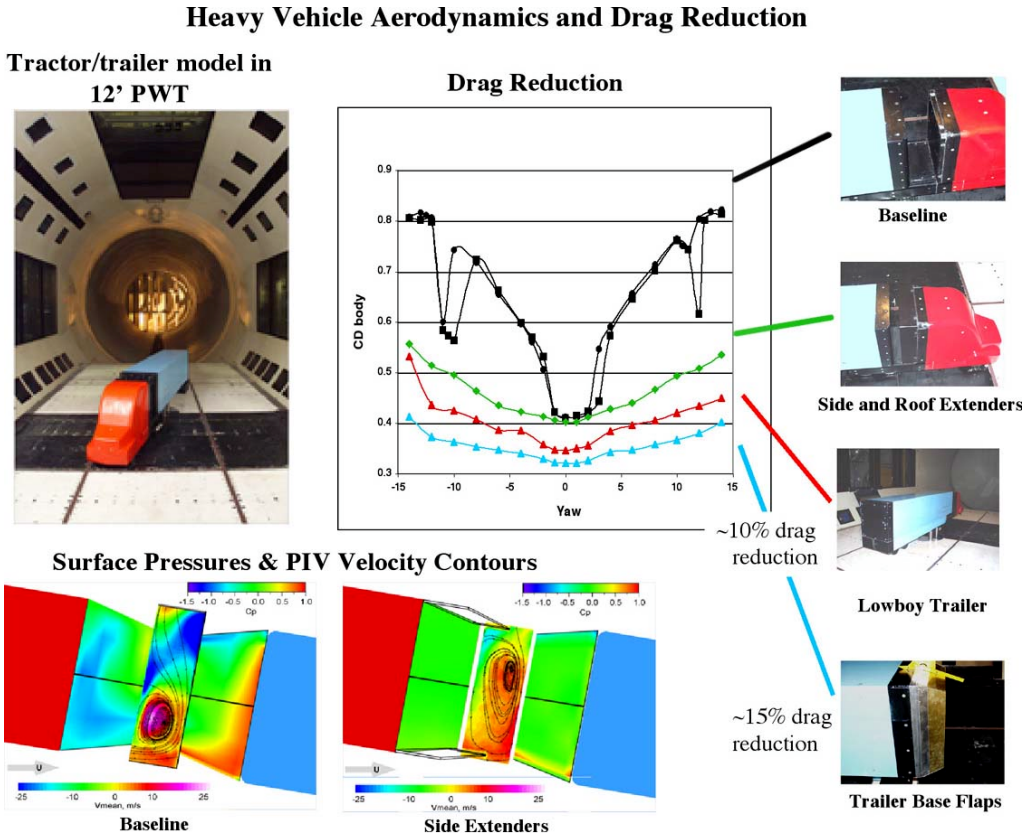

Figure 1. GCM in tunnel, variation in body drag coefficient with yaw angle for various configurations and device add-ons, and PIV and pressure sensitive paint results for baseline and with side extenders

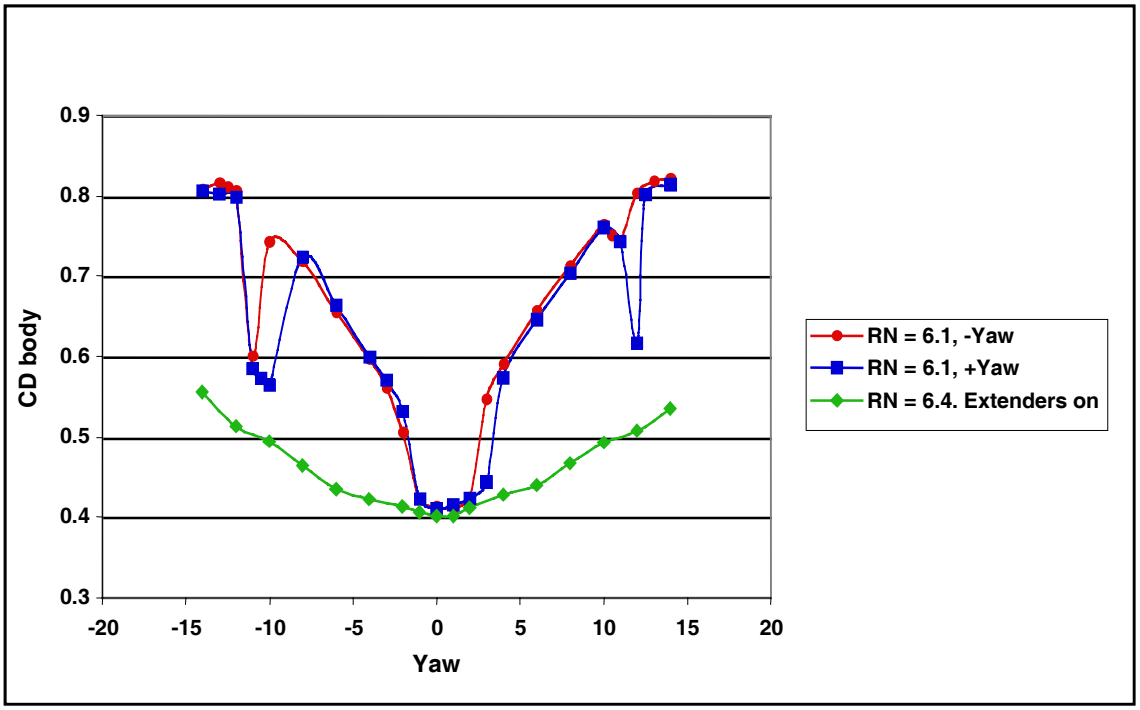

Figure 2. Drag coefficient versus yaw angle with and without side extenders for Re = 6 million

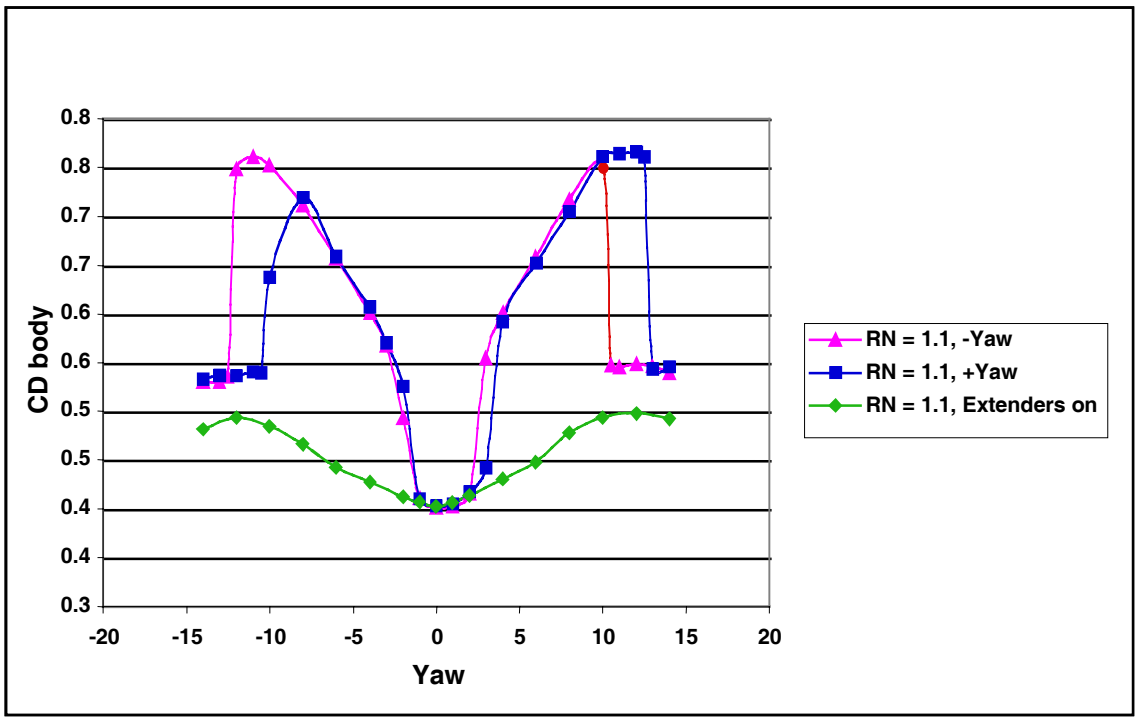

Figure 3. Drag coefficient versus yaw angle with and without side extenders for Re = 1.1 million

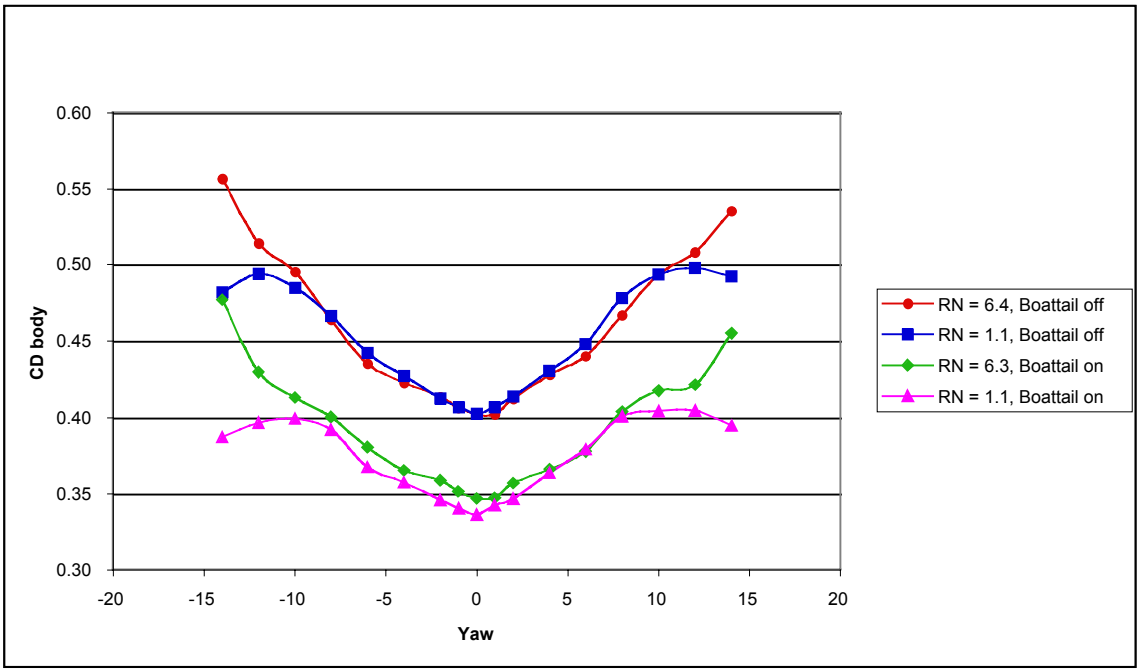

Figure 4. Drag coefficient versus yaw angle with and without boattail plates for Re = 1.1 and 6 million

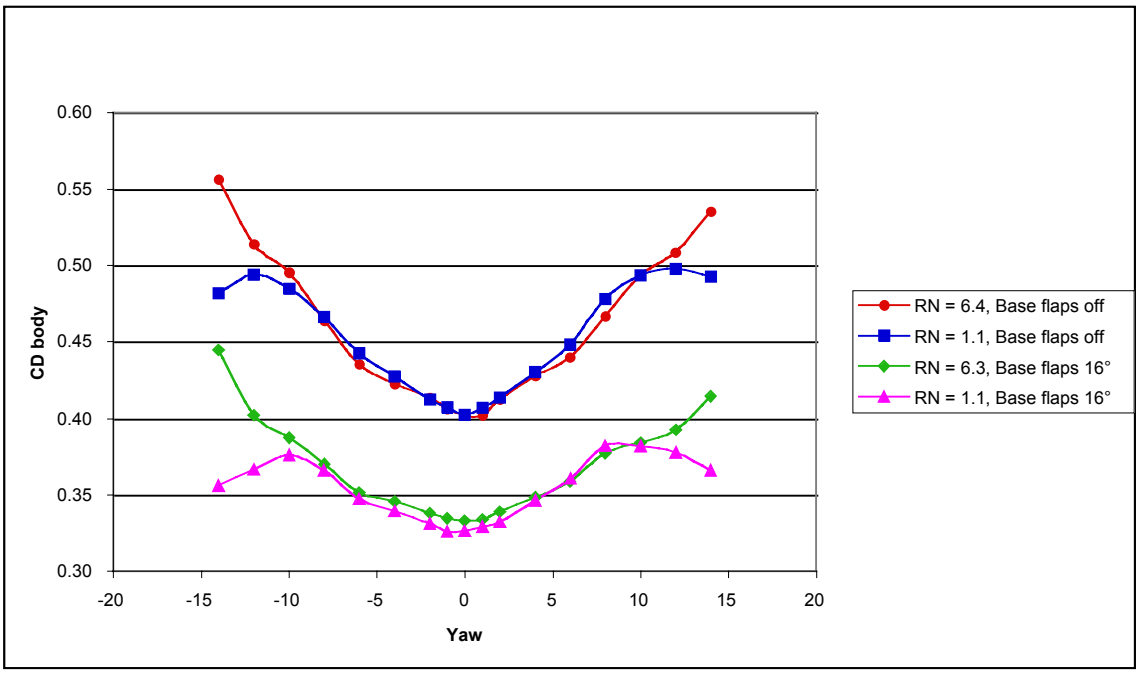

Figure 5. Drag coefficient versus yaw angle with and without base flaps for Re = 1.1 and 6 million

devices. The basic truck geometry produced high levels of drag at yaw angles greater than 4°. The increase in drag was eliminated with the addition of the side and roof extenders. The lowboy trailer produced drag reduction on the order of 10% and was comparable to the boattail plates. The base flaps were the most successful trailer modification and produced drag reduction on the order of 15%. If the lowboy trailer is combined with the boat tails or base flaps, the results are additive with a drag reduction of over 20%. Although there were some Reynolds number effects, for the most part the effects were small and results were adequately predicted using data generated at lower Reynolds numbers.

A significant portion of the effort was expended in gathering the PIV data. This was the first time a PIV system was used in a pressurized facility, which made a complex system even more complicated [1]. Although the 12-foot wind tunnel has better optical access than most wind tunnels, the access that was available created additional challenges for the PIV system. Significant changes in the flow field between the tractor and trailer are documented by the PIV system in Figure 1 with and without the rear side extenders. The addition of the roof extender provided a slight improvement in the drag reduction to that provided by the side extenders.

Conclusions and Future Activities

Two test entries were completed in the 12-foot pressure wind tunnel to obtain the aerodynamic data on the GCM. The results indicated limited Reynolds number effects. The base flaps were the most effective drag reduction device for trailers tested. Trailer skirts produced some drag reduction but the lowboy trailer configuration was more effective. Side and roof extenders were effective drag reducers for the tractor.

Future activities planned for FY04 include documentation of the test results and publish the database for computational code validation support, begin experimental efforts for the evaluation of wheel and wheel well aerodynamics for brake cooling and reduction of splash and spray, and begin experimental efforts for the evaluation of coal car aerodynamics.

Reference

1. J.T. Heineck, S.M. Walker, D.M. Yaste, “The Development of a 3C-PIV System for the 12-Foot Pressure Tunnel at NASA Ames Research Center,” 20th International Congress for Instrumentation Aerospace Simulation Facilities (ICASF), DLR Gottingen, August 25-29, 2003.

C. Experimental Measurement of the Flow Field of Heavy Trucks

Principal Investigator: F. Browand
Co-Investigators: M. Hammache and T.-Y. Hsu
Aerospace & Mechanical Engineering, University of Southern California
RRB 203, Los Angeles CA 90089-1191
(213) 740-5359; fax: (213)740-7774; browand@spock.usc.edu

Technology Development Manager: Sid Diamond
(202) 586-8032; sid.diamond@ee.doe.gov
Technical Program Manager: Jules Routbort
(630) 252-5065; routbort@anl.gov

Contractor: DOE Oakland Operations Office, Berkeley Site Office
Contract No.: DE-AC03-98EE50512

Objective

- Improve the performance of heavy trucks by reducing aerodynamic drag.

Approach

- Produce a smaller truck wake and a lower truck drag by providing for active flow control at the base of the trailer utilizing an arrangement of base flaps.
- Evaluate the importance of the gap between tractor and trailer in producing drag.

Accomplishments

- Wind tunnel tests of flow control device at trailer base document improvements in drag of ΔC_D = .06-.08, or about 13–14% for a modern truck.
- Wind tunnel flow field studies document the appearance of violent cross-gap flows under certain conditions. The cross-gap flow separates the flow along the side of the trailer and increases drag. Suggestions have been made to minimize this unwanted cross-gap flow.

Future Direction

- Test for additional drag saving in wind tunnel models by increasing the strength of the active flow control.
- Perform over-the-road testing to verify drag savings for the base flap device.
- Initiate a program and a new testing apparatus to study wheel/tire splash and spray.

Introduction

This report describes the progress we have made on two separate aerodynamic problems (a) reducing the base drag of a tractor-trailer with a combination of passive and active control devices, and (b) describing the sensitivity of the drag to the geometry of the gap between tractor and trailer. Included in this report is a description of work we have completed, and work we will continue into FY04.

Reducing Base Drag

There are two general approaches for the reduction of base drag. One approach, we would term passive control, is to alter the geometry of the base region in some way. Cooper shows that the drag coefficient

for a typical straight-sided truck at 0.78 can be reduced to a value on the order of 0.72 by the use of thin plates attached along the edges of the trailer base [1]. Further, Cooper demonstrates that the effectiveness of the drag reduction increases with non-dimensional flap length, *l*, defined as $l = L_f/\mathrm{sqrt}(A)$, where L_f is the flap length and A is the cross-sectional area of a truck. He points out that most of the drag reduction is accomplished for flap length less than a value of approximately, $l = 0.18$. Flaps such as those studied by Cooper can be seen in Figure 1 installed on a model truck test in a wind tunnel at NASA Ames.

The second approach is to seek additional drag reduction by means of an active forcing (such as an oscillating flap, or a blowing slot), meant to alter the boundary layer properties — usually to avoid an unwanted separation. Nishri and Wygnanski (1998) show that the effectiveness in delaying flow separation is determined by the location of the jet, the frequency of the induced oscillation, the net momentum flux coefficient, and the shape size of the slot. The frequency of the induced oscillation, f, is non-dimensionalized by the flap length and free-stream velocity, U_∞. It is defined as $F^+ = \frac{f^* L_f}{U_\infty}$. The net oscillatory momentum flux coefficient, C_μ, is defined as $C_\mu = 2 * \frac{g}{L_f} * (\frac{U_j}{U_\infty})^2$, where g is the slot height, i.e., the gap between the flap and the side wall, and U_j is the amplitude of the oscillatory jet fluctuation. Favorable delays in separation are obtained for slot heights on the order of 1/3-1/2 of the incoming boundary layer displacement thickness, and for C_μ values less than 0.1%. The most effective non-dimensional frequencies appear to lie in the range $F^+ = 0.3–1.5$.

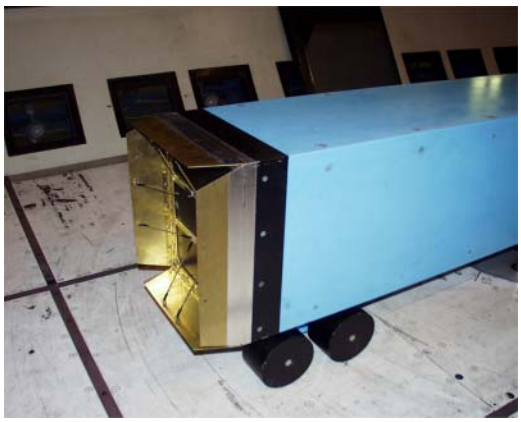

Figure 1. Base flaps (gold colored) mounted on back end of trailer (blue) in NASA's 12-ft pressure wind tunnel

Our approach encompasses both a modification of the base geometry by means of the addition of flat-panel flaps, and an additional active control by means of an oscillatory mass flow perturbation within the boundary layer meant to delay flow separation over the surface of the flaps. The (flat) flaps are attached to the trailer base along the trailer base edges, and are inclined to the free stream to close the wake more efficiently.

The experiments utilizing oscillatory perturbations are conducted in the Dryden wind tunnel at the USC Ground Vehicle Aerodynamics Laboratory. A roughly 1/15 scale model resembling a trailer is utilized for the study (see Figure 2). The model is fitted with a shaped nose-piece to ensure attached flow over the forward portion of the model. The model is equipped with a force balance to measure drag. The Reynolds numbers (based on the square-root of the model cross-sectional area), range from 0.1×10^6 to 0.4×10^6. A sine wave is chosen as the forcing function. The forcing frequency is zero or within the range 40–600 Hz. The corresponding non-dimensional frequencies are, $F^+ = 0$, 0.17–3.93. The oscillatory momentum flux coefficient, C_μ, ranges from 0 (no forcing) to 2%.

The present study has found that a simple, passive base-flap deflection — no forcing — produces significant drag saving. The effect of flap angle upon drag reduction is shown in Figure 3. The horizontal axis represents the flap angle in degrees, and the vertical axis represents the change in drag coefficient, $\Delta C_D = C_{Dnoflaps} - C_{Dflaps}$. A positive value of ΔC_D corresponds to a *reduction* in drag. Data is shown here from three widely different experiments — one performed in our wind tunnel, one test recently performed in the 12-foot wind tunnel at NASA Ames, and Cooper's original results. All of the ΔC_D curves have a roughly similar shape. Drag savings first increase and then decrease with increasing flap angle. Thus there is an optimum angle for maximum drag saving. The maximum saving is in the range $\Delta C_D \approx .06 - .08$ for all three

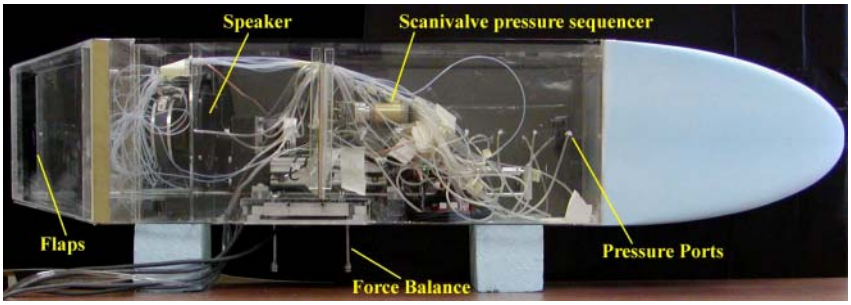

(a)

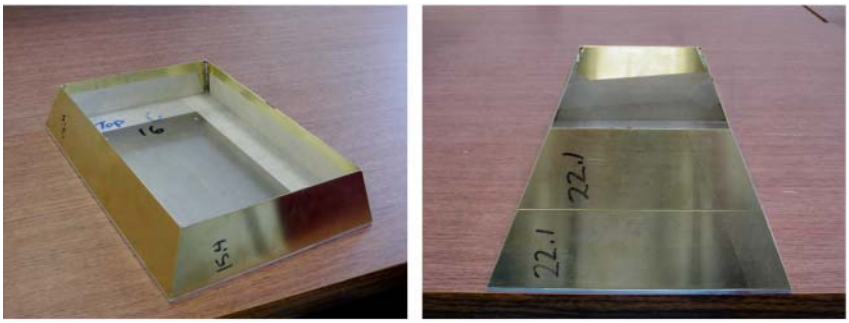

(b)

Figure 2. USC model equipped with rounded nose and base flaps

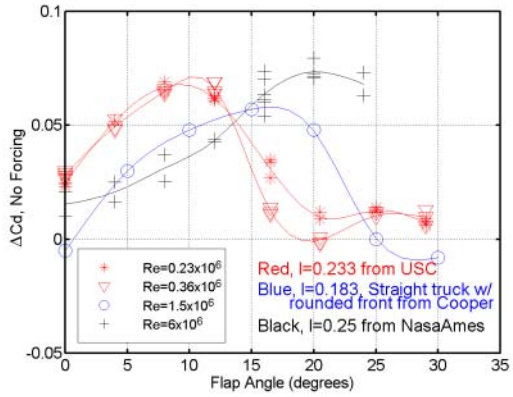

Figure 3. Base drag improvements, expressed as a change in drag coefficient for three separate experiments

experiments. The three separate tests are accomplished in three different wind tunnels using models of different geometry. The data thus suggest a robust drag saving that is neither particularly dependent upon the details of truck shape nor upon the Reynolds number of operation. However, the angle for maximum saving does seem to depend upon Reynolds number. The optimum angle seems to increase steadily from 9° to 12° at 0.3×10^6 to perhaps 20° at 6×10^6.

Now consider the addition of oscillatory blowing/suction along the edges of the model base, coincident with the origin of the flap. The purpose of the oscillatory blowing/suction is to attempt to maintain attached flow over the flap for larger flap deflection angles, and thereby to further reduce drag. Figure 4 summarizes the best of our results. The drag coefficient difference, $\Delta C_{D,}$ is shown for the short flap length — with and without oscillatory blowing. The experimental reliability is indicated by the scatter of data points representing multiple trials. Blue curves are the no-force cases. The results in red, for a momentum coefficients of $C_\mu = 0.15\%$ and 2%, demonstrate the effectiveness of oscillatory blowing/suction. There is a modest additional drag saving at the higher flap angles, but the application of forcing has very little effect in the vicinity of peak saving. Thus the peak saving is almost unchanged. The cause of this unexpected result is still under investigation. Examination of the forced and unforced results in the vicinity of 12° suggests that the momentum addition does delay the onset of

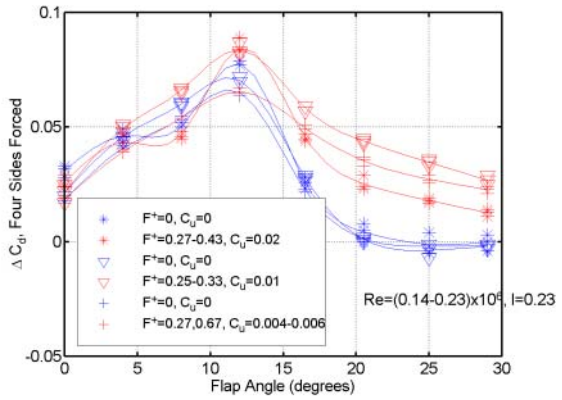

Figure 4. Effect of oscillatory forcing on drag decrease

separation in some manner. However, we had anticipated that in the presence of forcing and delayed separation, the drag saving would continue to increase beyond the unforced peak at 9–12°. Rather, the demonstrated effect of forcing is to broaden the peak region by extension to larger angles but not to increase the maximum value of drag saving.

The optimum forcing frequency definitely lies in the range $F^+ \approx 0.27$ that will effect flow modification, but that forcing amplitude is critical. We begin to see noticeable change only at momentum coefficients on the order of 10^{-3} or greater ($C_\mu \geq 0.1\%$). Nishri & Wygnanski show observable increases in lift over deflected flaps at momentum coefficients as small as 0.01% [2]. Evidently drag reduction for a three-dimensional body such as ours is a much more subtle proposition. The present results also show that oscillatory momentum addition has little effect on drag reduction unless the net oscillatory momentum flux coefficient is equal or greater than 0.1%. Increasing the oscillatory momentum perturbation to a coefficient value of 2% produces drag savings at angles greater than 9–12°, but has very little effect upon the maximum saving at 9–12°.

We are presently performing DPIV studies (Digital Particle Image Velocimetry) of the flow adjacent to the flap with and without the oscillatory acoustic/blowing. The intent is to answer the question regarding the state of the boundary layer and the degree of attached/unattached flow present. The cases studied to date are the 0° and 12° flap angles. For the 0° flaps angle, the wake profiles obtained from the ensemble average of 350 image pairs suggest that there is no difference between forcing and non-forcing.

The preliminary data also suggests that the flow is attached up to flap angle equal to 12°. However, there is a small drag reduction at a 12° flap angle (see Figure 4), and this drag reduction is reflected in the flow over the flap as seen by the detailed flow field (DPIV) map shown in Figure 5. Velocity contours are shown in the wake region just downstream from the flap — blue for the unforced case, and red for the forced. The suggestion is that the wake is slight more narrow when oscillatory forcing is present.

Follow-on experiments are planned to investigate a larger range of forcing amplitudes, and a variety forcing-function duty cycles. In addition, DPIV will be used to capture the detailed flow-field in the vicinity of the flap for all cases.

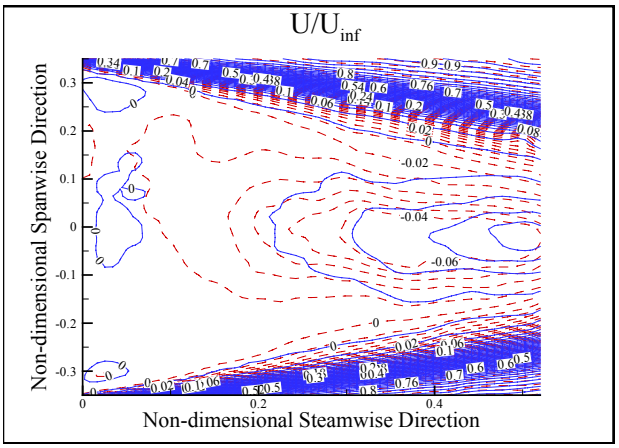

Figure 5. Contour plot of free-stream velocity in the wake region

Drag Rise Due to the Geometry of the Gap Between Tractor and Trailer

The second part of this report summarizes the wind tunnel experiments on the aerodynamics of tractor-trailer models to show that the drag on the model is sensitive to the width of the tractor-trailer gap (G), and to the angle of yaw with respect to wind direction. The measurements are performed at a wind tunnel speed of approximately 26 m/s. The model Reynolds number for the tests, based upon the square root of the truck cross-sectional area, $\sqrt{A}$, is about 310,000. Figure 6 shows both tractor and

trailer resting on an interior turntable in the ground plane. The turntable allows the models to be yawed with respect to the flow direction.

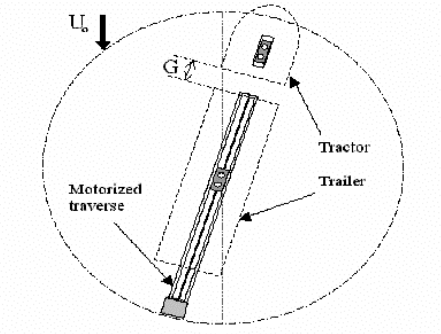

Figure 6. Detail of turntable and traverse mechanism inside ground plane

The drag on the tractor and trailer, at zero-yaw, as a function of gap width are plotted in Figure 7. In the range of G/√A of 0.1 to 0.5, the trailer experiences less drag than the tractor, due to the shielding effect. As the gap opens up beyond approximately 0.5, the total drag rises rapidly to large values — most of the increased drag is attributable to the trailer.

The DPIV measurement technique is adopted in this experiment to visualize and quantify the flow in the gap area. Whole-field velocity measurements are obtained for various combinations of gap width and angles of yaw, though the present discussion is limited to zero-yaw cases. A total of 350 instantaneous realizations are acquired for each combination of gap and yaw, and for three horizontal planes within the gap — a total of 36 combinations. Changes of the flow structure

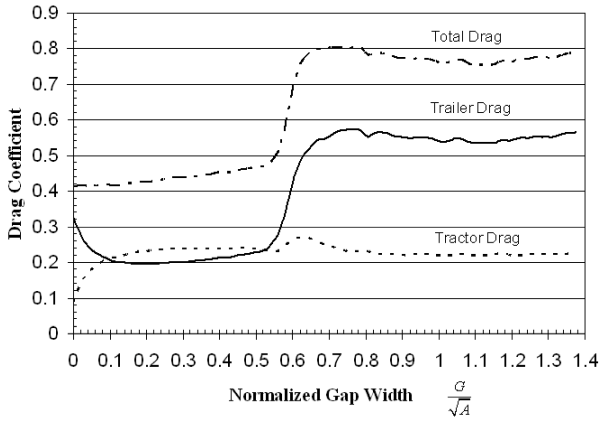

Figure 7. Drag coefficient versus gap length

within the gap region are investigated by performing various forms of conditional-averaging.

At low gap width, typically below G/√A ~ 0.5, the flow in the gap is turbulent, but steady in a broad sense — consisting of a re-circulating in the form of a torus. As the gap increases, the flow in the gap becomes highly unsteady with large cross-gap flows that alternate from side to side. An example of this variability is demonstrated in Figure 8. A certain fraction of the time, the flow behavior is described by the left-hand portion of the picture labeled symmetric. At other times, the flow exhibits a highly asymmetric pattern and exits from one side of the gap. The mirror image of this state is also seen, although it is not illustrated here. These highly asymmetric flow states produce large wake regions along the sides of the trailer, and signal the drag rise onset seen in Figure 8.

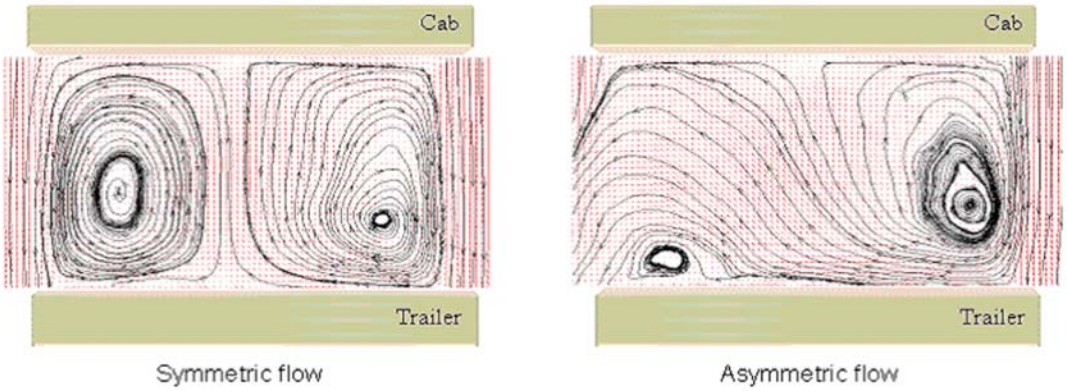

Figure 8. Ensemble-averaged streamline patterns of the flow in the gap at zero yaw, G/√A = 0.55; (a) symmetric flow, (b) asymmetric flow

The final figure describes the drag savings that can be realized by arranging two truck-like models in a tandem configuration. The truck-like models are either "blunt" or "rounded." Separately, the truck shapes have drag coefficients of approximately 0.94, and 0.51, respectively. Four tandem combinations are possible from the two shapes, as depicted in Figure 9. The quantity plotted in Figure 9 is the total drag of the two trucks divided by their drag in isolation as a function of the separation between the trucks. All of the curves should asymptote to unity at large values of separation. At small separations all of the four combinations experience a drag saving as one might anticipate. It is interesting — and unanticipated — that the degree of drag saving for the pairs of trucks depends upon which truck leads!

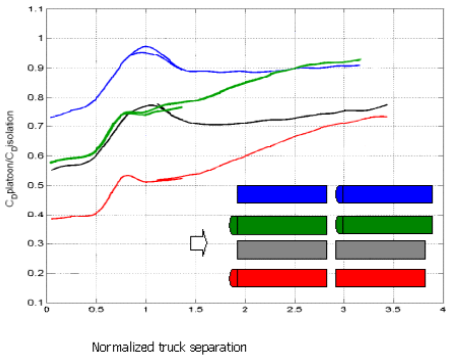

Figure 9. The average drag of the two-truck platoon for all four configurations

References

1. K.R. Cooper: The effect of front-edge rounding and rear-edge shaping on the aerodynamic drag of bluff vehicles in ground proximity. SAE paper No. 850288 (1985).
2. B. Nishri & I. Wygnanski, "Effects of Periodic Excitation on Turbulent Flow Separation from a Flap," *AIAA Journal*, Vol. 36, No. 4 (April 1998).

D. Continued Development and Improvement of Pneumatic Heavy Vehicles

Principal Investigator: Robert J. Englar
Georgia Tech Research Institute (GTRI)
Atlanta, GA 30332-0844
(770) 528-3222; fax: (770) 528-7077;
bob.englar@gtri.gatech.edu

Technology Development Manager: Sid Diamond
(202) 586-8032; sid.diamond@ee.doe.gov
Technical Program Manager: Jules Routbort
(630) 252-5065; routbort@anl.gov

Contractor: DOE – NNSA, NNSA Service Center, Oakland, CA
Contract No.: DE-AC03-02EE50691

Objective

- Previous smaller-scale experimental evaluations at GTRI have demonstrated up to 15-18% reduction in aerodynamic drag coefficient due to blowing (without consideration of the energy required to blow) and 10-12% due to the device's corner rounding for a combined drag reduction of 25-30%. We are continuing the development of this pneumatic aerodynamic technology for parasitic energy loss reduction, fuel economy improvement, reduced emissions, and increased safety of operations for Heavy Vehicles (HV).
- Confirm these same benefits for Pneumatic Sports Utility Vehicles (PSUVs).

Approach

- Enhance the pneumatic aerodynamic capabilities of existing wind-tunnel and full-scale HV test models/vehicles, and then modify them to improve the drag-reduction properties exhibited during our Phase I of SAE Type-II fuel economy on-track testing.
- Identify pneumatic aerodynamic and geometry improvements to increase fuel economy by an additional factor of 2 to 4 over that exhibited in full-scale HV track tests.
- Conduct full-scale wind-tunnel development of Pneumatic SUVs with blowing applied to reduce drag; increase braking; increase traction; and improve stability and control.

Accomplishments

- New wind-tunnel tests have shown blowing produces drag reductions due to both aft flow separation elimination and base pressure recovery. New tests also demonstrated that active blowing control can increase drag and also reduce side-wind effects showing that the device has the potential to help braking and safety of operation for both pneumatic HVs and SUVs.
- Improvements needed for the Phase II full-scale PHV track test have been identified; new tunnel model is designed and being constructed to test in GTRI tunnel and confirm these before test vehicle modifications.
- Design of full-scale PHV Phase II test vehicle based on these results is underway. These tests will be used to confirm the reduction in drag measured in wind tunnel tests. The energy required to blow the air will be measured.

Future Direction

- Conduct Phase II of on-road full-scale HV testing and demonstrations of pneumatic aerodynamic drag-reduction, fuel-economy and safety of operation techniques to provide a confirming database allowing application of this technology to operational heavy vehicles and SUVs.

Introduction

Since aerodynamic drag is the major component of Heavy Vehicle (HV) resistance at highway speed and thus their related fuel economy, GTRI has been applying advanced aircraft aerodynamic technology using blowing to reduce that drag generation on generally-bluff high-drag vehicles. Using the pneumatic aerodynamic technology known as Circulation Control [1] and certain trailer and gap geometry changes, we have been able to reduce drag coefficient (C_D) on HV models by up to 15-18% reduction in aerodynamic drag coefficient due to blowing and 10-12% due to the device's corner rounding, for a total of 25-30% during a 4-year tunnel test program for DOE [2]. Of further advantage, we could also increase drag as needed for braking during downhill operation by rapidly blowing select trailing edge surfaces on the trailer without any moving parts, or could potentially also reduce the huge drag increase and loss of stability which occur when an HV experiences side winds or gusts. This multi-function potential of the blown configurations is seen in the wind tunnel data shown of Figure 1.

Full-scale fuel economy tests were conducted [3] at the beginning of the current 2-year DOE program. Whereas preliminary tuning tests showed unofficial Fuel Economy Increase (%FEI) of over 15%, the SAE Type-II official test-track results on a somewhat different Pneumatic HV (PHV) configuration showed maximum %FEI of only 5% - 6%, not accounting for energy use for blowing. The current program has thus concentrated on: determining the difference between wind-tunnel results and the less-than-expected full-scale performance; correcting the blown configuration; and preparing for a second fuel economy evaluation with the improved PHV vehicle. It is noted here that the present DOE program does not correspond directly to FY03. Funding for year-long Phase V discussed below started 7/14/2002, and Phase VI (FY 03 funding) was not initiated until May 29, 2003. The recent results of both Phases are presented

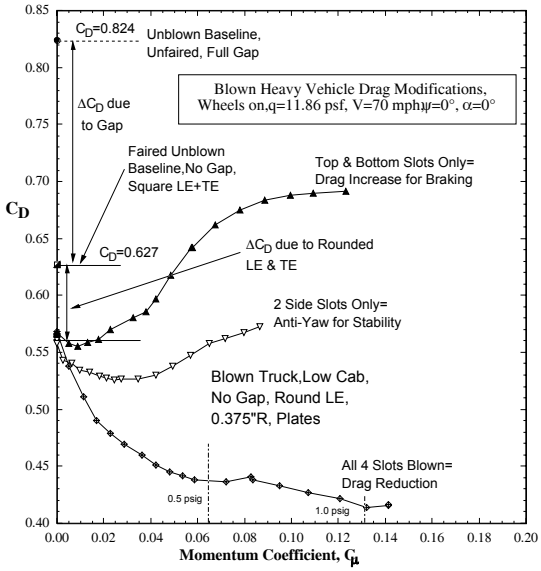

Figure 1. Drag reduction or drag increase demonstrated by GTRI model PHV, depending on blowing location

as FY03 results for PHVs and for Pneumatic Sports Utility Vehicles in the following sections because they occurred in FY03.

Experimental Details and Results

Experimental wind-tunnel developments of this technology conducted on smaller-scale PHV model under previous DOE funding [2,3,4] led to two full-scale Tuning Tests conducted at Volvo Truck's facilities, plus an SAE Type-II Fuel Economy Test conducted at the 7.5-mile test track at Transportation Research Center in Ohio, with the results reported above. Since this drag reduction and the fuel economy increase were less on the test PHV vehicle than the tunnel data predicted, we returned to the tunnel to determine the reasons. The generic tunnel model was modified so that it more closely resembled the "more-draggy" full-scale test article, and then re-tested. Then, implicated components from the track-test vehicle were corrected and the model re-tested each time. Figure 2 shows how correction of each component on the track-test PHV reduced the C_D below that of the unblown Baseline

reference truck (Run 36). Run 239's configuration is most like our TRC blown test truck. Figure 3 shows the drag reductions that would occur for this test truck if these less-than-optimum geometries were corrected, and then Figure 4 shows the increases in fuel economy projected for highway speeds (where drag is half or more of total resistance) relative to the Baseline truck if these items were revised. Results

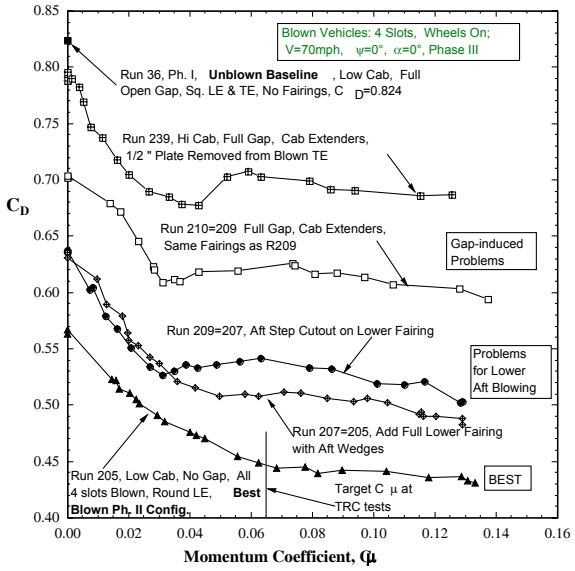

Figure 2. Tunnel results: drag changes with model correction and also with blowing variation

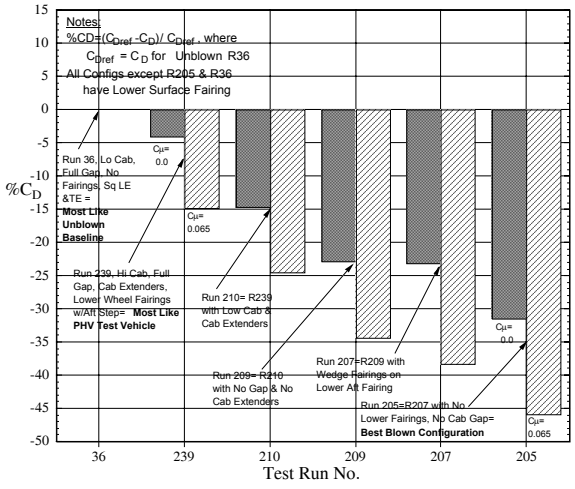

Figure 3. Incremental drag changes relative to the unblown baseline configuration of Figure 2

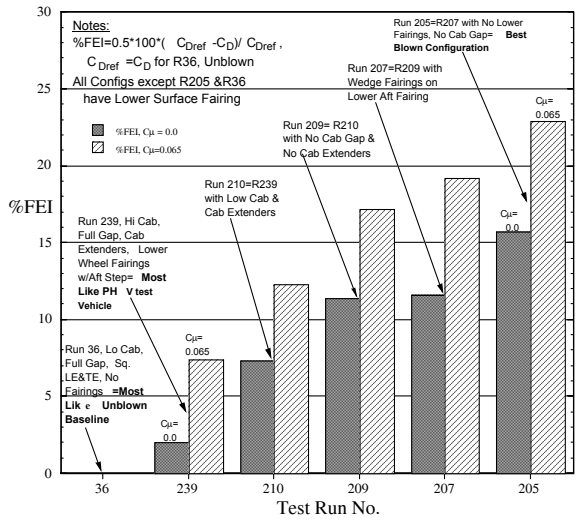

Figure 4. Resulting fuel efficiency increase with configuration and blowing variations

show fuel economy increases (%FEI) of up to 16% for the unblown PHV geometry, and up to 23% for the blown vehicle at test Cμ. This indicates a 7% FEI for blowing without considering geometry modifications which provides a slightly better result than the recent on-track results of 5-6% FEI, and thus these data provide a guide towards redesign of the test vehicle for an improved low-drag PHV truck.

An important finding in this data is the effect of the gap between the tractor and trailer. Figure 5 shows our PHV test vehicle, which even with its cab extenders, still has an obvious gap. Note in Figures 2, 3, and 4 the adverse effect of a gap discontinuity on the small scale model. An appropriate gap side plate was developed. Tunnel test results, Figure 6, show this simple but feasible device to be nearly as effective in eliminating the gap disruption as a non-feasible solid gap ("NO Gap"). Note the continued drag reduction occurring with additional leading-edge (LE) blowing incorporated with these gap plates.

Figure 5. PHV test vehicle with gap between tractor and the trailer

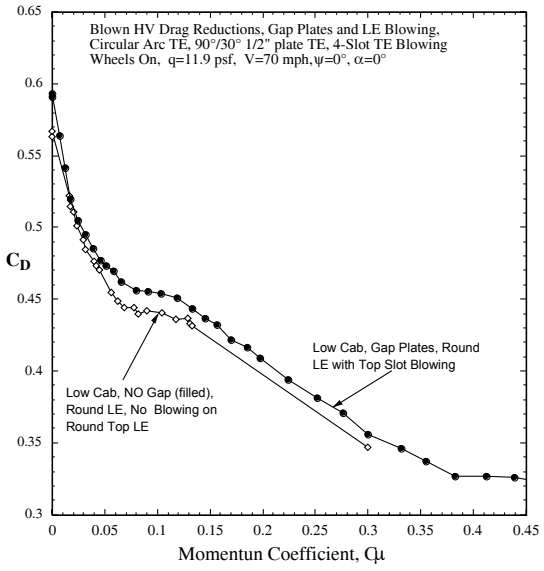

Figure 6. A practical solution for gap separation: Gap Side Plate

In addition to drag reduction due to elimination of aft flow separation, two other improvements were shown during these recent tunnel tests. Blowing on the aft trailer corners converted the suction on the aft doors (a drag component) into overpressure there (a drag reduction = a "push"). Figure 7 confirms this (+Cp is pressure), as does integration of the rear door pressure force to yield negative incremental drag components produced by blowing. Up until the higher values of blowing coefficient Cμ, the incremental C_D values due to the blowing overpressures are greater than the total Cμ expended. Additional ΔC_D still missing from these blowing gains are drag reductions due to flow-separation prevention (not shown here).

Blowing on only one vertical slot of the trailer has been shown experimentally to dramatically reduce drag experienced during a side wind (yaw), it also could produce aft side force to counteract destabilizing yawing moment, and thus possibly yield directional control. Figure 8 shows how the unstable yawing moment, C_N, at Cμ=0 during nose-left yaw of the small-scale model can be reduced to zero by blowing the aft left side slot, and then a stabilizing opposite moment can be generated by slightly increasing left-slot blowing.

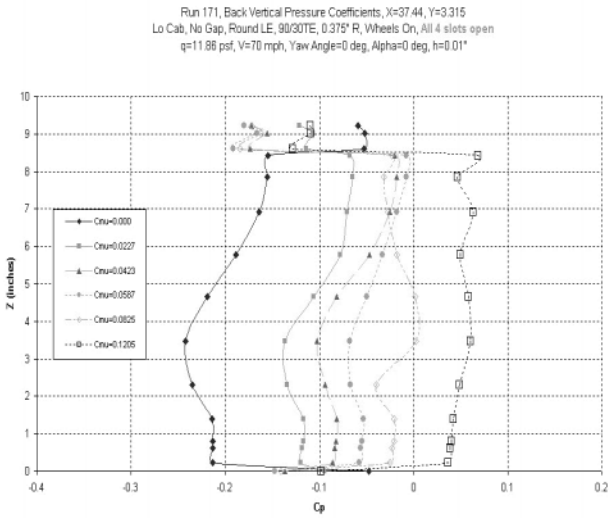

Figure 7. Static pressure recovery on back doors due to blowing

Cμ	ΔC_D from Base Pressure
0.00	0.000
0.023	- 0.034
0.042	- 0.052
0.059	- 0.060
0.083	- 0.075
0.121	- 0.114

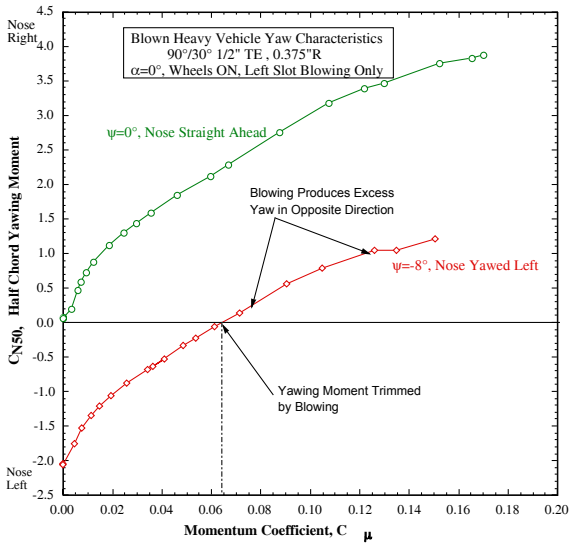

Figure 8. Directional control capability from blowing on left side slot only

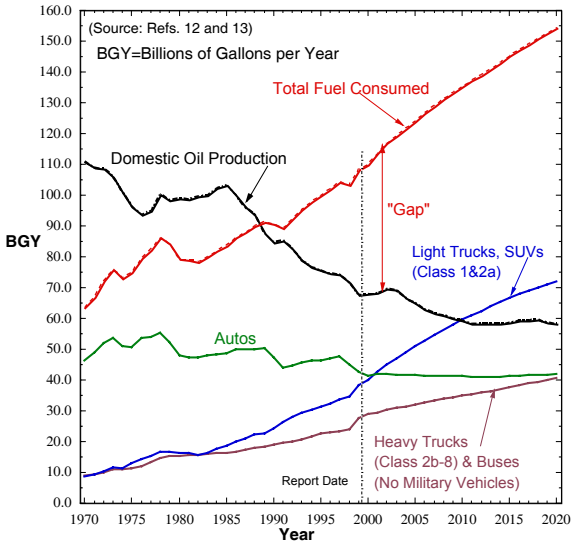

Figure 9. Highway energy usage comparisons by vehicle type (from DOE [5])

Figure 10. Tufts showing blowing and jet turning on PSUV in Lockheed wind tunnel

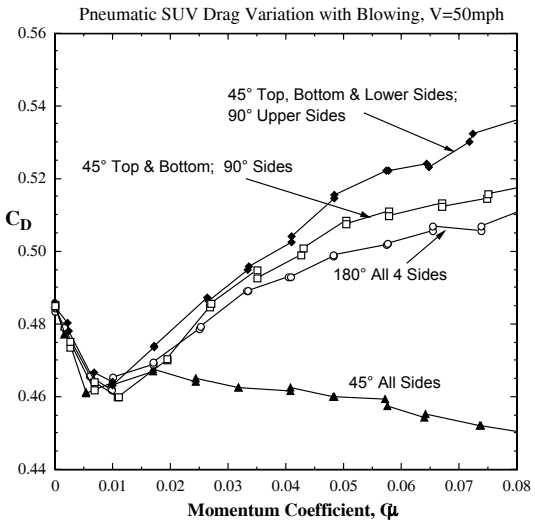

Figure 11. PSUV drag coefficient changes due to blowing on various configurations

Realizing that drag reduction may be even more important for Sports Utility Vehicles (SUVs) than HVs (see Figure 9 DOE fuel usage data, from [5]), we conducted full-scale wind tunnel development of this pneumatic technology applied to a GM Suburban SUV, Figure 10. With a variety of blowing configurations tested, we showed in Figure 11 that blowing could either reduce drag for fuel efficiency or could increase drag for braking. We also confirmed again that blowing only one side slot could effect drag and yaw during high side-wind angles, as Figure 12 shows. The restoration of directional stability using no moving surfaces is thus verified.

Discussion

The above wind-tunnel tests to identify reasons for the less-than-expected drag reduction on the full-scale PHV road test vehicle have determined a number of configuration improvements needed in the blowing geometries, the trailer under-side fairings and the tractor-trailer gap. These, when corrected, should yield the earlier-recorded small-scale model drag reductions of up to 18% reduction in aerodynamic drag coefficient due to blowing (without consideration of the energy to blow) and 10–12% due to the device's corner rounding, for a total of 25–30%. We have incorporated these into the design of a next-generation smaller-scale PHV tunnel model that now incorporates a generic current-day tractor geometry, Figure 13. This new model (CAD details of which are available but drawings are too large to include herein) includes new blown trailing-edge geometries to yield higher base pressure recovery, no lower surface fairings, and other more realistic under-trailer and wheel geometries. A new mounting strut is now from the top of the model so that interaction between the wheels, lower surface geometries and the road can be properly simulated. We will test this new PHV configuration in the GTRI Model Test Facility tunnel for comparison to the previous model

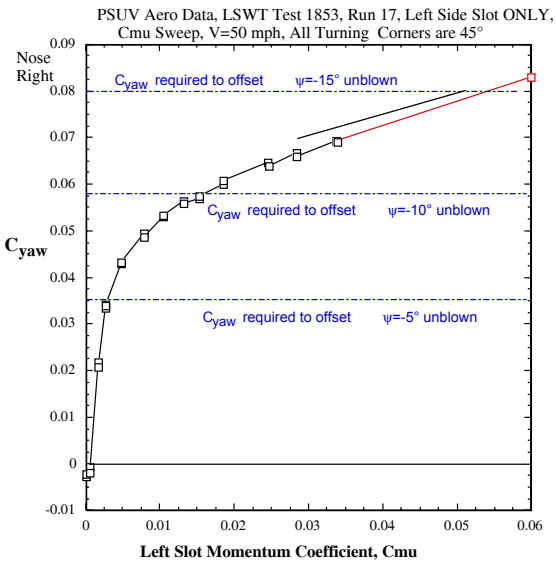

Figure 12. PSUV drag coefficient changes due to blowing on various configurations

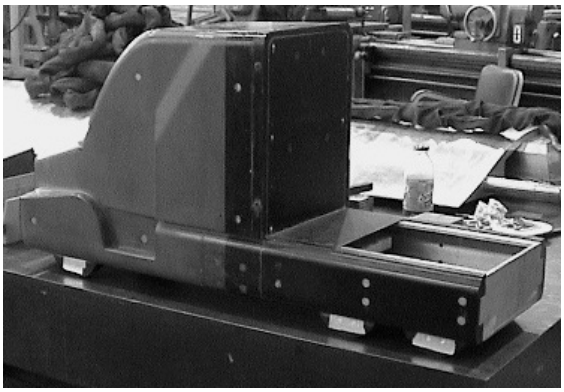

Figure 13. Generic Conventional Model (GCM) tractor to be included with new GTRI PHV test model

performance and to estimate new full-scale PHV performance. This data will include many of the real vehicle protrusions (such as struts, differentials, floor spars, etc.) that could easily be detrimental to full-scale performance and fuel economy. Test results are to be incorporated into modification of the real test vehicle (see Figure 5) into the best-performing blown configuration in preparation for a Phase II SAE fuel economy test program for the PHV and baseline trailer in FY04.

The full-scale wind tunnel results for the Pneumatic SUV confirmed both drag reduction, yaw control, stability restoration and braking increase. These full-scale aerodynamic stability and control results are virtually impossible to determine during road tests, so these PSUV tests provide invaluable data for stability & control, and safety for SUVs. We realize that we have not yet optimized the blowing geometries on the contoured back surfaces of the SUV (far more complex than the square-edged HV trailer aft end) and that future work is needed here. However, as Figure 9 verifies, the sheer number of SUVs and pickup trucks on the American roads make this drag-reduction effort quite important, as does the promise of improved stability and braking for vehicles frequently in need of both.

Conclusions

To advance the state of development of pneumatic aerodynamics for improvement of HV and SUV drag reduction, fuel economy, braking, stability and safety of operation, GTRI and its team members have continued in FY03 our previous program for DOE. We have conducted investigations for both model-scale wind tunnel and full-scale test track HVs and full-scale tunnel investigations on an SUV of these advanced capabilities, as well as to identify and correct aerodynamic problems areas on our first fuel-economy test on a full-scale Pneumatic Heavy Vehicle. Results of this recent effort include:

- We have identified the aero problem areas of our first PHV road test and how to correct these; current indications are that drag reductions of 14% and fuel economy increases of 7% are projected to result for these new configurations at highway speeds due to blowing alone. Geometric modifications will also increase drag reduction.

- A new model test configuration based on current generic tractor geometry and the above results has been designed, the upcoming tunnel testing at GTRI of which will provide the guidance for modification of the full-scale PHV test vehicle.

- Full-scale tunnel testing of pneumatic aerodynamics on an SUV has verified pneumatic drag reduction, directional stability, and the versatility of these blown no-moving-part, performance-enhancing, economy-increasing, and stability devices to improve the operation of SUVs. These results now lead to re-design and modification of the PHV road-test vehicle in

preparation for the Phase II SAE Type-II fuel economy test scheduled for FY04.

References

1. Englar, Robert J., "Circulation Control Pneumatic Aerodynamics: Blown Force and Moment Augmentation and Modification; Past, Present and Future," AIAA Paper 2000-2541, Denver, CO, June 19–22, 2000.
2. Englar, Robert J., "Advanced Aerodynamic Devices to Improve the Performance, Economics, Handling and Safety of Heavy Vehicles," SAE Paper 2001-01-2072, Washington, D.C., May 14–16, 2001.
3. Englar, R.J. "Pneumatic Heavy Vehicle Aerodynamic Drag Reduction, Safety Enhancement, and Performance Improvement," in the Proceedings of the UEF Conference on "The Aerodynamics of HeavyVehicles: Trucks, Buses, and Trains", Monterey-Pacific-Grove, CA, Dec. 2–6, 2002.
4. Englar, Robert J. "Drag Reduction, Safety Enhancement and Performance Improvement for Heavy Vehicles and SUVs Using Advanced Pneumatic Aerodynamic Technology," SAE Paper 2003-01-3378, accepted and to be presented November 10–12, 2003.
5. "EIA Annual Energy Outlook 2000," DOE/EIA-0383 (2000), December 1999 and "AEO 2001."

E. Computational and Experimental Investigation of Drag-Reducing Add-on Devices and the Flow Field around a Simplified Tractor-Trailer Geometry

Principal Investigator: K. Salari
Co-Investigators: J. Ortega, R. McCallen
Lawrence Livermore National Laboratory
P.O. Box 808, Livermore, CA 94551-0808
(925) 423-0958; mccallen1@llnl.gov

Technology Development Manager: Sid Diamond
(202) 586-8032; sid.diamond@ee.doe.gov
Technical Program Manager: Jules Routbort
(630) 252-5065; routbort@anl.gov

Contractor: Lawrence Livermore National Laboratory
Contract No.: W-7405-ENG-48

Objective

- Increase the fuel economy of class 8 tractor-trailers by reducing the aerodynamic drag.
- Identify and to understand the key flow structures around the vehicle that significantly impact the aerodynamic drag.
- Investigate the capability of modern computational tools to predict the flow field around a tractor-trailer type geometry, in the wake of the trailer, in the underbody, and in the gap between the tractor and the trailer.
- Design new add-on devices that significantly reduce aerodynamic drag for class 8 tractor-trailers achieved by small-scale wind tunnel tests supported by computational modeling and simulation.
- Present a list of effective drag-reducing add-on devices to the OEM's for further full-scale testing.

Approach

- LLNL is developing and utilizing state-of-the-art numerical algorithms and advanced turbulence models to create computational tools that can accurately predict the complex flow field around modern tractor-trailer type geometries. Significant emphasis is placed on validation calculation to ensure proper evaluation of the computational results compared to experimental data.
- Investigate key flow structures, such as trailer wake, the gap flow between the tractor and the trailer, and underbody, which significantly impact the aerodynamic drag of heavy vehicles. This is accomplished through use of careful discovery and validation experiments and computational modeling and simulation of the complex flow field around these vehicles.
- Three truck-like geometries, GTS, USC modified GTS, and GCM, are used to investigate the predictive behavior of various numerical approaches and turbulence models. These models represent simple to modern tractor-trailer geometries, with the GCM representing a realistic/modern model.
- Discovery experiments at NASA Ames's small-scale $3' \times 4'$ wind tunnel provide a mechanism to study the effectiveness of LLNL proposed drag reducing add-on devices.
- Given the knowledge obtained from the discovery experiment and computational simulations for the flow structures in the wake of the trailer, underbody, and the gap, new add-on devices can be designed to reduce aerodynamic drag of the class 8 tractor-trailer.

Accomplishments

- The steady and unsteady turbulent flow fields around a tractor-trailer geometry have been successfully simulated with emphasis on the wake of the trailer, underbody, and the gap flow structure
  - LLNL completed simulations at 0° and 10° yaw for GTS geometry with three different turbulence models for a total of nine runs. The predicted result for each turbulence model is compared to the experimental data of NASA Ames's 7' × 10' wind tunnel. A detailed study was conducted to investigate the sensitivity of the solution to grid resolution around sharp corners and in the vicinity of the separated region.
  - Completed unsteady gap flow simulation for USC modified GTS model using a coarse mesh (6.2 million elements). Unsteady results are compared to USC experimental data.
  - The LLNL add-on device for the gap was successfully simulated with the USC modified GTS geometry. The new add-on device stabilizes the unsteady flow in the gap and, in turn, potentially reduces the aerodynamic drag.
- New LLNL drag reducing add-on devices have been designed based on the ascertained knowledge of the flow field from the experimental investigation and computational simulations. Five records of invention for new LLNL add-on devices have been filed.
- Experimental discovery is underway at NASA Ames to determine the effectiveness of the proposed new add-on devices and to investigate the complex flow field around the vehicle.

Future Direction

- Continue with development of the predictive modeling capability through use of the state-of-the-art turbulence modeling and numerical algorithms to simulate the complex flow field around the class 8 tractor-trailer.
- A new hybrid RANS/LES turbulence model is under development that could improve the accuracy of the flow field prediction around the heavy vehicle.
- Continue with testing the proposed LLNL add-on devices to reduce the aerodynamic drag of heavy vehicles through the discovery experiments.
- Present a list of effective add-on devices to OEM's for further full-scale testing.
- Investigate the aerodynamics of wheels and wheel wells for brake cooling.
- Investigate the aerodynamics of coal rail cars.
- Investigate the aerodynamics of underbody/wheel splash and spray.

Summary

The LLNL activities for FY03 include computational modeling and simulation, design of drag reducing add-on devices, and performing discovery experiments at the NASA Ames facility. The LLNL goal for the computational effort is to provide guidance on drag reduction strategies that could be implemented with add-on devices. This is accomplished by utilizing the computational results to provide insight into the flow structures that have been identified as key to reducing the aerodynamic drag of heavy vehicles. The focus of the design of add-on devices is to improve or stabilize the turbulent unsteady flow field in the gap, the wake, and the underbody of the vehicle to reduce the aerodynamic drag. The focus of the experimental effort is to provide detailed information on various LLNL proposed drag reduction concepts. There are three geometries under investigation, GTS, USC modified GTS, and GCM (Figure 1). These geometries represent simple to modern tractor-trailer models with GCM representing a realistic/modern tractor-trailer geometry.

Significant emphasis is placed on validation calculation to ensure proper evaluation of the computational results compared to experimental data. The validation calculation requires modeling a section of the NASA Ames's 7' × 10' wind tunnel and properly matching the flow condition in the test section of the tunnel to the experimental data. The boundary layer profile and static pressure at the

Figure 1. Generic Conventional Model (GCM)

wind tunnel test section are typically used to properly set the inflow and outflow to the computational domain. The advantage of this approach is to use the raw or unmodified experimental data to validate the computational results. This is a requirement for performing the validation calculation.

Steady and unsteady RANS simulations are performed to model the complex flow field around the vehicle, in the gap between the tractor and the trailer, and the trailer wake. The experimental data of USC and NASA are used to benchmark and validate the computational results. The small-scale $3' \times 4'$ wind tunnel at NASA Ames is providing an inexpensive and flexible way to fully investigate the selected drag reduction devices using the USC modified GTS model. The goal for the experimental investigation is to identify one or two add-on devices that clearly standout from other known and effective drag reducing devices.

Computational Simulations

Flow simulation of the GTS model at 0° and 10° yaw in the NASA Ames's $7' \times 10'$ wind tunnel and the modified GTS with the non-dimensional gap distance of 0.72 at 0° yaw in the USC tunnel are completed. Steady and unsteady RANS flow simulations are performed with NASA's Overflow code that uses overset grids.

For all GTS simulations in the NASA wind tunnel, the flow condition is obtained from the available experimental data, run 7 point 9. The following flow conditions were provided for this run: Mach number 0.28, Reynolds number 2.08×10^6 (based on trailer width), total pressure 102649.2 N/m^2, total temperature 284.5 °K, static pressure 97339.1 N/m^2, static temperature 280.2 °K, and air density 1.206 kg/m^3.

The following simulations have been completed for GTS geometry:

- 0° and 10° yaw.
- Three turbulence models, 1-equation model of Spalart-Allmaras (SA), two-equation models of Wilcox *k*-ω and Menter SST.
- Two-grid sizes of 3.7 and 12.2 million elements.

Figure 2 shows a complex flow field with multiple vortical structures and a separation bubble at the leeward side of the vehicle highlighted by particle traces around the GTS geometry at 10° yaw in the NASA Ames's $7' \times 10'$ wind tunnel.

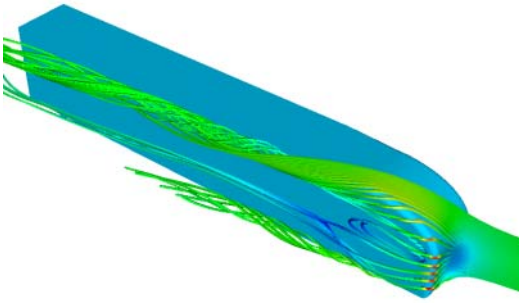

Figure 2. Particle traces are colored by velocity magnitude, 10° yaw, and GTS model

Table 1 shows the computed drag coefficient and the experimentally measured drag values. The subscript W refers to the static pressure measured on the test-section tunnel wall and the subscript R refers to the static pressure measured upstream of the test section [1]. The drag coefficients obtained from the simulations are based on the dynamic pressure calculated using the test section dynamic pressure. All turbulence models have similar prediction for viscous drag; however, the SA and SST models significantly over-predict the pressure drag. Similarly, the Wilcox *k*-ω model over predicts the pressure drag, but provides a drag coefficient closest to the experimental value. All tested RANS turbulence models have difficulty with predicting the correct pressure drag. Since the trailer wake has a significant influence on the pressure drag, this suggests that RANS turbulence models could have difficulty predicting the correct flow structure in the wake of the trailer. Previous simulations on the GTS

geometry using the SA model are presented in [2]. This work includes careful investigation of the influence of grid resolution and inflow and outflow boundary conditions on the predictive capability of the SA model. Similar results are reported on the aerodynamic forces.

Table 1. Computed aerodynamic forces, GTS model, 0° yaw, coarse grid (cg), and medium grid (mg)

Drag	Viscous	Pressure	Total
k-ω, cg	0.103	0.188	0.290
k-ω, mg	0.101	0.176	0.277
SST, cg	0.091	0.273	0.364
SST,mg	0.092	0.258	0.350
SA, mg	0.096	0.294	0.390
NASA Experiment, $C_{D,W}$			0.249
NASA Experiment, $C_{D,R}$			0.263

Figure 3 shows a velocity vector field in the wake of the GTS trailer at the symmetry plane with SST turbulence model. Figure 4 shows the time-averaged PIV data from NASA Ames at the same cut plane as that in Figure 3. In the experimental data, there is a dominant recirculation zone at the lower base of the trailer. On the other hand, there are two similarly sized recirculation zones on the lower and the upper part of the base of the trailer in the computational result. Noticeably, the flow structures in the computational result do not match that of the experimental PIV data and, hence, this difference may explain the disagreement in the predicted drag. The Wilcox *k*-ω model has a similar wake prediction as that of the SST model; however, the SA model predicts a much smaller wake size with two symmetric recirculation zones at the lower and the upper part of the base of the trailer.

The RANS models used in this study did a reasonable job in predicting the pressure and skin friction distributions on the surface of the GTS. However, if absolute drag and predicting the wake flow structure is of interest, other turbulence more sophisticated turbulence models should be investigated.

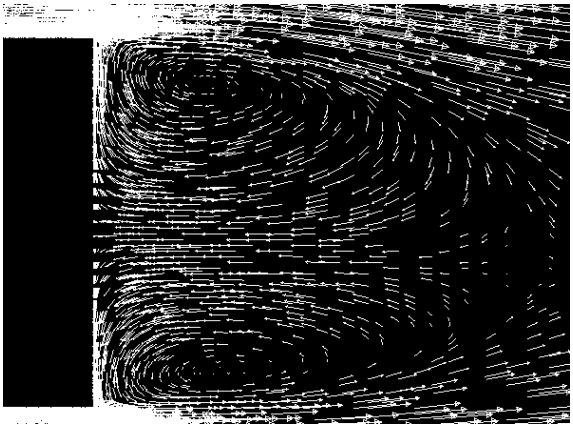

Figure 3. Wake flow structure, SST model, 0° yaw, symmetry plane, GTS model

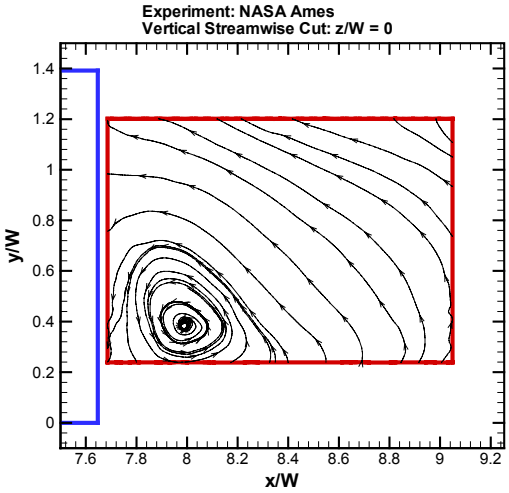

Figure 4. Wake flow structure, NASA time averaged PIV data, 0° yaw, symmetry plane, GTS model

Table 2 shows the computed lift, drag, and side force coefficients for the 10° yaw case and the experimentally measured values. The Wilcox *k*-ω and the Menter SST model have problems in predicting the lift coefficient. Similarly, the predicated drag coefficient is off significantly. However, both turbulence models have a better prediction for the side force. Note that there exists a significant flow separation (Figure 5) at the leeward side of the GTS model. This type of flow separation poses a challenge for the RANS turbulence model.

Table 2. Computed aerodynamic forces, GTS model, 10° yaw, coarse grid (cg), and medium grid (mg)

	Lift	Drag	Side
k-ω, mg	-0.004	0.581	1.127
SST, cg	0.006	0.651	1.129
SST, mg	-0.010	0.664	1.137
Exp, $C_{D,W}$	0.021	0.292	1.253
Exp, $C_{D,R}$	0.022	0.312	1.338

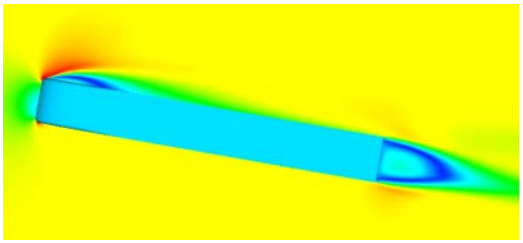

Figure 5. 10° yaw, velocity magnitude contours, half height cut plane, SST model, GTS geometry

Figure 6 shows the vortex cores that are present in this complex flow field. The presence of multiple vortex cores on the top surface of the GTS geometry, suggest multiple separation and reattachment lines. Similarly, a dominant vortex is present on the leeward side of the GTS that extends the length of the trailer. The position of these separation and reattachment lines can be compared to that of the NASA experimental data.

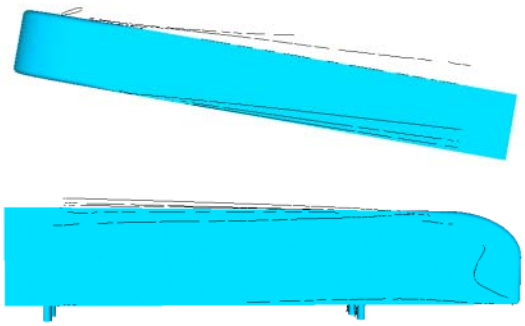

Figure 6. Vortex core positions, 10° yaw, SST model, GTS geometry

Unsteady RANS simulations are conducted on the USC modified GTS geometry with a normalized gap distance of 0.72, which is above the critical gap distance of 0.5. At this gap distance, the flow experiences unsteadiness and could have multiple stable modes that are either symmetric or asymmetric. Also, the drag contribution from the gap flow significantly increases due to this unsteady behavior. Low drag for the gap relates to stable symmetric flow and high drag relates to the unsteady asymmetric flow. Figure 7 presents a snapshot of the unsteady flow field around the modified GTS model highlighted by particle traces colored by velocity magnitude. This figure shows the external flow reaching into the gap and exiting on the side. This is the typical unsteady asymmetric flow representing a high drag situation.

The gap flow also significantly interacts with the external flow and the wake of the trailer as shown in Figures 8 and 9. This suggests that previous investigations [3], which isolated the base of the trailer for reasons of reducing the size of the computational domain, may not properly capture the unsteady turbulent flow in the wake.

The unsteady RANS simulation conducted with Overflow is capturing the symmetric and asymmetric flow field in the gap as shown in Figure 10. This figure compares the computed results with the USC experimental data. A simple splitter plate was introduced in the gap and shown in Figures 11 and 12 to stabilize the gap flow. This device will be further investigated by USC as a possible drag reducing add-on device for the gap.

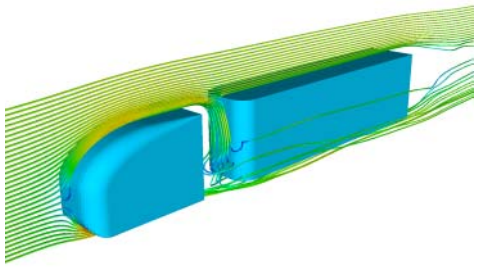

Figure 7. Particle traces colored by velocity magnitude, 0° yaw, *k*-ω model, modified GTS geometry with 0.72 gap size

Discovery Experiment

The goal of our discovery experiment in the small-scale NASA Ames 3' × 4' wind tunnel is to provide an inexpensive and flexible means of testing and exploring various LLNL drag reduction concepts for heavy vehicles. The construction of the 1/16 scaled wind tunnel model which is similar to the USC modified GTS and the proposed LLNL add-on

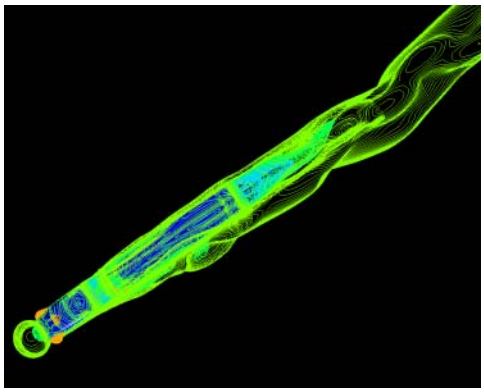

Figure 8. Velocity magnitude contours, 0° yaw, *k*-ω model, modified GTS geometry with 0.72 gap size

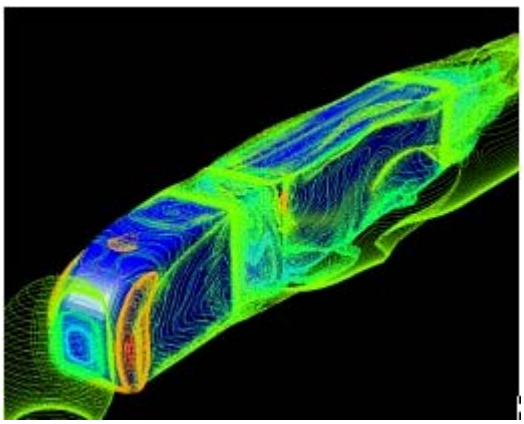

Figure 9. Velocity magnitude contours, 0° yaw, *k*-ω model, modified GTS geometry with 0.72 gap size

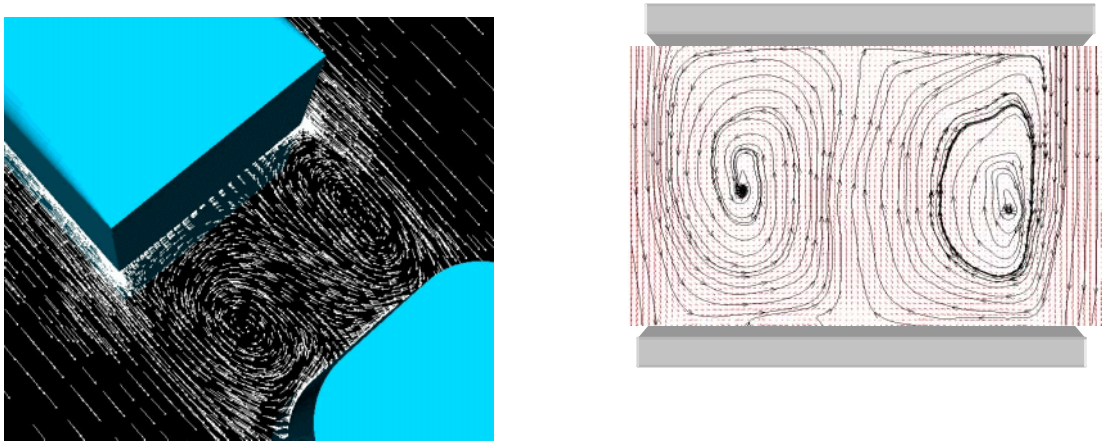

a) Computation (left image), USC experiment (right image), symmetric condition

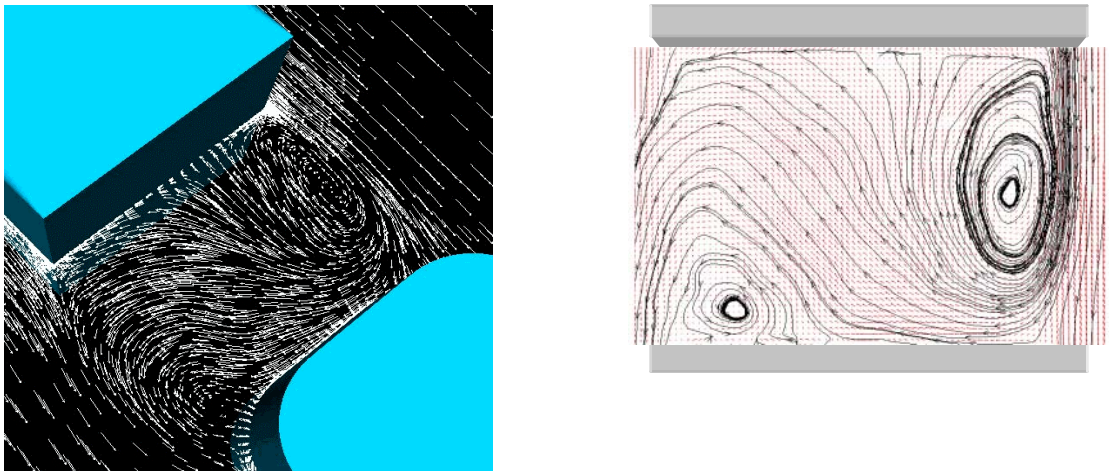

b) Computation (left image), USC experiment (right image), asymmetric condition

Figure 10. Comparison of computed and USC experimental data at the gap mid-height, 0° yaw, *k*-ω model, modified GTS geometry with 0.72 gap size

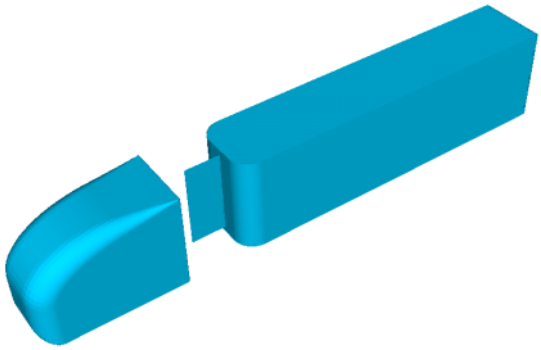

Figure 11 Add-on device (splitter plate) to stabilize the gap flow

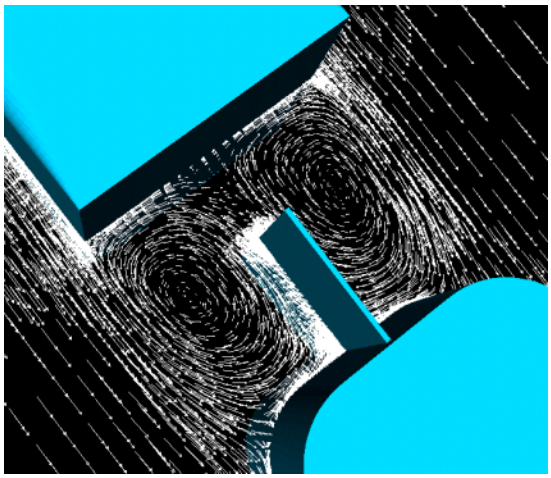

Figure 12. Velocity vector field in the gap in the presence of the splitter plate, mid-height, 0° yaw, *k*-ω model, modified GTS geometry with 0.72 gap size

devices have been completed. The initial flow visualization about the modified GTS indicates flow separation on the side and the top of the tractor (Figure 13). It is crucial to minimize the flow separation since it could adversely impact the evaluation of add-on devices. The flow separations are minimized by tripping the flow. The overall flow structure around the modified GTS model is complex with 3-D flow patterns on the downstream side of the tractor under yaw conditions. The trailer top and downstream side have recirculation zones that cover a significant portion of the trailer. Currently, force and moment measurements are being obtained for the baseline configuration with and without add-on drag reducing devices.

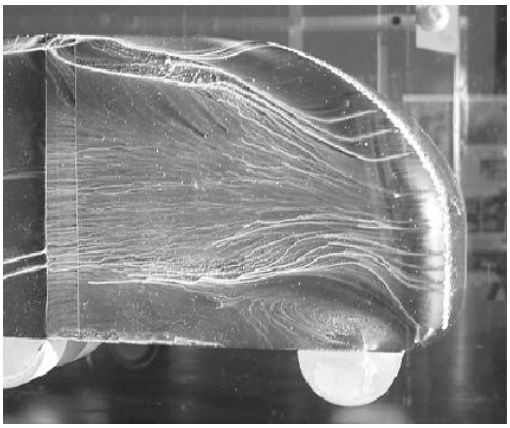

Figure 13. 1/16-scaled wind tunnel model similar to USC modified GTS geometry

Conclusions

The steady and unsteady turbulent flow around the GTS and USC modified GTS was successfully completed. The RANS turbulence models at 0° yaw, excluding the wake, performed reasonably well in predicting the surface properties and the overall flow behavior around the vehicle. The steady RANS turbulence models had difficulty capturing the right flow structure in the wake of the trailer. More sophisticated turbulence models, such as the hybrid RANS/LES model, should be investigated to improve the accuracy of the wake flow structure. Such a model is currently under development by LLNL.

The unsteady turbulent gap flow was successfully modeled compared to the USC experimental data. The symmetric and asymmetric flow states in the gap were properly represented. A new add-on device was suggested and tested computationally to stabilize the gap flow and reduce the aerodynamic drag.

The discovery experiment is under way at NASA Ames facility to provide better understanding of the flow structure associated with drag reducing add-on devices. Also, several add-on devices will be recommend as the outcome of this experiment to the DOE heavy vehicle project for full-scale road tests.

References

1. Storms, B., et. al., "An Experimental Study of the Ground Transportation System (GTS) Model in the NASA Ames 7- by 10-Ft Wind Tunnel," NASA/TM-2001-209621, Feb. 2001.
2. Salari, K., McWherter-Payne, M., "Computational Flow Modeling of a Simplified Integrated Tractor-Trailer Geometry," SAND2003-3383.
3. Ortega, J.M., Dunn. T., McCallen, R., Salari, K., "Computational Simulation of a Heavy Vehicle Trailer Wake," United Engineering Foundation, Aerodynamics of Heavy Vehicles: Trucks, Buses, and Trains Conference, Monterey, CA, December 2–6, 2002.

F. Reynolds-Averaged Navier-Stokes Simulations of a Simplified Tractor/Trailer Configuration

Principal Investigators: L.J. DeChant
Co-Investigators: C.J. Roy, J.L. Payne, and B. Hassan
Sandia National Laboratories
P.O. Box 5800, MS 0825, Albuquerque, NM 87185-0825
(505) 844-4250; ljdecha@sandia.gov

Technology Development Manager: Sidney Diamond
(202) 586-8032; sid.diamond@ee.doe.gov
Technical Program Manager: Jules Routbort
(630) 252-5065; routbort@anl.gov

Contractor: Sandia National Laboratories
Contract No.: DE-AC04-94AL85000

Objective

- Evaluate the use of Reynolds Averaged Navier-Stokes (RANS) to predict the aerodynamic drag on tractor/trailers. This goal will be accomplished by computing accurate numerical solutions to representative tractor/trailer geometries, then validating those computations by comparisons to experimental data. These validated models will then be used to assess drag reduction techniques which have the potential to reduce the net oil consumption and operating costs for the trucking industry.

Approach

- Compute solutions with varying mesh resolution for the Ground Transportation System (GTS) geometry.
- Assess the numerical accuracy of the computed solutions.
- Validate the models by comparison to experimental data for surface pressure, flowfield velocity, and drag coefficient obtained in the NASA-Ames 7 × 10 ft wind tunnel.

Accomplishments

- Completed a new GTS fine mesh with appropriate y+ values to allow the removal of every other point in each direction to provide a consistently coarsened mesh.
- Successfully completed both coarse grid (2.5 million cells) and fine grid (20 million cells) solutions on the GTS geometry using both the Spalart-Allmaras and Menter k-omega turbulence models.
- Completed assessment of the numerical errors in the fine grid GTS simulations.
- Compared simulation results to experimental data for surface pressure, wake velocities, and drag coefficient.
- Generated new flowfield mesh on a truncated GTS geometry to allow more detailed resolution of the truck wake region and the assessment of unsteady turbulence modeling approaches.
- Developed a reduced-order model for bluff-body drag on simplified geometries.

Future Directions

- Compare steady RANS simulations on the truncated geometry to results for full geometry.
- Compute additional steady RANS simulations on the truncated mesh with additional mesh resolution in the wake.

- Compute unsteady turbulent simulations of the GTS geometry using the truncated geometry.
- Continue to develop a reduced order model for bluff-body drag.

Introduction

In a typical class 8 tractor/trailer, energy losses due to rolling resistance and accessories increase linearly with vehicle speed, while energy losses due to aerodynamic drag increase with the cube of the speed. At a typical highway speed of 70 mph, aerodynamic drag accounts for approximately 65% of the energy output of the engine [1]. Due to the large number of tractor/trailers on the US highways, even modest reductions in aerodynamic drag can significantly reduce domestic fuel consumption. Lower fuel consumption will result in a reduction in pollution emissions, and, more importantly, a reduced dependence on foreign oil.

The most common turbulence modeling approach for engineering applications involves solving the Reynolds-Averaged Navier-Stokes (RANS) equations. With this approach, the effects of the inherently three-dimensional and time-varying turbulent eddies on the mean flow are modeled and not simulated. The goal of this study is to assess the ability of steady-state RANS turbulence models to accurately predict the flowfield and aerodynamic drag for tractor/trailer configurations.

Problem Formulation

The configuration to be examined is the Ground Transportation System (GTS) studied experimentally at the NASA Ames research center by Storms et al. [2]. The GTS geometry is a simplified tractor/trailer configuration which is mounted on four posts in the wind tunnel. A photograph of the GTS in the NASA Ames 7 × 10 ft wind tunnel is shown in Figure 1. The GTS model is an approximately 1/8 scale class 8 tractor/trailer configuration. The Reynolds number based on the trailer width (W=0.3238 m) is 2 million, approximately one-half of full scale.

The GTS geometry, including the wind tunnel walls, is discretized using two mesh levels: a coarse mesh using 2.5 million grid points and a fine mesh using 20 million grid points. The grids are generated such

Figure 1. GTS model in NASA Ames 7 × 10 ft wind tunnel

that the wall y^+ values on the truck surface, supports, and lower wind tunnel wall are everywhere less than unity on the fine mesh. The side and top wind tunnel walls employ slip flow conditions. Structured meshes are employed using point-to-point match up at the block boundaries. The coarse mesh is domain-decomposed into 125 zones and is shown in Figure 2. The fine mesh is decomposed into 1149 zones. Both the coarse and fine meshes are run on the massively parallel ASCI Red machine using one processor for each zone. The axes employed in the current effort are shown Figure 2, with the x axis starting at the front of the tractor and running downstream, the y axis in the vertical direction, and the z axis starting at the GTS symmetry plane and running spanwise towards the side wall.

In order to ensure that the simulated flow matches closely with the flow in the wind tunnel, a number of freestream conditions are matched. First, the inflow plane is set with the appropriate stagnation conditions of the tunnel shown in Table 1. The back pressure at the simulated outflow plane is then adjusted until the reference pressure located at (x/W=4.47, y/W=2.59, and z/W=-4.7) on the tunnel side wall reaches the wall reference pressure given in the table. The boundary layer on the bottom wall was measured in a tunnel-empty configuration. Sample boundary layer profiles upstream of the GTS model from the simulation using the Menter k-ω model gave good agreement with the tunnel empty-profile from the experiment.

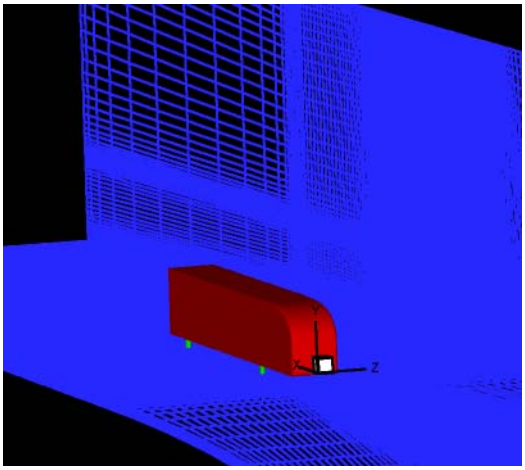

Figure 2. Computational mesh on GTS geometry

Table 1. Freestream conditions used in the simulations

Tunnel Condition	Value
Stagnation Pressure	102,653.2 N/m^2
Stagnation Temperature	282.06 K
Wall Reference Pressure	97,582. N/m^2
Reference Mach number	0.27
Back Pressure	100,136.0 N/m^2
Tunnel Floor BL Thickness	0.053 m
Wall Temperature BC	adiabatic

Numerical Formulation

The CFD code is SACCARA, the Sandia Advanced Code for Compressible Aerothermodynamics Research and Analysis, and was developed from a parallel distributed memory of the INCA code [3], originally written by Amtec Engineering. The SACCARA code employs a massively parallel distributed memory architecture based on multi-block structured grids. A number of code verification studies have been performed which give confidence that the code is free from coding mistakes including comparison to established numerical benchmark solutions and code-to-code comparisons [4]. The fine grid and coarse grid simulations presented herein were run in parallel on the ASCI Red parallel processing machine using 1149 and 125 processors, respectively.

Two turbulence models are examined in the current work: the one-equation eddy viscosity transport model of Spalart-Allmaras [5] and the Menter k-ω model [6]. The strengths and limitations of these models are described in the indicated references. The Menter k-ω model is a hybrid model which uses a blending function to combine the best aspects of both the k-ω and the k-ε turbulence models. In both cases, the turbulence models were integrated to the wall in order to avoid model validation issues associated with wall functions.

Numerical Accuracy

The solutions are marched (iterated) in pseudo-time until a steady-state answer is obtained. Iterative convergence is assessed by examining the steady-state residuals of the momentum equations. The steady-state residual is defined by plugging the solution at the current iteration into the discretized form of the steady-state governing equations (omitting the time derivative). The iterative error in the solution tends to drop in a similar fashion as the residual. The solutions were converged by approximately seven orders of magnitude.

The discretization error is estimated by generating solutions on two mesh levels. Since the coarse mesh is determined by eliminating every other gridline from the fine mesh, the grid is consistently refined throughout the entire domain, and Richardson extrapolation can be used to estimate the exact solution. This extrapolated solution is then used to judge the error in the fine grid solutions. While the coarse and fine grid results for surface pressure on the front of the tractor do show some sensitivity to grid refinement, the estimated error in the fine grid solution is approximately ±0.05 ΔCp. Coarse and fine grid results for the base of the trailer are shown in Figure 3, with the maximum estimated error to be less than ±0.01 ΔCp (note the expanded scale for ΔCp). The Spalart-Allmaras model was only run on the fine mesh; however, the spatial discretization error is expected to be similar to that of the Menter model.

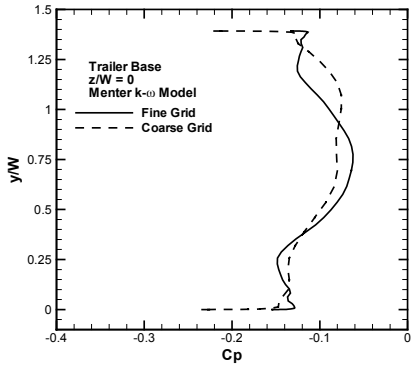

Figure 3. Pressure on base of trailer (coarse and fine meshes)

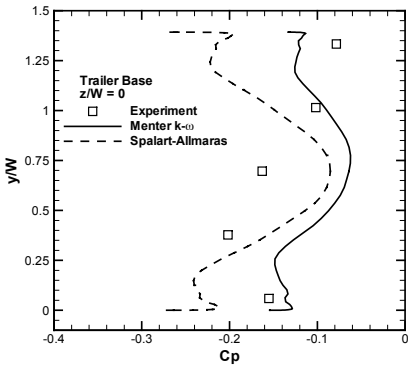

Figure 5. Surface pressure on trailer base

Surface Comparisons

The surface pressure for the two turbulence models using the fine mesh is compared to experimental data [2] on the front of the tractor in Figure 4. Both simulations show good agreement with the experimental data. Simulation results are presented for the base of the trailer in Figure 5. In this case, the Menter k-ω model does a reasonable job of matching the pressure levels, while the Spalart-Allmaras model [5] significantly underpredicts the pressure on the base.

Aerodynamic Drag

Aerodynamic drag predictions using the two turbulence models as well as the experimentally measured drag are presented in Table 2. These drag results (both predicted and experimental) are for the GTS model only and do not include the support posts. The Menter k-ω results are approximately 7.5% higher than the experimental value, while the

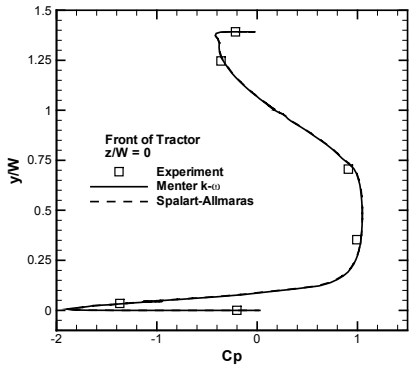

Figure 4. Surface pressures on front of tractor

Table 2. Drag coefficients

	Drag Coeff., C_D	Estimated Uncertainty/Error
Storms et al. Experiment [2]	0.25	±0.01
Menter k-ω [6]	0.298	±0.06
Spalart-Allmaras [5]	0.413	--

Spalart-Allmaras results [5] are nearly 50% high. The overprediction of the drag with the Spalart-Allmaras model is due to the poor prediction of the base pressure. Also shown in the table is the estimated uncertainty in the experimental drag coefficient [2], and the estimated numerical error for the fine grid Menter k-ω simulation [6]. This numerical error estimate is determined by performing Richardson extrapolation using the coarse and fine grid drag coefficients, 0.474 and 0.298, respectively. The resulting extrapolated value for the drag coefficient using the Menter k-ω model is 0.239, which is essentially within the experimental uncertainty bounds.

Field Comparisons

Velocity data are available from PIV measurements performed at the NASA Ames 7 × 10 ft wind tunnel [2]. These PIV data represent a time-averaged picture of the flow in the wake regions immediately behind the trailer base. Figure 6 gives streamlines based on the PIV data in a vertical streamwise cut through the wake (z/W = 0). The flow is from left to right, with the base of the trailer shown on the left; the PIV window is also shown in the figure. A large,

counter-clockwise-rotating vortex is centered at approximately x/W = 8, y/W = 0.4. Also, the presence of a clockwise-rotating vortex is suggested by the vertical nature of the streamlines in the upper right-hand corner of the PIV window. A similar view of the streamlines from the fine grid computations using the Menter k-ω model is shown in Figure 7. These Menter k-ω computations predict a more symmetric pair of vortices than is indicated from the experimental data. The location of the experimental PIV window is shown in the figure for reference. Streamlines for the Spalart-Allmaras model are presented in Figure 8, showing a much shorter recirculation zone than the Menter model. This shorter recirculation zone produces larger velocities in the outer flow as the flow accelerates around the wake. The higher velocities result in lower pressures and hence higher drag (see Table 2). Although not depicted, comparison to experimental PIV results for a horizontal streamwise cut through the wake (y/W = 0.696) showed that the location of the vortices was accurately predicted by the RANS model.

Truncated Geometry

A truncated GTS mesh was generated which omits the upstream wind tunnel and the front "tractor" section of the GTS. Steady-state RANS simulations on this geometry are underway and will be completed early in Fiscal Year 2004. Our goal here is to develop the minimum computational problem that adequately represents the large-scale separation effects in the flow and, thereby, recovers the dominant drag component. Simulations are to be

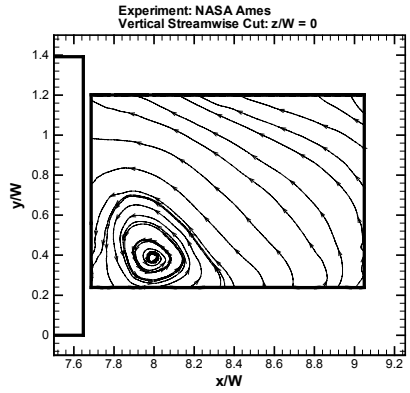

Figure 6. Experimental streamlines: vertical streamwise cut (z/W = 0)

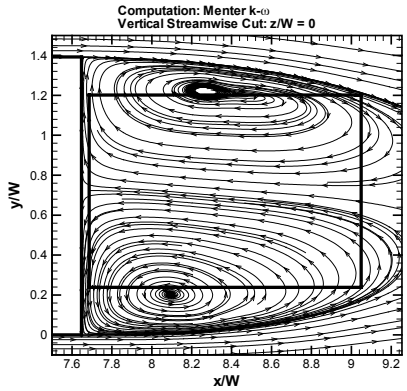

Figure 7. Computational streamlines: vertical streamwise cut (z/W = 0)

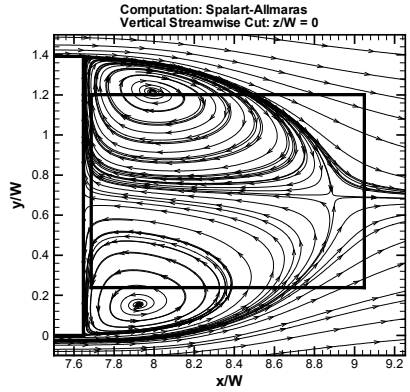

Figure 8. Computational streamlines: vertical streamwise cut (z/W = 0)

performed on both supercomputer and multiple workstation class platforms. The ability to model these flows on widely avaliable work station clusters (10–20 processors) is of particular interest, since it can be expected that many end users will have this level of computing resources currently available.

Reduced Order Modeling

Here, the self-similar, far-field, turbulent wake models are extended to estimate the 2-d, axi-symmetric and (simple) 3-d drag coefficient for a range of bluff body problems. The self-similar wake velocity defect that is normally independent of the initial condition, e.g. bluff body geometry, is modified using a Gram-Charlier series approach to retain the initial condition information. Preliminary results indicate that drag estimates computed using this method are within approximately 20% as compared to published values for flows with large

separation. The potential value of this method is as a way to utilize poorly resolved simulation results to provide an inexpensive estimate of body drag or as the basis of a physically consistent correlation scheme. This methodology may be of use as a supplement to CFD and experimental solutions in reducing the heavy computational and experimental burden of estimating drag coefficients for blunt body flows for preliminary design type studies.

Conclusions

Steady-state RANS simulations were conducted for the flow over the GTS geometry. The numerical accuracy of the computed flowfields was assessed by performing the computations on multiple grids. Simulation results using the Menter k-ω turbulence model gave good agreement with the experimental data for surface pressure, field velocities in the wake, and drag coefficient; however, this model predicted a more symmetric pair of counter-rotating vortices in the vertical streamwise plane than was indicated in the experiment. These results suggest that the Menter k-ω model can accurately predict the drag for tractor/trailer configurations when performed on highly refined meshes using integration to the wall, although some time-averaged flow structures are not captured. Simulation results with the Spalart-Allmaras turbulence model showed good agreement with experimental data for the surface pressure in the attached flow regions, but significantly underpredicted the pressure in the base region. As a result, the Spalart-Allmaras model overpredicted the drag coefficient by nearly 50%. Initial development of reduced-order drag prediction models were also introduced, with the preliminary results yielding drag estimates within 20% of established values.

References

1. McCallen R., Couch R., Hsu J., Browand F., Hammache M., Leonard A., Brady M., Salari K., Rutledge W., Ross J., Storms B., Heineck J.T., Driver D., Bell J., Zilliac G. (1999) Progress in reducing aerodynamic drag for higher efficiency of heavy duty trucks (class 7-8). SAE Paper 1999-01-2238.
2. Storms B.L., Ross J.C., Heineck J.T., Walker S.M., Driver D.M., Zilliac G.G. (2001) An experimental study of the ground transportation system (GTS) model in the NASA Ames 7- by 10-ft wind tunnel. NASA TM-2001-209621.
3. Wong C.C., Soetrisno M., Blottner F.G., Imlay S.T., Payne J.L. (1995) PINCA: a scalable parallel program for compressible gas dynamics with nonequilibrium chemistry. Sandia National Laboratories Report SAND 94-2436, Albuquerque, NM.
4. Roy C.J., McWherter-Payne M.A., Oberkampf W.L. (2000) Verification and validation for laminar hypersonic flowfields. AIAA Paper 2000-2550.
5. Spalart P.R., Allmaras S.R. (1994) A one-equation turbulence model for aerodynamic flows. La Recherche Aerospatiale 1: 5-21.
6. Menter F.R. (1994) Two-equation eddy-viscosity turbulence models for engineering applications. AIAA Journal 32: 1598–1605.

G. Commercial CFD Code Validation for External Aerodynamics Simulations of Realistic Heavy-Vehicle Configurations

Principal Investigator: W.D. Pointer
Argonne National Laboratory
9700 S. Cass Avenue, NE-208, Argonne, IL 60439
(630) 252-1052; fax: (630) 252-4500; dpointer@anl.gov

Technology Development Manager: Sid Diamond
(202) 586-8032; sid.diamond@ee.doe.gov
Technical Program Manager: Jules Routbort
(630) 252-5065; routbort@anl.gov

Contractor: Argonne National Laboratory
Contract No.: W-31-109-ENG-38

Objective

- Evaluate capabilities in standard commercial computational fluid dynamics (CFD) software for the prediction of aerodynamic characteristics of a conventional U.S. Class 8 tractor-trailer truck.
- Develop "best practice" guidelines for the application of commercial CFD software in the design process of Class 8 vehicles.

Approach

- Develop computational models of the experiments completed in the NASA Ames Laboratory's 7 ft. by 10 ft. wind tunnel using the Generic Conventional Model (GCM).
- Compare the predictions of the computational models with experimental measurements of vehicle aerodynamic drag force and pressure field distributions.

Accomplishments

- Experimental measurements and computational predictions of the vehicle drag coefficient agree within less than 1% in the best case simulations.
- Experimental measurements and computational predictions of the pressure distribution along the surface of the vehicle agree within the experimental error.

Future Direction

- Continue development of "best practice" guidelines through comparison of computational predictions with experimental measurement for the GCM as well as grid, model geometry, and turbulence model studies.
- Evaluate capabilities for prediction of aerodynamic drag in cases in which there is a cross-wind component (i.e., consider wind tunnel experiments where the vehicle is placed at some yaw angle).
- Consider alternate GCM configurations using various add-on devices to examine capabilities for the prediction of changes in drag coefficient.

Introduction

The issue of energy economy in transportation has grown beyond traditional concerns over environment, safety and health to include new concerns over domestic energy security. In collaboration with the U. S. Department of Energy Office of FreedomCAR and Vehicle Technologies' Working Group on Aerodynamic Drag of Heavy Vehicles, Argonne National Laboratory is developing guidelines for the accurate prediction of heavy vehicle aerodynamic drag coefficients using commercial Computational Fluid Dynamic (CFD) software. In these studies, computational predictions from the commercial CFD code Star-CD [1] will be compared with detailed velocity, pressure and force balance data from experiments completed in the 7 ft. by 10-ft. wind tunnel at NASA Ames [2,3] using a Generic Conventional Model (GCM) that is representative of typical current-generation class 8 tractor-trailer geometries. Initial evaluations have focused on the effects of selection of computational mesh size parameters and turbulence modeling strategies on the accuracy of the drag coefficient prediction.

Generic Conventional Model

The Generic Conventional Model (GCM) is a simplified representation of a conventional U.S. tractor-trailer truck. The model is 1/8th scale and can be configured in four different geometries as illustrated in Figure 1. The nominal, or Standard Truck, configuration is a representative model of a current-generation U. S. conventional class 8 tractor-trailer truck. Alternate GCM configurations include the addition of a lo-boy device under the length of the trailer, a full fairing between the cab and the trailer, and the combination of the fairing and lo-boy device.

Computational Model

The computational model employed in these studies was developed using the ES-Aero tool for aerodynamic drag simulation that is available as part of the Star-CD software package. The mesh is developed using a semi-automated process that progresses in eight stages:

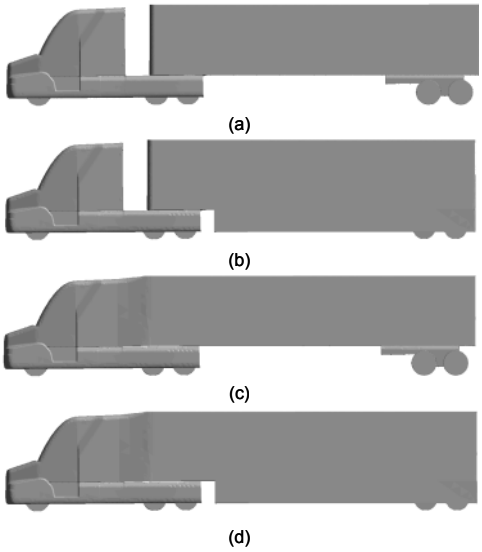

Figure 1. Four configurations of the generic conventional model: (a) standard truck, (b) standard truck with lo-boy trailer, (c) faired truck, (d) faired truck with lo-boy trailer

1. A three-dimensional hexahedral mesh is created that completely fills the volume of the wind tunnel.

2. The mesh is refined in successively smaller zones surrounding the vehicle until the mesh adjacent to the vehicle surface reaches the prescribed near-vehicle cell size. The resulting unstructured mesh of hexahedral cells exhibits 2-to-1 matching at all unstructured interfaces.

3. The near-vehicle mesh is locally refined based upon features of the vehicle surface definition. Local refinement limits are determined through the near-wall cell size parameter and direct user identification.

4. The surfaces that define the vehicle are "wrapped" by projecting the refined hexahedral mesh onto the surface. The components of the vehicle are merged into a single surface, and a quadrilateral surface definition is created.

5. The quadrilateral surface definition is volumetrically expanded to create a sub-surface.

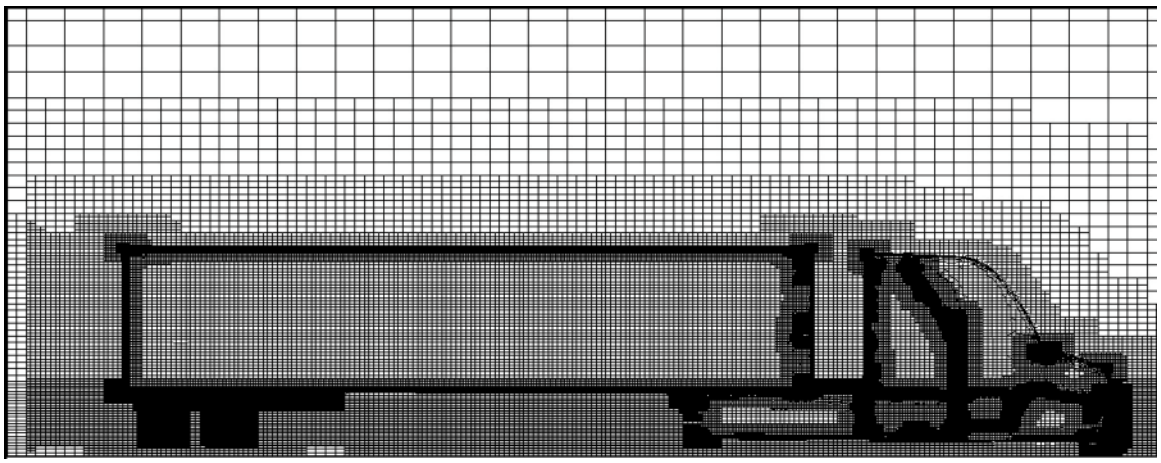

Figure 2. Two-dimensional projection of the near-vehicle region of the computational mesh employed in these studies

6. The sub-surface is used to cut away the parts of the hexahedral mesh that fall within a short distance of the vehicle surface.

7. A brick and prism extrusion layer is created to fill the gap between the sub-surface and the quadrilateral surface definition. Thus, the polyhedral trimmed cells that are generated when the vehicle shape is cut from the mesh are not in the critical boundary layer region of the problem.

8. Upon completion of the basic mesh, the wake and ground layer regions are automatically further refined to better capture important flow features.

In this study, the generated mesh has a near-wall cell size of 8.0 mm. The minimum cell size used in local refinements is 0.5 mm, and a minimum of 16 points are required to define any full circle. In addition to automatic refinements, cells adjacent to the surface are refined to a size of 2.0 mm in order to preserve the quality of the surface in the wrapping stage and improve the quality of the trimmed cells. The extrusion layer consists of two layers of brick and prism cells where the outer layer has a thickness of 1.0 mm and the inner layer has a thickness of 0.5 mm. A sample computational mesh is shown in Figure 2.

In all simulations discussed herein, the GCM is centered at zero yaw on the floor of a wind tunnel test section that is 2.133 m (7 ft) tall by 3.048 m (10 ft) wide. Since the GCM is approximately 2.5 m long, a total test section length of 10.0 m is assumed, where one model length is included upstream of the model and two model lengths are included downstream of the model. Based upon a Reynolds number of 1.1 million, a uniform velocity of 51.45 m/s is enforced at the inlet boundary. A uniform pressure condition is applied at the outlet boundary. In these studies, the surface of the standard configuration GCM is defined using approximately 500,000 triangular surface elements that are based upon CAD representations taken from optical scans of the actual model.

Mesh Sensitivity Studies

The Star-CD external aerodynamics analysis tool ES-Aero uses a local feature-size-based automatic meshing system to build a partially-unstructured, primarily-hexahedral computational mesh. In the generation process, a bulk near-vehicle cell size and a minimum cell size for local feature-based refinement regions, or near-wall cell size, are specified. In these studies, the effects of changes of these two parameters on predicted drag coefficient are evaluated.

For each steady-state simulation, 3,000 iterations were calculated using Star-CD's standard conjugate gradient solver and the PISO predictor-corrector algorithm. In these simulations, the standard high Reynolds number two-equation turbulence model and a logarithmic wall function are employed for prediction of turbulent kinetic energy and

dissipation. Convergence criteria were set to insure that all cases would reach 3,000 iterations before stopping. However, all residuals reach the normal stopping criteria of 10^{-3} well before the 3000th iteration and are no larger than 2.0×10^{-4} at the 3000th iteration. In addition to standard velocity and mass parameter residual monitoring, the drag coefficient of the vehicle is monitored as the solution develops to insure that the drag coefficient reaches a converged solution. In order to reduce computational cost for these studies, only half of the GCM is included in the model and a symmetric boundary condition is employed at the centerline.

The effects of the near-vehicle cell size parameter on the accuracy of drag coefficient prediction were first considered. The near-vehicle cell size was varied in size from 6 mm to 16 mm in five cases. The results, shown in Table 1, indicate that the drag coefficient can be predicted within 1.7% using a cell size of 6 mm and 10.5% using a cell size of 16 mm. Further reductions in near-vehicle cell size are not possible without violating the memory limits of the 32-bit system used in the development of these computational meshes. Further increases in the near-vehicle cell size will result in cells that are two large to capture significant vehicle features such as the rear wheel axels.

The effect of the near-wall cell size parameter on the accuracy of drag coefficient prediction was also considered. In this case, the near-vehicle cell size is set to 8mm and the minimum cell size for local refinement was reduced from 1mm to 0.5 mm. This increases the number of computational elements from 3,282,426 to 4,264,232 and the total CPU time used from 610,958 seconds to 703,027 seconds. The change in the near-wall refinement parameter results in a reduction in the error of the drag coefficient prediction from 4.2 to 1.0%.

Table 1. Effects of near-vehicle cell size parameter on accuracy of drag coefficient prediction

Near-Vehicle Cell Size (mm)	Predicted Drag Coefficient	Error in Drag Coefficient
experiment	0.398	
16	0.449	12.0
12	0.441	10.3
10	0.418	4.9
8	0.415	4.2
6	0.405	1.7

Turbulence Model Sensitivity

In order to evaluate the sensitivity of the solution to the turbulence model employed, a study was completed using three different turbulence models that are included as standard options in the Star-CD software package: the standard high-Reynolds number k-epsilon model with logarithmic wall function, the Menter k-omega SST model [4], and the renormalization group (RNG) formulation of the k-epsilon model [5]. The standard k-epsilon model and the SST model are identical in the far field, but the SST model incorporates additional detail in the near-wall region. The SST model should be more sensitive to separation, but the two should show reasonable agreement. The RNG model is similar to the standard k-epsilon model, but includes an additional term to account for the mean flow distortion of the dissipation. With all three models, logarithmic wall functions are employed for boundary layer modeling. All simulations use a highly refined mesh with a near-vehicle cell size of 8.0 mm and a minimum cell size of 0.5 mm. As in previous studies, only one symmetric half of the vehicle is considered to reduce the computational requirements. Again, 3,000 iterations are completed for each case and the convergence of the drag coefficient is monitored. Results of the study, as summarized in Table 2, indicate that the Menter k-omega SST model provides a slight performance improvement over the other models.

Table 2. Results of the evaluation of two-equation turbulence models for prediction of tractor-trailer truck drag coefficients

Turbulence Model	Predicted Drag Coefficient	Percent Error in Prediction
Experiment	0.398	--
High-Reynolds Number k-epsilon Model	0.402	1.0
Menter k-ω SST model	0.401	0.8
RNG model	0.389	2.3

Half Vehicle Versus Full Vehicle

In order to evaluate the effects of considering only half of the vehicle rather than the full vehicle, two models were created using the full vehicle geometry. These models use the same mesh parameter settings as the two coarsest models considered in the mesh sensitivity study, with near-wall cell sizes of 12 mm and 16 mm. As in all previous studies, 3,000 iterations were completed for each steady-state simulation and the convergence of the drag coefficient was monitored. As shown in Table 3, drag coefficient predictions show a slight improvement in agreement with experimental measurements when the full vehicle model is used.

Pressure Field Comparisons

Since the drag coefficient is an integrated quantity, comparison of the simulation predictions of surface pressure distribution with the experimentally measured surface pressure distribution provides another measure of the accuracy of the simulation. The pressure distribution along the vehicle surface from the case using a half-vehicle model with a near-vehicle cell size of 8 mm, a near-wall cell size limit of 0.5 mm and the Menter k-ω SST model is shown in Figure 3. The comparison of the predicted pressure distribution along the vehicle centerline with experimental measurements, as shown in Figure 4, indicates that the surface pressure distribution is predicted with reasonable accuracy. A more detailed comparison of the pressure distribution along the rear face of the trailer, which is typically, the most difficult region to predict accurately, is shown in Figure 5.

Conclusions

In these studies, the predictions of heavy vehicle aerodynamic characteristics generated using standard mesh generation and turbulence modeling options within the commercial computational fluid dynamics (CFD) code Star-CD have been compared with wind tunnel experiments using the Generic Conventional Model (GCM). The computational predictions show good agreement with the experimental measurements of the drag coefficient. The predicted surface pressure distribution also show good agreement with measured values with the maximum error occurring along the rear faces of the cab and the trailer. While the results of these studies are promising, they should not be viewed as conclusive, since the capabilities of the software for the prediction of changes in drag coefficient with changes in vehicle geometry are not yet known. In foreseeable applications within the truck manufacturing industry, the ability to predict changes in aerodynamic characteristics resulting from small changes in vehicle design is likely to be more valuable than the ability to predict the absolute value of the drag coefficient.

Future Work

The next phase of this project will duplicate the analyses discussed herein for each of the alternative configurations of the GCM. Additionally, the capability of the commercial CFD software to predict the aerodynamic characteristics of the Standard Truck configuration when a cross-wind component is present will be evaluated by comparison with measurements from experiments using the GCM placed at a set yaw angle within the 7 ft by 10 ft wind tunnel. These future studies will provide information on the capability of the code to predict changes in the aerodynamic characteristics of a heavy vehicle resulting from changes in design or environment.

Table 3. Comparison of drag coefficient predictions from half-vehicle and full-vehicle models

	Half-Vehicle		Full-Vehicle	
Near-Vehicle Cell Size (mm)	Predicted Drag Coefficient	Percent Error in Prediction	Predicted Drag Coefficient	Percent Error in Prediction
16	0.449	12.0	0.441	10.3
12	0.441	10.3	0.426	6.7

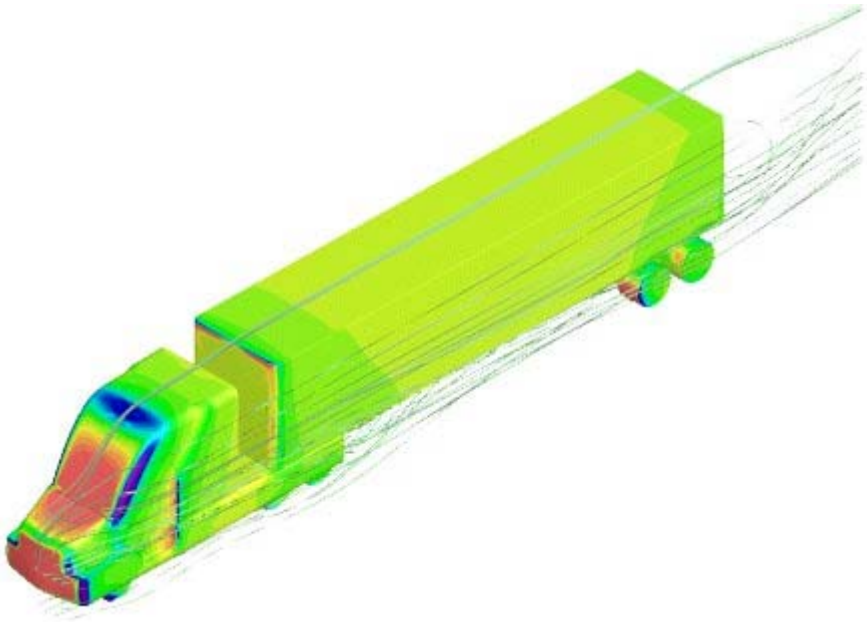

Figure 3. Surface contour plot showing the predicted surface pressure distribution along the surface of the GCM. Areas shown in red are areas of peak positive pressure and areas shown in blue are areas of peak negative pressure. Selected flow streamlines are also shown to illustrate the movement of air over the vehicle.

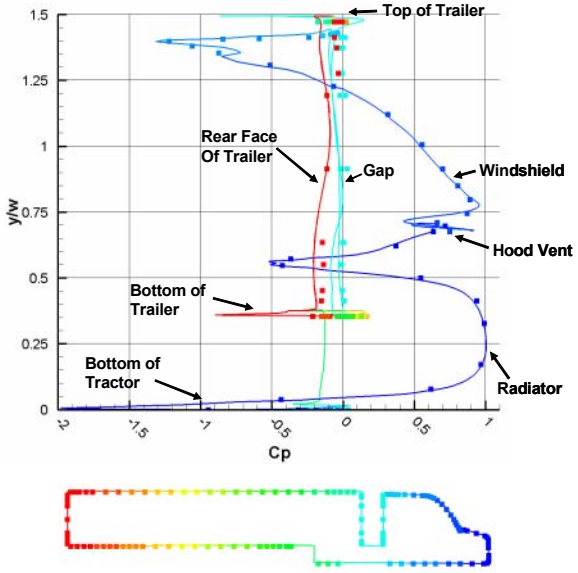

Figure 4. Comparison of predicted (line) and measured (dot) pressure distributions along the centerline of the Generic Conventional Model. As shown in the outline of the GCM, shading indicates axial position with blue indicating the grill and bumper area and red indicating the rear face of the trailer.

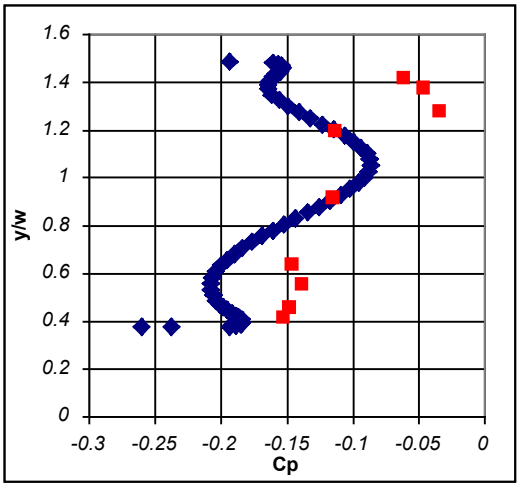

Figure 5. Comparison of predicted (diamond) and measured (square) pressure distributions along the centerline of the rear face of the trailer

References

1. Star-CD, version 3.150A, CD-Adapco Group, Melville, NY.
2. Dale Satran, "An Experimental Study of the Generic Conventional Model (GCM) in the NASA Ames 7-by-10-Foot Wind Tunnel," United Engineering Foundation Conference on The Aerodynamics of Heavy Vehicles: Trucks, Buses, and Trains, Monterey, CA, Dec. 2–6, 2002.
3. J.T. Heineck, Stephen Walker, Dale Satran, "The Measurement of Wake and Gap Flows of a 1/8th Scale Generic Truck Using Three-Component Particle Image Velocimetry," United Engineering Foundation Conference on The Aerodynamics of Heavy Vehicles: Trucks, Buses, and Trains, Monterey, CA, Dec. 2–6, 2002.
4. Menter, F.R., "Zonal Two Equation k-ω Turbulence Models for Aerodynamic Flows" in 24th Fluid Dynamics Conference (Orlando), AIAA paper 93-2906, July 1993.
5. Yakhot, V., Orszag, S.A., Thangam, S., Gatski, T.B., and Speziale, C.G. 'Development of turbulence models for shear flows by a double expansion technique,' Phys. Fluids, A4, No. 7, pp. 1510–1520, 1992.

H. Vortex Methods

Principal Investigator: A. Leonard
Co-Investigators: M. Rubel and P. Chatelain
California Institute of Technology
1200 East California Blvd. MC 301-46, Pasadena, CA 91125
(626) 395-4465; tony@galcit.caltech.edu

Technology Development Manager: Sid Diamond
(202) 586-8032; sid.diamond@ee.doe.gov
Technical Program Manager: Jules Routbort
(630) 252-5065; routbort@anl.gov

Contractor: California Institute of Technology
Contract No.: DE-AC03-98EE50506

Objective

- Develop and demonstrate gridless flow field method for computationally modeling heavy vehicle aerodynamics.

Approach

- Improve and extend vortex method approach and demonstrate capabilities on generic shapes and Ground Transportation System geometry.

Accomplishments

- Developed treatment of spinning boundaries.
- Study of boundary elements has led to a method for representing near-wall vorticity.
- Developed new method for redistribution of vortex particles.
- Development of a "Closest Point Transform" algorithm for improved runtime efficiency.
- Continued improvements in adaptive time integration to facilitate complex geometry applications.
- Modeled flow around GTS.

Future Direction

- Continued development of vortex method approach and application to generic shapes and the GTS geometry.

Introduction

During FY03, Caltech continued to improve and extend its vortex method approach to flow past complex bodies. These activities included treatment of spinning boundaries, research on boundary elements, high order isotropic redistribution, development of a fast algorithm for the Closest Point Transform and adaptive time integration. With our colleagues at UCL in Belgium, we also completed an application of our method to the GTS geometry.

Spinning Boundaries

In our framework, because the fields are computed using the unbounded Biot-Savart law, it is necessary to include the contribution of the vorticity present inside any spinning body. The subsequent volume integral is transformed into a surface one, better

suited for our boundary element method. Figure 1 shows the sheet diffused by an impulsively started spinning body; because we included the contribution of the forementioned *spin vorticity*, the sheet — found by a panel solver — has the correct total circulation.

Near-Wall Elements

Near-wall vorticity can now be represented by attached elements (Figure 2). These panels interact viscously with the regular-free-elements and induce a velocity field (Biot-Savart law). Derivation of an appropriate Biot-Savart law is in progress.

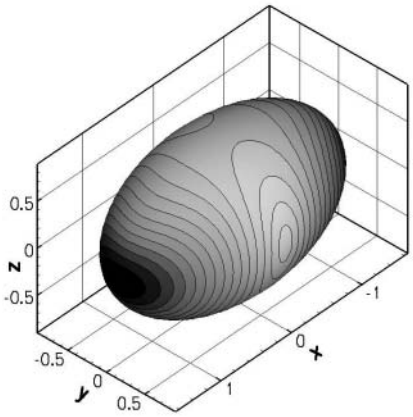

Figure 1. Vorticity flux magnitude for an impulsively started spinning ellipsoid (rotation about y-axis)

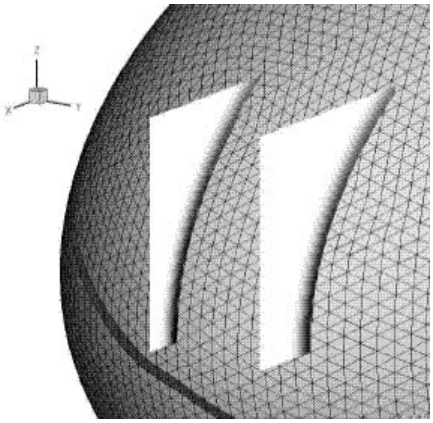

Figure 2. Near-wall vorticity magnitude at $t = 0^+$, slices taken near the tip of the ellipsoid

High-Order Isotropic Redistribution

We pursued the work on the redistribution schemes in Face Centered Cubic (FCC) lattices. A higher order scheme was designed which shows remarkable isotropy when compared to equivalent schemes for cubic lattices (Figures 3 and 4). Let us emphasize that the redistribution of the vortex particles every few time steps is critical for the convergence of the method, hence the importance of its isotropy and accuracy.

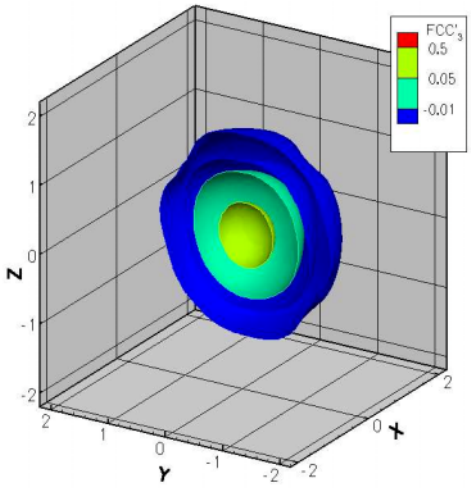

Figure 3. Isosurfaces of the third order FCC scheme (FCC'3)

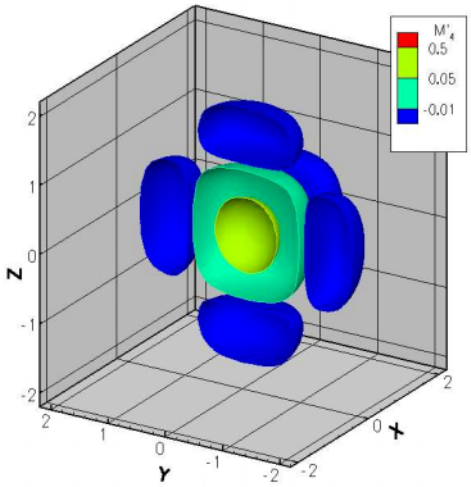

Figure 4. Isosurfaces of the third order cubic scheme (*M'4*)

Fast Closest Point Transform

A paper on the new Characteristic/Oct Tree (C/OT) algorithm for the closest point transform, which allows the code to work on arbitrarily complicated boundary geometries, was submitted. The algorithm works by separating space into families of characteristic lines of an Eikonal equation, and sorting them according to how they intersect cells of an oct tree (Figures 5 and 6).

This algorithm is now implemented and used in many areas of the code: generation/redistribution of particles around arbitrary geometries, sampling fields as in Figure 2, etc.

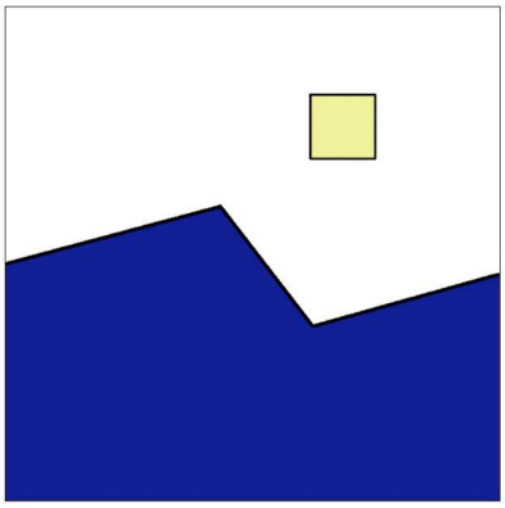

Figure 5. Boundary and cell of interest

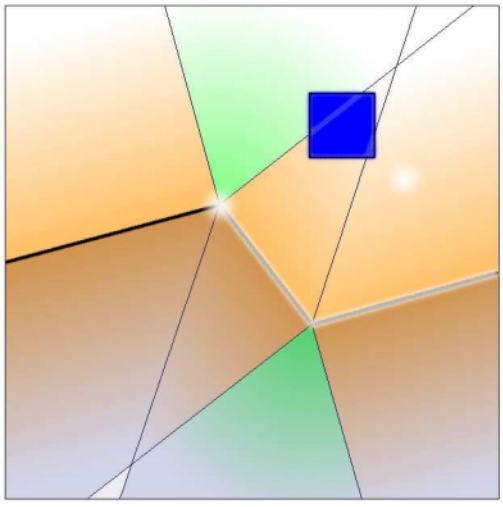

Figure 6. Characteristic regions and intersection with cell

Adaptive Time Integration

One of the group's ongoing research projects has been the development of an efficient asynchronous *dead reckoning* numerical time integrator for the large systems of differential equations that arise when vortex methods are applied to complicated geometries at high Re. In the past year, work in this area focused on tweaking the strategy to make it scale better to the dense operators typically seen in vortex problems, primarily by eliminating the wake-on-change strategy employed in earlier incarnations of the algorithm.

GTS Model

The flow around the GTS model was computed in collaboration with G. Winckelmans' group at the Universit´e Catholique de Louvain (UCL) (Figure 7). To make this run affordable, attached vortex elements were used on the front part of the truck and free elements were introduced upstream of the region of separation.

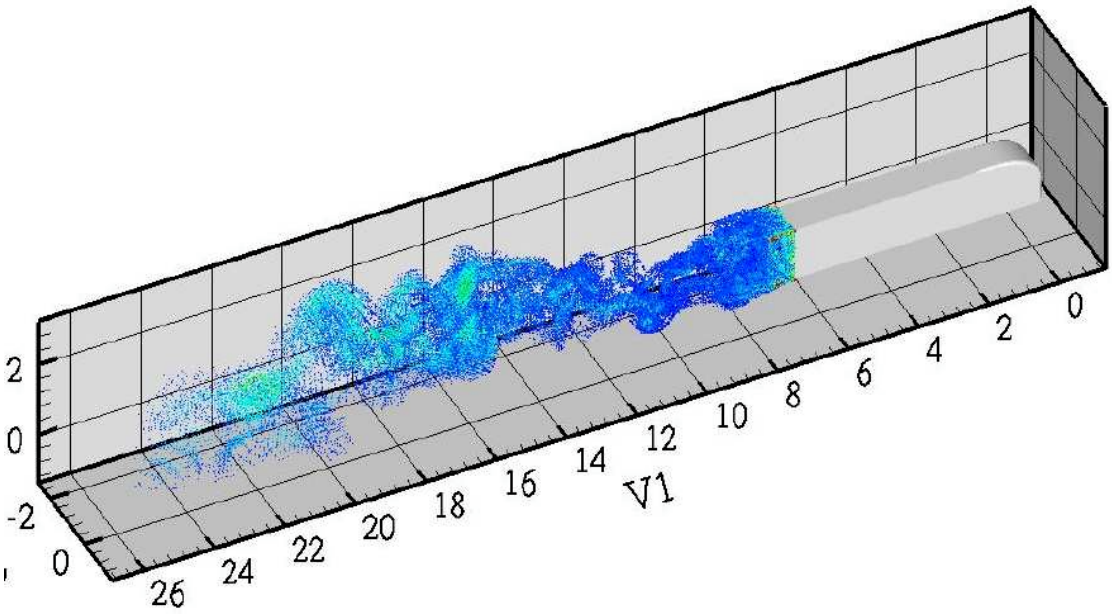

Figure 7. GTS model, positions and strengths of vortex elements

II. Thermal Management

A. Cooling Fan and System Performance and Efficiency Improvements

Principal Investigator: R.L. Dupree
Caterpillar Incorporated
Technical Center Building E
P.O. Box 1875, Peoria, Illinois 61656
(309) 578-0145; fax: (309) 578-4277; dupree_ron_l@cat.com

Investigator: J.L. Bender
Caterpillar Incorporated
Technical Center Building E
P.O. Box 1875, Peoria, Illinois 61656
(309) 578-6452; fax: (309) 578-4277; bender_john_l@cat.com

Technology Development Manager: Sid Diamond
(202) 586-8032; sid.diamond@ee.doe.gov
Technical Program Manager: Jules Routbort
(630) 252-5065; routbort@anl.gov

Contractor: Caterpillar Inc
Contract No.: DE-FC04-2002AL68081

Objective

- Develop cooling system fans and fan systems that will allow off-highway machines to meet Tier 3 emissions regulations and reduce spectator sound levels with improved fuel efficiency, and within the functional constraints of machine size.

Approach

- Task 1 is to develop a large, high-performance axial fan
- Task 2 is to develop an active fan shroud for use with large axial fans
- Task 3 is to develop fan modeling techniques to improve the ability to predict fan performance and component airflows in cooling systems with side by side heat exchangers
- Task 4 is to demonstrate the performance of a lab developed swept blade, mixed flow fan in an off-road machine.
- Task 5 is to develop a high efficiency continuously variable speed fan drive for use in high horsepower fan systems
- Task 6 is to develop cooling system air filtration concepts that can allow more dense (higher performance) heat exchangers to be used in off-road machines

Accomplishments

- Task 1- completed the design and performance measurement of a high performance axial fan using Genetic Algorithms. Fan blading has been redesigned to improve performance with knife edge shrouds and prototype is in process of being built.
- Task 2- not planned to have significant accomplishments in this FY

- Task 3- Michigan State University has acquired velocity map data near the fan. Caterpillar has completed initial CFD models of fan and fan system.
- Task 4- Prototype fan has been built and tested in an off-road machine. Fan performance in lab conditions equals baseline axial fan, but in the machine its flow is only 78% of the axial fan. Lab testing of the configuration shows that the performance loss of the prototype fan is due to the conical hub and ring shroud design which do not allow the air to leave the fan radially, like what occurs with the baseline axial fan. This loss of flow is unacceptable, and as a result the fan concept has failed its gate review. Task is completed.
- Task 5- The design of a dual modulating clutch variable speed fan drive was completed, along with performance analyses to determine the potential fuel savings for different control methods and different locations throughout the world. The dual clutch fan drive showed the potential of 1.4% fuel savings over a single ratio design, but the dual ratio design cannot meet commercial requirements for production, so further development was halted at the gate review. Task is completed.
- Task 6- Sensitivity testing of radiator designs to determine debris sizes needed to be filtered has begun.

Future Direction

- Task 1- Second generation concept fan is on order for evaluation ahead of a planned task gate review.
- Task 2- Michigan State University is completing the design of an active shroud design for lab evaluation. When the shroud design is done, MSU will optimize fan/shroud combination, concentrating on reducing the amount of auxiliary air required. Caterpillar will test the same fan in a conventional venturi shroud design for performance comparisons.
- Task 3- Michigan State University will provide localized flow data to Caterpillar. Caterpillar will use the local flow data to modify fan analysis methods to improve the ability to predict both fan performance and heat exchanger flow in side by side heat exchanger designs.
- Tasks 4 and 5- Tasks completed. Final documentation due.
- Task 6- Quantify the particle size range needed to be filtered to allow higher performance heat exchangers to be used in off-road machines. Design filtration system to provide the needed filtration performance.

Introduction

This project involves predicting the fuel savings potential of variable-speed fan drives in off-road equipment.

The value of demand fan drives, either in the form of variable-speed or declutching fan drives, for reducing the fuel consumption of trucks and other on-road machines is well recognized. The cooling system of the truck is designed to maintain acceptable operating temperatures at very high load factors, at relatively low travel speeds, and high ambient temperatures. The net result is that the average truck has significantly more cooling system performance than needed during most operations. Trucks hauling freight between cities have at least 55 mile per hour ram air available to them, providing significant cooling system performance even when the cooling fan is disengaged. The use of demand fan drives is not well accepted in off-road machines because:

- Off-road machines are expected to operate at a higher load factor than on-highway trucks.
- Off-road machine cooling systems must cool powertrain and hydraulic systems in addition to the engine coolant. These non-engine systems can represent a significant percentage of the total cooling system heat load.
- The travel speed of many off-road machines never exceeds 7 miles/hour, so cooling provided by ram air is not available.

The value of demand fan drives in reducing off-road machine sound has been recognized by the EEC in their directive 2000/14/EC (“Directive of the European Parliament and of the Council on the Approximation of the Laws of the Member States Relating to the Noise Emission in the

Environment by Equipment for Use Outdoors" dated May 8, 2000), where special sound test procedures are permitted for machines using continuously variable fans. The use of demand fan drives for machines that must meet EEC off-road machine spectator sound regulations has brought a renewed interest in the use of continuously variable-speed fan drives for large off-road machines. Before variable-speed fan drives would be provided as either a product option or standard feature, the tractor design groups needed to know the fuel savings potential of the device, often for a specific application in a specific location. By combining machine performance, fan drive performance, and ambient temperature data, we can provide an accurate estimate of the potential fuel savings that a continuously variable speed fan drive can provide for a specific machine application.

Fan Speed vs. Ambient Temperature

The required cooling system fan speed is a function of the machine operation (load factor), the cooling system characteristics, and the ambient air temperature. The required fan speed can be determined using a dynamic machine performance simulation model. The machine operating cycle to be evaluated must be modeled in a simulation tool that can accurately account for engine and drive train performance and heat load, then the cooling system performance is incorporated in the dynamic simulation model, so that as the machine operates at a given ambient temperature, the average fan rpm can be determined. This is repeated over a variety of different ambient temperatures until the relationship of fan speed vs. ambient temperature can be determined as shown in Figure 1.

Figure 1 also shows the significant effect that the presence of air to air aftercooling (ATAAC), as required on many emissions regulated engines, can have on fan speed at higher ambient temperatures. The presence of ATAAC, as well as the performance of the aftercooler can have a significant effect on fan speed (and fuel consumption of the cooling system) in the critical 30°C to 40°C ambient temperature range that many machines will experience during the summer months.

Fan System Input Power

The next step is to determine the fan system (combination of fan and fan drive) input power as a function of fan speed. Figure 2 compares the input power of a conventional belt driven fan with the power LOSSES of a continuously variable-speed fan

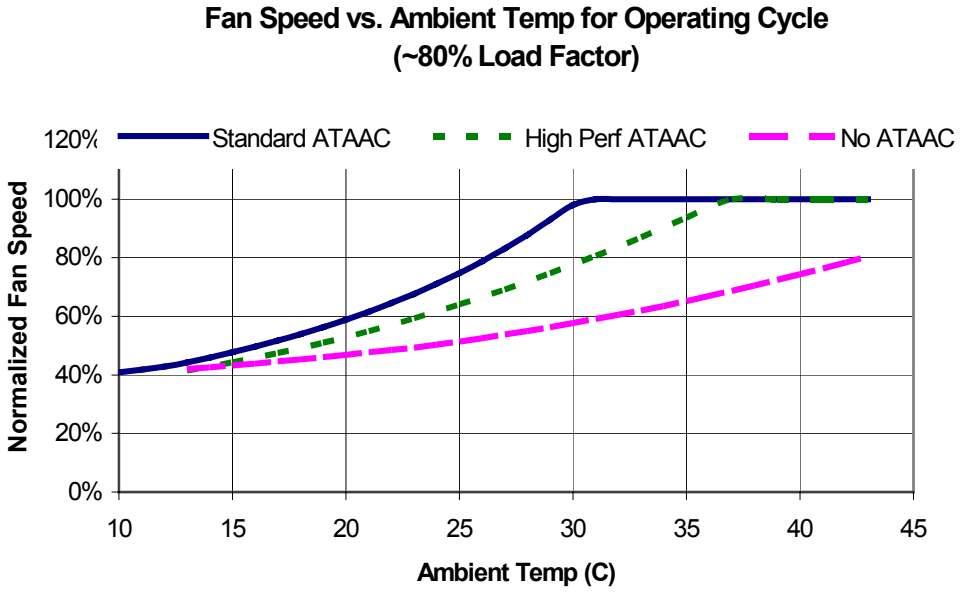

Figure 1. Fan speed vs. ambient temperature

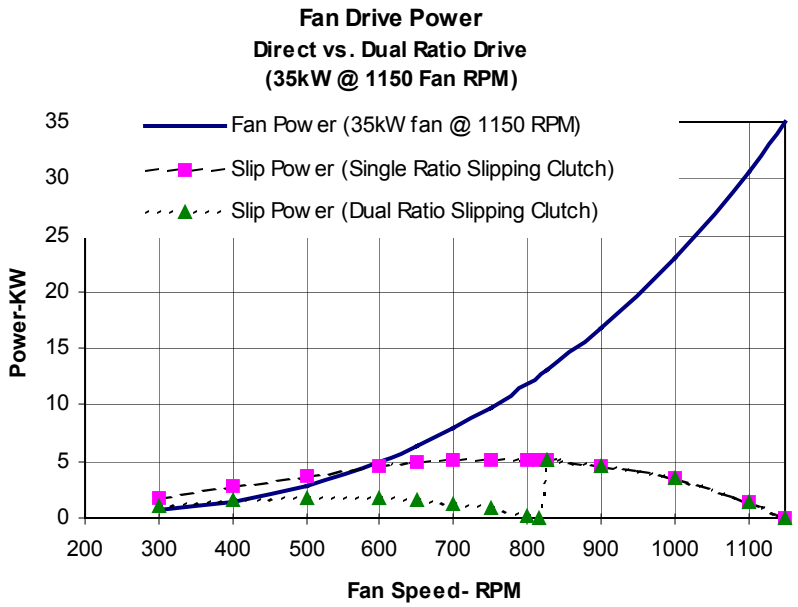

Figure 2. Fan power and drive losses

drive utilizing a single ratio slipping clutch, versus a similar fan drive design with dual ratio clutches to minimize power losses. The fan input power for the clutch equipped fans would be the sum of the fan input power and the slip power (the power loss in the clutch). The chart compares the slip power of the two fan clutch concepts to contrast the losses between the two designs. The losses are very similar at high drive ratios (corresponding to high ambient temperatures), but the dual ratio concept significantly reduces drive losses at lower drive ratios (corresponding to lower ambient temperatures).

Ambient Temperature Data

Ambient air temperature data, is available from from the EnergyPlus database on the U.S. Department of Energy's web site (http://www.eere.energy.gov/ buildings/energy_tools/ energyplus/cfm/ weatherdata_us.cfm). This location provides weather data from an ASHRAE/DOE data base used to calculate building energy savings. Temperature data is average *per hour* for each month of the year. This lets us look at first shift only, all three shifts, or only summer operation if we choose. ASHRAE has selected the data to provide *typical* temperatures for that hour, month, and location, so quoted temperatures are slightly different from Weather Bureau data, and may be 2–3°C different from what the Weather Bureau will quote for average or high temperature for the month. The example data shown in Figure 3 is available for is available for worldwide locations.

Estimated Cooling System Fuel Use

This fuel consumption for the belt driven fan is $fuel = fanpower * time(hours) * bsfc$ regardless of load factor or ambient temperature. The fuel consumed by the continuously variable-speed drive is determined by calculating the fuel used in each hour/month combination (288 cells of data for 24 hour/day operation) for the year. For each hour/month combination we know the average temperature from the Energy+ data in Figure 3. The ambient temperature determines the fan speed from curves like Figure 1. The fan input power is the sum of the required fan power plus the slip power (or drive losses) from Figure 2. The total fuel consumed in a day is the sum of the fuel consumed in the individual 24 hourly segments (assuming the machine is used 24 hours/day). The individual hourly data was converted into monthly data by assuming the number of working days in a month (up to 30 days/month for high production machines) and assuming the machine was in use 80% of the time it was available.

```
Statistics for USA_IL_Peoria_TMY2
Location -- PEORIA IL USA
     (N 40° 40') (W  89° 40') (GMT -6.0 Hours)
Elevation --   199m above sea level
Data Source -- TMY2-14842

- Using Design Conditions from "United States Climate Design Data 2001 ASHRAE Handb
   Design Type HDB 99.60%      HDB 99% X WS 1% X WS 2.50%      X WS 5% CM WS .40%
   Units       (°C)    (°C)    (m/s)   (m/s)   (m/s)   (m/s)   (°C)    (m/s)   (°C)
   HEATING     -21.1   -18.1   11      9.7     8.7     11.7    -8.7    10.1    -7.2
   Design Type CDB .40%        C MXB .40%      CDB 1%  C MXB 1%        CDB 2%  C MX
   Units       (°C)    (°C)    (°C)    (°C)    (°C)    (°C)    (°C)    (°C)    (°C)
   COOLING     33.3    24.3    31.7    23.4    30.2    22.8    25.8    31.6    24.9


-  642 cooling degree-days (18°C baseline)
- 3511 heating degree-days (18°C baseline)

- 1893 cooling degree-days (10°C baseline)
- 1839 heating degree-days (10°C baseline)

- Monthly Statistics for Dry Bulb temperatures °C
                     Jan     Feb     Mar     Apr     May     Jun     Jul     Aug
       Maximum        10.6    13.9    26.1    30.0    31.7    33.3    36.1    32.
       Minimum       -25.6   -15.6   -12.2    -3.9     1.7     6.9    10.6     9.
       Daily Avg      -5.3    -2.3     2.6    11.0    15.4    22.0    23.7    22.
  - Maximum Dry Bulb temperature of  36.1°C on Jul  1
  - Minimum Dry Bulb temperature of -25.6°C on Jan  7

- Average Hourly Statistics for Dry Bulb temperatures °C
                     Jan     Feb     Mar     Apr     May     Jun     Jul     Aug
       0:01- 1:00     -6.9    -4.0     0.7     8.0    11.6    18.4    19.9    19.
       1:01- 2:00     -7.1    -4.3     0.3     7.5    10.6    17.7    19.4    18.
       2:01- 3:00     -7.3    -4.7     0.0     7.1    10.3    17.5    19.2    18.
       3:01- 4:00     -7.5    -4.9     0.0     6.8    10.0    17.1    18.7    18.
       4:01- 5:00     -7.6    -5.1    -0.2     6.6     9.8    17.0    18.2    17.
       5:01- 6:00     -7.6    -5.3    -0.4     6.5    10.7    18.0    19.3    17.
       6:01- 7:00     -7.5    -4.8    -0.2     7.8    12.5    19.4    21.2    19.
       7:01- 8:00     -7.2    -4.3     0.7     9.5    14.3    20.8    23.1    21.
       8:01- 9:00     -6.9    -3.7     2.0    10.8    15.9    22.3    24.7    22.
       9:01-10:00     -5.8    -2.3     3.3    12.3    17.1    23.8    26.2    24.
      10:01-11:00     -4.7    -0.8     4.7    13.5    18.1    24.5    27.3    25.
      11:01-12:00     -3.5     0.6     5.8    14.3    19.2    25.2    28.3    26.
      12:01-13:00     -3.1     0.9     6.3    15.1    19.7    25.8    28.7    26.
      13:01-14:00     -2.7     1.2     6.8    15.8    20.2    26.6    28.9    27.
      14:01-15:00     -2.2     1.6     6.8    15.8    20.4    26.9    28.8    27.
      15:01-16:00     -2.7     0.8     6.6    15.4    20.5    26.9    28.5    27.
      16:01-17:00     -3.2     0.0     5.8    14.8    20.1    26.7    27.7    26.
      17:01-18:00     -3.7    -0.8     4.5    13.8    19.3    26.0    26.8    25.
      18:01-19:00     -4.1    -1.4     3.4    12.8    17.9    24.5    25.5    23.
      19:01-20:00     -4.5    -2.0     2.8    11.7    16.2    22.8    23.8    22.
      20:01-21:00     -4.9    -2.7     2.4    11.0    15.0    21.5    22.4    21.
      21:01-22:00     -5.2    -2.9     1.9    10.2    14.1    20.4    21.5    20.
      22:01-23:00     -5.5    -3.2     1.4     9.6    13.4    19.7    20.9    20.
      23:01-24:00     -5.8    -3.4     1.0     8.8    12.5    19.2    20.3    19.
       Max Hour         15      15      14      15      16      16      14      15
       Min Hour          6       6       6       6       5       5       5       5
```

Figure 3. Energy+ temperature data example

Cooling System Fuel Consumption

The machine to be evaluated is an off-road machine used in mining. The fan requires 35kW at 1150 rpm, and will be evaluated using the fan speed vs. ambient temperature relationships shown in Figure 1, for a work cycle that represents an 80% load factor (the machine burns 80% of the fuel that would be consumed if the machine were operating at rated speed and power). The fan drives to be considered are: direct drive, single ratio slipping clutch and dual ratio slipping clutch with the loss characteristics as shown in Figure 2, and the machine is assumed to be operating in the Midwest in ambient temperature conditions as shown in Figure 3. The machine is available for use 24 hours per day, 30 days per month, and is actually in use 80% of the time it is available. The fuel consumed to operate the cooling system under these operating conditions is:

Aftercooling	Ideal (no losses) (liters/yr)	Dual ratio clutch (liters/yr)	Single ratio clutch (liters/yr)
Jacket Water	5427	9434	14214
Large ATAAC	7198	11243	16663
Small ATAAC	9813	14555	19770

To put these numbers in perspective, a 35kW fan would consume 61,824 liters/yr of fuel, out of a total machine fuel consumption of approximately 650,000 liters/yr. The "ideal" fuel consumption is the power required by the fan itself, and assumes a drive that is

100% efficient. If the machine consumes 650,000 liters/yr of fuel, and the fixed ratio fan consumes roughly 62,000 liters of fuel/yr then the fuel consumption of the machine without the fan would be 588,000 liters/yr. Total machine fuel consumption would then become:

Aftercooling	Ideal (no losses) (liters/yr)	Dual ratio clutch (liters/yr)	Single ratio clutch (liters/yr)
Jacket Water	593,427	597,434	602,214
Large ATAAC	595,198	599,243	604,663
Small ATAAC	597,813	602,555	607,770

Installing the single ratio fan clutch on a machine with a small ATAAC could reduce total fuel consumption from 650,000 liters/yr to 607,770 liters/yr, a savings of 6.5% in fuel consumption. The dual ratio clutch design considered would save 7.3%, and an ideal variable-speed fan drive would save 8% of the total fuel consumed by the machine. The example machine represents a high percentage of engine output power being used by the cooling fan, but is not out of line with potential tier 3 losses on machines that are significantly constrained relative to frontal area, and must provide more cooling performance by increasing fan speeds. High load factor machines may not see as much fuel savings, because some of the greater available net power may be used to perform more work in the same amount of time. In that case, the fuel consumption savings would have to be viewed in the context of work performed/liter of fuel. In addition, the milder summers of the Midwest will show higher fuel savings potential than areas of the country with higher ambient temperatures, and machines operating three shifts will save more fuel than machines operating only during a single daytime shift. If our same example machine is used for eight hours/day, 20 days/month from the months of March through October, the fuel consumed by a fixed ratio fan would be 9,114 liters, vs. 4631 liters for a single ratio clutch. This is a 3.3% fuel savings, based on fuel consumption of the machine (not including the fuel consumption of the fan) of 130,667 liters during this same time frame.

Conclusions

Powertrain and cooling system dynamic performance models can be used to predict the relationship of required fan speed vs. ambient temperature for a variety of off-road machine configurations, and operating cycles. The resulting fan speed vs. ambient temperature relationship can be combined with ambient temperature data in the Department of Energy's Energy+ database to provide estimates of fuel savings potential for a variety of fan drive designs.

As cooling system demand grows, with little increase in frontal area, the fan input power will continue to grow as a percentage of gross horsepower. The fuel savings potential of a continuously variable speed fan drive is significant, while the exact value of the fuel savings is a function of machine design, ambient temperature, and machine load factor. Considering that the majority of large off-road machines do not use any form of variable speed fan drive, the adoption of a conventional single ratio drive can provide a significant reduction in fuel consumption. The adoption of a more complex dual ratio drive could provide further fuel savings, and begin to approach the fuel efficiency of an ideal fan drive that has no losses as it varies the fan drive ratio.

B. Efficient Cooling in Engines with Nucleate Boiling

Principal Investigator: J.R. Hull
Argonne National Laboratory
9700 South Cass Avenue, Building 335, Argonne, IL 60439
(630) 252-8580; fax: (630) 252-5568; jhull@anl.gov

Technology Development Manager: Sid Diamond
(202) 586-8032; sid.diamond@ee.doe.gov
Technical Program Manager: Jules Routbort
(630) 252-5065; routbort@anl.gov

Contractor: Argonne National Laboratory
Contract No.: W-31-109-ENG-38

Objective

- Investigate potential of two-phase flow in engine cooling applications.
- Determine limits on two-phase heat transfer (occurrence of critical heat flux or flow instability).

Approach

- Experimentally determine heat transfer rates and critical heat fluxes in small channels with water and 50% ethylene glycol in water mixture.
- Perform experiments over a concentration range of ethylene glycol in water.
- Perform experiments with alternative fluids.

Accomplishments

- Completed two-phase heat transfer experiments and analysis with 50/50 ethylene glycol/water mixture.
- Developed a new general correlation for flow boiling in small channels including water, 50/50 ethylene glycol/water mixture, and refrigerants.
- Performed preliminary experiments on boiling flow stability.

Future Direction

- Perform two-phase heat transfer experiments with ethylene glycol/water mixtures at other concentrations for off design automotive conditions.
- Study the impact of vertical vs horizontal flow on two-phase heat transfer.
- Perform systematic experiments with alternative fluids.

Introduction

Analyses of trends in the motor vehicle development sector indicate that future engine cooling systems will have to cope with greater heat loads because of more powerful engines, more air conditioning, more stringent emissions requirements, and additional auxiliary equipment. Moreover, there is considerable interest in reducing the size of the cooling systems to obtain a better aerodynamic profile. To meet these conditions, it is necessary to design cooling systems that occupy less space, are lightweight, have reduced fluid inventory, and exhibit improved performance. Among various new cooling systems proposed by

researchers, the nucleate-boiling cooling system has high potential to meet these challenges. Order-of-magnitude higher heat transfer rates can be achieved in nucleate-boiling cooling systems when compared with conventional, single-phase, forced-convective cooling systems. However, successful design and application of nucleate-boiling cooling systems for engine applications requires that the critical heat flux and flow instability not be reached. Therefore, a fundamental understanding of flow boiling mechanisms under engine application conditions is required to develop reliable and effective nucleate-boiling cooling systems.

Cooling engine areas such as the head region often contain small metal masses that lead to small coolant channels. This geometry, in turn, leads to low mass flow rates in order to minimize pressure drop. Although significant research has been performed on boiling heat transfer and the critical heat flux phenomenon, results on the conditions necessary for engine cooling systems are limited. It is the purpose of the present study to experimentally investigate the characteristics of coolant boiling, critical heat flux, and flow instability under conditions of small channel and low mass flux.

The test apparatus used in this investigation was designed and fabricated to study boiling heat transfer, critical heat flux, and flow instability of flowing water, ethylene glycol, and aqueous mixtures of ethylene glycol at high temperatures (up to 250°C) and low pressure (<345 kPa). Figure 1 shows a schematic of the apparatus. It is a closed-loop system that includes two serially arranged pumps with variable speed drives, a set of flowmeters, an accumulator, a preheater, a test section, and a condenser. The flowmeter set, including various types and sizes, was chosen to cover a large range of flow rates and was calibrated with a weighing-with-stop-watch technique. The estimated uncertainty in the measurements of flow rates was ±3%. The bladder-type accumulator allows for stable control of the system pressure. The preheater provides a means to set the inlet temperature of the test section at various desired levels. Both the preheater and test section were resistance-heated with controllable DC power supplies. Provisions were made to measure temperatures along the test section for calculating heat transfer coefficients. The pressures and temperatures at the inlet and outlet of the test section were also measured. Pressure transducers and thermocouples were calibrated against known

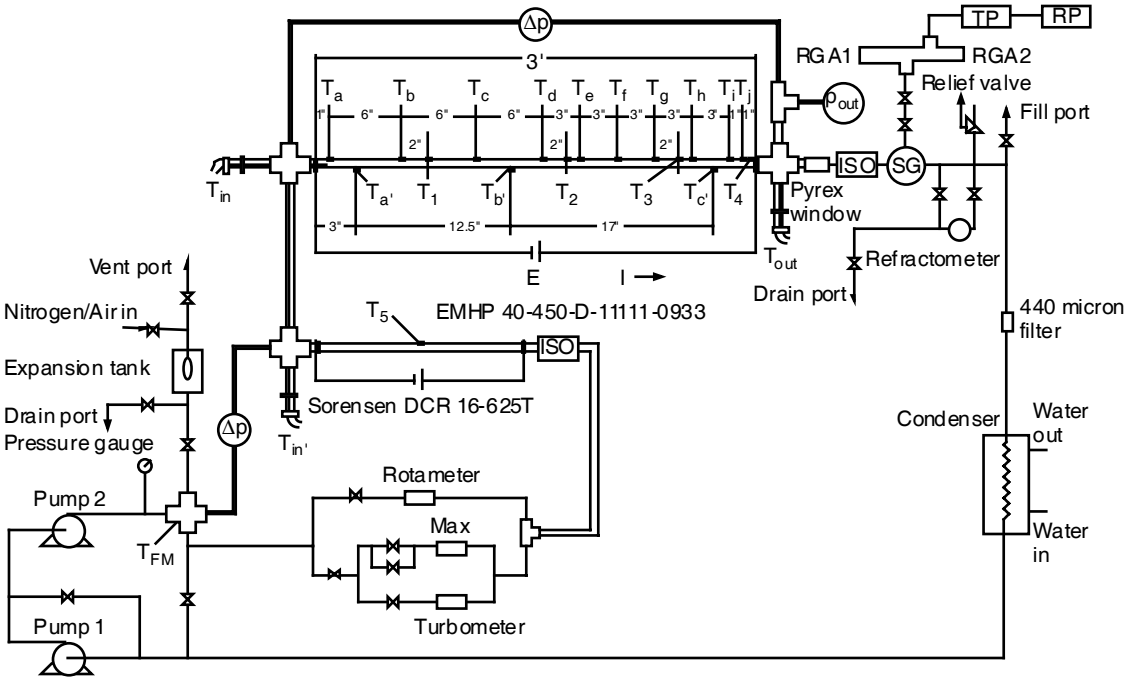

Figure 1. Schematic diagram of nucleate-boiling cooling test apparatus

standards. The estimated uncertainty in the measurements of pressures and temperatures were ±3% and ±0.2°C, respectively. As a safety precaution, both the preheater and test section were provided with high-temperature limit interlocks to prevent them from overheating. After leaving the test section, the two-phase flow was condensed into a single-phase flow, which returned to the pumps to close the system.

A data acquisition system consisting of a computer and a Hewlett-Packard multiplexor was assembled to record outputs from all sensors. A data acquisition program, which includes all calibration equations and conversions to desired engineering units, was written. The data acquisition system provides not only an on-screen display of analog signals from all sensors and graphs of representative in-stream and wall-temperature measurements but also a means of recording temperature measurements and pertinent information such as input power, mass flux, outlet pressure, pressure drop across the test section, and outlet quality for further data reduction.

Results and Discussion

During FY 2003, both experiments and analysis on boiling heat transfer with 50/50 ethylene glycol/water mixture have been completed. The main results are reported below.

Boiling Curve

Figure 2 shows the heat flux as a function of wall superheat for boiling of water and 50/50 ethylene glycol/water mixture in small channels. As it can be seen from Figure 2 that, generally, the saturation boiling in small channels can be divided into three regions, namely convection-dominant-boiling region, nucleation-dominant-boiling region, and transition-boiling region. Both convective heat transfer and boiling heat transfer exist in all three regions, but their proportions are different in these three regions. In the convection-dominant-boiling region, the wall superheat is low, usually less than a few degree centigrade. Although there is boiling heat transfer, the dominant mechanism is convective heat transfer. As a result, the mass quality and heat transfer rate are quite low comparing with those in the other two regions. In the nucleation-dominant-boiling region, the wall superheat is higher than that in the convection-dominant-boiling region but lower than certain upper limits that depend on mass flux. Opposite to the convection-dominant-boiling, the boiling heat transfer in the nucleation-dominant boiling is so developed that it becomes dominant and the heat transfer rate is much higher than that in convection-dominant boiling. As can be seen from Figure 2, the heat flux in this region is independent of mass flux and can be predicted with a power-law function of wall superheat. This characteristic was

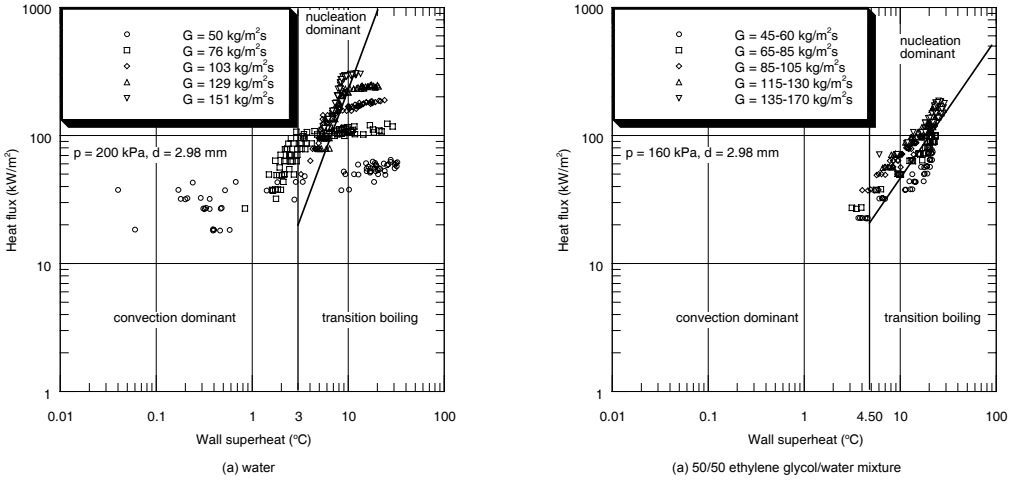

Figure 2. Heat flux as a function of wall superheat

used in correlating the heat transfer data. In the transition-boiling region, the wall superheat is relatively high. The heat flux in this region is also high and close to the critical heat flux. The boiling in this region is unstable and a small change in the heat flux will result in a big change in wall superheat. If the heat flux increases further, it is possible for the system to reach the critical point producing an undesirably large jump in the wall superheat.

The above discussion shows that the nucleation-dominant boiling is desired in engineering applications for both high heat transfer rate and stable flow boiling without reaching the critical point.

Two-Phase Pressure Drop

The concept of two-phase multipliers proposed by Lockhart and Martinelli and the correlation of those multipliers by Chisholm was used to compare with the present experimental data. As can be seen from Figure 3, the two-phase frictional pressure gradient data of 50/50 ethylene glycol/water follow similar trends as those of water. The experimental data are considered to be in reasonable agreement with the Chisholm predictions both in values and trends although the Chisholm correlation slightly overpredicts the experimental data.

Boiling Flow Stability

Preliminary experiments on boiling flow stability with 50/50 ethylene glycol/water mixture have been carried out for low mass qualities. Figure 4 shows an example of a long term boiling test. It can be seen from Figure 4 that after the initial transient, both the flow rate and mass quality gradually tend to stable values, which has essential importance in engine cooling applications. The results suggest that as long as the mass quality is kept below a certain level, stable nucleate-boiling cooling is possible. Further experiments are necessary to identify this mass quality level.

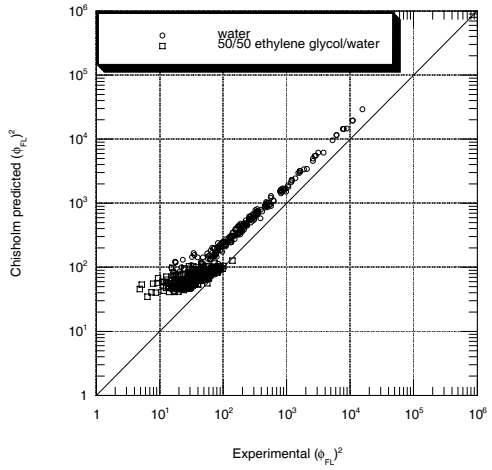

Figure 3. Two-phase frictional pressure gradient

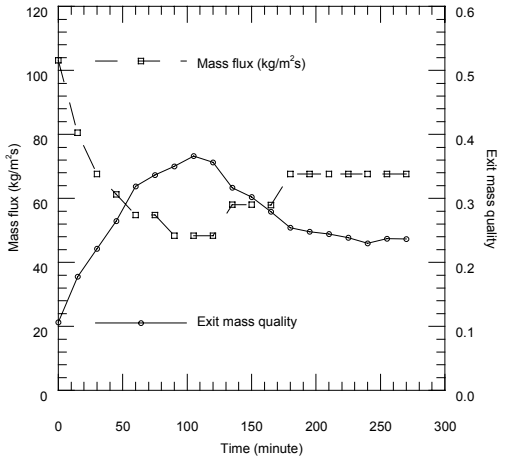

Figure 4. Boiling flow stability

Heat Transfer Coefficient

In the present study, the nucleation-dominant boiling data have the following characteristics.

(a) Although both convective heat transfer and nucleate boiling heat transfer exist, the dominant heat transfer mechanism is nucleate boiling. Since nucleate boiling heat transfer rate is much higher than convective heat transfer, the latter can be neglected.

(b) As shown in Figure 2, the boiling heat transfer is dependent on heat flux but almost independent of mass flux, which means that, for a certain fluid, the boiling heat transfer coefficient can be expressed as a function of heat flux.

(c) The heat transfer coefficients have different dependence on heat flux for different fluids. Therefore, to get a general correlation for boiling heat transfer coefficients, it is necessary to include fluid properties in the correlation.

(d) Argonne researchers employed the dimensionless parameter combination form of Boiling number, Weber number, and liquid-to-vapor density ratio in developing different predicted correlations for boiling heat transfer coefficients to different fluids, and the predicted results are quite good.

Based on the above facts, we extended the property term to including liquid-to-vapor viscosity ratio and were able to correlate boiling heat transfer data for water, 50/50 ethylene glycol/water mixture, refrigerant 12, and refrigerant 134a as

$$h = 135000(BoWe_l^{0.5})^{0.5}\left[(\rho_l/\rho_v)^{-0.5}(\mu_l/\mu_v)^{0.7}\right]^{1.5}$$

In the above equation the Boiling number Bo and the Weber number We_l are defined respectively by $Bo = q''/(Gi_{fg})$ and $We_l = G^2 D/(\rho_l \sigma)$, where ρ is the density, μ is the viscosity, G is the mass flux, D is the diameter, and σ is the surface tension.

Figure 5 shows the experimental data and the predicted values obtained with the equation for four fluids. The predictions of the equation are in good agreement with the experimental data, and most of the predictions are within ±30% of the experimental data. It should be noted that the comparisons are only for the data within the nucleation-dominant-boiling region. The success of the equation in predicting the heat transfer coefficients of four fluids boiling in small channels is directly related to the trend, as presented in Figure 2, that the heat transfer data are heat flux but not mass flux dependent. The fact that the equation is also heat flux but not mass flux dependent is in accordant with the experimental data.

Conclusions

Excellent progress has been made on both the experiments and analysis during FY 2003.

(a) Two-phase frictional pressure gradients of 50/50 ethylene glycol/water mixture follow similar trends as those of water. The results are in reasonable agreement with the predictions of the Chisholm correlation.

(b) The experiments show a very high heat transfer rate with 50/50 ethylene glycol/water mixture, which is positive to engine cooling applications. A general correlation has been developed based on data of water, 50/50 ethylene glycol/water mixture, and refrigerants. This correlation predicts the experimental data quite well, and most of the predicted values are within ±30% of the experimental data.

(c) It was found that the boiling heat transfer of 50/50 ethylene glycol/water mixture is mainly limited by flow instability rather than critical heat fluxes that are usually the limits for water boiling heat transfer. Preliminary tests show that stable long-term two-phase boiling flow is possible for 50/50 ethylene glycol/water mixture as long as the mass quality is less than a certain critical value (approximately <0.2). The heat transfer rate at this mass quality is significantly higher than that of conventional, single-phase, forced-convective heat transfer. However, the limiting quality or wall superheat for stable nucleate-dominant boiling is the final part of the 50/50 mixture correlating equation required for automotive applications. Determining and predicting the limits is in progress.

(d) It is difficult for vehicles to maintain the coolant concentration at exact 50/50. Therefore, it is necessary to investigate boiling heat transfer of ethylene glycol/water mixtures at concentrations other than 50/50. Experiments are in progress using mixtures 10% off the idea concentration, or 40/60 and 60/40 ethylene glycol/water mixtures. The tests will provide essential information for nucleate-boiling cooling system design.

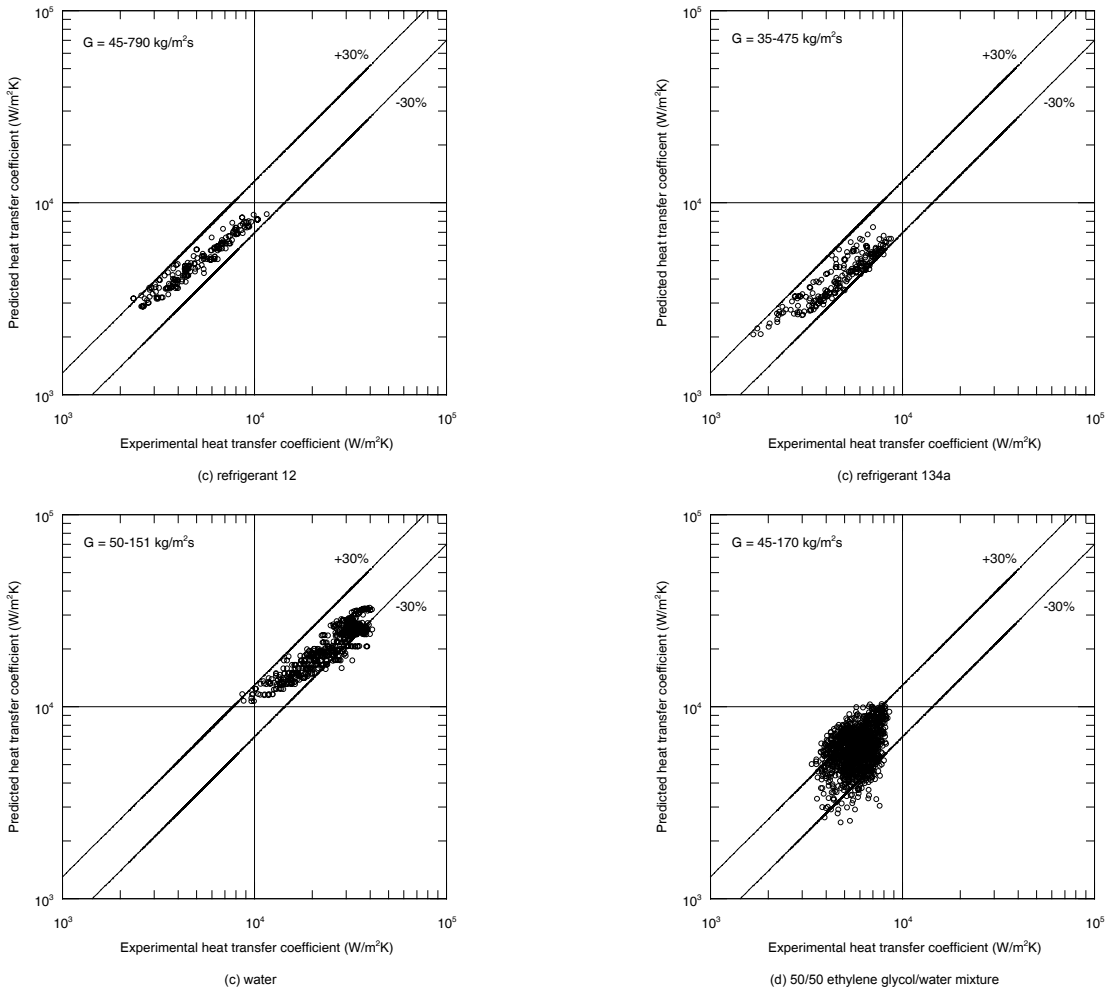

Figure 5. Heat transfer coefficient comparisons (nucleation-dominant-boiling region)

C. Evaporative Cooling

Principal Investigator: S.U.S. Choi
Argonne National Laboratory
9700 South Cass Avenue, Argonne. IL 60439
(630) 252-6439; fax: (630) 252-5568; choi@anl.gov

Technology Development Manager: Sid Diamond
(202) 586-8032; sid.diamond@ee.doe.gov
Technical Program Manager: Jules Routbort
(630) 252-5065; routbort@anl.gov

Contractor: Argonne National Laboratory
Contract No.: W-31-109-ENG-38

Objective

- Improve air-side heat transfer of the radiator.
- Reduce radiator size.
- Reduce radiator weight.

Approach

- Conduct evaporative cooling tests on flat and cylindrical heaters.
- Characterize evaporative cooling with microporous surfaces.

Accomplishments

- Evaporative cooling tests have shown that evaporative cooling with microporous coating on a flat heater increases the heat transfer coefficient by about ~400% relative to dry air cooling on uncoated surface.
- The increase was less for the cylindrical than the flat heater due to the nonwetting of the surface opposite to the spray.

Future Direction

- Develop a thermally conductive microporous coating (TCMC) technique.
- Initiate prototype radiator tests.
- Conduct preliminary radiator tests.

Introduction

One of the general strategies for improving the thermal management performance in heavy vehicles is to make better use of phase-change heat transfer. In particular, the performance on the air side of the radiator could be improved if evaporative heat transfer could be used. A number of methods to incorporate evaporative cooling are under evaluation, and in FY02 an experimental facility was completed and operated to demonstrate the performance enhancements by one of the techniques. A collaboration has been established with the University of Texas at Arlington to carry out this work. We have successfully demonstrated that evaporative cooling with microporous coating on a flat heater increases the heat transfer coefficient by about ~400% relative to dry air cooling on uncoated surface.

In FY2003, we have completed cross flow evaporative cooling tests on flat and cylindrical heaters. We have performed dry and evaporative cooling experiments with two cylindrical heaters to compare heat transfer data for the microporous-coated heater with the smooth heater data. We have characterized evaporative cooling with microporous surfaces including the structure of microporous surfaces using a SEM, the effects of coating thickness and coating particle size. These characterization studies are focused on discovering optimum microporous structure, particle size and thickness of coating. In addition, the effect of the flow rate of spray water has been investigated to find optimum water flow rate.

Results and Discussion

The focus of the present study is to determine the effect of evaporative spray cooling on flat and cylindrical heaters and to extend the evaporative cooling process by application of a microporous coating. Furthermore, we investigated the effects of water flow rate, particle sizes of the coating, and coating thickness on evaporative heat transfer performance. The heat transfer coefficient values were compared at the same heat flux to define heat transfer enhancement before "dryout." Dryout is defined as the state where the sprayed water droplets vaporize before reaching the heated surface due to the excessive heat load and similar phenomenon with critical heat flux in boiling heat transfer. If the wall temperature increases more rapidly (over 30°C increase for the nominal heat flux increment of 1 kW/m^2) than the previous average wall temperature, it is assumed that dryout has occurred, and power is cut off automatically.

Dry Air-Jet Cooling — Reference Case

The dry air-jet cooling tests were performed for plain and microporous surfaces at the same nozzle inlet pressure of 7 psig. For checking of the data, each experiment was performed twice. The microporous structure enhanced the two-phase heat transfer performance significantly; however, negligible differences between the plain and coated surfaces occurred when an air jet was used to cool the surfaces. This finding indicates that the increase of area due to the microporous surface structures is negligible for heat transfer by single-phase air convection. The cooling performance of the cylindrical heater was inferior to that of the flat heater due to the inefficient cooling at the back half of the heater surface. The results from dry air-jet cooling were regarded as a reference case to assess the heat transfer enhancement by evaporative cooling on plain and microporous surfaces.

Spray Cooling Results on Plain and Microporous Surfaces

Figure 1 shows the heat transfer coefficient vs. heat flux for the different surfaces, as well as spray cooling and dry air. When heat flux is less than 10 kW/m^2, the coated and plain surface show significant increase compared to the dry air case (reference). At this heat flux range, the microporous coating does not provide much additional enhancement over the plain surface. However, at higher heat flux, the coating does provide additional heat transfer. The heat transfer coefficient of the evaporative cooling with the microporous surface was approximately 500 W/m^{2}K up to a heat flux of almost 20 kW/m^2, which is about a 400% increase compared to the reference case. This excellent performance is probably due to the delay of partial dryout.

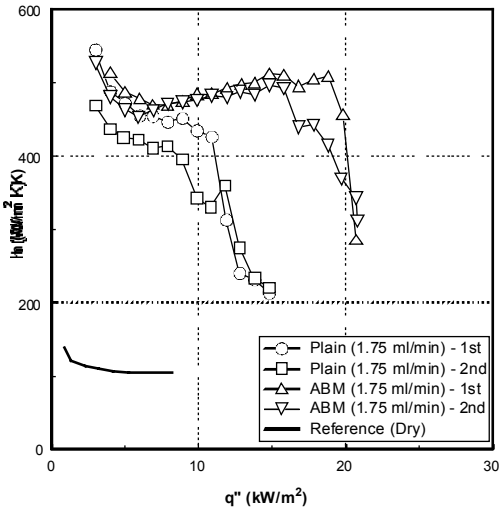

Figure 1. Heat transfer coefficient versus heat flux for plain and microporous surfaces with flat heater

The cylindrical heater (diameter of 1.6 cm and length of 7.7 cm) was used to investigate the effects of heater surface geometry. The microporous coating had the same size of particles and thickness as the flat heater. The water flow rate of cross-flow spray

for the cylindrical heater was approximately 3.0 ml/min, as determined by the ratio of the surface areas of the heaters. The heat transfer coefficient versus heat flux for the cylindrical heater is plotted in Figure 2.

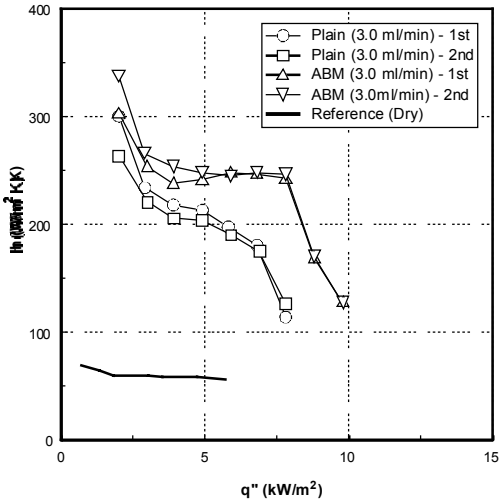

Figure 2. Heat transfer coefficient versus heat flux for plain and microporous surfaces with cylindrical heater

The plain surface showed about 300% increased performance for sprayed water compared to dry air, and additional improvement was found with the microporous surface over the plain surface.

Effects of Sprayed Water Flow Rate

Water flow rates of 1.25, 1.75, and 2.4 ml/min were tested to investigate the trends of evaporative spray heat transfer on plain and microporous surfaces of the flat heater. The results are plotted in Figure 3.

Air flow through the nozzle was controlled consistently by maintaining air pressure at the nozzle inlet (7 psig). When heat flux was less than ≈10 kW/m^2, the flow rates had no effect on the spray cooling curves. However, for higher heat fluxes with spray cooling, the heat transfer increased as the water flow rate increased for both plain and microporous surfaces. This improvement resulted because the available amount of water, fed from the sprayed droplets to be vaporized, increases as the water flow rate increases. For all three flow rates at a given ΔT, the microporous structure consistently generated ≈50% enhancement in heat transfer compared to that of the plain surface. For both plain

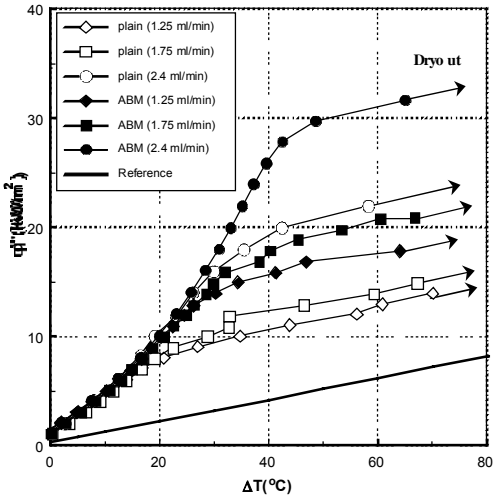

Figure 3. Effect of water flow rate on heat transfer performance for flat heater

and microporous coated surfaces, the dryout heat flux also increased by about the same amount as the water flow rate was increased.

Microporous Coating Optimization

We attempted to optimize the microporous structures for evaporative spray heat transfer. The particle sizes and coating thicknesses were investigated as experimental variables. The water flow rate was 1.75 ml/min.

Three ranges of particle size, 8-12 μm, 30-60 μm, and 100-300 μm, were employed to form microporous structures on the flat heater. The coating thicknesses were measured to be ≈50 μm for 8-12 μm particles, ≈150 μm for 30-60 μm particles, and ≈500 μm for 100-300 μm particles. The results reveal that the tested particle sizes produced similar heat transfer curves. The capillary pumping phenomenon should be stronger as the coating particle size decreases. On the other hand, fluid flow resistance for the soaked water within the microporous passageways increases as the particle size decreases. Also, the wall temperature increases due to the additional thermal resistance of conduction as the layer thickness increases for a given heat flux. Therefore, the possible enhancement from less fluid flow resistance due to larger cavity size is believed to be counterbalanced by degradation due to additional thermal resistance from conduction and less capillary pumping power.

The smallest particle size (8-12 μm) was selected to investigate the optimum coating thickness. The 8-12 μm particles are the most convenient for the coating method. Microporous coatings with 150 and 200 μm thicknesses showed smaller enhancement in spray heat transfer than coatings with 50 and 100 μm thicknesses. The 100 μm coating thickness attained the highest heat transfer coefficient among the tested thicknesses. This thickness produced up to ≈50% increase in evaporative heat transfer coefficient over the 200 μm thickness. The thicker microporous coating retains more water droplets as the coating thickness increases due to the larger number of microporous cavities. However, the evaporative heat transfer coefficient degrades extensively due to the additional thermal resistance to conduction as the thickness exceeds 100 μm.

Conclusions

Evaporative spray cooling from plain and microporous coated surfaces was investigated to understand the heat transfer performance compared to that of dry air cooling. The current study investigated the effect of heater geometry (flat and cylindrical heaters) and water flow rates on spray evaporative cooling. The effects of particle sizes and coating thicknesses were also investigated.

Important findings from this study are:

(1) Evaporative cooling with spraying water dramatically enhances the heat transfer coefficient over dry air cooling due to the added heat transfer by evaporation (heat of vaporization).
(2) The microporous coating further increases the heat transfer coefficient of evaporative spray cooling over the plain surface due to capillary pumping action. However, the heat transfer coefficient for dry air-jet cooling is unaffected by the surface microstructure.
(3) The combination of evaporative cooling and coated microporous surface enhances the heat transfer coefficient by up to 400% relative to the reference case (dry air cooling with uncoated, plain surface).
(4) The microporous coating extended the dryout heat flux significantly (≈21 kW/m^2) over the plain surface (15 kW/m^2).
(5) Similar heat transfer improvements were observed for both flat and cylindrical heaters. The increase was less for the cylindrical than the flat heater due to the nonwetting of the surface opposite to the spray.
(6) When heat flux is less than ≈10 kW/m^2, water spray amounts (1.25-2.4 ml/min) have no effect on evaporative cooling for microporous coating. However, for higher heat fluxes, the heat transfer increased with the water flow rate for both plain and microporous surfaces.
(7) The size of coating particles has a negligible effect on heat transfer performance. A nanoporous surface is recommended for further study of particle size effect.
(8) The 100-μm coating thickness gave the maximum heat transfer performance.

Future Direction

In FY2004 we will develop a thermally conductive microporous coating (TCMC) technique, initiate prototype radiator tests, and conduct preliminary experimental study of evaporative cooling with microporous coating using a prototype radiator.

The microporous coating enhances heat transfer coefficient of evaporative cooling and it is attributed mainly to the capillary pumping action within the microporous structures. The microporous coating contains Aluminum particles, Devcon Brusable Ceramics epoxy, and methyl-ethyl-ketone (MEK). The epoxy component has a poor thermal conductivity within the microporous structure and thus potentially increases the conduction thermal resistance through the layer especially when the coating becomes thick. Also, use of epoxy appears to prohibit the porosity variation within the microporous structures even if the aluminum particle size was changed. In order to overcome these inferior thermal characteristics in evaporation heat transfer, a new innovative conductive microporous coating method needs to be developed. Therefore, we will develop a thermally conductive microporous coating (TCMC) technique based upon experiences involved with the invention of microporous coating technique.

D. Nanofluids

Principal Investigator: S.U.S. Choi
Argonne National Laboratory
9700 South Cass Avenue, Argonne, IL 60439
(630) 252-6439; fax: (630) 252-5568; choi@anl.gov

Technology Development Manager: Sid Diamond
(202) 586-8032; sid.diamond@ee.doe.gov
Technical Program Manager: Jules Routbort
(630) 252-5065; routbort@anl.gov

Contractor: Argonne National Laboratory
Contract No.: W-31-109-ENG-38

Objective

- Exploit the unique properties of nanoparticles to develop ultra-high thermal conductivity heat transfer fluids.
- Characterize the thermal properties and heat transfer performance of nanofluids.
- Develop nanofluid technology for vehicle thermal management.

Approach

- Develop simplified models of a nanofluid.
- Measure thermal conductivity of nanofluids at temperatures up to 80°C.
- Measure the heat transfer coefficient of nanofluids.

Accomplishments

- Proposed that the solid/liquid interface or nanolayer acts as a thermal bridge between a nanoparticle and a liquid and modified the Maxwell equation.
- Developed a simplified one-dimensional drift velocity model of a nanofluid.
- Modified the transient hot-wire cell to measure temperature-dependent conductivities.
- Measured the heat transfer coefficient of nanofluids.

Future Direction

- Characterize the flow behavior of nanofluids in tubes.
- Measure the heat transfer coefficient of nanofluids in tubes.
- Design and fabricate a temperature oscillating system for temperature-dependent thermal conductivity measurements of a tiny quantity of nanofluids.
- Characterize metallic and oxide nanofluids in pool boiling for two-phase engine cooling applications.
- Refine models of nanostructure-enhanced and nanoparticle mobility-enhanced thermal conductivity of nanofluids.

Introduction

Many industrial technologies face the challenge of thermal management. With an ever-increasing thermal load due to trends toward greater power output for engines, smaller micro-electronic devices and brighter beams for optical devices, cooling of such devices and related systems is a crucial issue in high-tech industries such as transportation and microelectronics. The conventional approach for increasing cooling rates is use of extended surfaces such as fins and microchannels. However, current designs have already stretched this approach to its limits. Therefore, an urgent need exists for new and innovative concepts to achieve ultra-high-performance cooling.

Modern fabrication technology provides great opportunities to process and produce materials at the nanoscale. The thermal, mechanical, optical, magnetic, and electronic properties of nanophase materials are superior to those of conventional materials with coarse grain structures. Consequently, nanophase materials have drawn considerable attention from material scientists and engineers alike. Thus, taking a different tack from extended surface approaches and exploiting the unique properties of nanoparticles, Argonne National Laboratory has pioneered a new kind of ultra-high-thermal-conductivity fluids, called nanofluids, by uniformly and stably suspending a very small quantity (preferably <1% by volume) of nanoparticles in conventional coolants [1].

In fact, numerous theoretical and experimental studies of the effective thermal conductivity of dispersions that contain solid particles have been conducted since Maxwell's theoretical work was published about 100 years ago [2]. However, the studies on thermal conductivity of suspensions have been confined to millimeter- or micrometer-sized particles. The major problem with suspensions containing millimeter- or micrometer-sized particles is the rapid settling of these particles. In contrast, nanoparticles remain in suspension almost indefinitely. Furthermore, we have demonstrated that the dispersion of a tiny amount of nanoparticles in traditional fluids dramatically changes their thermal conductivities. For example, small amounts (<1 vol.%) of copper nanoparticles or carbon nanotubes dispersed in ethylene glycol or oil can increase their inherently poor thermal conductivity by 40 and 150%, respectively [3-4].

Since the pioneering work of Choi [1], outstanding discoveries and seminal achievements have been reported in the emerging field of nanofluids. Among them, the four key features of nanofluids are thermal conductivities far above those of traditional solid/liquid suspensions [3-4], nonlinear relationship between thermal conductivity and concentration [4], strongly temperature-dependent thermal conductivity [5], and significant increase in critical heat flux (CHF) [6] (see Figure 1). These key features of nanofluids make nanofluids strong candidates for the next generation of coolants for improving the design and performance of thermal management systems.

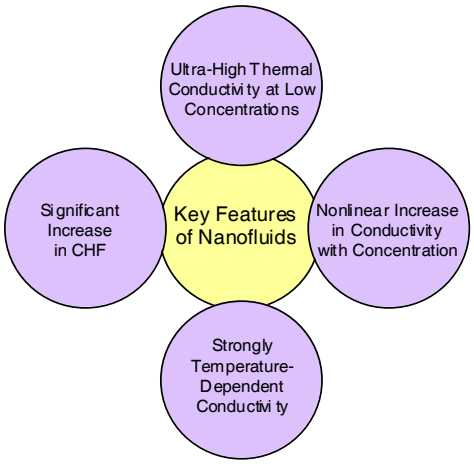

Figure 1. Four key features of nanofluids which have been discovered by a number of recent studies

Results and Discussion

It has long been known that liquid molecules close to a solid surface form layered solid-like structures, but little is known about the connection between this nanolayer and the thermal properties of the suspensions. We proposed for the first time that that this nanolayer acts as a thermal bridge between a solid nanoparticle and a bulk liquid [7]. We then modified the Maxwell equation for the effective thermal conductivity of solid/liquid suspensions to include the effect of this ordered nanolayer. Subsequent calculations have shown

the importance of nanolayers in nanofluid thermal conductivities [7]. Figure 2 shows that this ordered nanolayer has a major impact on nanofluid thermal conductivity when the particle radius is <5 nm. This finding suggests that adding smaller (<10 nm diameter) particles could be potentially better than adding more particles to concoct next-generation coolants for faster cooling of high-heat-load devices and systems.

We have developed a simplified one-dimensional drift velocity model of a nanofluid [8]. We found that, if the thermophoretically drifting particles drag a modest amount of the surrounding fluid with them, the contribution to the thermal conductivity is approximately one-third of the experimental measurements. Yet, it is an order of magnitude improvement compared to conventional models.

The thermal conductivity of nanofluids have been measured at room temperature by the transient hot-wire (THW) method. To measure nanofluid thermal conductivities as a function of temperature we have modified the transient hot-wire apparatus and demonstrated that the thermal conductivities of nanofluids can be measured at temperatures from ambient to about 85°C.

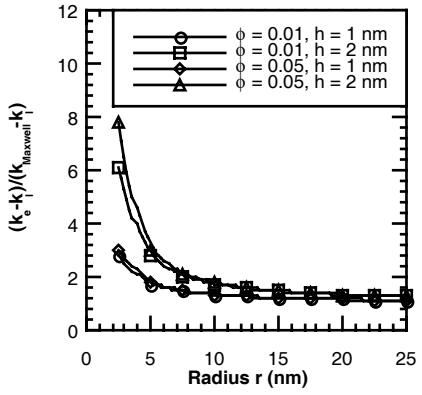

Figure 2. Thermal conductivity enhancement ratio as a function of particle radius for copper-in-ethylene-glycol suspensions ($\boldsymbol{k}_{layer} = \boldsymbol{k}_p$). Here, r and ϕ are the particle radius and particle volume concentration, respectively. h is the thickness of the nanolayer. A three- to eight-fold increase in the thermal conductivity of nanofluids compared to the enhancement without considering the nanolayer occurs when nanoparticles are smaller than r = 5 nm. However, for large particles ($r >> h$), the nanolayer impact is small.

A small volume (~100 ml) flow loop has been constructed to measured the heat transfer coefficient of nanofluids (see Figure 3). A variable displacement pump is used to control the fluid flow rate and direction, and its displacement settings are calibrated to determine the volumetric flows (62 to 507 cm^3/min). The fluid first passes through the thermostatic heating jacket in which water is used as heating fluid, with its temperature set at either 50°C or 70°C. Four thermocouples are placed as shown in the diagram, two of which, 1 and 4, measure the fluid temperature at the inlet and outlet of the test area, and the other two, 2 and 3, are placed at the inlet and outlet of the heating jacket to measure water temperature. Static mixers are put at the ends of the test section to mix the fluids and improve accuracy of the fluid temperature measurement. A thermostatic cooling jacket system, which is adjusted to 5°C, is used to run the loop in a steady state. The bubble collector collects and separates air bubbles from the fluid.

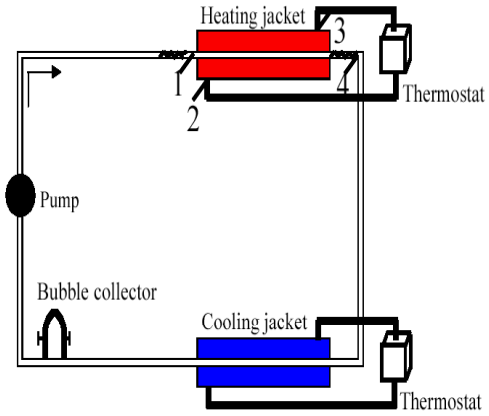

Figure 3. Schematic diagram of heat transfer test apparatus

Two series of nanofluids are investigated in this study: graphite nanoparticles-in-commercial automatic transmission fluid (ATF) and graphite nanoparticles-in-synthetic oil with commercial additive packages [9]. Although the graphite nanoparticles are obtained from two commercial sources, they are of very similar size and shape, with the average diameter of the "disk" about 1 μm and thickness around 30 nm. However, the measured heat transfer coefficients (normalized to that of the base fluid) of nanofluids at 2 wt.% and 2.5 wt.% nanoparticles differ by a factor of more

than five. It seems some special factors, which are still unknown to us, in the nanofluids, are affecting the heat transfer performance of the mixture. We believe that it is critical to characterize the flow behavior of nanofluids in tubes in order to explain strongly concentration-dependent heat transfer coefficient of nanofluids in tubes.

Inspired by our discoveries of these features of nanofluids, other groups across the world have begun nanofluid research and provided further breakthroughs. Among them, Das et al. explored the temperature dependence of the thermal conductivity of nanofluids containing Al_2O_3 or CuO nanoparticles [5]. Their discovery of a 2- to 4-fold increase in thermal conductivity enhancement for nanofluids over a small temperature range (21-51°C) implies that nanofluids could be smart fluids "sensing" their thermal environment. This new feature makes nanofluids even more attractive as coolants for devices with high energy density. Das et al. suggested that the strong temperature dependence of thermal conductivity is due to the motion of the nanoparticles. You et al. [6] measured the critical heat flux (CHF) in a boiling pool of nanofluids containing an extremely small amount of alumina nanoparticles. They discovered a dramatic increase (up to about 200%) in CHF when the nanofluid is used as a cooling liquid instead of pure water.

The nanofluid team at Argonne in collaboration with researchers in several universities has published pioneering journal articles on nanofluids including the first review article on nanofluids [10].

Future Direction

A major focus in nanofluids has been on the thermal conductivity of nanofluids. Nanofluids will be produced and characterized to generate a data base on their thermal conductivity. However, a new focus will be on the flow and heat transfer of nanofluids. The strongly concentration-dependent heat transfer coefficient of nanofluids in tubes suggests that it is critical to characterize the flow behavior of nanofluids in tubes. For example, theories of flow in tubes or porous materials have been developed at the macroscopic level. However, we believe that it is vital to connect the structure and mobility of nanoparticles at the nano- or micro-scale to the properties of nanofluids measured at macroscopic level. Therefore, we will explore the flow characteristic of nanofluids in tubes and measure the heat transfer coefficient of nanofluids in tubes. We will then relate enhanced thermal conductivity and flow characteristic to enhanced heat transfer coefficient of nanofluids. The flow and heat transfer data for nanofluids will be used to determine whether the flow and heat transfer correlations developed for homogenous fluids could be applied to nanoparticle dispersions with aspect ratios different from one.

A transient hot-wire cell, which has been used to measure nanofluid thermal conductivities, requires a large quantity of nanofluid samples. We will design and fabricate a temperature oscillating system for temperature-dependent thermal conductivity measurements of a tiny quantity (2-10 ml) of nanofluids.

Most studies carried out to date are limited to the thermal characterization of nanofluids without evaporation or condensation. However, nanoparticles in nanofluids can play a vital role in two-phase heat transfer systems. Therefore, there is a great need to characterize nanofluids in boiling and condensation heat transfer. The high critical heat flux of nanofluids is important particularly for two-phase engine cooling. The nanofluid tested by You et al [6] contains alumina (Al_2O_3) nano-particles dispersed in distilled and deionized water. We will design and fabricate a pool boiling test facility and characterize metallic and oxide nanofluids in pool boiling.

We have developed simple models of nanostructure-enhanced [7] and nanoparticle mobility-enhanced thermal conductivity of nanofluids [8]. However, much is still unknown about the mechanisms of the anomalous thermal behavior of nanofluids. Therefore, we need to understand the fundamentals of energy transport in nanofluids. As we discover new energy transport mechanisms that are missing in existing theories we will refine simple models of nanostructure-enhanced and nanoparticle mobility-enhanced thermal conductivity of nanofluids or develop a

new model of energy transport in nanofluids integrating new mechanisms. A better understanding of the mechanisms behind the thermal-conductivity enhancement will likely lead to recommendations for nanofluid design and engineering for industrial applications.

Conclusions

Nanofluids have some potential impacts. For example, improved thermal conductivity of nanofluids translates into cost and energy savings from smaller, lighter cooling systems and a cleaner environment. Nanofluids could be smart fluids "sensing" their thermal environment.

The key features such as thermal conductivities far above those of traditional solid/liquid suspensions, nonlinear relationship between thermal conductivity and concentration, strongly temperature-dependent thermal conductivity, and significant increase in critical heat flux (CHF). These key features of nanofluids make nanofluids strong candidates for the next generation of coolants for improving the design and performance of thermal management systems.

References

1. S.U.S. Choi, "Enhancing Thermal Conductivity of Fluids with Nanoparticles," *Developments and Applications of Non-Newtonian Flows*, eds. D.A. Siginer and H.P. Wang, The American Society of Mechanical Engineers, New York, FED–Vol. 231/MD-Vol. 66, pp. 99–105 (1995).
2. J.C. Maxwell, *Electricity and Magnetism*, 1st Ed., Clarendon Press, Oxford (1873).
3. J.A. Eastman, S.U.S. Choi, S. Li, W. Yu, and L.J. Thompson, "Anomalously Increased Effective Thermal Conductivities of Ethylene Glycol-Based Nano-Fluids Containing Copper Nano-Particles," *Applied Physics Letters*, **78**, 718–720 (2001).
4. S.U.S. Choi, Z.G. Zhang, W. Yu, F.E. Lockwood, and E.A. Grulke, "Anomalous Thermal Conductivity Enhancement in Nano-tube Suspensions," *Applied Physics Letters*, **79**, 2252–2254 (2001).
5. S.K. Das, N. Putra, P. Thiesen, and W. Roetzel, "Temperature Dependence of Thermal Conductivity Enhancement for Nanofluids," ASME J. Heat Transfer, Vol. 125, pp. 567–574.
6. S.M. You, Kim, J.H., and Kim, K.H., 2003, "Effect of Nano-Particles on Critical Heat Flux of Water in Pool Boiling Heat Transfer, to be published in *Applied Physics Letters*.
7. W. Yu and S.U.S. Choi, "The Role of Interfacial Layers in the Enhanced Thermal Conductivity of Nanofluids: A Renovated Maxwell Model," *J. Nanoparticle Research*, in press (2003).
8. W. Yu, J.R. Hull, and S.U.S. Choi, "Stable and Highly Conductive Nanofluids – Experimental and Theoretical Studies," Presented at the 6th ASME-JSME Thermal Engineering Joint Conference, Hawaiian Islands, March 16–23 (2003).
9. Y. Yang, Z.G. Zhang, E.A. Grulke, W.B. Anderson, G. Wu, Heat transfer properties of nanoparticle-in-fluid dispersions (nanofluids), *in preparation*.
10. S.U.S. Choi, Z.G. Zhang, and P. Keblinski, "Nanofluids," To be published in the Encyclopedia of Nanoscience and Nanotechnology, H.S. Nalwa, ed., American Scientific Publishers, Stevenson Ranch, CA (2003).

E. Application of Single- and Two-Phase Flow Microscale Technologies for Automotive Thermal Management

Principal Investigators: N.T. Obot and J.R. Hull
Argonne National Laboratory
9700 South Cass Avenue, Argonne, Illinois 60439
(630) 252-7638; fax: (630) 252-5568; obot@anl.gov

Technology Development Manager: Sid Diamond
(202) 586-8032; sid.diamond@ee.doe.gov
Technical Program Manager: Jules Routbort
(630) 252-5065; routbort@anl.gov

Contractor: Argonne National Laboratory
Contract No.: W-31-109-ENG-38

Objective

- The goal is to determine the suitability of single phase and two-phase flow microscale technologies such as arrays of microchanel and micro heat pipes for automotive thermal management.

Approach

- Review the literature to understand and evaluate previous and current research and thermal management issues.
- Develop a model to study heat rejection from automotive components fitted with microscale devices.
- Design, fabricate and test heat transfer devices to determine the performance of devices in automotive environment.

Accomplishments

- Completed comprehensive review of the literature on friction and heat/mass transfer in microchannels.
- Completed review of the literature on conventional heat pipes and micro heat pipes.

Future Direction

- Complete the development of model and thermal analysis.
- Design, fabricate and qualify the micro devices for operation.
- Perform full-scale testing in automotive environment.

Introduction

Single-phase and two-phase flow microscale thermal control technologies such as micro heat exchangers and micro heat pipes appear attractive for automotive applications where substantial cooling capacity and high degree of temperature uniformity and control are desired. Potential benefits of these technologies include significant reductions in weight and size and overall simplification in design of thermal management systems. These benefits are due to the fact that microscale devices usually operate in laminar flow, requiring minimum fluid volume and weight.

Microscale thermal control devices have been used to address thermal management problems in the semiconductor industry, satellite and spacecraft electronics and high-performance aircraft engines.

But little has been done to determine their suitability for thermal management of automotive power systems.

Literature Review

Because micro thermal devices are best fabricated in the form of microchannels, it was necessary to begin the feasibility study by reviewing the literature on friction and heat/mass transfer in microchannels. The results of the review were published in the journal of *Microscale Thermophysical Engineering*, Vol. 6, #3, pp. 155-173, 2002. Figure 1 shows the variation of the average heat transfer coefficients, expressed in dimensionless form as the Nusselt number (Nu), with the mass flow rate, also expressed in dimensionless form as the Reynolds number (Re). The Prandtl number (Pr), used to scale Nu in Figure 1, is the fluid properties expressed in dimensionless form. In the figure, the results of Obot et al. obtained with a much larger diameter smooth tube, 13.39 mm, are included for the purpose of comparison.

The main conclusions from the review were (a) there is hardly any evidence to support the occurrence of transition to turbulence in smooth microchannels for $Re \leq 1{,}000$; (b) $Nu \propto Re^{1/2}$ in laminar flow; and (c) estimates of transfer coefficients for smooth microchannels, accurate within experimental errors, can be obtained by using either conventional correlations or experimental results for channels of large hydraulic diameter.

With the completion of the microchannel friction and heat/mass transfer literature review, a review of the relevant literature on micro heat pipes was undertaken to evaluate their suitability for automotive thermal management. This phase of the research was completed. It was determined that arrays of micro heat pipes would lend themselves readily to integration into automotive power systems.

Future Research Plans

The main focus of future research is modeling of heat removal and subsequent dissipation from automotive power systems with microchannels of various designs. To accomplish this goal, the development of a comprehensive 1-D system model is in progress. Upon completion, the code will be used to simulate heat removal with single phase and two-phase flow. The arrays of flow passages or

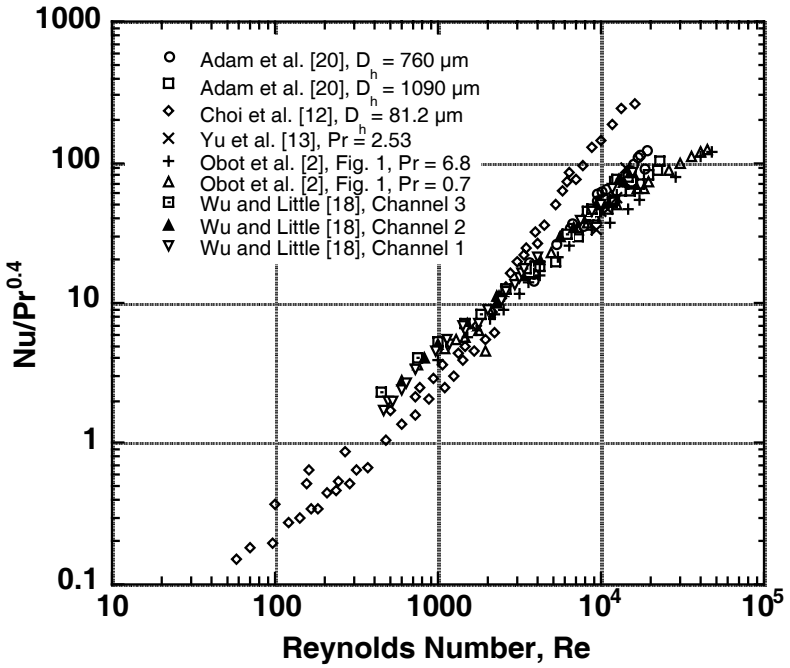

Figure 1. Comparison of various results for average heat transfer coefficients

micro heat pipes will consist of parallel rectangular microchannels or branching patterns to provide precise temperature uniformity.

The results of the study will enable comparison of the performance of conventional thermal management scheme with that using micro thermal devices. Also, practical issues and technical challenges of using microscale devices in thermal management of automotive power systems will be identified. Further, the results will form the basis for subsequent experimental design and testing.

Conclusions

This research project is in its infancy. The progress to date is good. If the concept of microscale thermal management for automotive power systems can be successfully demonstrated, the prospects for industry participation are excellent.

F. Underhood Thermal Analysis

Principal Investigator: F.-C. Chang, T. Sofu, and J.R. Hull (contact)
Argonne National Laboratory
9700 South Cass Avenue, Argonne, Illinois 60439
(630) 252-8580; fax: (630) 252-5568; jhull@anl.gov

Technology Development Manager: Sid Diamond
(202) 586-8032; sid.diamond@ee.doe.gov
Technical Program Manager: Jules Routbort
(630) 252-5065; routbort@anl.gov

Contractor: Argonne National Laboratory
Contract No.: W-31-109-ENG-38

Objective

- Gain insight into the ventilation needs for an enclosed engine compartment of an off-road machine, and help understand the effects of ventilation air flow on heat rejection and component temperature.
- Perform an assessment of 1-D and 3-D simulation methodology for optimized ventilation air flow rate, component temperatures and engine heat rejection.

Approach

- Perform an assessment of 1-D and 3-D simulation methods to predict underhood ventilation air flow and component temperatures using the experimental data.
- The 1-D thermal-fluid network model was developed to account for overall energy balance and simulate cooling system response. The 3-D CFD model was built to determine the flow paths and the surface heat transfer coefficient for ventilation air system.

Accomplishments

- A combined 1-D and 3-D simulation methodology was developed for optimization of engine compartment ventilation air flow. The results indicate that temperature and the distributed heat rejection rates can be estimated within reasonable accuracy when 1-D and 3-D models are used in combination.

Future Direction

- Use the combined 1-D and 3-D simulation methodology to study the effect of air flow inlet location on ventilation air and component temperatures, and engine heat rejection.
- Perform the sensitivity analysis for all airflow inlet locations to evaluate the system performance for off-road vehicle's thermal management.

Introduction

Construction equipment and other types of heavy vehicles have common underhood thermal management challenges: restrictive enclosures and ever-increasing variety of heat sources. But off-road machines have rather unique additional underhood thermal management issues such as

- High auxiliary loads,
- Severe operating conditions involving dust and debris,
- Wide range of altitudes and temperatures,
- Lack of ram air, and
- Increasingly restrictive sound regulations.

In addition to the cooling system design, the thermal management challenge for a system with separate engine enclosure (as shown in Figure 1) is to maintain acceptable underhood component temperatures in a relatively well sealed enclosure with limited ventilation. The specific issues for underhood temperature control are the ventilation air flow requirements and the effect of ventilation on thermal balance (e.g., cooling system design).

To address these issues, a Cooperative Research and Development Agreement (CRADA) has been executed between Argonne National Laboratory and Caterpillar, Inc. for measurement and analysis of underhood ventilation air flow and temperatures. The experimental effort by the Caterpillar team has focused on building a prototypical test-rig for an off-road machine engine, and conducting tests with controlled ventilation air flow rates from various inlet locations to estimate the ventilation needs in an enclosed engine compartment [1]. The purpose of the analytical studies by the Argonne team (with modeling support from Flowmaster USA) has been the assessment of various simulation methods that could be used in predicting underhood ventilation air flow and temperatures. The work involved development and validation of combined 1-D and 3-D simulation models of the Caterpillar test-rig for optimized ventilation air flow rate. Although the separated cooling system compartments are unique to off-road machines, the Caterpillar tests and the complementary analyses provide an opportunity to understand the isolated effect of air cooling on the engine performance for a wide range of heavy-vehicles.

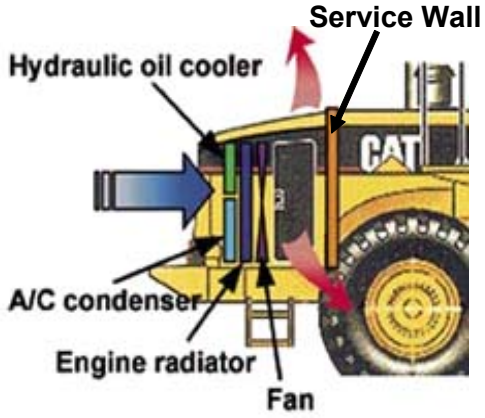

Figure 1. Schematic of an off-road machine with separated engine and cooling system compartments divided with service wall

Analytical Studies

Computer simulations can improve the understanding of interactions between the engine subsystems [2]. The main purpose of this study has been an assessment of simulation methods that could be used in predicting underhood ventilation air flow field and temperatures for an off-road machine. The work involved development and validation of combined 1-D and 3-D simulation models of the Caterpillar test-rig. A 1-D thermal-fluid network model was developed to account for overall energy balance and simulate cooling system response using the commercial software Flowmaster [3]. A 3-D underhood model of the complex test rig was built using the commercial CFD software Star-CD [4] to determine the flow paths for the ventilation air system and the surface heat transfer coefficient.

3-D CFD Analysis

Starting with a CAD model of the test rig, an unstructured hexahedral mesh was generated using Star-CD's underhood expert system module ES-Uhood. First the IGES surface definitions were extracted from the CAD model, and then the ProSurf utility was used to generate a triangulated surface mesh. Starting from this mesh, surface fixing functions were used to merge the overlapping surfaces, fill the open holes, generate feature lines, and create a new "wrapped" surface which captures the details of computational domain boundaries in 8 mm resolution (Figure 2a). This wrapped surface formed the basis of an extrusion layer through which the suitability of turbulence wall function is assured. Although the flow is expected to separate over the complex engine geometry, the inherent assumption of attached flow is made through the use of logarithmic wall function since the integration to the wall is computationally prohibitive. After filling the computational domain with regular brick cells with gradual mesh refinement near the engine and enclosure surfaces, the volume mesh was completed by cutting those hexahedral cells that intersect the extrusion layer (Figure 2b).

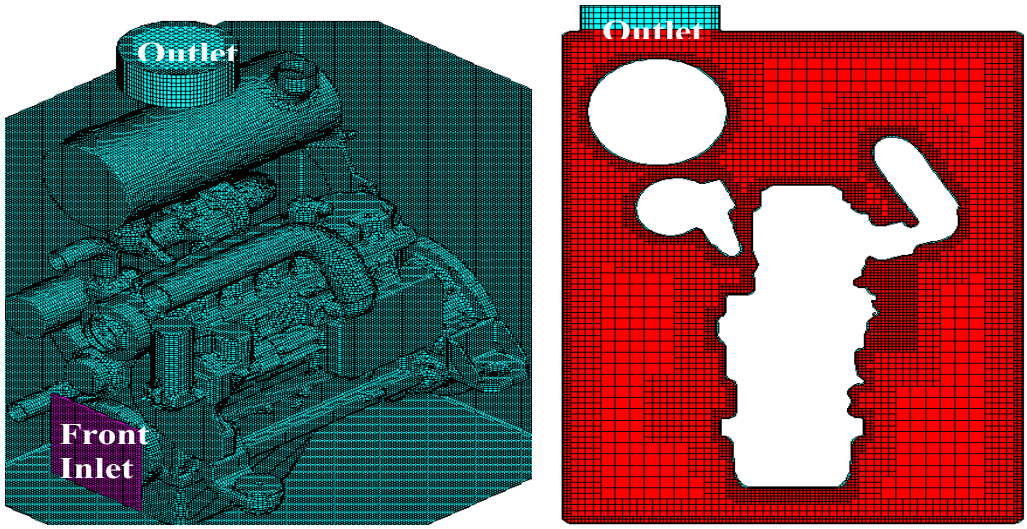

Figure 2. CFD mesh of the test rig (a) cutaway view of the surface mesh (b) a cross section of the volume mesh

In order to capture the ventilation air flow distribution at the enclosure inlet accurately, a large inlet plenum (not shown in Figure 2) was also included in the model to represent ambient conditions (pressure and temperature). The desired flow rate through the enclosure was assured by imposing a proportional uniform flow field at the plenum inlet as the boundary condition. The enclosure outlet pipe was considered much longer than what is shown in Figure 2 and its top end was treated as a standard outlet boundary. The final CFD model consists of 1.34 million fluid cells, with a 3 mm thick extrusion layer surrounding the engine and enclosure surfaces to give a maximum y+ value of 200 for airflow ratio of 1.5.

1-D Network Thermal-Flow Analysis

The complete thermal system analyzed with the network flow model is a collection of different thermal subsystems of an off-road machine engine including the air, coolant, and oil loops. The model consists of 1-D descriptions of these three loops combined with a lumped parameter approach to characterize the thermal interactions between them through the engine structure as the major conduction paths (Figure 3). This approach simplifies the complex engine system by discretizing it based on known heat transfer paths under steady-state conditions; i.e., the heat generated from combustion is considered to be transferred to various discrete surface points on the engine using specified conduction paths. This 1-D network flow model served as a tool to analyze the interactions of the engine with the ventilation air, coolant, and oil loops for predicting the complete thermal system performance.

Air flow paths in the 1-D model are based on 3-D simulation results. In the air loop, the entering ventilation air is considered to gain heat as it passes through individual surface points on the engine as shown in Figure 3. In the oil loop, after losing heat through the oil pan, the flow splits into three separate branches (the turbo, the cylinder head, and the engine block) before returning to the sump. In the coolant loop, the water cools the lubrication oil in the oil loop and circulates inside the engine block and the cylinder head. The radiator is simply modeled as a source with constant flow rate and with known inlet temperature.

Steady-state simulation was done for a given engine rated condition with conduction, convection, and radiation models. The air enters at the enclosure inlet with given temperature, pressure, and flow rate and exits at the enclosure outlet with another temperature, pressure, and flow rate. The heat loads were calculated at the engine surfaces. Once the model is validated, similar models can be quickly created to analyze engines of similar geometry.

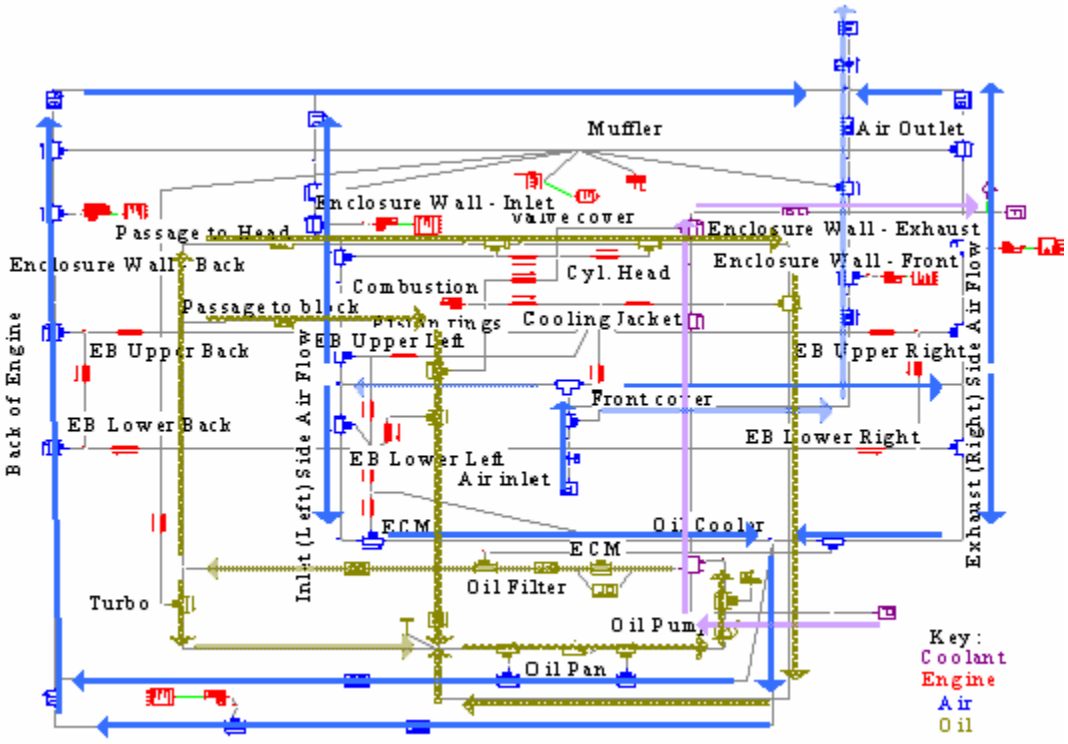

Figure 3. 1-D network flow model of the test rig for front-inlet configuration

Interface between 3-D CFD and 1-D Network Flow Models

Figure 4 shows the schematic of the sequential analyses with the 1-D network flow and 3-D CFD models. The 1-D model requires flow rates and inlet temperatures as the boundary conditions in the air and coolant loops and oil pump speed in the oil loop to account for overall energy balance and predict the engine component temperatures. In the 3-D thermal analysis, these predictions are prescribed as surface temperature boundary conditions for various engine components and enclosure walls, and they are used to calculate ventilation air flow field and temperatures. The results of the 3-D CFD analysis are, in return, provided back to the 1-D model to improve component temperature predictions by modifying the air flow paths and heat transfer coefficients between the engine components and ventilation air. The typical values of estimated heat transfer coefficients between the engine components and ventilation air are found to vary in the range from 10 to 50 W/m^2-K.

3-D CFD Results and Restriction

As examples of the results obtained with the CFD model, the ventilation air flow field and temperature distributions are shown in Figure 5 on a vertical plane through the enclosure front inlet. The results indicate that the most significant pressure drop takes place near the inlet and outlet restrictions. Consistent with the experimental observations, the results indicate a well mixed flow inside the enclosure with no significant difference in component temperatures for different ventilation inlet locations.

The comparison of the experimental and 3-D model predictions for pressure drop through the test rig is shown in Figure 6 as a function of airflow ratio. The y axis is the normalized pressure drop for flow through the enclosure. A good agreement for such "system restriction curves" is the first indication that CFD model captures the flow field accurately. The other comparisons (air temperatures throughout the enclosure) are consistent with the experimental values when accurate surface temperatures are specified as the boundary conditions.

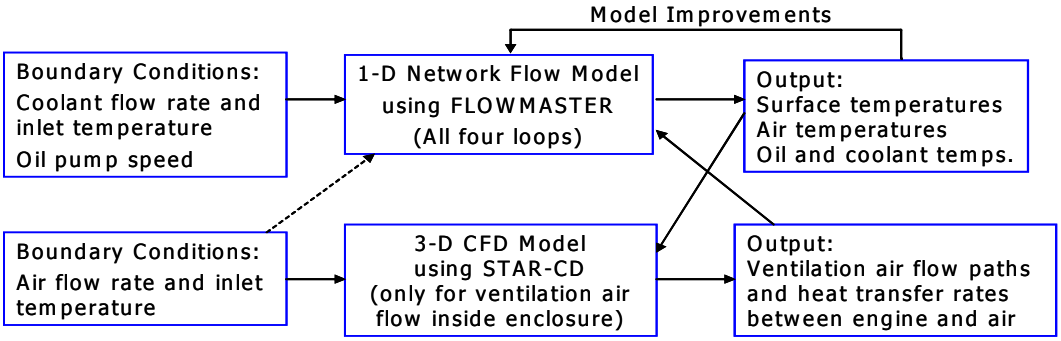

Figure 4. Flowchart of coupled computations between FLOWMASTER and STAR-CD

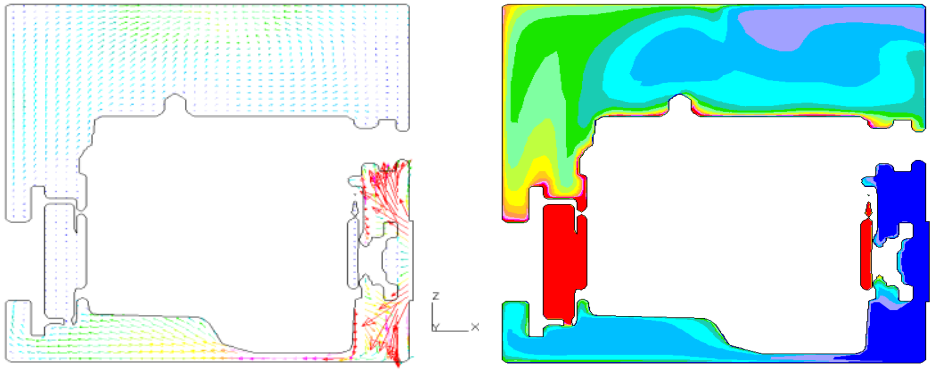

Figure 5. Calculated ventilation air flow field and temperature distributions on a vertical plane that intersects the front inlet

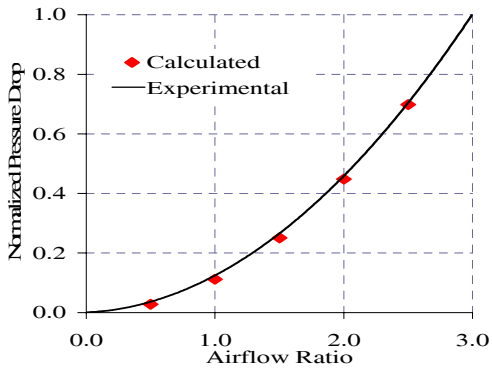

Figure 6. System restriction curve comparisons for front inlet

1-D Temperature Comparisons

The various temperatures in the 1-D model are calculated based on the engine component dimensions and the heat transfer coefficients at the solid-fluid interfaces as input. Some physical dimensions for the internal loops of the engine were supplied by Caterpillar and others were interpreted based on CAD data. A comparison of measured and calculated ventilation air, coolant water, and oil temperatures is shown in Figure 7 and surface temperatures is shown in Figure 8. Most of the predictions with the 1-D network model are within 10% of the experimental values. For a complex network of engine and its thermal subsystems of coolant, oil, and ventilation air, these small discrepancies are considered a respectable degree of accuracy.

Although the discrepancies are generally small, the attempts to resolve them are part of the overall modeling effort to provide a better description of the underhood system. For example, based on the CFD results, the discrepancy for the exhaust-side rear ventilation air temperature is attributed to a local recirculation zone in that region. However, since the estimated temperature is small and its impact on overall temperature distributions is negligible, a

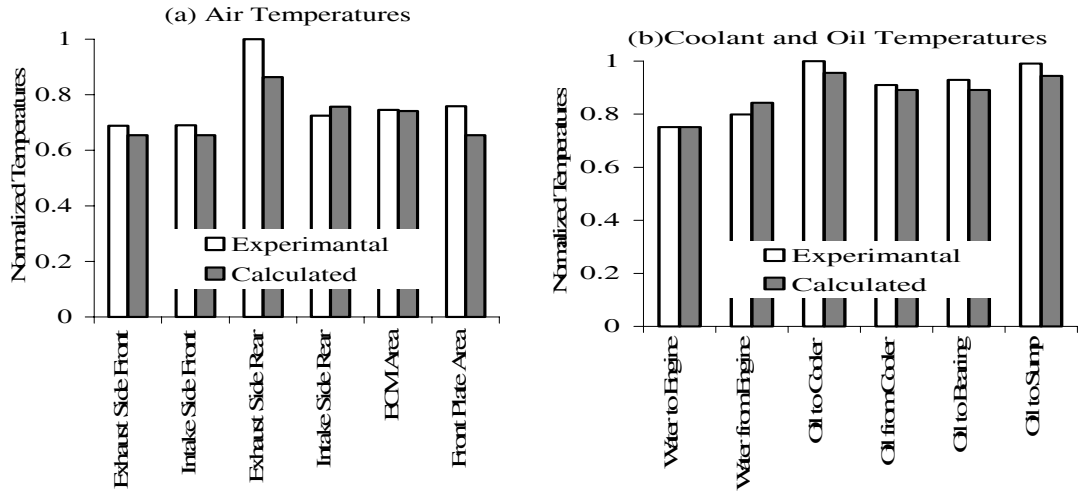

Figure 7. Comparison of temperatures between measured data and model predictions: (a) ventilation air temperatures, (b) coolant and oil temperatures

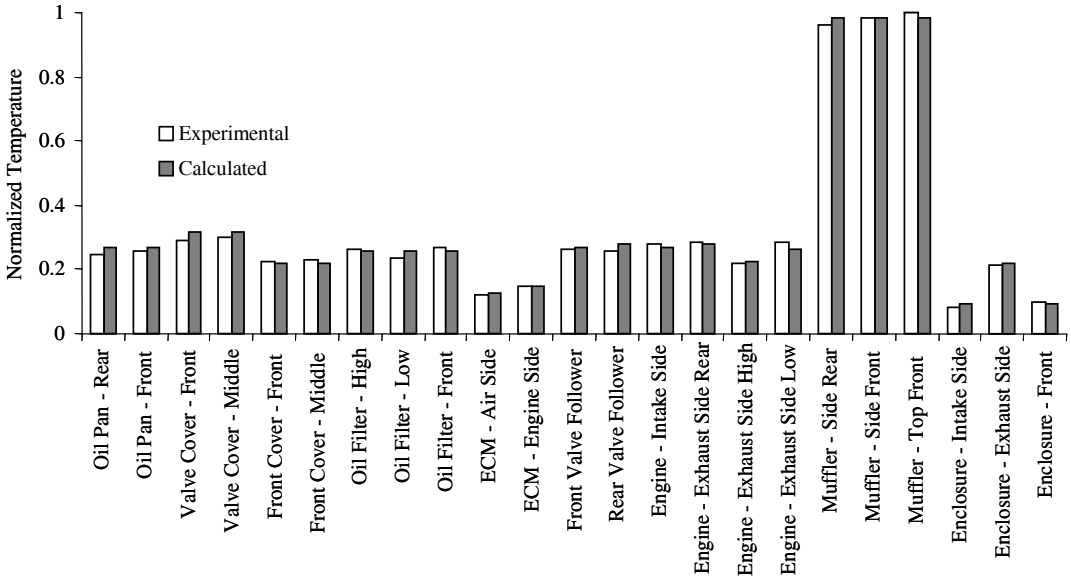

Figure 8. Comparison of surface temperature measurements and model prediction

modification to the network flow model for the front inlet configuration is not considered to be essential.

Conclusion

Experiments were conducted to gain insight into the ventilation air flow needs for an enclosed engine compartment of an off-road machine. These laboratory experiments were well controlled to provide good accuracy and to draw important conclusions on minimum ventilation flow requirements for maintaining acceptable underhood temperatures. About 96% of the total fuel energy was accounted for during the test. Underhood temperatures in the areas of concern are found to be generally stabilized near an airflow ratio of two. Data obtained were also used to provide boundary conditions and validation information for simulation methods.

A combined 1-D and 3-D simulation methodology was developed for optimization of engine compartment ventilation air flow. The air flow field and the rate of heat transfer between engine and ventilation air inside the enclosure were determined with the 3-D CFD simulations. A 1-D network model was built by discretizing the various fluid paths and the solid metal structure in the system. Once the ventilation air flow paths and heat transfer coefficients were determined with CFD, the 1-D network model with reduced complexity was used to simulate thermal interaction of the engine structure with the air, coolant, and oil flow. The results indicate that the temperatures and distributed heat rejection rates can be estimated within reasonable accuracy when 3-D and 1-D models are used in combination.

References

1. Srinivas R. Malipeddi, "Underhood Thermal Management Guidelines," Jan 2003, Caterpillar Internal Document.
2. C. Hughes, et al., "Heavy-Duty Truck Cooling System Design Using Co-Simulation," SAE Technical Paper Series 2001-01-1707, Proceedings of Vehicle Thermal Management Systems Conference & Exhibition, Nashville, TN, May 14–17, 2001.
3. D.S. Miller, Internal Flow Systems, 2nd edition, Flowmaster International Ltd., published by BHR Group Limited, 1996.
4. Star-CD, Version 3.150A, CD-Adapco Group, Melville, NY.

III. More Electric Truck

Parasitic Energy Loss Reduction and Enabling Technologies for Class 7/8 Trucks

Principal Investigator: W. Lane
Caterpillar Inc., Technical Services Division
P.O. Box 1875, Peoria, IL 61615
(309) 578-8643; fax: (309) 578-4722; bill.lane@cat.com

Technology Development Manager: Sid Diamond
(202) 586-8032; sid.diamond@ee.doe.gov
Technical Program Manager: Jules Routbort
(630) 252-5065; routbort@anl.gov

Contractor: DOE, Albuquerque, New Mexico
Contract No.: DE-FC04-2000AL67017

Objectives

- Reduce parasitic losses for fuel savings
- Provide idle-reduction solutions
- Reduce radiator heat load

Approach

- Electrify truck accessory functions and hotel loads
- Decouple accessories from main truck engine
- Match accessory power demand to real time need
- Enable use of alternative power sources

Accomplishments

- Designed, fabricate, and tested electric accessories for on-highway truck applications
- Built Kenworth T-2000 demonstration truck with comprehensive electric accessory deployment
- Successfully completed functional over-the-road testing of technology demonstration truck

Future Direction

- Conduct over-the-road fuel economy testing on technology demonstration truck
- Test implemented idle-reduction solution and measure fuel savings realization
- Evaluate additional fuel savings opportunities enabled by truck electrification

---

Introduction

Over the years, as the price of fuel has continued to rise, the popularity of electric and hybrid electric vehicles has increased. The majority of developments have been focused on propulsion systems. Parasitic losses from truck auxiliary functions, such as pumps, compressors, etc., are another source of inefficiencies that have remained unchallenged. This research program covers developments associated with the electrification of Class 8 on-highway trucks to reduce parasitic losses Incremental gains in fuel economy could be attained even using the present 12-volt electrical system, if the efficiency of the alternator is improved. However, to elevate efficiency from its near 50% level into the 80's would require the application of a different type of alternator/generator technology. Such an improvement is likely to carry a cost premium that the trucking industry is unlikely to accept. This creates a significant cost challenge if the fuel efficiency of a truck is to be improved by boosting the efficiency of individual components.

An alternative to component-by-component replacement is to take an overall system perspective to truck electrification. In some cases, electrifying a component may only provide marginal improvements in fuel savings when used in the same manner as its conventional counterpart. However, an electric component could also be the enabler to a different mode of operation that could realize significant fuel savings. For example, idling a truck engine when the vehicle is parked is the common means of providing cabin heat or cooling while a driver sleeps or does paperwork. This practice uses fuel inefficiently, may increase engine maintenance, creates additional exhaust emissions, and generally increases operating expenses. The electrification of the truck heating, ventilation and air conditioning (HVAC) system provides the capability of conditioning the air to the cabin without having to run the truck engine. This is important because large quantities of fuel are burned just for that purpose.

With that precedent, this research program has been focused on converting conventional belt or gear driven accessories to electrically driven ones. This allows them to operate independently of the main engine, at only the actual speed, pressure, or flow required. By continuously adjusting to the desired operating points, there are multiple opportunities for parasitic loss reduction and control features. To show the benefits of electrification, a demonstration vehicle is being built as part of this program. This truck is illustrated in Figure 1.

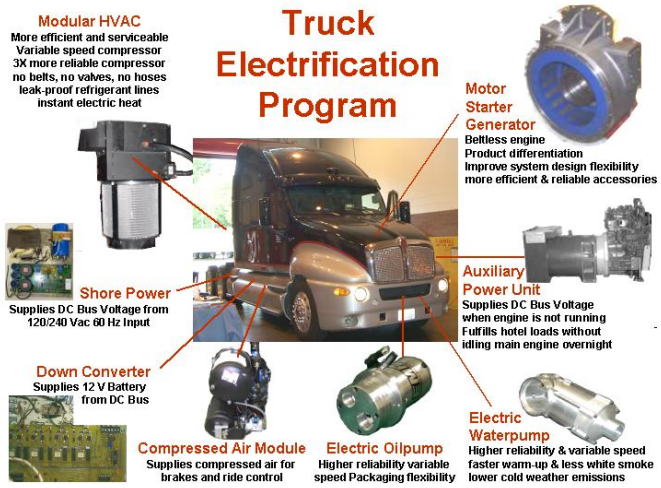

Figure 1. Demonstration vehicle

The "More Electric" Truck (MET) deploys a comprehensive electrification of truck accessory functions as a means to improve fuel economy, heat rejection, reliability, power management, and packaging flexibility. In it, several high power accessories are demonstrated in order to quantify the benefits of truck electrification, both during normal "over-the-road" operations and under "idling" conditions. Among the electrical accessory systems demonstrated in this program are: starter–generator, heating ventilation and air-conditioner, electronic battery charger, water pump, oil pump, brake air compressor, and auxiliary power unit. These components are described next.

Hardware Description

A dual voltage system (12 and 340 Vdc) was selected for this demonstration, because the level of electrification on the MET is massive in comparison to a conventional truck. The traditional/legacy electrical loads are powered from the lower voltage (12-volt). The new accessories require large amounts of electricity, and they are powered at a higher voltage. This is because, at this level of electrification, the capabilities of a 12-, or 24-, and even 42-volt system would be quickly overwhelmed. Thus, a 340-volt bus was selected for this appli-

cation. This system voltage is consistent with those found in hybrid-electric passenger cars. A discussion on the system components and their benefits follows.

Integrated Starter Generator

The heart of the MET electrical system is the integrated starter-generator (ISG) located inside the flywheel housing (see Figure 2). It provides the primary source of electrical power while the truck engine is running. It is a switched reluctance machine with a 30 kW rating at normal engine operating speeds, and 15 kW at low engine idle. The generator efficiency is approximately 90% over the entire nominal speed range of operation. The ISG is liquid cooled using engine coolant that may reach temperatures up to 120°C. The starter/generator frame fits inside the standard truck engine flywheel housing.

The ISG electronics are shown in Figure 3. The electronics are air-cooled to a heat sink temperature of 85°C. The unit is rated for 30 kW at the nominal voltage of 340 VDC. Rotor position and speed are determined using a sensorless algorithm based on winding current and flux linkage. Existing voltage and current transducers provide the information needed by the algorithm.

Figure 2. Integrated starter generator (Stator)

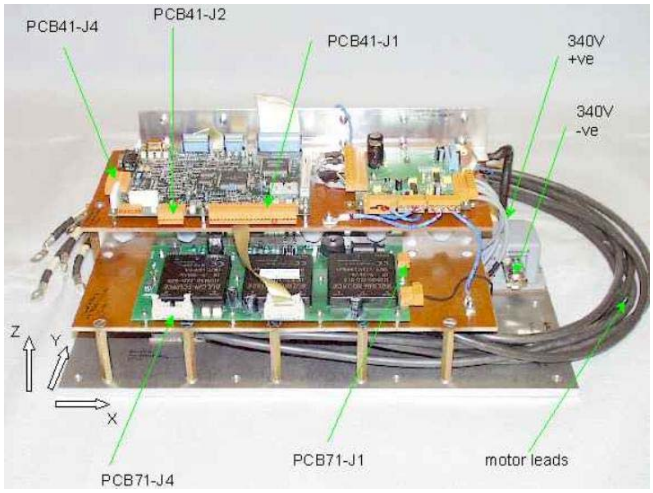

Figure 3. ISG electronics

Engine Coolant Pump

The electrically driven engine coolant pump (water pump) is shown in Figure 4. It operates from the 340 volt bus. It delivers a 50/50 ethlyene-glycol/water mixture to the engine block and cooling system. The rated flow is designed to satisfy the complete needs of the engine under all operating conditions. The coolant flow rate demand is set by a signal from the MET controller to the drive electronics. The pump speed is controlled to maintain the radiator top-tank temperature below a preset value and a minimum flow demanded by the engine. At the rated operating point, the power savings delivered by the electrically driven pump are almost 40% over the conventional pump. Further savings could be attained by matching the pump speed to the heat load present, i.e. engine temperature, instead of the engine speed, consuming only the power required to fulfill the cooling system needs. This approach reduces parasitic losses and improves fuel economy. Aside from fuel consumption, a variable speed water pump provides additional benefits. In cold weather, slowing down the pump leads to faster warm up, extended oil life, improved engine durability, and reduced cold start emissions.

Engine Oil Pump System

The primary specification driver for the electric motor is the torque requirement for cold starting conditions when the engine oil is at its highest viscosity (cold weather operation.) This makes it

Figure 4. Water pump hardware

impractical to provide all the oil flow with a single electrically driven pump. For this reason, the MET engine oil system uses a dual pump approach. The reduced flow mechanical pump, directly driven by the engine, provides most of the oil at higher engine speeds. An electrically driven gear pump supplements oil supply at lower engine speeds. In addition to requiring a much smaller electric motor, this approach provides further drive efficiency gains at higher engine speeds. The prototype hardware is shown in Figure 5. The mechanical pump is located inside the engine oil pan. For this demonstration, the electrically driven pump is external to the oil pan.

The control strategy for the engine oil pump is to maintain oil pressure according to a prescribed schedule reflecting given engine operating conditions, but without being exclusively coupled to

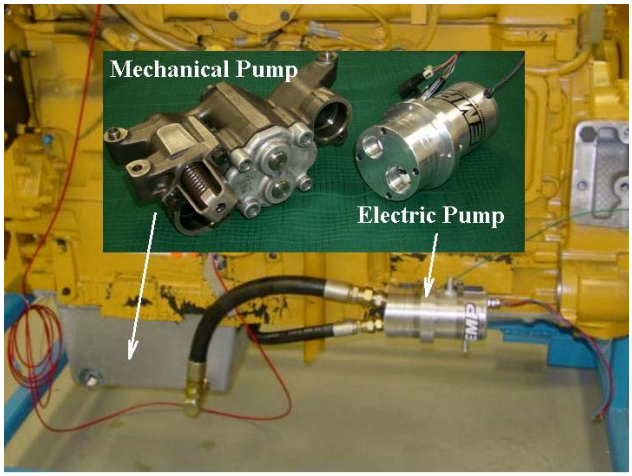

Figure 5. Dual oil pump engine installation

engine speed. This approach provides full lubrication to the engine, and eliminates bypass operation once the oil is at its nominal operating temperature. This, of course, reduces parasitic losses and improves fuel economy. In addition, the variable speed capability contributes to improving warm-up time and reducing cold start emissions.

Compressed Air Module

The air module supplies compressed air for braking and ride control. It is shown in Figure 6. It uses the basic components found in a standard truck air compressor system, standard dryer and controls, and dual air tanks. Compressor operation is functionally identical to the conventional belt driven unit, but in this case, the compressor is driven by an electric motor. When increased air pressure is required, the air module controller instructs the motor to run until the pressure is restored. By decoupling the air compressor from the engine it will be possible to implement more efficient power management strategies for charging the system. The design takes advantage of a more modular, plug-and-play approach which makes integration and assembly easier.

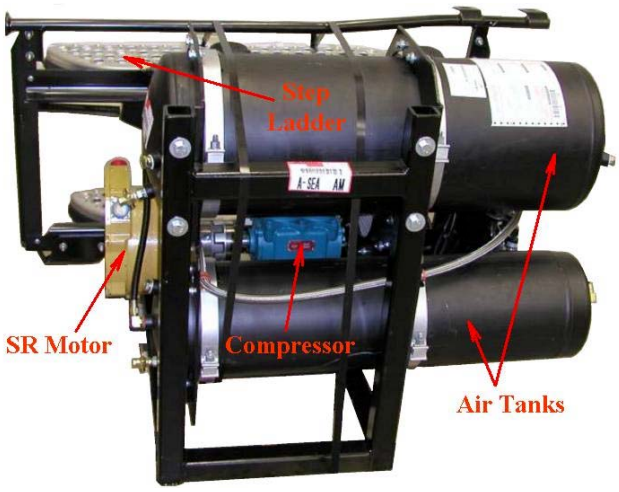

Figure 6. Compressed air module

Auxiliary Power Unit (APU)

The APU provides power to the MET truck when the main engine is not running. The functional requirements for the unit are: (1) provide adequate power for all non-running engine needs, (2) no objectionable operating characteristics that would affect sleeping, and (3) no adverse effects on vehicle

reliability, maintenance, service and repair. The lube and coolant systems have been integrated with those from the main engine. This allows the use of APU residual heat for warming the cabin and/or the main engine block (before start-up). It also eliminates the need for separate coolant and oil changes. The APU is shown in Figure 7.

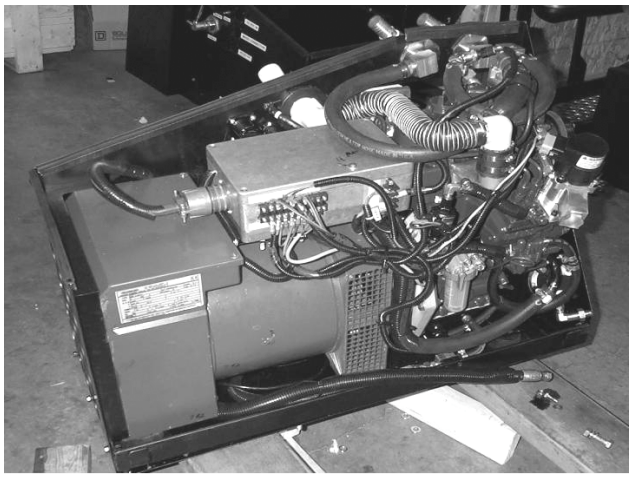

Figure 7. Auxiliary power unit

Heating Ventilation & Air Conditioning (HVAC)

The electric HVAC is a key component in the implementation of anti-idling solutions. It provides conditioned air to the cabin either when the main engine is running, or under APU or Shore Power modes of operation. The system is shown in Figure 8. The refrigerant compressor is highly reliable, efficient, and its speed is variable. After initial cool-down from a hot-soak condition, the cabin temperature can be maintained at comfortable levels with the compressor running at reduced speed, saving fuel and lowering power demands on the engine or APU. Also, the variable speed feature eliminates losses and it is very powerful for implementing automatic temperature control.

Cabin heat is provided by a conventional glycol heat exchanger when the engine is running, and by an electric heater when under APU or Shore Power modes. Since the APU engine shares coolant with the truck engine, glycol heat is also available when the APU is running. The electric heating module is made of an electro-ceramic material exhibiting positive thermal coefficient (PTC) characteristics. In cold weather conditions, the electric heat can also be

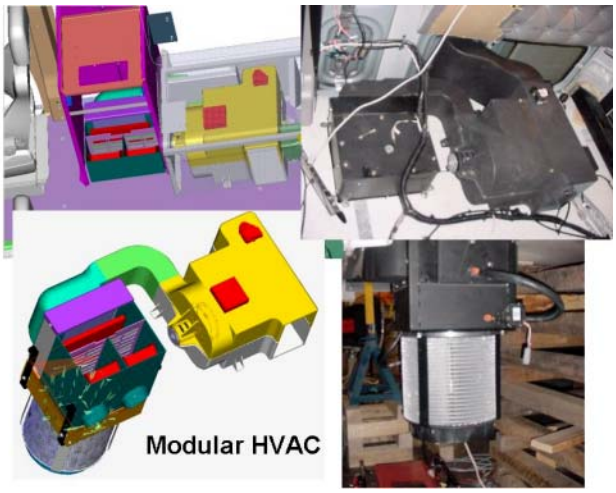

Figure 8. Electric HVAC unit

used as supplemental heat until the main engine warms up. This provides instant heat to the operator, and it mitigates engine overcooling. In fact, it puts additional load on the engine, which improves warm up times. In frigid conditions, both glycol and electric heat are used simultaneously.

Electronic Modules and Cooled Enclosure

The Down Converter replaces the traditional belt-driven alternator by stepping down the generator voltage from 340 volts to 12 volts to supply the standard electrical bus. This converter is a full bridge, current mode, switched mode power supply running at 40 kHZ using IGBT technology and Hall Effect current sensors for current control.

The Shore Power unit accepts either 120VAC or 240VAC and signals to the MEI controller as to which one is in use. The MEI controller then limits the 340VDC bus loads to be consistent with either a 15A (120VAC) or 30A (240VAC) source. This AC voltage is rectified to DC and then boosted to supply the 340VDC bus. An LC filter is placed between the rectifier and the boost converter to improve the form factor of the AC current waveform taken from the utility.

The Inverter supplies 120 volts, 60 hertz, for appliance/hotel loads, and the Shore-Power allows connection to the electric utility line (120/240 volt single phase power.) The inverter is a 12VDC to 120VAC single-phase converter system. It is a stand-alone unit which is not directly controlled by the MET controller.

These power electronic modules, the ISG converter, and the oil and water pump motor drives are confined to a single enclosure that is built around an air-cooled heat sink (see Figure 9). The box is sealed to 5 psi to protect the electronic modules from the elements. Power switches are cooled by conduction into an aluminum baseplate which then conducts heat into the main air-cooled heatsink. A variable speed blower provides the required air-movement to keep the baseplate temperature below 85°C.

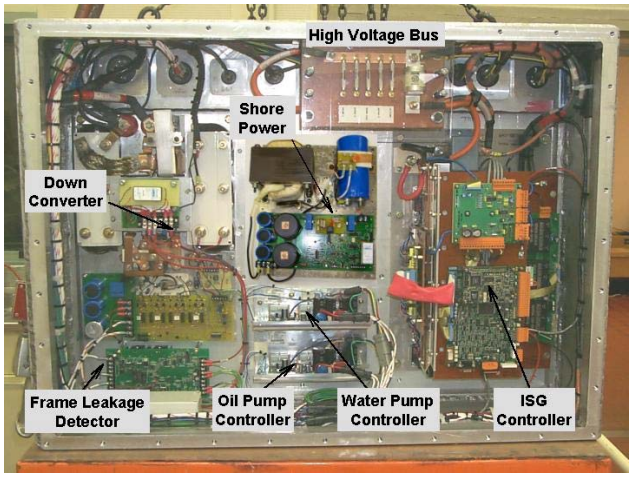

Figure 9. Electronics enclosure

Fuel Savings Opportunity

Estimating fuel savings for an average over-the-road cycle is challenging. The savings largely depend on how the truck is used, weather conditions, road characteristics, etc. It is difficult to conceive a single test cycle that would be representative of the average truck. Truck fleets use their own load cycles based on their more common routes. Engine manufacturers use proprietary engine load profiles to baseline the fuel economy of their engines. For the purpose of this analysis, a simplified load factor is used. It will be assumed that the over-the-road average engine load is 50% at a speed of 1,500 rpm. Under this condition, the fuel savings contribution of each accessory was computed. For the current implementation, analyses show that the electric accessories would collectively lower the fuel consumption of the truck by approximately 300 gallons per year.

A second fuel savings opportunity is by curtailing overnight idling. It has been estimated that long-haul trucks idle an average of 1,830 hours per year. Engine idling speeds range from 600 to 1,000 rpm depending on the driver's preferences and weather conditions. Thus, truck idling fuel consumption can be calculated, for defined climatic conditions, using measured engine fuel consumption at fractional loads. A chart plotting the engine fuel rate required to power truck accessories during idling conditions is shown in Figure 10. To determine the yearly fuel savings, the following seasonal load factor was used:

- 6 months of spring and fall-like weather
- 2 months of mild winter
- 2 months of mild wummer
- 1 month of cold winter
- 1 month of hot summer

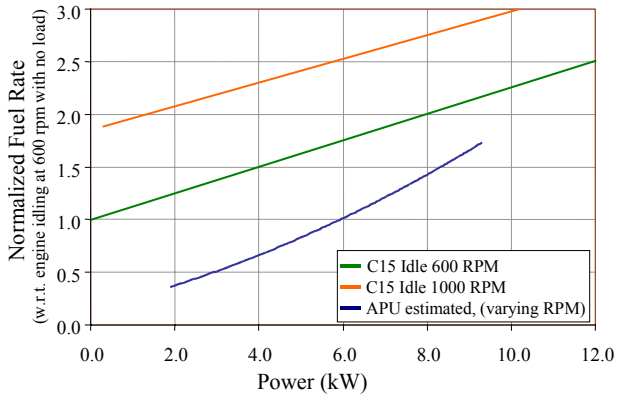

Figure 10. Truck and APU engine fuel rates vs. power

Table 1 lists the relative fuel consumption for various weather conditions. The entries are listed in normalized form. The nominal engine idling fuel rate (100%) is defined as the fuel rate on a bare engine running at 600 rpm with no load. The corresponding truck accessory load is listed in kW.

Given this breakdown, for a truck that idles 1,830 hours per year burning approximately 1,500 gallons of diesel fuel, the APU provides a savings of 900 gallons per year per truck. Further savings could be attained through Shore Power. Having the capability to power the electrified truck, without running an APU, would yield an annual savings of 1,500 gallons (amount currently wasted by idling.) Of course, electricity wouldn't be free,

Table 1. Relative fuel consumption by season

	Fuel Usage				
	600 rpm			1000 rpm	
	Spring/ Fall	Mild Winter	Mild Summer	Cold Winter	Hot Summer
Truck Idling	150% (3.7 kW)	150% (3.7 kW)	160% (4.7 kW)	230% (3.7 kW)	255% (6 kW)
APU Output 1.7/2.5 kW elect/mech	45%	---	---	---	---
APU Output 2.5/3.6 kW elect/mech	---	60%	60%	---	---
APU Output 5.2/7.4 kW elect/mech	---	---	---	130%	130%

and the economics of such savings would depend on the price of electricity at the site.

Test Plans and Future Work

A Kenworth T-2000 Class-8 truck with a Caterpillar® C-15 engine has been built with the electric accessories shown in Figure 1. This truck is shown in Figure 11. A comprehensive series of fuel economy tests will be conducted during the forth quarter of calendar year 2003 to validate the analysis results presented in the preceding section. These tests are designed to obtain real-world truck performance data over a range of terrain and conditions. They conform to the SAE Type-II (J1321) procedure, using a test vehicle and an unchanging control vehicle.

Figure 11. "More Electric" DOE truck

Summary and Conclusions

The More Electric Truck capitalizes on the wide spread use of electricity as a means to improve efficiency, power management, reliability, packaging flexibility, and customer value. Among the electrically driven accessory systems demonstrated in this program are the: starter–generator, heating ventilation and air-conditioner, electronic battery charger, water pump, oil pump, brake air compressor, and auxiliary power unit. This installation provides a significant opportunity for reducing fuel consumption on long-haul Class 8 trucks. The dominant fuel savings opportunity is in reducing the amount of time the main engine idles. Although shore power offers the largest potential benefits, the likelihood of developing such large infrastructure in the foreseeable future would be low. An APU based solution would provide an important initial step toward reducing the fuel consumption of Class 8 trucks. Although test results are not yet available, the fuel savings (from combined idle-avoidance and from over-the-road driving) are expected to be in the order of 1,200 gallons of diesel fuel per year, per truck. On a truck that consumes 20,000 gallons per year, this savings represents an approximate 6% reduction in fuel consumption. With a population of 458,000 Class 8, long-haul trucks that idle overnight, the total potential savings in the U.S. alone would be 550 million gallons of diesel fuel per year. The impact on the U.S. economy could be as much as $825 million annually.

IV. Friction and Wear

A. Boundary Lubrication Mechanisms

Principal Investigators: O.O. Ajayi, J.G. Hershberger, and G.R. Fenske
Argonne National Laboratory
9700 South Cass Avenue, Argonne, IL 60439
(630) 252-9021; fax: (630) 252-4798; ajayi@anl.gov

Technology Development Manager: Sid Diamond
(202) 586-8032; sid.diamond@ee.doe.gov
Technical Program Manager: Jules Routbort
(630) 252-5065; routbort@anl.gov

Contractor: Argonne National Laboratory, Argonne, Illinois
Prime Contract No.: W-31-109-Eng-38.

Objective

Develop a better understanding of the mechanisms and reactions that occur on component surfaces under boundary lubrication regimes. Specific objectives are

- Determine the basic mechanisms of catastrophic failure in lubricated surfaces in terms of materials behavior.
- Determine the basic mechanisms of chemical boundary lubrication.
- Establish and validate performance and failure prediction methodologies for lubricated components.
- Integrate coating and lubrication technologies for maximum enhancement of lubricated-surface performance.

Approach

- Characterize the dynamic changes in the near-surface material during scuffing. Formulate a material-behavior-based scuffing mechanism.
- Determine the chemical kinetics of boundary film formation and loss rate by in-situ X-ray characterization of tribological interfaces at the Advanced Photon Source (APS) at Argonne National Laboratory (ANL).
- Characterize the physical, mechanical, and tribological properties of tribo-chemical films, including the failure mechanisms.
- Integrate the performance and failure mechanisms of all the structural elements of a lubricated interface to formulate performance and/or failure prediction methodology; this will include incorporation of surface coatings.

Accomplishments

- Conducted extensive characterization of microstructural changes during scuffing of 4340 steel, using scanning electron microscopy (SEM) and X-ray analysis.
- Developed a model of scuffing initiation by an adiabatic shear instability mechanism.
- Using x-ray fluorescence, reflectivity and diffraction at the APS, demonstrated the ability to characterize tribo-chemical films generated from model oil additives.

Future Direction

- Develop and validate a model for scuffing propagation and integrate it with an initiation model for a comprehensive scuffing prediction method. Experimentally validate the scuffing theory for various engineering materials.
- Design and construct a tribo-tester for in-situ characterization of tribo-chemical surface film at the APS.
- Using various techniques, continue to characterize tribo-chemical films formed by model lubricant additives.
- Characterize the physical, mechanical, and failure mechanisms of tribo-chemical films with nano-contact probe devices.
- Evaluate the impact of various surface technologies, such as coating and laser texturing, on boundary lubrication mechanisms.

Introduction

Most critical components in diesel engines and transportation vehicle subsystems are oil lubricated. Satisfactory performance of these components and systems is achieved through a combination of materials, surface finish, and lubricant oil formulation technologies often by an Edisonian trial-and-error approach. Indeed, experience is often the sole basis for new design and solutions to failure problems in lubricated components. With more severe operating conditions expected for component surfaces in engines and vehicles, the trial-and-error approach to effective lubrication is inadequate and certainly inefficient. Departure from this approach will require a fundamental understanding of both boundary lubrication and surface failure mechanisms.

A major area of focus for Department of Energy development of diesel engine technology is emission reduction. Some essential oil lubricant and diesel-fuel additives, such as sulfur, phosphorous, and chlorine, are known to poison the catalysts in after-treatment devices. Although, reduction or elimination of these additives will make emission after-treatment devices more effective and durable, it will also render surfaces of many lubricated components vulnerable to catastrophic failure. Indeed, most of the effective methods to reduce diesel engine emissions will also render many critical-component surfaces vulnerable to catastrophic failure, thereby compromising their reliability.

Increases in vehicle efficiency will require an increase in power density and increased severity of contact between many components in the engine and powertrain systems. This, again, will compromise the reliability of various critical components, unless they are effectively lubricated. The efficacy of oil additives in protecting component surfaces depends on the nature and extent of chemical interaction between the surface and the oil additives.

In addition to reliability issues, durability of lubricated components also depends on effectiveness of oil lubrication mechanisms. Components will eventually fail or wear out over time. Failure mechanisms that limit the durability of lubricated surfaces are wear in its various forms, and contact fatigue. Wear is the gradual removal of material from contacting surfaces, and it can occur by various mechanisms, such as abrasion, adhesion, corrosion, etc. Also, the repeated contact stress cycles to which component contact surfaces are subjected can initiate and propagate fatigue cracks, and, ultimately lead to the loss of a chunk of material from the surface. This damage mode is often referred to as pitting. Wear and contact fatigue are both closely related to boundary lubrication mechanisms. Antiwear additives in lubricants are designed to form a wear-protective layer on the surface. The role of lubricant additives on the contact fatigue failure mode is not fully understood, although it is clear that the lubricant chemistry significantly affects contact fatigue. Again, lack of an adequate, comprehensive understanding of basic mechanisms of boundary lubrication is a major

obstacle to a reasonable prediction of component surface durability.

The desire to extend the diesel engine oil drain interval, with an ultimate goal of a fill-for-life system, is increasing. Successful implementation of the fill-for-life concept will require optimization of surface lubrication through the integration of materials, lubricant, and, perhaps, coating technologies. Such an effort will require an adequate fundamental understanding of surface material behavior, chemical interaction between the material surface and the lubricant and the behavior of material and lubricant over time.

Some common threads run through all of the challenges and problems in the area of surface lubrication of engine components and systems briefly described above. The two key ones are lack of an adequate basic and quantitative understanding of failure mechanisms of component surfaces, and lack of an adequate understanding of basic mechanisms of boundary lubrication, i.e., how lubricant chemistry and additives interact with rubbing surfaces and how this affects performance. To progress from the empirical trial-and-error approach to predicting lubricated-component performance, we believe a better understanding of the basic mechanisms of the events that occur on lubricated surfaces is required. Consequently, the primary objective of the present project is to address some of fundamental mechanisms of boundary lubrication and failure processes of lubricated surfaces. The technical approach taken in this study differ from the usual one of posttest characterization of lubricated surfaces, and, rather, will develop in-situ characterization techniques for lubricated interfaces that will use the X-ray beam at the APS located at ANL. Using a combination of X-ray fluorescence, reflectivity, and diffraction techniques, we will study, in real time, the interaction between oil lubricants and their additives and the surfaces they lubricate. Such study will provide the basic mechanisms of boundary lubrication. In addition to surface chemical changes, materials aspects of various tribological failure mechanisms will be studied.

Results and Discussion

Effort during the past year focused on two parallel tasks, namely, study of the scuffing mechanism and development of methods for X-ray characterization of boundary films.

Scuffing Study

Scuffing, defined as a sudden catastrophic failure of a lubricated surface, is poorly understood and a major source of reliability problems in engine components. It is usually accompanied by a sudden rapid rise in friction coefficient, noise and vibration, contact temperature and loss of surface integrity. Microstrutural changes that occur during scuffing of hardened 4340 steel were studied. Samples from scuffing tests were analyzed before, during, and after scuffing, as shown in Figure 1.

In a time span of an order of a microsecond, significant microstructual changes were observed to accompany scuffing. The original microstructure of tempered martensite was transformed into a layer of very fine-grained, severely deformed material. Figure 2 shows the SEM photomicrograph of the near surface layer before, during, and after scuffing.

X-ray analysis also showed that the surface layer after scuffing contained ≈60% retained austenite, indicating that the contact temperature after scuffing exceeded the austenitizing temperature of 4340 steel.

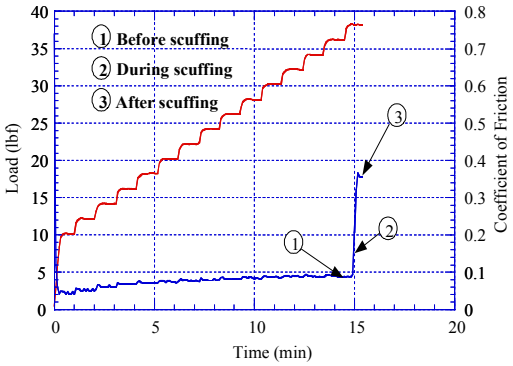

Figure 1. Friction variation during step loading scuffing test of hardened 4340 steel

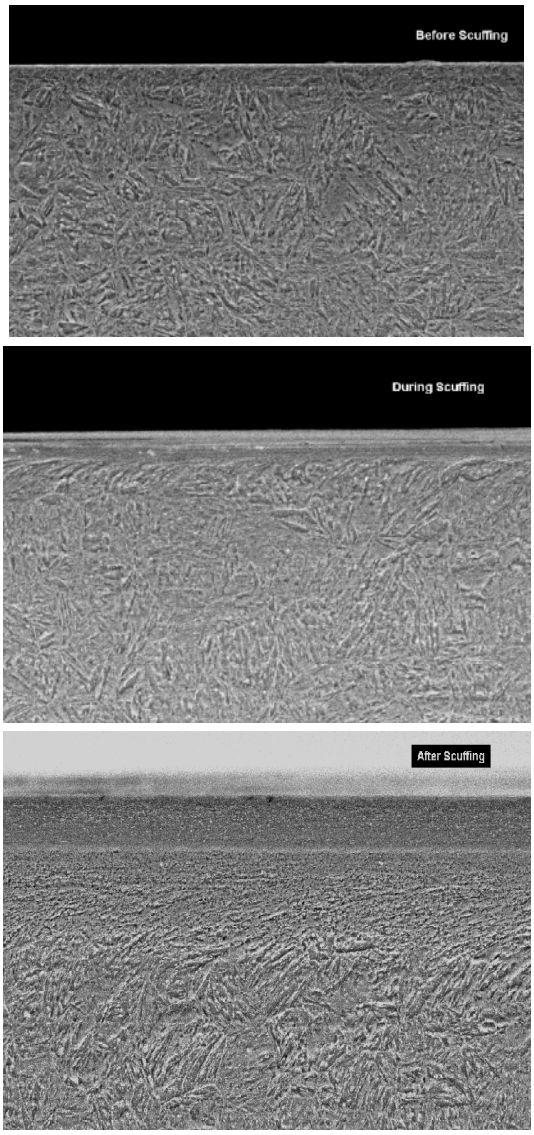

Figure 2. Microstructure before, during and after scuffing of hardened 4340 steel

Based on these microstructural changes and other phenomenological observations of the scuffing process, an initiation mechanism based on adiabatic shear instability is proposed. When surfaces are brought in contact, high contact stresses at asperities will lead to localized plastic deformation, which will lead to work hardening of the deformed area as dislocation density increases. With increasing contact severity, more work hardening will occur. As more plastic deformation of the surface layer occurs, some of the plastic work is converted into heat, leading to thermal softening. Scuffing is then initiated when the rate of thermal softening exceeds the rate of work hardening. At such a point, rapid deformation will occur in a very short time; hence, the adiabatic nature of the process. The large amount of heat generated will lead to a rapid rise in temperature, which will further accelerate plastic deformation and eventually lead to catastrophic failure called scuffing.

Based on this mechanism of scuffing, it is the possible to connect propensity of a material to scuffing with some material properties. Numerous criteria have been set for the initiation of adiabatic shear instability. Perhaps the simplest one is the critical strain (γ_c) at which the rate of work hardening is equal to the rate of thermal softening. Thus, scuffing will be initiated at a local point on a sliding surface when the shear strain at that point exceeds critical strain, give as

$$\gamma_c = \frac{n\rho C}{0.9\frac{\partial \tau}{\partial T}} \ ,$$

where n is the work hardening index, ρ is the density, C is the heat capacity, τ is the shear strength, and T is the temperature.

Preliminary validation of this model of scuffing initiation was conducted with hardened 4340 steel tempered at various temperatures as a means of varying the critical strain for shear instability. A more compressive validation with various materials and alloys is underway. With this model, it is possible to estimate susceptibility of various materials to scuffing. It also provides a means for a material-based solution or strategy to preventing scuffing in lubricated engine components.

X-ray Characterization of Tribo-Chemical Films

In this task, the composition and structure of tribo-chemical films generated from a model anti-wear lubricant additive Zinc diathiophosphate (ZDDP) was characterized by glancing-angle X-ray fluorescence, diffraction, and reflectivity at the APS. A typical fluorescence spectrum of a tribo-chemical film that identifyied the key elements present in the film is shown in Figure 3.

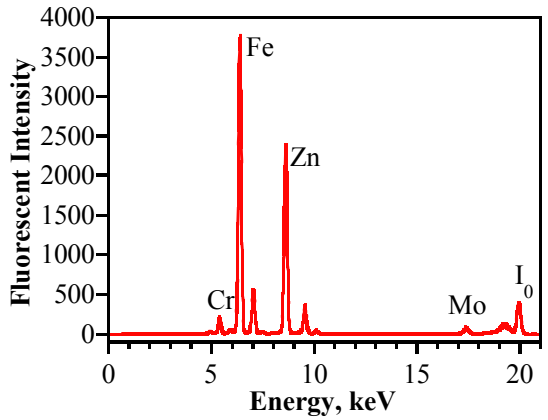

Figure 3. X-ray fluorescence spectrum of tribo-chemical film formed by ZDDP anti-wear oil additive

Depth profiling of the compositional variation of tribo-chemical films generated by two methods are shown in Figures 4a and 4b. For laboratory studies, tribo-chemical films are usually generated either by rubbing surfaces together in the presence of the additive-containing lubricant being studied, or thermally, by heating a piece of metal submerged in oil that contains the additive. Although, no universal agreement has not been reached among researchers, it is always assumed that the films generated by the two methods are essentially the same.

Results of our analysis of depth compositional variation of the films generated by the two methods clearly showed that the structure and composition of the films generated thermally and by tribo-contact are not the same.

Although it may be easier to produce boundary films for laboratory study by thermal treatment, the results from such a study may not be applicable to tribological interfaces because the films are not necessarily the same. Films produced by these two methods with other model additives will be characterized in our future effort to assess the generality of the current observation with ZDDP. It is conceivable that the thermally generated and the tribo contact generated films for some other additives may to be similar.

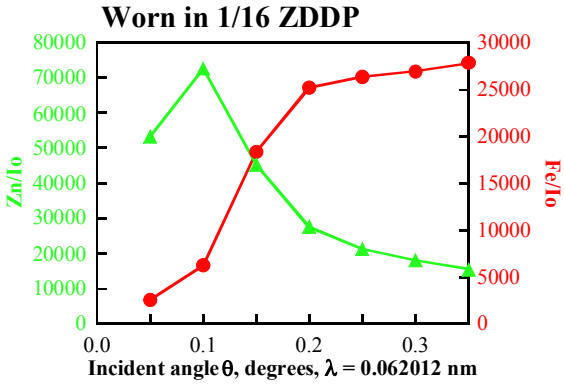

Figure 4a. Depth variation of Zn and Fe content of surface boundary film generated by tribo-contact in 1/16 ZDDP

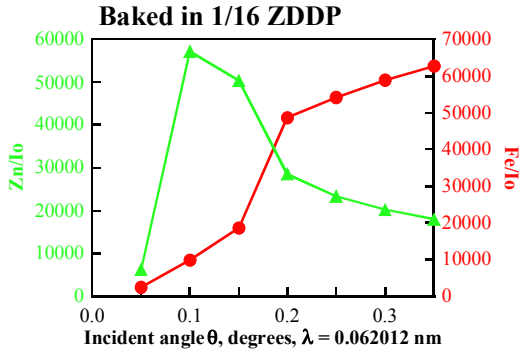

Figure 4b. Depth variation of Zn and Fe content of surface boundary film generated thermally in 1/16 ZDDP

Conclusions

Significant progress was made in the boundary lubrication project during the past year. Relying on microstructural changes and other phenomenological observations associated with scuffing, we developed a model of scuffing initiation based on adiabatic shear instability. Scuffing is initiated when the rate of thermal softening exceeds the rate of work hardening. This material-properties- based model is a significant development in our understanding of poorly understood scuffing failure. Material properties and behavior strategies for scuffing prevention are now possible. Surface characterization methods based on x-ray techniques are being developed. These techniques were able to show differences in the structure and composition of ZDDP boundary films generated thermally and by tribo contact.

Publications

1. J. Hershberger and O.O. Ajayi, "Nondestructive Characterization of Tribochemical Surface Films from Additives" Presented at STLE Annual Meeting, New York, April 28–May1, 2003.
2. J. Hershberger, O.O. Ajayi and G.R. Fenske,"Nondestructive Characterization of Surface Chemical Wear Films via X-ray" *Journal Thin Solid Film,* in press.
3. J. Hershberger, O.O. Ajayi, J. Zhang, H. Yoon, and G.R. Fenske, "Formation of Austenite During Scuffing Failure of SAE 4340 Steel" *Wear Journal,* in press.
4. O.O. Ajayi, J. Hershberger, and G.R. Fenske, "Shear Instability Mechanism of Scuffing in Lubricated Contacts" Presented at the International Conference on Boundary Lubrication, Copper Mountain, CO, August 3–7, 2003. To be published in *Tribology International*.

B. Parasitic Engine Loss Models

Principal Investigators: G. Fenske, A. Erdemir, L. Ajayi, and A. Kovalchenko
Argonne National Laboratory
9700 South Cass Avenue, Argonne, IL 60439
(630) 252-5190; Fax: (630) 252-4798; gfenske@anl.gov

Investigators: B. Brogdon, T. Torbeck, I. Fox, and J. Kezerl
Ricardo, Inc., 7850 Grant Street, Burr Ridge, IL 60527-5852
(630) 789-0003; fax: (630) 789-0127

Technology Development Manager: Sid Diamond
(202) 586-8032; sid.diamond@ee.doe.gov
Technical Program Manager: Jules Routbort
(630) 252-5065; routbort@anl.gov

Contractor: Argonne National Laboratory
Contract No.: W-31-109-ENG-38

Objective

- Develop and integrate a set of software packages that can predict the impact of advanced coating technologies on reducing parasitic energy losses from a number of diesel engine components.
- Develop a suite of computer codes that can predict the wear and durability of these components when exposed to low-viscosity lubricants.

Approach

- Predict fuel economy improvements over a wide range of oil viscosity.
- Predict change in wear loads due to reduced oil viscosity.
- Develop superhard and low-friction coatings that can reduce friction and wear in low-viscosity oils.

Accomplishments

- Simulations have shown that hydrodynamic friction decreased with reduced lubricant viscosity, while wear loads and asperity friction increased.
- With a 90% reduction in asperity friction, optimum lubricant viscosity was found to be lower than that of SAE 5, and the reduction in hydrodynamic friction was very significant. With a piston skirt alone, such a reduction in asperity friction nearly doubled the improvement in fuel consumption. Overall, more than 4% improvement in fuel economy was predicted with the combined uses of low-viscosity oils and superhard and low-friction coatings.

Future Direction

- Apply superhard and low-friction coatings on actual engine components and demonstrate their usefulness in low-viscosity oils.
- Optimize coating composition, surface finish, thickness, and adhesion to achieve maximum fuel savings.

Introduction

Friction, wear, and lubrication impact energy efficiency, durability, and environmental soundness of all kinds of transportation systems, including diesel engines. Total frictional losses in a typical diesel engine may alone account for more than 10% of the total fuel energy (depending on the engine size, driving condition, etc.). The amount of emissions produced by these engines is related to the fuel economy of that engine. In general, the higher the fuel economy, the lower the emissions. Higher fuel economy and lower emission in future diesel engines may be achieved by the development and widespread use of novel materials, lubricants, and coatings. For example, with increased use of lower viscosity oils (that also contain the least amounts of sulfur and phosphorus-bearing additives) the fuel economy and environmental soundness of future engine systems can be dramatically improved. Furthermore, with the development and increased use of smart surface engineering and coating technologies, even higher fuel economy and better environmental soundness will be feasible.

The main goal of this project is to develop a suite of software packages that can predict the impact of smart surface engineering and coating technologies (e.g., laser dimpling, NFC, and superhard nitride coatings) on reducing parasitic energy losses from diesel engine components. The project also aims to validate the predictions using experimental friction and wear studies at Argonne National Laboratory. Such information will help identify critical engine components that can benefit the most from the use of novel surface technologies, especially when low-viscosity engine oils are used to maximize the fuel economy of these engines by reducing churning and/or hydrodynamic losses. A longer-term objective is to develop a suite of computer codes capable of predicting the lifetime/durability of critical components exposed to low-viscosity lubricants.

In FY2003, Argonne and Ricardo, Inc., worked together to identify engine components that can benefit from low-friction coatings and/or surface treatments. The specific components considered included: rings, piston skirt, piston pin bearings, crankshaft main and connecting rod bearings, and cam bearings. Using computer codes, Ricardo also quantified the impact of low-viscosity engine oils on fuel economy. Ricardo also identified conditions that can result in direct metal-to-metal contacts, which in turn can accelerate engine wear and asperity friction.

Argonne has worked on the development and testing of a series of low friction coatings under a wide range of sliding conditions using low- and high-viscosity engine oils. These coatings (such as NFC and MoN) as well as laser textured surfaces were subjected to extensive tests using bench-top friction and wear test machines. The test conditions (i.e., speeds, loads, and temperatures) were selected to create conditions where direct metal-to-metal contacts will prevail as well as situations where mixed or hydrodynamic regimes will dominate. Using the ranges of frictional data generated by Argonne, Ricardo estimated the extent of potential energy savings in diesel engines and identified those components that can benefit the most from such low-friction coatings and or surface treatments. Wear data generated by Argonne can be used to develop models and computer codes that predict the lifetime/durability of diesel engine components.

Results

In a series of computer simulations, Ricardo has analyzed the effects of lubricant viscosity on engine wear loads, engine friction, and fuel consumption. With drastic reductions in oil viscosity, it was found that in addition to other engine components, crank-shaft bearings would also become highly vulnerable to high friction and wear losses. The situation with crank shaft bearings was analyzed using ORBIT software, which takes into account non-circular bearing/journal geometry, distortions, cavitation, and boundary-lubricated sliding conditions, where asperity contact and elastohydrodynamic lubrication may dominate. In addition to the ORBIT software, PISDYN, RINGPACK, and VALDYN simulations were carried out under both baseline and reduced viscosity conditions. The objective was to determine the impact of oil viscosity on overall engine friction and wear.

Piston Friction Studies

PISDYN simulations were carried out for varying levels of lubricant viscosity reduction at eight load and speed conditions. Hydrodynamic and asperity friction predictions were tabulated for each case. The

predicted optimum lubricant grade for the baseline piston was SAE 40. With a 30% reduction in asperity friction, the allowed reduction in lubricant viscosity did not result in a large reduction in frictional mean effective pressure (FMEP). A 60% reduction in asperity friction allowed a larger reduction in lubricant viscosity. With a 90% reduction in asperity friction, the predicted optimum viscosity was lower than SAE 5, and the reduction in hydrodynamic friction was very significant. These findings are summarized in Figure 1.

According to these predictions, for the piston skirt alone, with a 90% reduction in asperity friction, reducing lubricant viscosity nearly doubled the fuel economy. Also, with such a reduction in friction, the use of oil grades even lower than SAE 5 would have been feasible.

For the piston skirt considered in this study, significant asperity friction is predicted for high loads. However, the level of asperity friction and potential benefits of coating can vary significantly from one design to another.

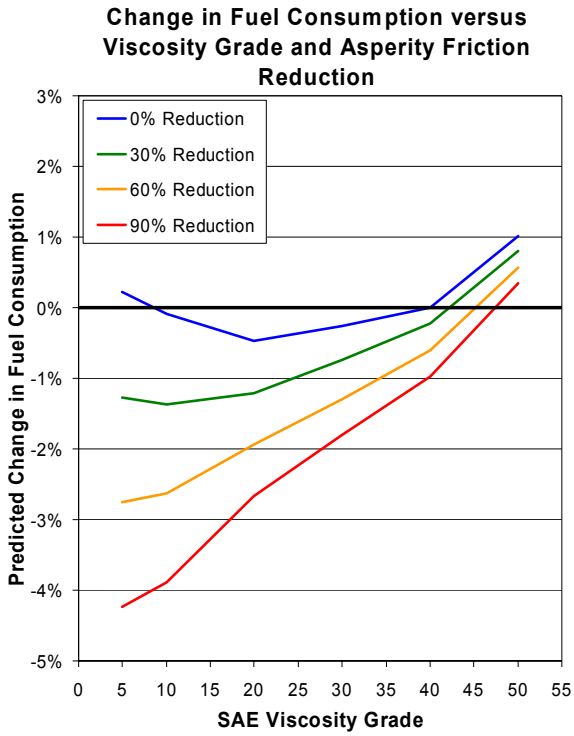

Figure 1. PISDYN predictions of FMEP vs. SAE lubricant viscosity grades and asperity friction reduction

Piston Wear Studies

As lubricant viscosity was reduced, wear loads on the piston skirt and cylinder liner were increased in both magnitude and extent, thus increasing the vulnerability of these components to rapid wear. As shown in Figure 2, the total average wear load per cycle is more than four times higher for SAE 5 than SAE 40 oil. These findings suggest that , to allow the use of SAE 5 oil, a surface treatment would have to provide approximately four times the wear resistance of the baseline engine material.

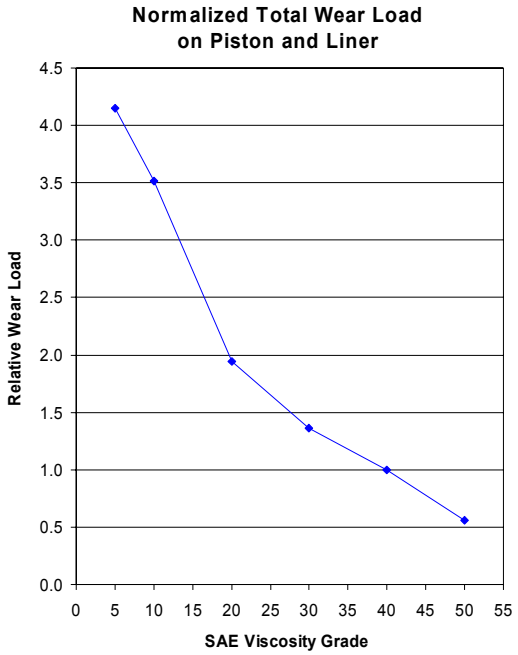

Figure 2. The effect of SAE lubricant viscosity grade on relative wear load index of piston and liner in an engine

Coating Studies

At Argonne, systematic studies were carried out to develop low-friction and high-wear resistant coatings for use in critical engine parts and components. One of the coatings studied extensively was near frictionless carbon (NFC), which can provide friction coefficients of 0.001-0.01 under dry sliding conditions, especially in inert gas environments. Under lubricated sliding conditions, depending on the additive package in an oil and the oil viscosity, this coating was able to reduce friction by more than 40%. Figure 3 shows its performance in TCP and moly-containing base synthetic oils. Figure 4 shows its friction performance in a fully

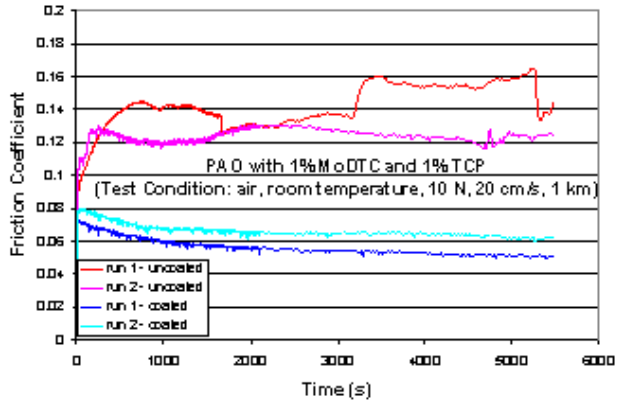

Figure 3. Frictional performance of NFC coating in 1% TCP and moly-containing polyalphadefin base oil

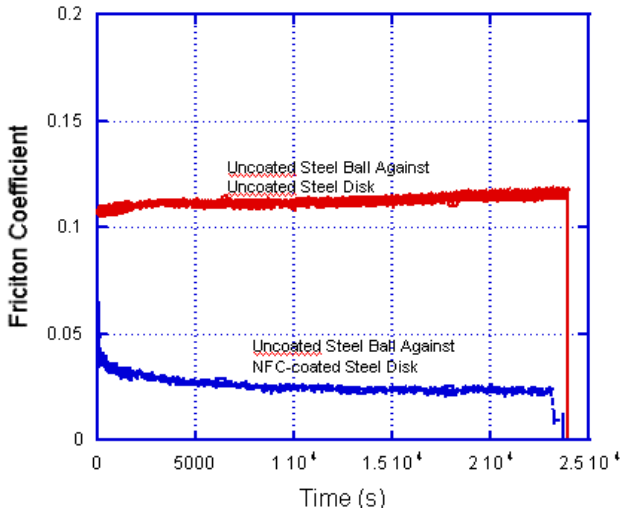

Figure 4. Friction coefficients of steel/steel and steel/NFC-coated steel test pairs in a fully formulated engine oil under boundary-lubricated sliding conditions

formulated synthetic oil. This coating was highly optimized to respond well to the lubricated test environments. The reduction in friction in this case is more than 80%.

In addition to NFC coatings, we have explored the properties and potential usefulness of a series of superhard nano-composite nitride base coatings. The measured hardness of these coatings is more than 50 Gpa, and their friction and wear performance (especially under lubricated sliding conditions) is exceptional. As shown in Figure 5, they can provide very low friction under even severe boundary-lubricated sliding conditions, as compared to the base steel samples used in these studies. The table below the graph summarizes the reductions in friction achieved under a wide range of sliding conditions. Because of their superhard nature, we could not measure any wear on these coatings, and the pins that slid against the coated surfaces had also suffered minimal wear losses.

Studies on Laser Textured Surfaces

Recent advances in laser beam technology have paved the way for large-scale utilization of lasers for a wide range of tribological applications. Laser dimpling or texturing is a unique process by which one can produce shallow (5 to 10 μm deep) pits or dimples on a tribological surface. At Argonne, we have been exploring the friction and wear performance of such dimpled surfaces under a wide range of lubricated sliding conditions. Laser dimpling of test samples was done at Technion-Israel by Prof. I. Etsion. When such dimpled surfaces were used under lubricated sliding conditions, significant increases in hydrodynamic efficiency or reduction in friction is expected. In a sense, these dimples can act as a reservoir and can deliver lubricants when and if they are needed on the sliding contact surfaces. They can also trap the wear debris particles so that the extent of third-body wear damage on sliding surfaces is reduced. Figure 6 shows the shape and morphology of such dimples produced on a steel surface and the results of lubricated sliding tests on highly polished, ground and dimpled surfaces. As is clear, the dimpled surface provides the lowest friction under a wide range of lubrication regimes.

Discussion

Preliminary results from computer simulations showed that hydrodynamic friction decreased with reductions in lubricant viscosity, while wear loads and asperity friction increased. This is mainly due to the reduction of churning losses associated with the shear rheology of high viscosity oils. However, the decline in hydrodynamic friction is eventually offset by the increase in asperity friction. For each level of asperity friction reduction, there is a lubricant viscosity that provides the minimum overall fuel consumption (Figure 1). For an SAE 5 grade oil, simulations predict an overall fuel savings of greater than 4%, if a surface treatment is used to reduce boundary friction by 90%. Contact severity and wear loads are substantially increased in such low viscosity environments, and they would need to be

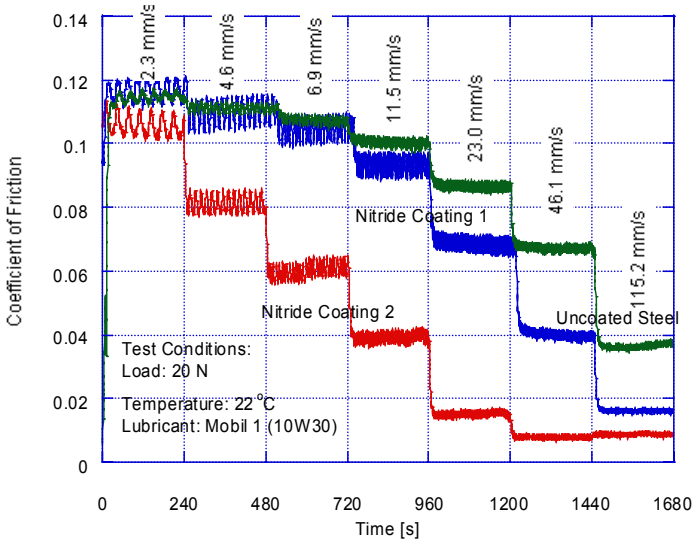

Linear Velocity [mm/s]	% Reduction of Friction Nitride Coating 1 vs. Uncoated Sample 3330	% Reduction of Friction Nitride Coating 2 vs. Uncoated Sample 3330
2.3	-1%	6%
4.6	2%	27%
6.9	3%	45%
11.5	7%	61%
23.0	21%	71%
46.1	39%	88%
115.2	56%	76%

Figure 5. Frictional performance of nano-omposite nitride coatings under boundary-lubricated sliding conditions. Table below the graph shows reductions in friction with new coatings at different sliding velocities.

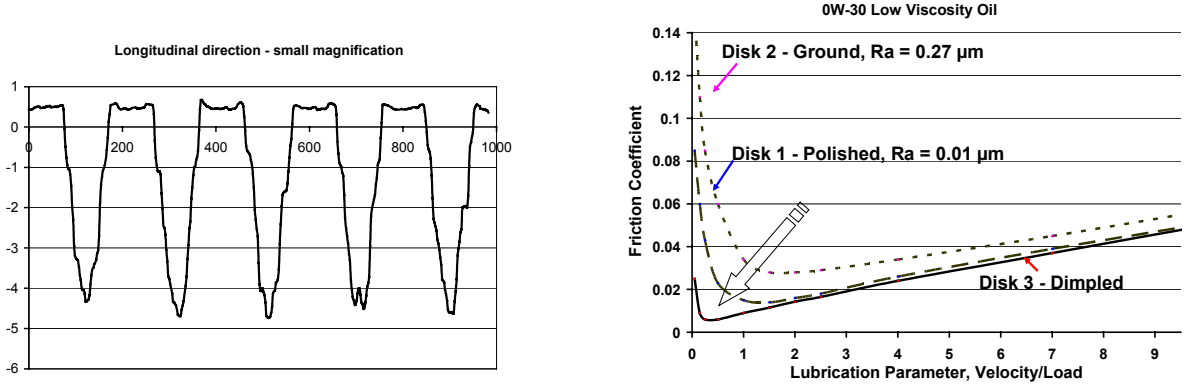

Figure 6. (a) Shape and morphology of dimples and (b) frictional performance of a laser-dimpled steel sample under lubricated sliding conditions. Performance of a ground and highly polished sample is also included for comparison. Dimples are typically 4 to 5 µm deep and 100 µm in diameter.

mitigated to avoid increased wear by using superhard coatings.

Work at Argonne has resulted in development of NFC films as well as superhard nitride coatings, providing not only very low friction but also much needed wear resistance in low-viscosity oils. With further development and optimization, these coatings may indeed prevent wear during sliding under conditions where low-viscosity oils are used. They can also provide low friction to help further increase fuel efficiency. Laser dimpling of selected engine components may also offer additional benefits in terms of reducing friction and thus increasing the fuel economy of engines. Some of these surface treatments and/or coatings will soon be applied on portions or segments of real piston rings and cylinder liners to further substantiate their effectiveness under conditions that closely simulate the actual engines. We also plan on producing these coatings on actual rings, liners, and other engine components and have them tested at Ricardo as well as at various OEMs.

Conclusions

Computer simulation studies to date have confirmed that using low-viscosity engine oils will increase fuel efficiency of future diesel engines. However, wear load and asperity friction will increase substantially. The use of low-friction and superhard coatings in engine parts and components may eliminate wear problem and enable the use of low viscosity oils so that the fuel efficiency of these engines is increased.

V. Autothermal Diesel Reformer

Diesel Fuel Reformer Technology

Principal Investigator: M. Krumpelt
Argonne National Laboratory
9700 South Cass Avenue, Argonne, IL 60439
(630) 252-8520; fax: (630) 252-4176; krumpelt@anl.gov

Technology Development Manager: Sid Diamond
(202) 586-8032; sid.diamond@ee.doe.gov
Technical Program Manager: Jules Routbort
(630) 252-5065; routbort@anl.gov

Contractor: Argonne National Laboratory
Contract No.: W-31-109-ENG-38

Objective

- Develop a device to convert diesel fuel into hydrogen-rich gas on-board a heavy duty vehicle in a small fuel processor.

Approach

- Evaluate engineering issues that need to be better understood with regard to diesel fuel reforming. The main issues are how to avoid pre-ignition and coke formation and how to achieve catalyst stability.
- Develop a fuel/exhaust-gas mixing device that will optimize diesel-fuel reforming process.

Accomplishments

- Completed design of a laboratory fuel/air/steam mixing test facility.
- Established collaboration with International Truck and Engine Corporation (ITEC).

Future Direction

- Complete construction of the test facility.
- Establish required sensors and instrumentation.
- Design and test fuel-air-steam mixing system.
- Conduct CFD simulation to confirm flow mixing.
- Conduct fuel injector tests
- Modify the facility for autothermal reforming tests
- Conduct autothermal reforming tests

Introduction

Converting diesel fuel into a hydrogen-rich gas has potential applications in auxiliary power units for heavy-duty vehicles and emissions control of diesel engines. ANL has developed a catalytic autothermal reforming process that may be used as a compact and potentially cost effective technology for diesel-fuel reforming. Because diesel fuel is more difficult to process due to high sulfur content, the reforming process may encounter pre-ignition and coke formation problems. Completely homogeneous mixing and preheating the air will mitigate these problems. This program will explore the feasibility of achieving the diesel-fuel reforming by optimizing fuel/exhaust-gas mixing dynamics. Several engineering issues, such as how to avoid pre-ignition and coke formation and how to maintain catalyst stability, will also be examined.

Results and Discussions

In FY 2003, we completed the test facility design and started construction. Figure 1 shows the schematic diagram of the facility, which consists of a fuel-injection assembly, simulated exhaust gas generating system, and fuel-exhaust-gas mixing apparatus. The proposed sensors and instrumentation for process measurement and control are also identified. We have also established the collaboration with International Truck and Engine Corporation (ITEC). ITEC will provide ANL their diesel-fuel injectors and fuel-injection controlling system.

Conclusions

This is a new startup program. In FY 2003 we have established the industrial collaboration and the overall program plan. The first year objective is to establish a laboratory test facility. The facility is partially constructed. In FY 2004, we will start fuel/exhaust-gas mixing tests to optimize the design of the mixing device. Numerical simulation will also be performed.

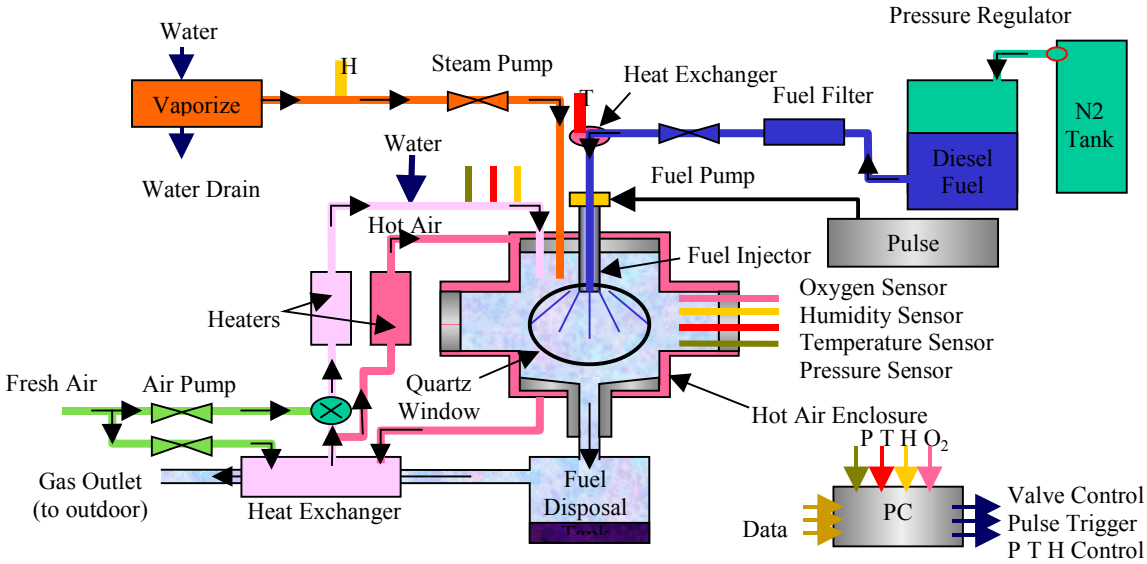

Figure 1. Schematic diagram of the diesel-fuel/air/steam mixing test facility

VI. EM Regenerative Shocks

EM Shock Absorber

Principal Investigator: J.R. Hull
Argonne National Laboratory
9700 South Cass Avenue, Argonne, Illinois 60439
(630) 252-8580; fax: (630) 252-5568; jhull@anl.gov

Technology Development Manager: Sid Diamond
(202) 586-8032; sid.diamond@ee.doe.gov
Technical Program Manager: Jules Routbort
(630) 252-5065; routbort@anl.gov

Contractor: Argonne National Laboratory
Contract No.: W-31-109-ENG-38

Objective

- Conduct experiment on a small-scale vehicle to verify the energy recovery from road induced vehicle motion.
- Develop simple models from available literature.
- Compare the experimental results with theoretical prediction.
- Develop stationary stand for testing and measurement of hardware to be installed in large vehicles.

Approach

- Increase magnetic field by experimenting with innovative electromagnetic shocks.
- Reduce bearing friction and increase efficiency.

Accomplishments

- Three different types of electromagnetic shocks with progressively better power generating capacities have been fabricated.
- These shocks have been mounted in an all-terrain vehicle in conjunction with existing shock. Power generated when the vehicle is driven over a sod field as well as over a 4x4 beam has been measured and analyzed.

Future Direction

- Use the electromagnetic shock as the only source of damping (i.e. leave the original shock with spring but no damping) and measure the power generated.
- Longer-term approach may switch to energy storage by hydraulic systems.
- Explore potential of developing technologies for dynamic control of vehicle.

Introduction

So far three different electromagnetic shock absorbers have been made: Mark 1, 2, and 3. In order to estimate the power generated by the EM shocks, these were mounted in an ATV as shown in Figure 1.

Figure 2 shows the front of the ATV with all the instrumentation for recording the voltage output of the ATV. Figure 3 shows one of the EM shocks (Mark 2) mounted in the ATV. The dynamics of the vehicle with respect to the EM shock absorber operation are shown in Figure 4. The vehicle is shown running over a 4×4 timber (Actual dimensions are 3.5×3.5 in.) about 8 ft. long, which was anchored to the ground in a field of cut grass. The arrowed lines with numbers 1 and 2 relate to the vehicle motion when the front or rear tires run over the 4×4, respectively.

Results

Mark 1 is the first design. It is quite big and heavy and when tested with a shaker (Figure 5), bearing friction was noticed to be so high that the damping force was masked by the inertia and friction force.

Peak power generated by this shock when the ATV went over a 4×4 beam was 7.4 watts. Again the insufficient magnitude of the power can be attributed to the bearing friction.

The next design of the EM shock was the rotary shock absorber (Mark 2). This shock absorber was tested in an electromagnetic shaker as shown in Figure 6 at 0.5 g. The results of the Mark 2 test are shown in Figure 7.

Figure 1. ATV used for EM shock testing

Figure 2. Instrumentation deck on the ATV

Figure 3. EM shock (Mark 2) mounted in ATV

The damping constant of this Mark 2 EM shock was measured to be 0.22 lb/in./sec or 38.5 N/m/s.

When mounted in the ATV (Figure 3.) and the vehicle is driven over a 4×4 beam, typical output response of the Mark 2 shock absorber is shown in Figure 8. The amplitude scales are modified to account for the 5:1 gain reduction of the tape recorder that was mounted on the vehicle. We can observe two large negative responses in Figure 8, which correspond to the front and rear wheels traversing the 4×4. The negative polarity is due to the mounting configuration of the rotary shock

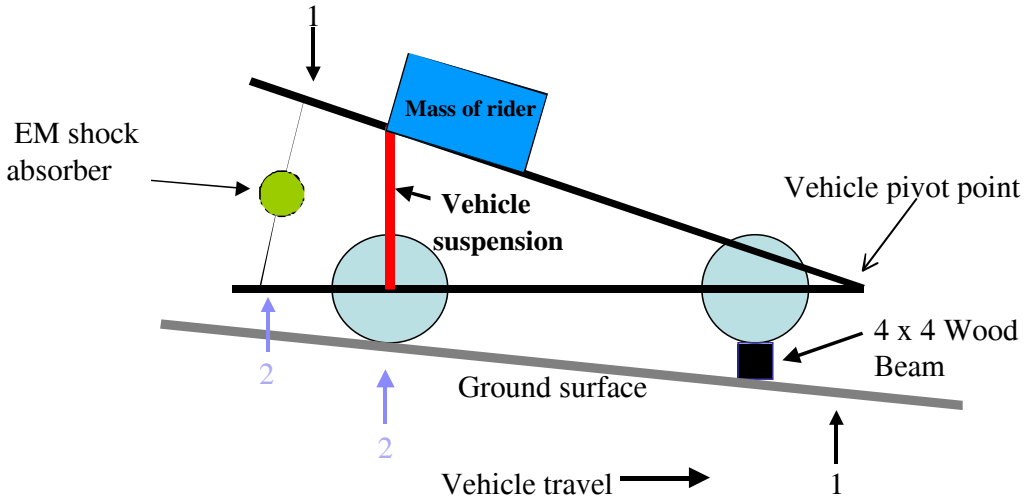

Figure 4. Vehicle dynamics

Figure 5. Shaker testing of Mark 1 EM shock

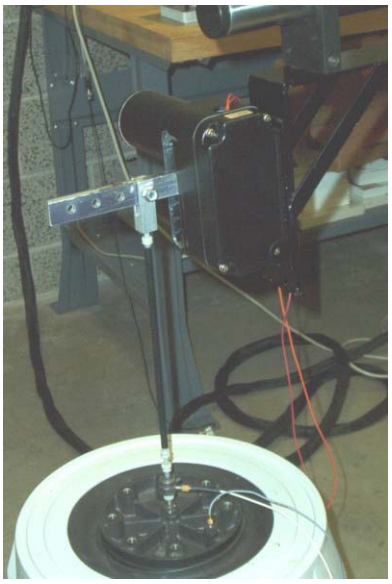

Figure 6. Shaker testing of Mark 2 shock

absorber on the vehicle. A downward motion on the shock absorber results in a negative output while an upward motion results in a positive output. The first output pulse, #1, is the result of the front wheels striking the 4 × 4, corresponding to the #1 arrowed lines of Figure 4. There is considerable rebound, as shown by the positive response immediately following the negative response. This is attributed to the response frequency of the vehicle-rider combination. Next we see an even larger negative response, #2, when the rear wheels strike the 4×4 beam, corresponding to the #2 arrowed lines of Figure 4.

Since the electric output of the shock absorber is terminated in a 1 ohm resistor, maximum power generated was calculated to be 88.8 watts. Now based on the stiffness measurement of the tires, suspension, unsprung weight, and sprung weight,

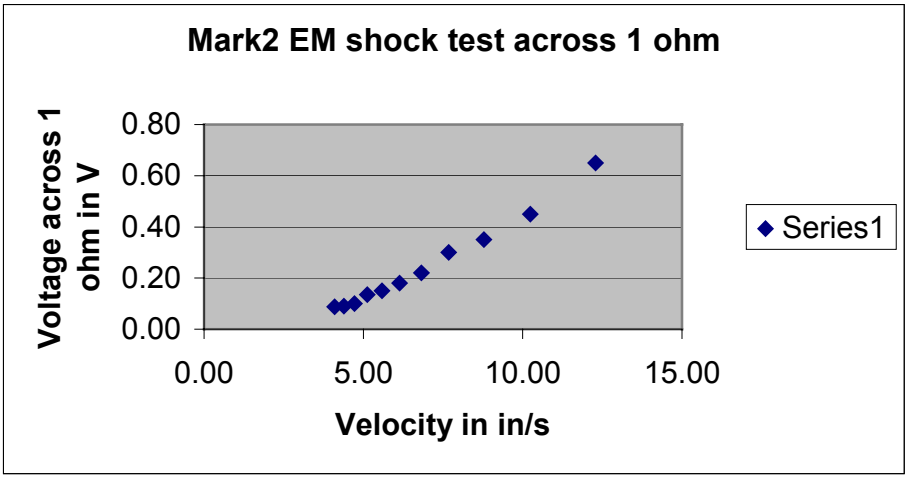

Figure 7. Shaker testing results of Mark 2 shock

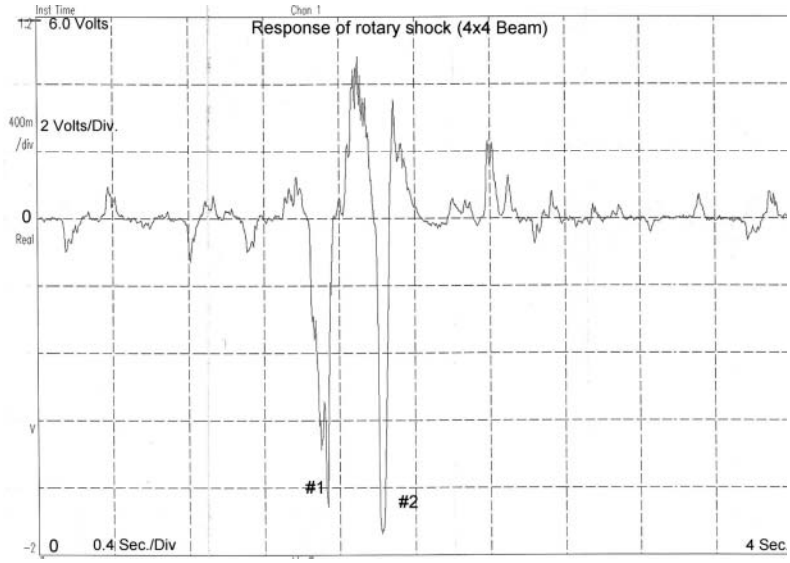

Figure 8. Response of Mark 2 (rotary) shock absorber transversing 4 × 4 beam

and damping constant of the suspension, theoretical simulation predicts maximum power of about 416 watts. The difference in theory and measurement can be explained by losses in bearings which called for further improvement of design. Subsequently Mark 3 has been designed and fabricated and currently is being tested. It may be noted that if the oil in the conventional shock is drained so that only the EM shock is providing the damping, then more power is expected to be generated. The ATV shock has been changed accordingly and currently experiment is being performed to measure the energy generation under such a condition. After the vehicle testing of the Mark 3 shock, shaker testing is planned to obtain the damping constant.

Discussion

Continuous improvement in the design and testing of the EM shocks is being made. Peak power generated during the traversing of the ATV over 4x4 beam increased from a meager 7.4 watts to 88.8 watts when the Mark 2 shock design replaced the Mark 1 design. Additionally, the suspension in the ATV has been modified to make the EM shock (the new design Mark 3) the primary source of damping and

not just supplementary damper. Using that configuration, based on the theoretical simulation, it is anticipated that the maximum peak power generated during the upcoming test of the ATV traversing over the 4×4 beam will be 625 watts (using the damping constant of Mark 2 and neglecting other losses). It may be noted that if an EM shock can be made with damping constant of the original suspension, then a maximum peak power of 3.33 kW is expected during the traversing of the 4×4 beam. The average power, however, is expected to be considerably less than the peak power.

VII. Joining Carbon Composites

Structural Characterization and Joining of MMC Components for Heavy Vehicles

Principal Investigators: J. Prucz and S. Shoukry
Department of Mechanical and Aerospace Engineering
West Virginia University
Morgantown, WV 26506-6106
(304) 293-4111ext.2314; fax: (304) 293-6689; Jacky.Prucz@mail.wvu.edu

Technology Development Manager: Sid Diamond
(202) 586-8032; sid.diamond@ee.doe.gov
Technical Program Manager: Jules Routbort
(630) 252-5065; routbort@anl.gov

Contractor: West Virginia University
Contract No.: EE50692

Objectives

- Quantify cost-performance tradeoffs associated with the development of Metal Matrix Composite (MMC) components for heavy trailers.
- Analyze multiple design and joining concepts for enhancing the potential benefits of employing MMC components in heavy vehicles.

Approach

- Assess the current state-of-the-art of technology development and commercial applications for advanced MMC materials.
- Design and analyze a critical structural component of a heavy trailer, such as a chassis I-beam, made of MMC or alternative materials.
- Model and analyze alternate approaches to joining structural components made of particulate MMC materials.
- Measure material properties of standard MMC specimens and structural characteristics of bolted joints made of the same MMC materials.

Accomplishments

- Integrated material –structural models predict marginal benefits and significant barriers to MMC applications in heavy trailers.
- Potential applications of MMC materials in heavy vehicles are limited to components identified as critical for either loadings or weight savings.

Future Direction

- Expand lightweight material-structural design concepts for heavy vehicles from the component to the system level.
- Validate innovative approaches for weight reductions in trailers, based on tailored materials, optimized geometries and fastener-free joining.

Introduction

Although recent advances in the area of Metal Matrix Composites (MMCs) have been spurred, mainly, by applications that require high structural performance at elevated temperatures, the heavy vehicle industry could also benefit from this emerging technology. Growing requirements of weight savings and extended durability are the main drivers for potential insertion of MMC technology into the heavy vehicle market. Critical elements of a typical tractor-trailer combination, such as highly - loaded sections of the structure, engine components, brakes, suspensions, joints and bearings could be improved through judicious use of MMC materials. Such outcome would promote the DOE's programmatic objectives of increasing the fuel efficiency of heavy vehicles, reducing their life cycle costs and pollution levels. However, significant technical and economical barriers are likely to hinder or even prevent, broad applications of MMC materials in heavy vehicles. The tradeoffs between such expected benefits (lower weights, longer durability) and penalties (higher costs, brittle behavior, difficult to machine) must be thoroughly investigated, both from the performance and cost viewpoints, before the transfer of MMC technology to heavy vehicle systems can be properly assessed and implemented.

Technology Assessment for MMC Applications in Heavy Vehicles

Metal matrix composite materials are formed, usually, of a low-density metal alloy, such as aluminum or magnesium, reinforced with particles, whiskers, or fibers of a ceramic material, such as silicone carbide or graphite [1]. Their performance is superior to that of the un-reinforced metal, especially with respect to higher specific strength and stiffness, higher operating temperatures, and greater wear resistance. The disadvantages of MMC materials are related, mainly, to their high cost and complex manufacturing processes, though two of their drawbacks relate also directly to their mechanical properties, namely lower ductility and lower toughness than corresponding, unreinforced metals [2].

High costs due to low production volumes, insufficient characterization data, lack of reliable models and standardized design, manufacturing and testing methods, remain to this date the major barriers to widespread commercialization of MMC materials. It is highly unlikely that drastic weight reductions can be achieved in heavy vehicle structures by using such materials. Continuously reinforced MMCs are unlikely to be economically feasible for the trucking industry, whereas discontinuously reinforced MMC's are attractive only for limited, low-volume applications, in selected components of a tractor-trailer system. Life-cycle-cost (LCC) studies and integrated material-structural designs, where material properties and geometric configurations are tailored to each other, are essential for developing cost-effective applications of MMC materials in heavy vehicles.

Weight Comparisons for Cross Beam in Chassis of Heavy Trailer

Chassis components contribute 73% of the overall mass of an empty van trailer (6,850 kg for a 48 ft-long trailer). About 47% of the total structural weight is contributed by the oak floor panels, as well as by the cross beams that support the floor. One set of such cross beams comprises simply supported I-beams evenly distributed along the central section of the van, whereas the other set consists of I-beams with overhanging cantilevers over the suspension rail.

The static loading scenario assumed for this analysis includes structural dead weight and a live load of 11 kN per wheel of a loaded fork lift that moves inside the trailer. The stresses and deflections associated with such loading were calculated for each of the above two groups of cross beams, along with the corresponding factors of safety.

The design criteria used for comparing different material candidates are:

- The factor of safety in flexure should not be less than 2.0.
- The deflections should not exceed the maximum levels that are currently achieved for steel cross-beams.

The candidate materials considered in this study for weight comparisons with reference to steel were aluminum, magnesium, carbon-carbon composites

and MMC LANXIDE, which is aluminum matrix reinforced with 55% silicon carbide particles.

Table 1 illustrates the minimum cross-section of a standard I-beam that is required for different materials to meet the above criteria, as well as the corresponding values of factor of safety and edge deflection.

Table 1. Alternate material solutions

Material	Yield Strength (MPa)	Section	Zx (cm^3)	Factor of Safety	Edge Deflection (mm)
Steel	550	120 × 64	42.8	4.4	3.55
Aluminum	240	152 × 89	116.0	5.2	2.43
Magnesium	150	178 ×	171.0	4.8	2.28
Aluminum Reinforced with 55% Silicon Carbide	145	127 × 76	74.9	2.0	1.56
Carbon-Carbon Composite (Carbo/Epoxy AS4/3501-6)	900	127 × 76	74.9	12.5	2.77

Table 2 illustrates a weight-based comparison of the same candidate materials for an I-cross beam in a van trailer, along with the cost of each material.

Table 2. Weight and cost-based comparison of candidate materials

Material	Density (kg/m^3)	Total Mass (kg)	Weight Saving (%)	Cost ($)
Steel	7850	1058.00	0.0	831
Aluminum	2700	644.96	39.0	1,292
Magnesium	2950	885.69	16.3	4,986
Aluminum Reinforced with 55% Silicon Carbide	1738	323.75	69.4	5,604
Carbon-Carbon Composite (Carbo/Epoxy AS4/3501-6)	1580	294.32	72.2	13,347

The results presented in Table 2 reveal that both MMC and carbon-carbon materials allow similar weight savings as compared to steel (about 70%) or aluminum (53%), but MMC materials are 85% more expensive than steel and 77% more expensive than aluminum. However, the cost of a MMC cross-beam is half that of a similar beam made of carbon-carbon composite. Furthermore, the cost penalty associated with the use of MMC materials can be reduced substantially through integrated material and structural design.

Design and Analysis of Bolted Joints

Three dimensional finite element models have been developed for three different types of joining techniques in order to compare the behavior of the MMC materials with other structural materials.

These models cover both single and double lap joint configurations, including load spreaders, or washers, inserted between the plates and the bolt head or nut. The contact interfaces between the jointed plates, between the load spreaders and the jointed plates, as well as between the bolt surface and the surrounding hole have been modeled explicitly, as illustrated in Figure 1 by the finite element mesh of a double lap joint.

An axial tension load was applied on the model, and the resulting stress field around the bolt was determined and analyzed. As one could expect, the results of the finite element simulation confirm the presence of bending of the jointed plates in single lap joints, caused by the load eccentricity between the two plates. This bending effect significantly reduces the contact stresses between the bolt and the cylindrical hole surface. However, high contact stresses develop around the hole in the case of double lap joints, as illustrated in Figure 2.

Parametric analysis of single and double lap joint configurations have been conducted over a wide variety of design parameters, such as the material properties of the jointed plates, the washer (load spreader) diameter, the clearance between the hole and the bolt, the diameter of the bolt, and its

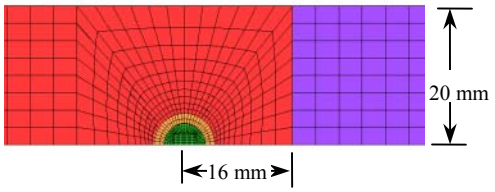

Figure 1. Finite element model of a double lap bolted joint

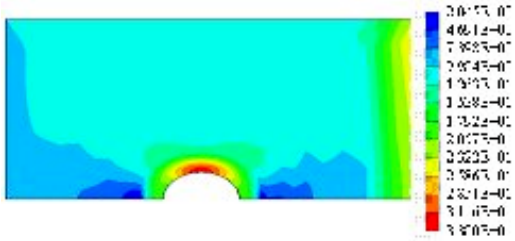

Figure 2. Von-Mises stress distribution around a hole in a double lap joint

tightening pressure. The main findings of this parametric study can be summarized as follows:

a) The average effective stress around the hole increases by about 75% when the bolt tightening force increases from 0 to 30kN.

b) The Young's Modulus of the connected plates has an insignificant effect on the stress distributions around the hole. The strain levels around the hole increase, however, as the Young's Modulus decreases.

c) In single lap joints, the effective stress around the hole increases when the bolt diameter or the washer diameter increases. This effect is, most likely, due to the bending associated with the asymmetric loading of such a joint.

d) The effective stress around the hole of a double lap joint with a 6 mm-diameter bolt decreases by about 70% when the diameter of the load spreader increases from 8 to 12 mm.

e) When the clearance between the hole and the bolt is increased from 0.02 to 0.15 mm, the level of stresses around the hole decreases by about 65%.

f) An increase of about 30% in the maximum stress around the hole is predicted when the bolt diameter is increased from 5 to 6.5 mm.

Failure analysis has been conducted for double lap bolted joints made of different materials, such as steel, aluminum alloy, and Al/SiC MMC with 30% and 55% volume fraction of Silicon Carbide reinforcement particles.

Figure 3 depicts the effective stress distribution around the hole before the onset of failure. The results confirm the expected drawbacks associated with the brittle failure of MMC materials. The MMC joint is predicted to fail in the "bearing" mode, where the rear wall of the hole that is in direct contact with the bolt is crushed without yielding. Moreover, the use of such MMC materials for the jointed plates may cost 12-14 times more than equivalent aluminum joints, with no performance benefits.

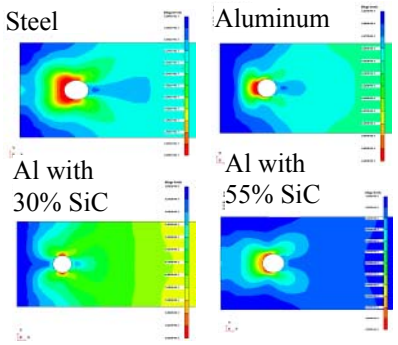

Figure 3. Stress distribution around hole before failure

Bonded single and double lap joints have also been modeled for extensive parametric studies over a wide range of adhesive and adherent material properties, as well as various geometric configurations. The main conclusions of this study can be summarized as follows:

a) The shear stress distribution along the overlap length becomes more uniform as the thickness of the adhesive increases, so that the maximum shear stress is reduced.

b) The shear stress at the free edge in the adhesive can be reduced significantly by tapering the outer adherent. For example, a 45° taper reduces the maximum shear stress by about 60%.

c) The addition of spew fillets at the edge of the adhesive can reduce by about 65% the average shear over the bond length of the joint.

Experimental Characterization of MMC Materials and Bolted Joints

Different versions of a particulate aluminum/silicon carbide MMC material marketed under the "LANXIDE" trademark have been tested for possible applications in heavy vehicle structures. The material characterization tests were carried out according to the relevant ASTM standards and ranged from micro-structural evaluation to hardness, thermal, elastic and strength properties.

The test results indicate that the brittleness of this MMC material degrades seriously its strength properties. However, the stiffness of this material is more than twice that of aluminum, while its Vickers hardness is also higher than that of aluminum (by

52% for 30% SiC reinforcement and by 37% for 45% SiC reinforcement). The coefficient of thermal expansion of this MMC material is lower than that of aluminum, most likely due to the low conductivity of SiC particles.

The quality of the LANXIDE material turns out to be highly inconsistent, while its machining is extremely difficult, expensive and time consuming. Such problems are likely to become major barriers to any structural application of this material in heavy vehicles.

A test matrix of 36 Aluminum and MMC specimen has been planned and carried out for experimental characterization of double lap bolted joints of different geometric configurations. Figure 4 illustrates a schematic drawing of the experimental setup used for testing double-lap bolted joints.

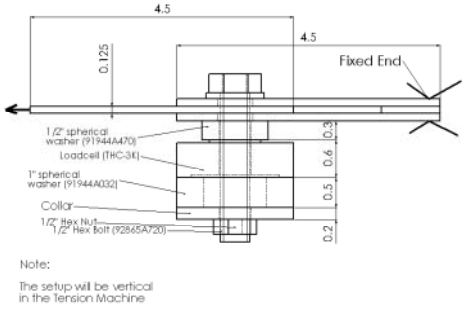

Figure 4. Test setup for bolted joints

The test results indicate that both the failure load and the mode of failure depend on two main aspect ratios:

1. The ratio between the width of the specimen and hole diameter (w/d).
2. The ratio between the distance from the edge of the joint to the center of the hole and the hole diameter (e/d).

The test matrix included specimens with "e/d" ratios varying from 1.2 to 5, for three different "w/d" ratios: 3, 4, and 8. Table 3 captures a summary of the various failure modes observed in these tests, as function of the "w/d" and "e/d" ratios of the test specimens.

Figure 5 shows photos of MMC joint specimens that failed either in the "net-section" or "bearing" modes of failure.

Table 3. Variation of failure modes with the geometry of joint specimens

e/d	w/d ratio		
	3	4	8
1.2	Shear out	Shear out	Shear out
2	Net-Section	Bearing	Bearing
3	Net-Section	Bearing	Bearing
4	Net-Section	Bearing	Bearing
5	Net-Section	Bearing	Bearing

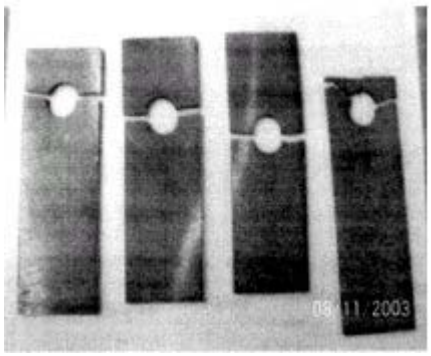

Net-Section failure (w/d=3)

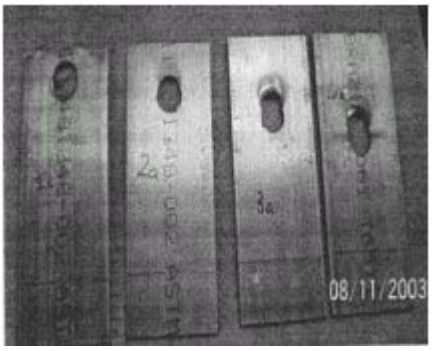

Bearing failure (w/d=4)

Figure 5. Failure modes of joint specimens

As the joint begins to fail, a substantial increase is observed in the tensile force applied on the bolt. This effect is probably associated with the piling up of crumbled material at the contact surface on one side of the bolt, as a result of the bearing mode of failure. The rise in the tensile force experienced by the bolt is more pronounced for higher values of the "w/d" ratio. For example, the bolt tension increases at the

onset of failure by 1,500 lb when w/d=3.0, but this rise is amplified to 4,500 lb when w/d=4.

Conclusions

The main technical challenge of joining particulate MMC components is their low ductility and poor workability. Since fiber breakage is not a concern with such materials, joining methods used for metal alloys are applicable also to particulate MMCs. However, the "over-design" necessary to prevent bearing failure in bolted joints is likely to diminish weight savings that might be enabled by the superior specific stiffness or strength properties of MMC materials.

References

1. Department of Defense Handbook: Composite Materials Handbook, Volume 4: Metal Matrix Composite, September 1999.
2. ASM International. Engineered Materials Reference Book, Second Edition, Material Park, Ohio, USA, 1999.

VIII. Analysis

A. Systems Analysis for Heavy Vehicles

Principal Investigator: L.L. Gaines
Argonne National Laboratory
9700 South Cass Avenue, Argonne, IL 60439
(630) 252-4919; fax: (630) 252-3443; lgaines@anl.gov

Technology Development Manager: Sid Diamond
(202) 586-8032; sid.diamond@ee.doe.gov
Technical Program Manager: Jules Routbort
(630) 252-5065; routbort@anl.gov

Contractor: Argonne National Laboratory
Contract Number: W-31-109-ENG-38

Objective

- Identify areas with significant potential for energy conservation in transportation, especially heavy vehicles, that could be facilitated by DOE-sponsored R&D

Approach

- Perform broad scope analysis, with cooperation from industry, to find set of promising areas;
- Conduct in-depth analysis to identify
  - promising new technologies,
  - fruitful areas for technology research and development, and
  - areas where objective analysis could support market penetration of new technologies
  - policy options that could encourage implementation of new technologies.
- Critically review ongoing DOE R&D efforts to assure they maintain their promise.

Accomplishments

- Achieved sufficient visibility and credibility to start receiving actual data on idling and equipment performance from other researchers, equipment manufacturers, and truck fleets and railroads.
- Completed and published survey of promising R&D areas for railroads and locomotives
- Analyzed and presented energy savings from dynamic brake energy recovery
- Presented truck idle reduction information at Truck Show and SAE Truck and Bus meeting
- Wrote 21CT idling reduction white paper
- Coordinated with DOE groups, EPA, DOT, states, and manufacturers, on idle reduction
- Provided input to decision making by EPA and CARB on idle reduction
- Visited TTCI and U of I
  - Attended and presented at U of I Railroad Environmental Conference
  - Attended RSI and other trade conferences
- Observed Green Goat, DDHS demonstrations

- Attended EPA Smartway rollout

Future Direction

- Continue work in idling reduction
  - All-stakeholder meeting
  - Comprehensive report on idling reduction
- Complete analysis of technology needs for locomotive dynamic brake energy recovery
- Investigate options for domestic and low-carbon production of liquid transport fuels
- Continue critical analysis of selected DOE projects

Introduction

Transportation energy research today is concentrated on long-term solutions for passenger cars. However, the potential for increased efficiency, decreased emissions, and reduced dependence on imported oil remains high for all time frames in the heavy vehicle sector. The technologies developed for light-duty vehicles may not be applicable to heavy vehicles; it is therefore important to continue our R&D efforts to reduce the impacts from use of trucks and trains. Analysis at ANL is aimed at identification of the most fruitful areas for further investigation.

Discussion and Results

ANL has focused effort in several areas. These are idling reduction, locomotive and railroad energy conservation, alternative domestic fuels, and critical project review.

Idling Reduction

It is important for ANL to revise its study of idling reduction. This study is the definitive reference, with many other groups using our results. However, since publication, the available options have changed (storage devices are defunct, inverter-chargers are available, and electrical options have evolved). In addition, actions by the EPA distort the picture (they support only electrical options, neglect impacts of electricity generation, and promulgate misleading information). It is also important to extend the analysis to other transport modes, which also idle, and may share many similarities in equipment needs (locomotives, buses, inland marine).

ANL will continue analysis of heavy vehicle idling to identify R&D needs. Desired tasks include study of equipment requirements, energy use and emissions for alternatives, regulations, emissions trading, and costs (including wear from idling), as well as information dissemination. The analysis will be extended to inland marine and off-road vehicles. ANL will continue to attend meetings and provide input on work related to idling reduction, in order to provide information and help OFCVT monitor research needs and progress in this area.

It is appropriate for DOE to facilitate coordination among the many groups involved in idling reduction activities. The are several groups involved at DOE, including OFC&VT Systems studies and the MET (Diamond), the Advanced Vehicle Testing Activity IR Demonstration (Slezak), Fuel Cell APU development (Garbak), and the Maryland locomotive APU demonstration. Other stakeholders include the 21st Century Truck Partnership, the EPA (which funded a plug-in project [EPRI] and electrification demonstrations [Idle-Aire], and launched its SmartWay program), DOD (currently developing a quiet APU), several states (NYSERDA is funding electrification demonstrations [Idle-Aire and plug-in], CARB has proposed regulations, and Iowa is performing a study), and trade and manufacturer organizations (DIRP, TMC, and the newly proposed manufacturer organization). A broadly based national conference is being planned to facilitate communication among these numerous and diverse groups, who are currently duplicating effort and working at cross purposes.

Locomotive and Railroad Energy Conservation

As a result of the locomotive emissions workshop and subsequent working group studies, ANL published a compilation of railroad R&D needs and

selected several areas for further investigation. These included dynamic brake energy recovery, freight car drag reduction, and reduction of idling.

Dynamic brake (DB) energy recovery: During dynamic braking , freight locomotives reduce the train's large kinetic energy by reversing their electric motors and generating electricity, most of which is sent through resistors to dissipate the energy in the form of heat. This practice is common to electric locomotives, such as those used in Europe, and diesel-electric locomotives, used in the U.S. It is well-known that this wastes a significant quantity of energy, and recovery would be desirable. As with automobiles, brakes that recover energy are called regenerative. Line-haul trains spend about 10% of their time in DB. BN estimates that 20% of the energy consumed in a cross-country run is dissipated during dynamic braking. However, the rate at which the energy would need to be recovered, and the necessity of a suitable storage medium have been technical barriers.

ANL scoped out the problem and considered the technical feasibility of several options for recovery of dynamic brake energy. Any of the devices could be either on the train (in the locomotive or in a tender behind it) or by the wayside. An on-board unit could be housed on an un-manned unit (slug). Energy storage is the key difficulty for dynamic brake energy recovery. There are several types of mechanisms that could be considered for storage of energy recovered from dynamic braking. These include flywheels, ultracapacitors, batteries, and chemical reactions. Important considerations for evaluating these mechanisms include rate of energy transfer, energy storage capacity, mass, volume, safety, and cost. In addition, any device placed on the train must be able to endure significant vibration over long time periods. Flywheels are already being used or proposed for both on-board and wayside applications (the London Underground is installing 1 MW flywheels at stations and the ALPS program is planning a 3 MW on-board unit).

The storage medium requires both high storage rate and high total energy storage capacity. The rate turns out to be a very important and difficult constraint. Combinations of devices could enable suitable energy storage. As an alternative to local storage, it is possible to consider dumping the power onto the local electrical grid.

A wayside unit could achieve a larger capacity factor than an on-board system and avoid concerns about large storage system mass and volume on the train.[1] This is the result of a key advantage for trains: trucks can go anywhere, so they need to slow down or stop at a large number of locations. Trains, however, are restricted to move on a very small number of routes– i.e. their tracks. Furthermore, the hills (and stations) are always in the same place (trivial but crucial). Therefore, a wayside unit could be put where needed (because it would always be needed in the same place) and service all trains coming by, recovering energy from the downhill trains and providing it to the ones going up. The result is a much higher capacity factor, greatly improving the economics for the installation.

Regenerative braking of freight trains with wayside recovery stations warrants in-depth investigation. We examined the case of one hill that many coal trains go over (Crawford Hill, NE) to get to eastern markets. Each train uses 20 MWh used round trip, and up to 17 MWh could be recovered theoretically. Currently, helper locomotives are needed. Their use is labor-intensive and time-consuming because you need to stop the train to add/remove locomotives. A wayside unit would have high utilization and could recover energy from loaded and empty trains, about 40 per day each way. We estimate that road locomotives in the U.S. could generate up to 7,500 MW, the equivalent of about 8 large electrical power plants. It would take about 0.6 Q or 100 million barrels of oil to generate this much power annually. We propose to further examine transfer and storage mechanisms and to explore economics for both wayside and on-board systems.

Freight car drag reduction represents another area of investigation. Empty coal cars are reported to have 2.5 times as much drag as loaded ones, and they move at high speed, so losses are greater. Drag could be reduced by covers, but development of maintenance-free covers has thus far proven to be problematic. BN estimates that about 300 million

[1] Another way to achieve a higher capacity factor would be to install regenerative braking on short-haul units that made frequent stops.

gallons of fuel are used annually to move coal trains, and 15% of the energy is dissipated due to drag. Of the 34 million gal/yr attributed to drag from empty coal cars, 21 million gal/yr could be saved with covers. Similarly, the new double-stack container trains have large gaps between cars, causing high drag coefficients. Modification of design could reduce drag. Research in this area could provide a high return.

Alternative Domestic Fuels

ANL has identified for study several possible novel schemes that could supply liquid fuels for heavy vehicles in the future, utilizing of domestic (or Canadian) feedstocks, including coal, tar sands (already imported in large quantities as bitumen), biomass, and possibly CO_2. The study objective is to identify technical pathways for production of clean liquid fuels without imports, in a way that minimizes carbon emissions, energy use, and economic costs. The elements of the work include a novel liquid fuel supply assessment literature survey, identification of promising options, evaluation of technical and economic feasibility, and evaluation of production and delivery schemes.

H_2 may not be the ideal future fuel for heavy vehicles. Our objectives are to reduce U.S. dependence on imported fuels, to reduce emissions of CO_2, and to retain convenient, liquid fuels and affordable vehicles. Domestic liquid fuel alternatives include biofuels, and liquids derived from coal, tar sands, oil shale. North America has lots of coal, oil shale, and tar sands. Conventional conversion to liquids has low yields and produces large quantities of CO_2, because much of feedstock goes to H_2 production. These hydrogen-poor feedstocks could instead be upgraded with H_2 produced using nuclear power (by electrolysis or thermochemically) to reduce net carbon emissions from liquefaction. Nuclear power is suitable for producing H_2 on large scale, but H_2 transport and storage are expensive; therefore local use is preferable. Our scheme proposes co-located liquefaction and hydrogen plants, to enable the local utilization of H_2 produced efficiently on a large scale, without the technical and economic pitfalls of transportation, distribution, and storage. ANL will evaluate this option.

Liquids could also be produced from waste carbon dioxide using nuclear power. The CO_2 could be recovered from power plants and large factories; there would be no net carbon emissions from combustion of liquid fuels produced from CO_2, and no imports would be required for their production. The conceptualized process begins with the reaction of CO_2 with lithium to form carbide (exothermic), followed by reacting the carbide with water to produce acetylene (exothermic). The acetylene would then be used as a feedstock for production of S-free liquid fuel. The reactions are as yet unspecified, but would be simpler than those involved in current petroleum refining processes. The lithium would be regenerated by electrolysis using nuclear power. Nuclear power would also generate the small amount of H_2 needed to produce the acetylene. Complete analysis of this concept is needed, followed by laboratory demonstration, if feasibility is promised.

Critical Project Review

In FY 2003, L. Gaines attended program reviews at ANL and ORNL. The functions she performed included critical review and facilitation of coordination among laboratory programs. ANL will continue its critical monitoring of selected OFCVT experimental projects at the discretion of the program manager. This activity is still necessary, for both new and continuing projects. It is also important to evaluate the potential of these projects for energy and petroleum savings as well as emissions reduction as data are developed. Therefore, project managers will be requested to submit data for analysis. For well-established projects, it would also be desirable to develop cost data to ensure economic viability as well as technical feasibility. Analysis of ORNL-developed composite manufacturing techniques and comparison to processes for production and fabrication of competing materials would be of particular interest. Results could be applied to truck and/or trailer

System	Energy saving (gal/d)	Annual savings ($1000s)	Cost ($1000s)	Payback (months)
Start/stop	36	15	7.5-15	6-12
APU or DDHS	60	25	25-35	12-17
Plug-in	50	19	4-12	3-11
Green Goat	291	122	200	20
Basis: GP38 -2 with EPA switcher cycle for all technologies, 330 d/y, 50% idl e replacement by AESS (will be less in cold climate), 90% by APU, DDHS, or plug -in unit, .05 gal oil used/gal fuel, $0.10/kWh				

components and rail cars. In conjunction with this, ANL would estimate the cost of mass reduction, evaluate the best current information on fuel economy as a function of mass reduction, and estimate the fuel price at which mass reduction pays.

Conclusions

Locomotive idling reduction devices are being accepted and installed in large numbers by industry. These devices meet the needs of the railroads quite well, and all have short payback times (see table on previous page).

No development by DOE is recommended in this area. However, idling reduction devices for trucks are not doing as well. Installation rates remain fairly low, and equipment manufacturers seem to be struggling. The available devices all have at least one of the following drawbacks: too expensive, too big/heavy, too noisy, don't supply all required functions, or not available where and when they are needed. There is significant potential to improve this situation via research on smaller, lighter, cheaper auxiliary power units, as well as truck electrification options. Financial incentives such as weight waivers, fuel and excise tax waivers, tax credits, low-interest loans, leasing programs, etc. could boost introduction of these technologies. In addition, education is still required.

Another factor slowing the introduction of idle-reduction technology on trucks is the uncertain and volatile regulatory environment. Various states are developing different idle-reduction restrictions, equipment requirements, and inconsistent policies. There is no nationwide guidance to help craft a consistent set of state rules and policies. In addition, national legislation has been proposed that could restrict the types of devices allowed, and could favor some over others. These factors create a significant risk to the truck-owner that the system he chooses might not even be permitted in some states after it is installed. These considerations deter purchases. Therefore, in addition to specific technology development, it is important for DOE to bring all of the stakeholders together, and to continue its analysis to pull together all of the relevant reports, draft rules, proposals, demonstrations, and other program elements so that — if not a coordinated national effort — at least a harmonious mix of programs can be fostered.

Buses are another fruitful area for idle-reduction. In particular, school and tour buses idle at local schools and at national monuments and museums, with obviously harmful emissions. Although the total potential for energy conservation is less than for trucks, because the sector is smaller, similar technologies are applicable, and so the research can be easily extended to include this very visible sector. Off-road vehicles, whose primary function is often not transportation, should also be examined to see what the potential is for savings; these vehicles may have unique challenges and opportunities because of their varying functional equipment and duty cycles.

B. 21st Century Locomotive Technology 2003

Field Project Manager: L. Salasoo
GE Global Research
1 Research Circle, Niskayuna, NY 12309
(518) 387-5000; fax: (518) 387-6675; salasoo@crd.ge.com

Technology Development Manager: Sidney Diamond
(202) 586-8032; sid.diamond@ee.doe.gov
Field Technical Manager: Jules Routbort
(630) 252-5065; routbort@anl.gov

Contractor: GE Global Research
Contract No: DE-FC04-2002AL68284

Introduction

The goals of the 21st Century Locomotive program are to research freight locomotives that are 25% more efficient by 2010, while meeting Tier 2 emissions standards. The technology state-of-the-art will be dramatically advanced at both the diesel engine and locomotive system levels. This 2003 annual report addresses work on locomotive system developments for 15-20% efficiency improvement, in the areas of energy management and optimization (tasks 3, 4 and 5 of the program) including capturing and storing regenerative braking energy, combined with fuel optimization control that takes advantage of route, terrain, and train characteristic data.

The objective of the locomotive system developments is to develop and demonstrate a modular commercial energy storage unit and associated energy management system, including fuel optimizer software, for an advanced hybrid locomotive. The goal is a 760 million gal/yr reduction in fuel usage. This unburned fuel directly translates into ~9 tons of emissions avoidance. Task 3 is to develop and test advanced modular energy storage and energy management subsystems to recover braking energy in a diesel-electric freight locomotive. Utilization of the braking energy will displace a significant portion of the overall energy requirement from the diesel engine and produce significant fuel savings without compromising performance. The first milestone will be the demonstration of the advanced energy management system (EMS), which consists of a power electronic interface to regulate the interchange of energy between the energy storage system (ESS) and the locomotive main electrical bus, and a microprocessor-based controller which commands the power flow to and from the ESS, the diesel engine, and the braking grid resistors. The advanced hybrid locomotive EMS will be demonstrated on the locomotive test track at GE Transportation Systems using GE-provided, off-the-shelf energy storage units. In addition advanced energy storage system modules will be developed and tested.

For Task 4, advanced locomotive system controls, including a novel fuel-optimal trajectory generation system, will coordinate throttle setting, energy storage and recovery, and braking, providing additional synergistic fuel savings over a hybrid system alone. The optimization software will exploit knowledge of the route ahead, track speed limits, required arrival time, on-board energy storage state, and other constraints to minimize total fuel consumed. The goal is to demonstrate on a test track a locomotive with fuel optimizer control algorithms.

The objectives of Task 5 will be to demonstrate a hybrid locomotive with full-scale energy storage modules and a fuel optimizer. The goal is to perform advanced hybrid locomotive system tests and demonstrations on a test track, incorporating the intelligent fuel optimization controls developed in Task 4. Energy storage will provide extra degrees of freedom to the optimizer; the combination of these technologies has the potential to produce synergistic benefits beyond their separate contributions.

Hybrid Locomotive Modular Energy Storage and Energy Management

While the fundamental proof-of-principle demonstrations of hybrid locomotive operation have been carried out prior to this program, development is required in the areas of energy storage system technology to develop locomotive-worthy systems with high performance in terms of energy storage capacity and power transfer capability. Hand-in-hand with the development of the energy storage system technology, development of appropriate energy management techniques is required to realize the potential high performance of the the advanced energy storage technology, and to ensure operational life of the energy storage.

Energy Storage

Recent tests by GE of today's energy storage technologies for hybrid locomotive proof-of-concept have shown that more development is required to get energy storage systems suitable for locomotive applications. Development is required in the energy storage system capabilities through a combination of improved energy storage technology and also system technology that interfaces the energy storage to the locomotive. The 21st Century Locomotive Hybrid Systems task proceeds to address this systematically by determining the energy storage system specification, identifying parameters and capabilities to be advanced in this program, and then implementing these.

Determination of the hybrid locomotive advanced energy storage requirements is based on railroads' hybrid locomotive application requirements, GE's experience with existing systems developed before this project, and dialog with battery vendors. Discussion with two Class 1 railroads Burlington Northen and Santa Fe (BNSF) and Union Pacific (UP) revealed a longtime desire to utilize the "wasted energy" that is produced when diesel-electric locomotives carry out dynamic braking, and considerable enthusiasm that the hybrid locomotive concept can provide such utilization. As a result, specific types of candidate hybrid locomotive missions were identified. Hybrid capability can provide lower life-cycle cost through improved fuel economy for heavy-haul road locomotives performing coal haul, grain haul, intermodal transportation and pusher applications. A specific coal haul mission in the Powder River Basin district of Wyoming and Nebraska was identified as a typical example: a 100-coal car train with 12,000 hp locomotive power (19,000 tons total) hauling coal 215 miles from Caballo Junction WY to South Morrill NE (Figure 1).

The initial section has many steep uphill grades of 1% or higher, followed by generally downhill section descending approximately 1,400 ft altitude. The descent requires much dynamic braking by the locomotives to avoid exceeding the speed limit: this is the energy that would be captured by a hybrid locomotive. As the empty coal train returns from South Morrill it has to climb the same 1,400 ft altitude and the stored hybrid locomotive energy is used to displace significant amounts of fuel that would otherwise be used. On the final section returning the empty coal cars to the mines in the Caballo Junction area, the hybrid energy storage system would be partially recharged during the downhill grades. This stored energy would be applied to displace fuel used when the loaded train begine the climb from Caballo Junction on the next coal haul.

In addition to the analysis of the candidate missions provided by the railroads, experience from GE's recent proof-of- hybrid-locomotive-concept tests provided input to the development of hybrid locomotive energy storage system requirements. The energy storage system thermal performance is very important and baseline thermal system performance was determined by testing the existing hybrid system that will be used for the advanced energy management system track test in the next year. Key requirements are energy storage system power and energy performance, operating environment capability and operational life. The detailed requirements were discussed with advanced battery manufacturers, and studies were initiated to address battery system technology developments that would meet the hybrid locomotive requirements. These studies will be completed in the 1st FY2004 quarter and lead to a 1-year development of evaluation battery system modules. Preliminary discussions with the vendors suggest that significant improvements in battery cycle life, charging power capability and thermal management are feasible.

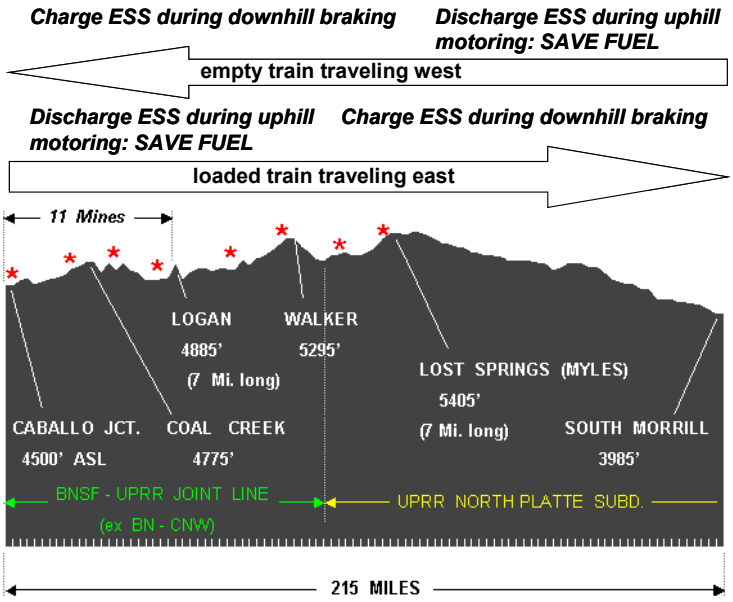

Figure 1. Example hybrid coal haul mission

The advanced battery system modules developed under this program will be evaluated on a bench-test level and subsequently on a full-scale locomotive platform. Evaluation of other currently available lithium-ion battery technology systems has been initiated. One vendor's 42-V lithium-ion battery modules were tested for electrical characteristics such as Amp-hour capacity, open circuit voltage and terminal voltage variation with load, to yield data such a shown in Figure 2. It was found that the measured capacity was significantly below the rated capacity. The axis of Figure 2 is labeled with a revised state of charge (SOC). A key issue is that the charging power capability is significantly less than the discharge capability, while the hybrid locomotive application requirements are for higher charging than discharging power capability.

Design of Hybrid Locomotive Energy Management System (EMS) Controls

EMS controls are under development to have adequate capabilities to obtain high performance from the advanced energy storage modules developed in the earlier tasks. The approach is to identify additional features and capabilities that are required in addition to existing capabilities developed by GE prior to this project. Additional EMS capabilities to be developed were identified as temperature compensation and computed energy storage state recovery.

The cycle life capability of hybrid energy storage batteries is very important to the commercial success of a hybrid locomotive system. The cycle life is compromised when the energy storage batteries are operated outside their ratings and at high temperatures. Many battery systems will give good performance (in the short term) at temperatures close to the operating temperature specification; however internal degradation mechanisms proceed faster at higher temperatures, leading to premature battery failure. Therefore it is important to keep the battery pack temperature below long-term operating limits. High level charging and especially discharging operation will heat the batteries, and the approach developed here reduces the risk of overheating.

The control of hybrid energy storage batteries by the EMS must identify when the energy storage is receptive to charging and when it is capable to discharge stored energy. If energy storage batteries are overcharged past their maximum limit, undesirable chemical reaction may be caused, depending on the battery chemistry. Drying out of the electrolyte may be caused, internal gas generation may occur, or the battery temperature may be elevated. These effects may immediately degrade hybrid energy storage battery capability to store and deliver energy, as well as cause long-term reduction in battery life. If energy storage batteries

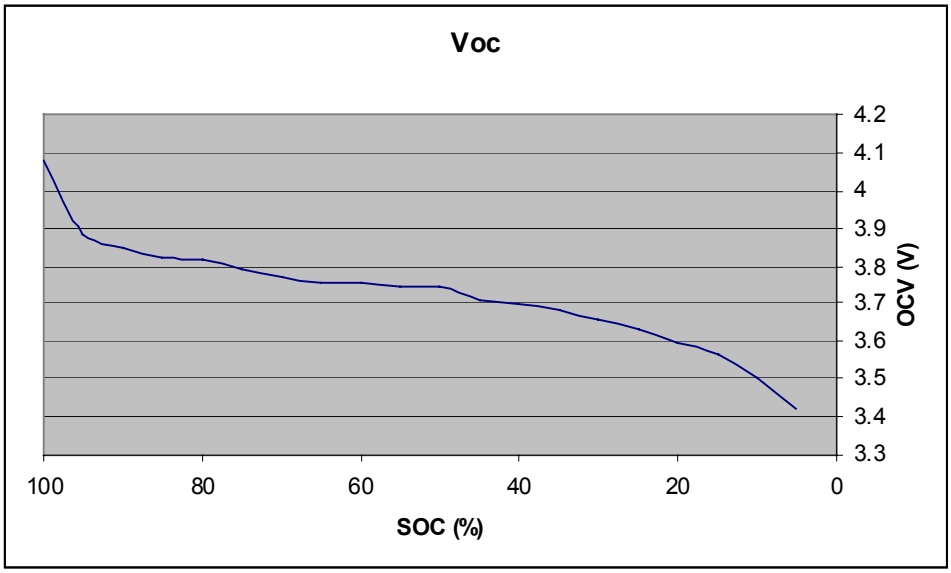

Figure 2. Lithium-ion cell open-circuit voltage characteristic

are discharged past their minimum SOC limit, rapid degradation in the battery immediate performance and battery life is seen. The advanced battery technologies that give higher energy and power performance are more sensitive to overcharge and overdischarge operation. Therefore the EMS must track the energy storage battery state so as to minimize overcharging and overdischarging. GE has developed one technique for tracking energy storage battery state irrespective of interfering factors in the locomotive environment. Initial tests of several candidate battery state algorithms were carried out with existing data and promising approaches were identified for subsequent development.

Fuel Use Optimization

The overall goal of this task is to develop and demonstrate advanced algorithms for driving and energy management of freight locomotive systems, both conventional and hybrid, to reduce fuel consumption. The algorithms are prototyped in a simulation environment, to demonstrate potential energy savings, with and without hybrid storage. Subsequently the algorithms will be implemented on a hybrid test locomotive platform on the GE Transportation test track at Erie, PA or other suitable test environment to demonstrate projected energy savings.

An existing flexible and configurable, system-level modeling environment for freight trains has been adapted for use in this program. The model includes dynamic and steady state model for a multiple locomotive consist, including power units, trailing cars and their loads, which takes throttle settings (and environmental variables like temperature and altitude) as input and produces numerous outputs, e.g. positions, velocities, power generated, fuel consumed per unit time. The track is modeled, including grade and drag effects from wheel-rail interactions, as is energy storage, including dynamic power limits and capacity, and how it is coupled to locomotive propulsion system. The model also includes means to identify required parameters from active tests and/or passive monitoring from locomotive data, on-line, with minimal or no train driver interaction.

It is necessary to have means to automatically determine particular train parameter values to make the ultimate system practical in the locomotive world. Techniques have been developed for performing such parameter identification to automatically determine the number of locomotives in consist, estimate train mass (with and without locomotives), determine combined effect of grade and drag, and estimate the fuel efficiency characteristics from internal power and periodic fuel tank refills.

The need to have such methods may seem counter-intuitive, in that one would think this data to be

available in the process of making up the train. However, in the real world, it is highly undesirable to rely on crews to enter data (like number and type of locomotives) and load factors are known only approximately. Even when the track data-base is known, the effective grade load depends on how the train is distributed behind the power consist. Finally, a lot of variation results from changes in weather, track condition over time, etc. Knowing all these parameters and how they vary over a route is vital to determining optimal driving strategies. A variety of techniques is utilized to determine the train mass, the prevailing drag and correctly identify the number of locomotives in trail within a few minutes of driving. The identification methods have been validated and integrated as part of the modeling environment for use in this study. A successful field test carried out a correct blind identification of the number of locomotives in a consist and also estimation of the train mass (Figure 3).

The figure shows the test with a 8,175-ton train. At 500sec the estimator made a first estimate of 14 million lb, which was improved by the next iteration at 1,000 sec that halved the remaining error. Ultimately the error is reduced to approximately 1%. Thus within several minutes, a high-quality parameter set is available for fuel optimization.

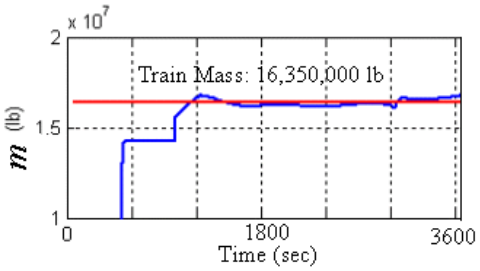

Figure 3. Field identification of train mass

Conclusion

This report covers progress in the first three project quarters. Hybrid system tasks are in progress to develop locomotive-specific high-performance hybrid energy storage systems and energy management systems. The development of fuel optimizer components has made good progress.

IX. Particulate Matter Characterization

Morphology, Chemistry, and Dynamics of Diesel Particulates

Principal Investigator: K.O. Lee
Argonne National Laboratory
9700 South Cass Avenue, Argonne, IL 60439
(630) 252-9403; fax: (630) 252-3443; klee@anl.gov

Technology Development Manager: Sid Diamond
(202) 586-8032; sid.diamond@ee.doe.gov
Technical Program Manager: Jules Routbort
(630) 252-5065; routbort@anl.gov

Contractor: Argonne National Laboratory
Contract No.: W-31-109-ENG-38

Objective

- Characterize the morphology, microstructure, dimensions, and chemistry of light-duty diesel engine particulates

Approach

- Provide soot samples collected from the exhaust system of a light-duty diesel engine using a thermophoretic sampling device, examine the morphology of the samples, and provide images using a transmission electron microscope (TEM).
- Measure particle sizes using the data acquistion/image processing systems and analyze the graphitic structures of the particles using a Raman spectroscope.

Accomplishments

- A novel thermophoretic sampling system was developed to sample soot particles from a light-duty diesel engine.
- The sizes and microstructures of diesel particulates were measured at various engine-operating conditions and theoretically verified their accuracy.
- Analysis for fractal geometry of diesel particulates standardized the morphology and shape by measuring fractal dimensions.
- The motion pictures of an aggregate particle were first demonstrated to reveal the real three-dimensional shapes of an aggregate particle.

Future Direction

- Investigate the effects of diesel engine exhaust components and fuel properties on particle morphology and sizes.
- Characterize the morphology of gasoline engine particulates.

Introduction

Accurate analysis of diesel particulate matter is an important issue to diesel engine and aftertreatment system manufacturers, and government agencies that regulate particulate emission standards or manage energy-efficient engine/vehicle-development programs. Undoubtedly, the impacts of diesel particulate matter on human health have brought increasing concerns to the public in recent years. Upon increasing needs for detailed research on these challenging issues, numerous investigators have attempted to analyze the sizes and structures of diesel particulates in several different ways [1–4].

However, most of commercially developed size measurement instruments have uncertainties in measurement accuracy. Over the measurement accuracy issue, an important question is also brought to technical communities; do the particle sizes measured by commercial size measurement instruments represent the actual dimensions of diesel particulates? Indeed, most of them provide particle dimensions, based on aerodynamic behaviors of sampling particles, which assumes the particles in measurement are perfectly spherical in shape [5].

In this project, therefore, the physical dimensions of diesel particulates were measured in terms of the radius of gyration of aggregate particles and the diameter of near-spherical primary particles. Fractal analysis was performed to standardize the morphology of particulates emitted from a light-duty turbocharged DI diesel engine. All these analyses were carried out, owing to the successful development of a novel thermophoretic sampling system and an image processing/data acquisition system that can be applied to internal combustion engines. The detailed internal microstructures of diesel particulates were observed at high TEM magnifications, and further analyzed to find the atomic structures of graphitic soot particles by using a Raman scattering spectroscope.

Experimental Descriptions

Thermophoretic Sampling Apparatus

For particulate sampling, a series of thermophoretic sampling system was installed on a rigid platform near the exhaust manifold. A custom-designed sampling chamber was connected to the exhaust manifold through a stainless steel tube and an on/off shutter valve that controls the release of exhaust emissions from the engine to the sampling chamber. Fine TEM sampling grids were used to collect soot particles, which were attached to a grid holder on the tip of probe. The sampling system was then activated by controlling a series of solenoid valve and electronic timing/trigger unit. The sampler collects particulates from the exhaust stream within a specific residence time, which was optimized to collect a sufficient number of particles for analysis, and to avoid possible particle overlapping on samples.

Diesel particulates were sampled at engine speeds of 675 rpm (idling), 1,000 rpm, 2,500 rpm, and 4,000 rpm with various loading conditions from 0% to 100%. EGR rates and equivalence ratios were also monitored to maintain constant values during each experiment. Particulates were then collected on the sampling grid by thermophoresis effects, which are driven by the temperature gradient generated between the hot exhaust stream and the near-room temperature grid surface.

TEM Analysis

The particulate samples were observed and photographed using a Philips CM30 TEM. The TEM micrographs were then digitized with a high-resolution closed-coupled device (CCD) camera and a customized image processing/data acquisition system to analyze detailed morphological properties, such as the primary particle diameter, radius of gyration, and fractal dimension. Detailed descriptions of this analysis technique can be found elsewhere [6,7].

Results and Discussion

Particulate Morphology

Figures 1 (a) and (b) are TEM photographs of the diesel particulates sampled at 1000 rpm and 25%, 75% engine loads. As seen in the figures, diesel particulates appeared to consist of an agglomeration of numerous spherical primary particles. These aggregate particles represented a variety of different shapes, from near spherical to stretched chain-like. The aggregate particles were distributed in a wide range of size — from tens of nanometers to a few microns. It is quite challenging to measure the sizes

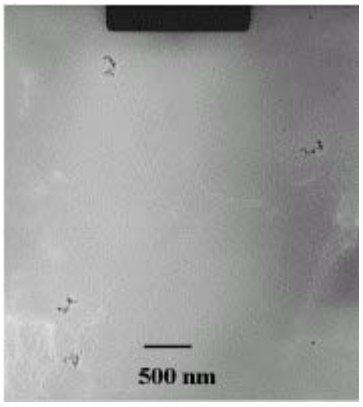

(a)

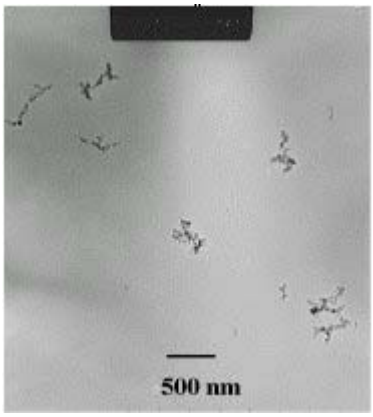

(b)

Figure 1. TEM photographs of particulates sampled at 1,000 rpm at (a) 25% load, (b) 75% load (magnification of 17,000X)

of those stretched chain-like particles with an approximation that they represent the same aerodynamic behaviors as spherical particles. Indeed, commercial instruments use the approximation.

Significant differences in morphology were observed depending on the engine load. Figures 2(a) and (b) show typical TEM micrographs of diesel particulates sampled at 780 rpm/0% load (idling) and 2,500 rpm/70% load. At the low load, many particles appeared to be nebulous in morphology. It is speculated that these amorphous soot particles may contain a significant amount of soluble organic compounds (SOC). On the other hand, the particulates sampled at the high engine load appeared to be more distinct in morphology. This trend is quite common in diesel particulates, as

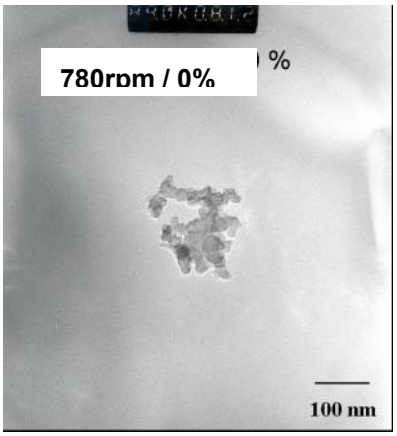

(a)

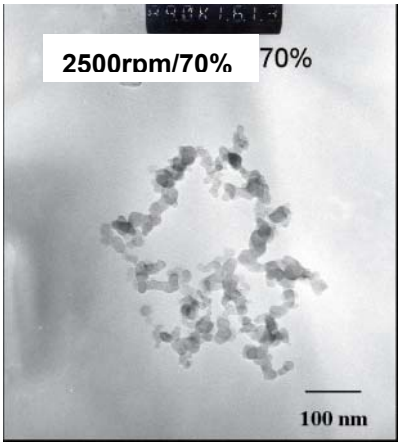

(b)

Figure 2. TEM photographs of particulates sampled at (a) 780 rpm/0% load, and (b) 2,500 rpm/70% load (magnification of 89,000X)

reported for heavy-duty diesel particulates in our previous literature [8–10].

Graphitic Structure of Diesel Particulates

A majority of particles sampled at high engine loading conditions appeared to be graphitic, while the particulates produced at low loading seemed to be amorphous. To validate the observation, Raman scattering spectroscopy was used, which characterizes the sizes, crystal structures, and disorder of graphitic carbon materials [11–13]. Figure 3 shows a Raman spectrum obtained for the particulates sampled at 2500 rpm and 100% load. The spectrum shows two distinct peaks, G peak (1,580 cm^{-1}–1,600 cm^{-1}) and D peak (1,350 cm^{-1}). The G peak results from the interaction between carbon atoms during the in-plane stretching

vibrational mode and the D peak from the one during the breathing vibrational mode [11]. With the Raman data, we calculated an average crystal size of 5.5 nm for the particulates sampled at 2,500 rpm/ 100% load. With further theoretical analysis [14], it was found that a carbon layer in a graphitic crystallite consists of 864 carbon atoms, and the interlayer distance between carbon layers and the distance between carbon atoms were calculated to be 0.34 and 0.141 nm, respectively. The corresponding distances of typical carbon graphite are known to be 0.3354 and 0.1422, respectively. This result implies that the internal microstructures of these diesel particulates closely resemble those of typical graphite.

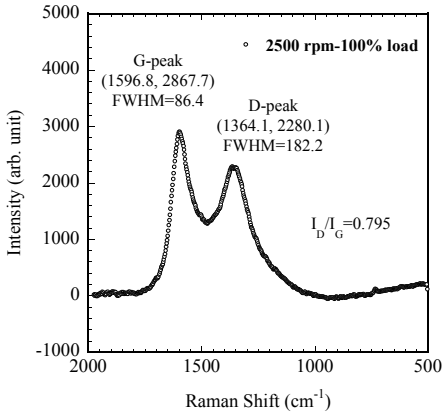

Figure 3. Raman spectrum of the diesel particulates sampled at 2,500 rpm/100% load

Primary Particle Size

Table 1 shows the particulate measurement data we obtained at various engine-operating conditions. For each experiment, the exhaust temperature, EGR rate, and equivalence ratio were recorded to find their effects on particulate properties. The sizes of primary particles were measured at various engine-operating conditions, and at each condition an average value of primary particles were evaluated by measuring the diameters of more than 200 primary particles randomly selected from different aggregates. As shown in the Table 1, average primary particle diameters (d_p) were measured in a range of 19.4 nm and 32.5 nm through the entire engine conditions. These diameters were smaller than those measured for heavy-duty diesel particulates (28.5 nm to 34.4 nm) in our previous study [8–10].

Figure 4 shows primary particle size distributions as a function of exhaust temperature for both light-duty and heavy-duty diesel engines. In general, the primary particle sizes decrease both in the heavy-duty [8–10] and light-duty engines as the exhaust temperature increases. The smallest average primary particle of 19.4 nm was measured to the light-duty engine at 2,500 rpm and 100% load. For the light-duty diesel engine, the particle formation was significantly affected by EGR modes, as described in next section.

In the particulate formation mechanism, primary particles experience a series of chemical and thermal processes, in which precursor particles nucleate, grow through coagulation and agglomeration with other primary particles, and oxidize to reduce the hydrogen/carbon (H/C) ratio. A major parameter to control these processes is known to be the combustion temperature. A higher combustion temperature enhances both particle nucleation and oxidation. Thus, the existence of a primary particle in the combustion field depends on competition of these two events. In the low temperature range shown in the figure, particle nucleation and growth are predominant and subsequently produce slightly larger particles as temperature increases.

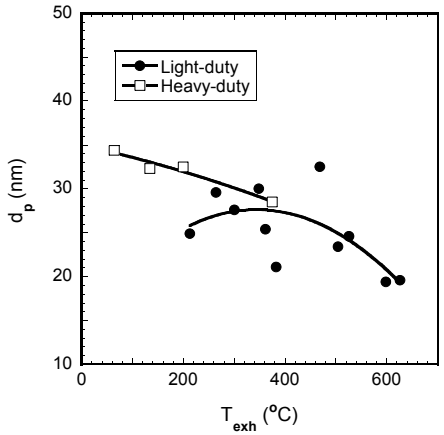

Figure 4. Primary particle size (d_p) as a function of exhaust temperature

Table 1. Engine operating conditions and particulate measurement data

Engine RPM	Engine Torque (Nm)	Engine Load (%)	Exhaust Temperature (°C)	EGR Rate (%)	Equivalence Ratio	d_p (nm)	R_g (nm)	D_f
675	0	0	140.0	0	N/A	28.6	N/A	N/A
1000	31	25	212.9	21.7	0.606	24.9	85.4	1.52
1000	62	50	300.5	11.4	0.638	27.6	98.0	1.48
1000	93	75	362.0	0.5	0.93	25.4	119.5	1.48
2500	18.8	10	264.3	28.7	0.379	29.6	77.4	1.70
2500	47	25	348.5	21.9	0.562	30.0	96.3	1.46
2500	94	50	468.6	11.9	0.627	32.5	94.2	1.60
2500	131.6	70	526.2	1.0	0.603	24.6	85.5	159
2500	188	100	598.7	0.5	0.816	19.4	95.0	1.63
4000	40	25	382.8	0	0.406	21.1	96.7	1.57
4000	79	50	504.4	0	0.594	23.4	134.1	1.46
4000	118.5	75	626.3	0	0.724	19.6	83.7	1.61

Effects of Exhaust Gas Recirculation (EGR)

Our light duty diesel engine was mapped to operate at different EGR modes, depending on engine speeds and loads. The sizes of average primary particles at three different engine speeds were displayed as a function of exhaust temperature in Figure 5. The percentage rate of EGR at each condition was noted on each data point. As shown in the figure, the primary particle diameters at 1,000 rpm and 2,500 rpm were overall larger than those at 4,000 rpm where EGR was inactive. This trend suggests that EGR should increase the primary particle size consistently. In a comparison of data measured at approximately the same EGR rates for 1,000 rpm and 2,500 rpm, the primary particle diameters at 2,500 rpm appeared to be larger than those at 1,000 rpm. Note that the fuel-air equivalence ratios of the counterpart data (at approximately same EGR rates) are comparable each other (see Table 1). However, exhaust temperatures were higher at 2,500 rpm for both 25% and 50% loads. The higher temperatures seemed to increase primary particles sizes at 2,500 rpm. In this case, therefore, the enhanced particle nucleation and growth seemed to dominate over particle oxidation. Furthermore, the residence time available for oxidation should decrease at the higher engine speed.

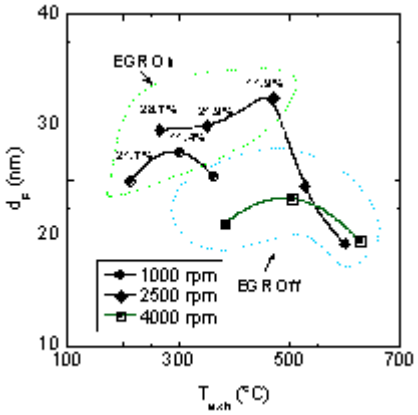

Figure 5. Effects of EGR on primary particle size as a function of engine load

Aggregate Particle Size

Most of diesel particulates were found to be a stretched chain-like shape in morphology, as described above. To represent the physical dimension of these complex particles most accurately, we measured the radii of gyration (R_g's) of aggregates at various engine conditions. As shown in Figure 6, the magnitude of radius of gyration was distributed in a range of 77.4 nm to 134.1 nm for the entire engine conditions. These values appeared to be quite larger than the

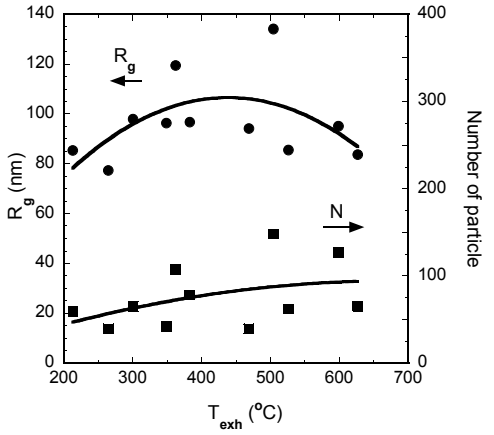

Figure 6. Radii of gyration (R_g) and number of particles (n) as a function of exhaust temperature

particulate sizes other investigators measured using commercially available instruments [1–3].

The radius of gyration initially increases with the exhaust temperature. This is mainly attributed to the particle growth increasing with temperature. In a temperature range higher than about 450°C, however, the radius of gyration decreases with temperature, mainly due to particle oxidation in the high temperatures. In this region, therefore, oxidation is likely to dominate the aggregate size over the particle growth. The morphology of oxidized particles was reported in our previous literature [9,10]. The particle number density (n) monotonically increases as the temperature increases, which will allow particles to be bigger in aggregate size. Although the number of primaries per aggregate (n) continued to increase with temperature, the aggregate size indeed decreased in the high temperature region, which was also shown in our previous study for a heavy-duty diesel engine [8–10]. A higher degree of particle oxidation is a major responsibility for the reduction of particle size.

Fractal Geometry

Fractal dimension explains under what formation mechanism aggregate particles are formed during combustion processes [10]. Simultaneously, the fractal dimension standardizes the complex morphology of diesel particulates with a single numerical number.

Figure 7 displays fractal dimensions (D_f) we measured for different types of engines and lab-scaled burners. The fractal dimensions of light-duty diesel engine were measured in a range of 1.46 to 1.70 at various engine conditions. In general, the smaller values were measured at low engine loads, and the larger ones at high engine loads. These values appear to be smaller than those measured for heavy-duty diesel particulates (1.80 to 1.88) [8–10]. This indicates that the light duty engine produces more stretched chain-like particulates, while the heavy-duty diesel engine produces more spherical particles.

It is interesting to note that the fractal dimensions measured for lab-scaled diffusion flames [6] are comparable to those of diesel particulates that were formed under high combustion chamber pressures. Although the pressure is a major parameter to control particle agglomeration, the residence time is likely to be another important parameter responsible for the analogy in fractal. The relatively long residence time available in the atmospheric pressure diffusion flames should allow particles to agglomerate together at a higher degree, while the diesel particulates experience significant oxidation during the shorter residence time in a combustion cycle. Meanwhile, the formation of light-duty diesel particulates was also controlled by the diffusion-limited growth mechanism, as found in our previous studies for heavy-duty diesel particulates [9,10].

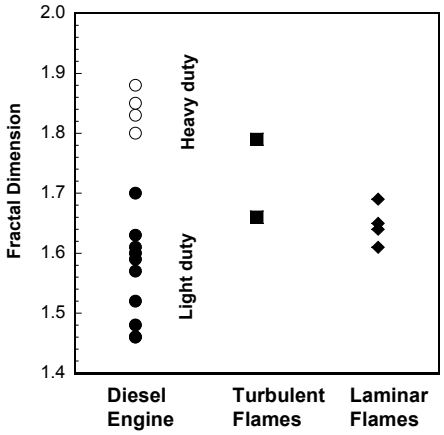

Figure 7. Fractal dimension for particulates produced from light-duty, heavy-duty, turbulent, and laminar flames

Conclusions

The morphology, sizes, internal microstructures, and fractal geometry of light-duty diesel particulates were characterized in detail. The analyses revealed that the light-duty diesel engine produces various shapes of particles from near spherical to stretched chain-like through the entire engine conditions. It was also found that the particulates produced at a low engine load were nebulous, and the ones produced at high engine loads were distinct in morphology and represented graphitic structures. Raman spectra and subsequent mathematical analyses revealed that these diesel soot particles closely resemble the typical carbon graphite in terms of atomic structures.

The mean values of primary particle diameter ranged from 19.4 nm and 32.5 nm through the entire engine operating conditions. They were significantly affected by the engine speed and load, EGR mode, and equivalence ratio. The decreasing trend of primary particle sizes with engine loads, similarly to heavy-duty diesel particulates, was mainly attributed to particle oxidation dominated by the high combustion temperature. EGR also increased primary particle sizes significantly in most engine speed and load conditions. Larger primary particles at 2,500 rpm than those sampled at 1,000 rpm are likely to result from the dominant effects of particle nucleation and growth exceeding oxidation. The radius of gyration was measured in a range of 77 nm to 134 nm, and the fractal dimensions were evaluated at 1.5–1.7. These fractal dimensions are smaller than those of heavy-duty diesel engine particulates, which suggests that the light-duty diesel engine produces more chain-like particles than does the heavy-duty diesel engine.

References

1. Vuk, C.T.; Jones, M.A.; Johnson, J.H., SAE 760131.
2. Carpenter, K.; Johnson, J.H., SAE 790815.
3. Baumgard, K.J.; Kittelson, D.B., SAE 850009.
4. Abdul-Khalek, I.S.; Kittelson, D.B.; Graskow, B. R.; Wei, Q.; Brear, F., SAE 980525.
5. Willeke, K., and Baron, P.A.: *Aerosol Measurement*, Van Nostrand Reinhold, New York, 1993.
6. Lee, K.O.; Megaridis, C.M.; Zelepuga, S.; Kennedy, L.A., Combust. Flame, 121:323–333 (2000).
7. Guenç, A.; Megraidis, C.M.; Campbell, A.; Lee, K.O.; Choi, M. Y., Combust. Sci. Technol. 171:71–88 (2002).
8. Lee, K.O.; Cole, R.; Sekar, R.; Choi, M.Y.; Zhu, J., U.S. Section Second Joint Meeting of the Combustion Institute, Oakland, CA, March 26–28 (2001).
9. Lee, K.O.; Cole, R.; Sekar, R.; Choi, M.Y.; Zhu, J.; Kang, J.; Bae, C., SAE 2001-01-3572.
10. Lee, K.O.; Cole, R.; Sekar, R.; Choi, M.Y.; Kang, J; Bae, C.S., Shin, H.D., 29th Proc. Comb. Inst. (2002).
11. Tuinstra, F.; Koenig, J. L., J. Chem. Phys. 53:1126–1130 (1970).
12. Knight, D. S.; White, W. B., J. Mater. Res. 4:385–393 (1989).
13. Ferrari, A. C.; Robertson, J., Phys. Rev. B 61:14095–14107 (2000).
14. Belenkov, E. A., Inorganic Materials, 37:928–934 (2001).

X. Brake Materials

Ceramic Braking Materials Development for Commercial Vehicles

Principal Investigator: P. Gray
Power Systems Composites, LLC
400 Bellevue Road, Newark, DE 19713
(302) 631-1319; fax: (302) 631-1320; paul1.gray@ps.ge.com

Technology Development Manager: Sid Diamond
(202) 586-8032; sid.diamond@ee.doe.gov
Technical Program Manager: Jules Routbort
(630) 252-5065; routbort@anl.gov

Contractor: DOE Office of Heavy Vehicle Technology (DOE-OHVT)
Contract No.: DE-FC04-2000AL66778

Objective

- Develop a cost-effective C/SiC brake rotor for Class 7 and 8 with improved performance over incumbent systems.
- Performance goals include decreased fade, weight reduction, stable friction coefficient and decreased wear at a price competitive with cast iron rotors and organic bonded pads.

Approach

- Utilize PSC/ ALS chopped fiber preform technology with PSC melt infiltration (MI) expertise.
- Perform sub-scale dynamometer testing at Greening Laboratories on both incumbent and developmental systems.
- Refine material system to achieve desired friction and wear properties.
- Measure material properties of downselected system.
- Perform full scale dynamometer testing at Bendix-CVS test facility and report results.

Accomplishments

- Showed that organic pads are unsuitable on C/SiC rotors; must use C/SiC pad/rotor couples.
- Demonstrated that C/SiC pad/ rotor couples resulted in stable friction coefficients of 0.5-0.6 with wear rates which were 20% that of conventional cast iron rotor/ organic pad couples.
- Demonstrated molded rotor preform technology which protected carbon fibers from molten silicon attack during MI.
- Performed scale-up trials with culminated in production of full-sized 17 inch C/SiC test rotor.

Future Direction

- Perform mechanical properties testing on pad and rotor materials.
- Work with Bendix-CVS to integrate C/SiC material into existing metal-backed pad design.

- Finalize dynamometer test plan and evaluate performance of full-sized rotor/pad couples at Bendix CVS.
- Possible vehicle testing at Bendix CVS if program resources allow.

Introduction

The DOE-OHVT Ceramic Brake Development program is part of the Department of Transportation's 21st Century Truck Initiative. One goal of this initiative is to drastically reduce the aerodynamic drag of the nation's freight-hauling fleet thus reducing fuel costs. As drag is reduced, the energy dissipated by the braking systems increases. Incumbent cast iron rotor/ bonded organic pad braking systems do not have the braking reserves necessary to implement these drag-reduction systems in current heavy vehicles.

Power Systems Composites (PSC), LLC (formerly Honeywell Advanced Composites Inc.) utilized its experience in both carbon-carbon materials development and silicon melt infiltration to design a suitable carbon fiber reinforced SiC brake pad and rotor material system. The key to producing these systems was to prevent fiber and interface attack during silicon melt infiltration.

Friction and wear screening tests on an 8-inch-dynamometer were used to optimize the pad and rotor characteristics. The program as written, initially planned to use commercially-available organic-bonded pads or SiC/Al2O3 (DIMOX) composite with the C/SiC rotors. The commercial pads were found to have low friction coefficient (mu) and high wear in contact with several types of C/SiC. The SiC/Al2O3 had reasonable mu but at a wear rate about twice that of the commercial pad on cast iron. PSC then tested several combinations of C/SiC pads and rotors they had previously made and generally found the C/SiC pad/ rotor combinations gave stable mu with lower wear than iron rotor/organic pad couples.

Full-sized C/SiC rotors were made from the downselected system during the fall of 2003. The sale of Bendix CVS from Honeywell to Knorr-Bremese stalled the full-scale testing of these rotors during Q2-Q3, 2003. The test program has been re-initiated and the full-scale rotor/ pad testing is expected to be initiated late in Q4 2003 and completed early in 2004.

Results and Discussion

Table 1 summarizes the friction and wear results obtained on the test matrix of cast iron baseline and three types of C/SiC rotors versus commercial organic pads, the SiC/Al2O3 (DIMOX) composite and the type 034 C/SiC.

Table 1. Friction and wear test results on candidate rotor/ pad combinations.

Rotor Type	Pad Type	Wear Rate (cu in/hp-hr*0.001)	Friction Coeff.
Cast Iron	Jurid 539	3.9	0.35-0.55
Cast Iron	Texstar T7400	4.2	0.27-0.70
C/SiC 034	Dimox I	300	<0.2
C/SiC 034	Dimox II	11.6	0.50-0.30
C/SiC 034	C/SiC 034	1.4	0.050-0.55
C/SiC 010	Dimox I	3.2	0.45-0.60
C/SiC 010	Dimox II	12	0.40-0.30
C/SiC 010	C/SiC 034	0.7	0.55-0.50
C/SiC 028	Dimox I	21.6	<0.2
C/SiC 028	Dimox II	8.8	0.40-0.60
C/SiC 028	C/SiC 034	0.7	0.6-0.55

The friction and wear testing was performed by Greening Test Labs on their Friction Assessment Screening Test (FAST) dynamometer. The test was conducted for 90 minutes and applies a varying load to maintain a constant torque on the rotor. The results are plotted as lining pressure, which is inversely proportional to mu, versus time.

The friction and wear performance of the organic (Jurid) pad on C/SiC is shown in Figure 1. Note the lining normal pressure exceeds the maximum obtainable on the FAST machine as the mu drops below 0.2 about half-way through the test.

Similar results were obtained on the other types of C/SiC with both the Jurid and Textron pads. These were unacceptable rotor/pad couples for further consideration.

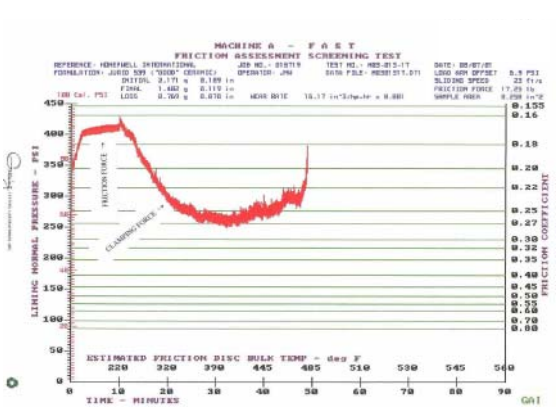

Figure 1. Friction behavior of Jurid organic pad on type 029 C/SiC rotor.

Figure 2 shows the behavior of the baseline Jurid organic pad on a cast iron rotor. The mu increased from 0.3 to 0.6 over the 90-minute test. Ideally, flat mu versus time is a desirable test attribute. The pad sample thickness was measured after testing and the reduction in thickness used with the normal pressure to calculate a wear rate as cu-in/hp-hr × 0.001. This gradual increase in mu over the test duration was typical for the organic pads on cast iron. Wear rates for these couples averaged 4 cubic inches/ hp-hr × 0.001.

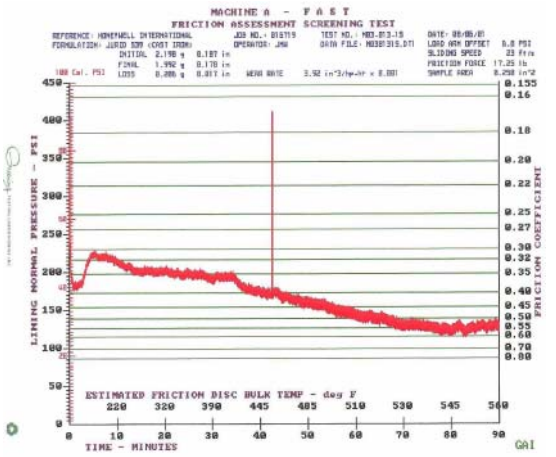

Figure 2. Friction behavior of commercial Jurid pad on cast iron rotor

Figure 3 shows the frictional behavior of the downselected C/SiC pad and rotor couple. Note the stable mu throughout the testing period.

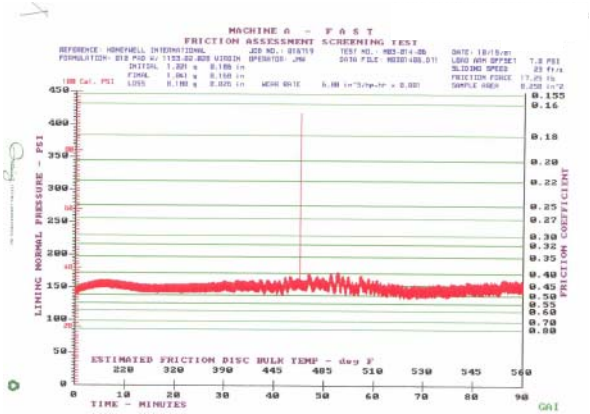

Figure 3. Friction behavior of downselected C/SiC pad on C/SiC rotor

Measured wear rates on the C/SiC pad material tested in Figure 3 were about a factor of 5 lower than the incumbent cast iron/ organic pad couple.

Much thought was given to the fabrication techniques needed to make both pads and rotors. A low cost chopped fiber molding compound (CFMC), previously developed at HACI, was targeted to make the rotors. This material has the advantage of being able to be made into complex shapes such as vented rotors. Figure 4 is an example of a 10-inch subscale vented rotor made using this process. Molding processes allow complex shapes to be made with minimal preform machining.

Figure 4. Melt infiltrated C/SiC brake rotor sub-element made using CFMC developed at PSC (size is 10" diameter)

The full-sized, 17 inch test rotors, which will be tested at Bendix-CVS, were also made using the CFMC approach. These rotors consisted of a disk with lugs on the rotor ID which were designed to mate with the hub design used by Bendix-CVS to test conventional cast iron rotors. No attempt was made to introduce venting holes into the C/SiC brake rotor at this time. Should venting be required, these features could be machined into the rotor during the preform stage prior to MI. Figure 5 shows the completed full-sized rotor mounted on the metallic hub at Bendix-CVS.

Figure 5. Completed full-sized rotor on hub assembly at Bendix-CVS

PSC is working with Bendix-CVS to develop a dynamometer test plan for the full-scale rotors. Bendix-CVS has supplied PSC with drawings for the brake pad assemblies as well as some sample pad assemblies used on cast iron rotors. The goal is for PSC to deliver C/SiC pad assemblies to Bendix-CVS by the end of 2003.

Mechanical testing of the rotor and pad materials will be performed late in 2003 in parallel with the dynamometer testing. The goal is to perform some simple finite element modeling to predict such factors as lug tear-out torque and burst speed.

Conclusions

The OHVT Ceramic Truck Brake program has performed materials development and friction screening experiments on candidate C/SiC pads and rotors. Early in the program, the use of commercial organic disk brake pads as well as SiC/Al2O3 composite pads with C/SiC rotors was found to exhibit unacceptable friction and wear performance.

Friction and wear performance of C/SiC pads and rotors in screening tests was excellent. The friction coefficient measured during the testing was constant and ranged from about 0.5 to 0.6. Pad wear rates also measured during the sub-scale dynamometer testing were a factor of 4–5 lower than the baseline organic pads on cast iron rotors.

Sub-scale and full scale rotor fabrication using chopped fibers in a thermosetting resin matrix compound was successfully demonstrated. Several 17-inch full-sized truck brake rotors were fabricated for dynamometer testing at Bendix-CVS.

The program is currently working on integrating the C/SiC pad materials into the current metal-backed organic matrix pads. Dynamometer testing and mechanical properties testing should begin January 2004.

XI. Off-Highway Vehicles

Advanced Hybrid Propulsion and Energy Management System for High-Efficiency, Off-Highway, 320-Ton Class, Diesel Electric Haul Trucks

Field Project Manager: L. Salasoo
GE Global Research
1 Research Circle, Niskayuna, NY 12309
(518) 387-5000; fax: (518) 387-6675; salasoo@crd.ge.com

Technology Development Manager: Sid Diamond
(202) 586-8032; sid.diamond@ee.doe.gov
Field Technical Manager: Jules Routbort
(630) 252-5065; routbort@anl.gov

Contractor: GE Global Research
Contract No: DE-FC04-2002AL68080

Introduction

This program addresses the "Off-Highway Thermal Management/Systems Efficiency Technologies" objective as given in the "Research and development to increase engine efficiency, reduce emissions, and improvement in systems efficiency for off-highway vehicles, including construction, agriculture and mining equipment" solicitation. In particular, the program will demonstrate improved mine haul truck efficiency in terms of energy efficiency by utilizing the recovery and reuse of braking energy which would otherwise be wasted as heat. The braking energy is utilized by adding a hybrid energy storage system to the architecture of the diesel-electric mine haul truck as shown in Figure 1. Initial analysis suggests 18% energy saving in a typical mission.

The program progresses in three stages: the first, to develop the hybrid energy storage subsystem (ESS) and hybrid energy management subsystem (EMS), the second to evaluate and test these systems first on a subscale level in the laboratory and then on a full scale static test; and the third to integrate the hybrid energy storage and hybrid energy management subsystems to a 320-ton-class mine haul truck, and demonstrate the operation of the hybrid truck. In the 2003 project year the initial system studies have been done, and the ESS and EMS subsystems have been defined, evaluated and bench-scale tested. The bench scale demonstration and evaluation of the combined ESS and EMS system has been initiated.

Configuration and System Studies to Determine System Requirements

A team visited the Komatsu Proving Ground, located in Green Valley, Arizona for familiarization with the proving ground and the 320-ton 930E mining haul truck. The proving ground is a former copper mine that is no longer active, with two pits which had haul roads spiraling to the bottom of each pit, as well as office space and workshops (see Figure 2 aerial photo). At present, one usable mine road is maintained, which descends part-way into a mine pit. In addition there is a constant 10% test grade section.

The mine road was inspected by driving a 930E mine haul truck over the route and electronically recording data on truck performance (including speed, power, torque) on several runs in both uphill and downhill directions, loaded and unloaded. Since the proving ground is not an operating mine, it was possible for each of the visiting team members to drive the mine haul truck. A mine haul truck was inspected (Figure 3) and candidate locations for installation of the hybrid system were identified. A potential total of approx. 560 cu. ft. was identified.

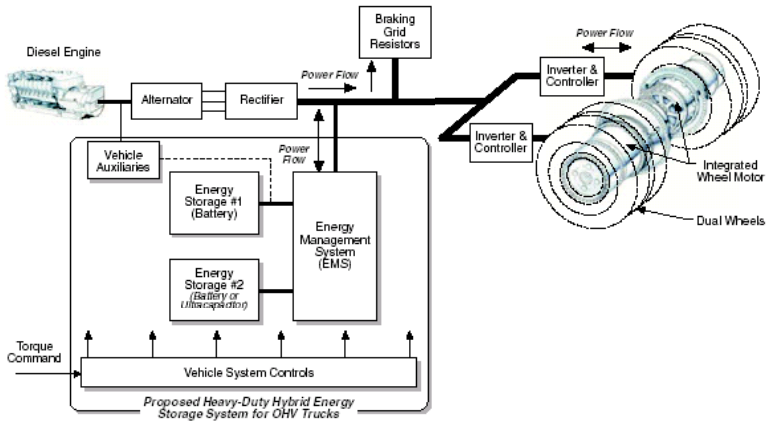

Figure 1. Top level system block diagram of the 320-ton hybrid mine haul truck demonstrator

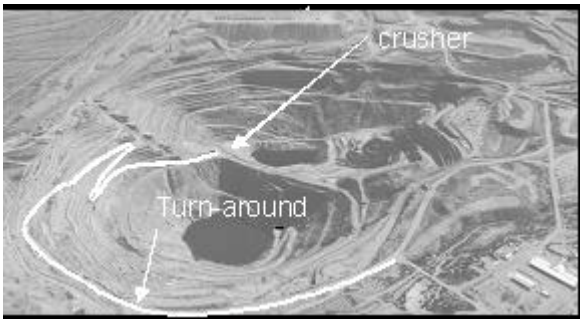

Figure 2. Mine haul truck proving ground

Figure 3. GE team with 930E mine haul truck

The datalogs and mine topographical data were analyzed to derive the mine road grade and elevation profiles (Figure 4). Two distinct missions are envisaged to be used in the demonstration of the hybrid mine haul truck: one will use the 10% grade ("termed the simple grade mission"), and the other ("composite grade mission") was selected from the total mine road, to run 6,500 ft between the lowest point, where a stone crushing plant is located, and a

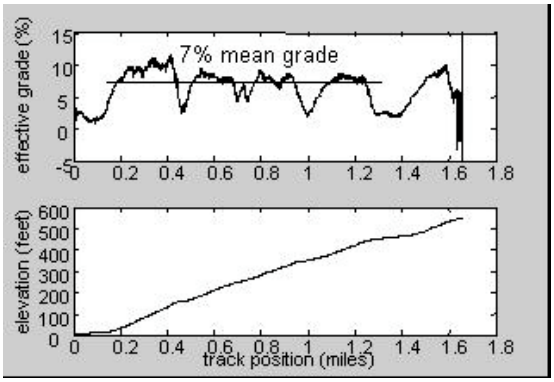

Figure 4. Mine road grade and elevation profiles

junction with another mine road which has a convenient stopping and turnaround location. The composite grade mission has approx. 7% average grade. One of the key variables in the hybrid truck demonstration will be the driving style of the truck operator, how he approaches curves, how he anticipates the need to brake and so forth. Operation on the simple grade mission will simplify the operator's task and eliminate many of the driving style judgment calls he needs to make, yielding a very reproducible performance that will be used to verify and calibrate analysis and model predictions.

Operation on the composite grade mission will provide a realistic scenario of operation in the operating mine environment and provide data to assess hybrid performance in the operating mine setting.

Hybrid mine haul truck performance was analyzed using mission analysis (MA) models. These models

handle the mine haul truck equations of motion, and power flow between diesel engine prime mover, auxiliary loads, traction system (both motoring and retarding) and the hybrid energy storage. Given the mission profile (grade vs. distance), mine haul truck parameters (weight, subsystem efficiencies and capabilities), driving commands (such as speed limit vs. distance) and hybrid system parameters (energy storage capability and energy management strategy), the MA model simulates the dynamic performance of the vehicle (speed, position, power flows and accumulated energies vs time). The output is post-processed to yield parameters such as diesel prime mover input, mission time, and hybrid system stored energy. Validation was performed against the datalogs obtained at the mine visit.

To guide sizing of the mine haul truck hybrid system, a benefits assessment study for an uphill haul composite grade cycle was done. The MA model was used to analyze the unloaded downhill (hybrid system charging from the retarding power) and loaded uphill (hybrid system discharging to augment traction power) runs. The downhill speed limit was varied: faster speeds reduced total cycle time but led to higher available retard power for shorter periods. The energy storage kW charge and discharge limit was varied. The hybrid mine haul truck charged up energy storage on downhill run, and on uphill run combined diesel 2700GHP power with stored energy to get higher traction power, which sped the uphill run and lowered cycle time. For each combination of parameters, the MA analysis provided the total cycle time and kWh energy provided by the diesel prime mover.

For the mine operator, key performance parameters are productivity (ton-miles hauled per hour) and fuel efficiency (ton-miles hauled per gallon). In this benefits assessment study, prime mover energy efficiency (ton-miles hauled per kWh) was used as a proxy for fuel efficiency. The results of the study were analyzed to show variation of relative efficiency and productivity vs a baseline cycle with 24-mph average downhill speed and 17 min. cycle time. As an example, a hybrid system with 800kW charging and discharging power capability, that is operated over the composite grade mission with 18mph average downhill speed, will display baseline productivity and 15% energy efficiency improvement.

The benefits assessment enabled the determination of hybrid system requirements. The hybrid system charging power rating is the key parameter that drives the energy efficiency improvement. All energy storage battery options that meet the power requirement have ample energy storage capacity to meet energy capacity requirements. The other key requirements relate to the mine haul truck operating environment, in particular the high ambient temperature operating capability. The truck manufacturer's specification requires operation in a 55ºC ambient temperature, and the climate data for Tucson, AZ (Figure 5) indicates that the proving ground summer temperature may approach the upper specification.

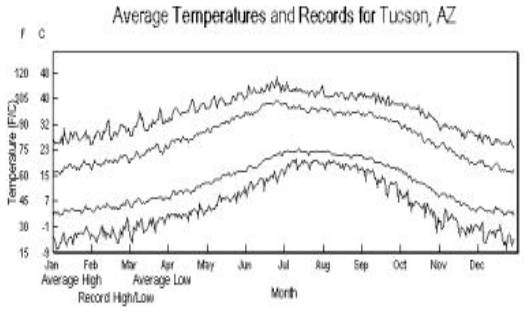

Figure 5. Tucson, Arizona, climatic data

System Specifications Development

A detailed survey of available energy storage technologies and vendors has been carried out, and the capabilities in terms of performance (energy and power densities), environmental capability, technical maturity, and battery management requirements have been evaluated.

As shown in Figure 1, the hybrid mine haul truck ESS concept has 2 energy storage banks and an EMS to control power interchange with the truck main electric bus. The EMS hardware configuration will be based on available GE Transportation Systems hardware, with projected capability to charge and discharge the ESS at rates up to 400 kW. More detailed design analysis is required to precisely evaluate the charging power limit. The ESS will be rated for 500 kW charging power and 40 kWh operating energy storage range.

A mix of two energy storage technologies will be used, in order to reduce risk in the hybrid mine haul truck demonstration task. Figure 6 shows the

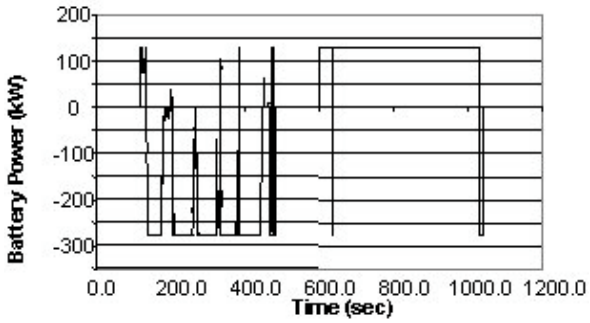

Figure 6. Mine haul truck uphill haul cycle: single battery bank terminal power demand

composite grade mission uphill haul duty cycle for each of the two. Nickel-cadmium technology will be the baseline element of the mix. The GE team has a lot of experience and confidence in this technology, which however has lower energy and power density than more advanced energy storage technologies. A higher-density advanced energy storage technology will be utilized together with the baseline technology; its demonstration in the program will develop required data and experience to enable use of the advanced technology for optional follow-on tasks in this program. The baseline and advanced energy storage systems will be separately controlled. Together they will supply the total power and energy requirements of the hybrid mine haul truck demonstration.

A detailed assessment of available technical solutions for energy storage battery thermal management was carried out, to support energy storage technology selection for the demonstration. The ESS will be operated at very high charge and discharge rates, leading to significant losses. The power duty cycle is significantly higher and more intensive than for on-road hybrid vehicle. For these reasons, aggressive cooling will be required, but for operation in the mining environment, the cooling system must be simple and rugged. It was determined that passive cooling systems will not have adequate performance, while active cooling techniques of refrigeration and forced air cooling merited further consideration. Three types of high-capacity refrigeration are available — stationary chilled-water systems, transportation air-conditioning units, and transportation refrigeration units. However their significant size, cost, and engineering effort required to integrate with the ESS drove the selection to forced air cooling.

All but one of the candidates ("ambient-temperature batteries") have maximum recommended operating temperatures between 50–70°C, quite close to the 45°C maximum environmental temperatures expected in the demonstration (see Figure 5). All the ambient temperature technologies have nominal operating temperatures 25–30°C, and operation above the nominal temperatures leads to premature degradation in battery long-term performance as shown by reduced cycle life. Thus reliance on ambient-temperature forced air cooling will inevitably result in degraded longterm cycle life. However sodium-nickel chloride ($Na\text{-}NiCl_2$) technology has an operating temperature around 300°C. Here ambient-temperature forced-air cooling will be effective in dissipating battery losses without degradation in cycle life, and therefore the high-temperature battery technology is preferred from the thermal management viewpoint.

Based on performance, density, technology maturity, thermal performance and demonstration risk reduction, a mix of nickel-cadmium and $Na\text{-}NiCl_2$ technologies was selected for the hybrid mine haul truck demonstration.

Design and Fabrication of Hybrid System Components

Performance testing of the nickel cadmium energy storage battery system was carried out to establish its baseline performance. Figure 7 shows the recorded voltages during controlled discharge for one battery box plotted against the discharged ampere-hours. The batteries performed according to manufacturer's specification.

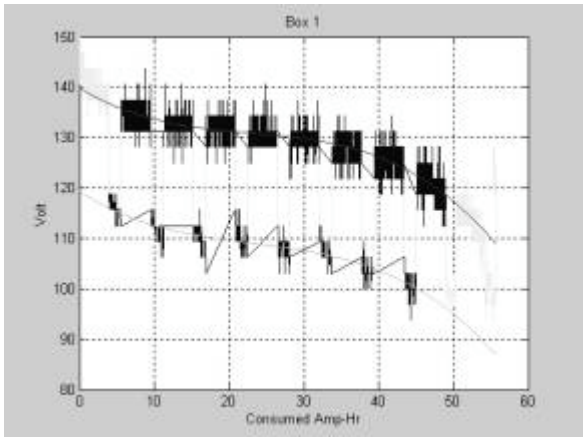

Figure 7. NiCd battery box performance test results

Detailed design was carried out of the Na-$NiCl_2$ system capability to operate in the haul truck high voltage environment, with respect to maximum terminal voltages, and control connection voltage referencing. Protection and isolation concepts have been addressed. The control interface between the Na-$NiCl_2$ system and the truck system utilizes CAN-bus.

A rigorous testing program was carried out to verify manufacturer's specifications for a Na-$NiCl_2$ battery subsystem and to determine internal parameters required for accurate modeling and prediction of hybrid mine haul truck system efficiency and benefits, such as open circuit voltage and internal resistance (Figure 8). High voltage compatibility was tested and cycling performance testing is ongoing. It was verified that there will be adequate cycle life to perform over the whole hybrid mine haul truck demonstration.

Candidate locations for the energy storage system were reviewed with Komatsu and specific mounting locations were decided. The energy storage battery assemblies will be mounted in several enclosures to provide structural support, electrical isolation and physical protection. A battery enclosure specification has been prepared to define detailed design and fabrication requirements.

Hybrid energy management strategies to coordinate the two energy storage banks and for temperature control were developed, implemented, tested and verified. The initial implementation was carried out in an interactive dynamic simulation software environment. Subsequently, battery and power conversion hardware was brought into the loop, to test out the strategies on physical batteries. The hardware-in-the-loop operation was under dynamic simulation software control, via a rapid control prototyping software interface module to control the battery controller gate drives. In particular, capabilities of power sharing between two energy storage banks, and temperature compensation have been verified. Figure 9 illustrates control of laboratory battery temperature using the compensation algorithm.

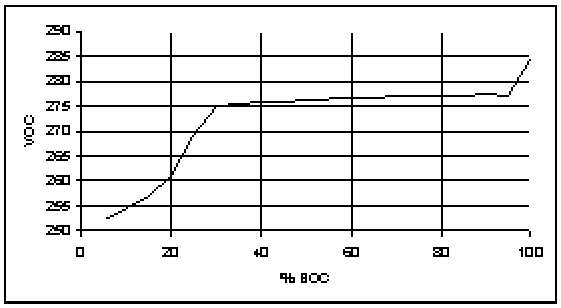

Figure 8. Na-$NiCl_2$ battery open circuit voltage

Subscale Demonstration

A subscale demonstration of the energy management system and energy storage system was prepared for the 100-hp level. The system incorporates representative modules of nickel-cadmium energy storage and Na-$NiCl_2$ energy storage interfaced through a power flow controller to the system dc bus. The dc bus is fed from an engine-alternator emulator, and also connected to a bidirectional traction drive emulator. The system models the electrical system of a diesel-electric mine truck. The performance of the hybrid during the uphill and downhill composite grade hauls was modeled to demonstrate the performance of the hybrid mine haul truck system. Analysis of the results is in progress.

Conclusion

The successful first project year has seen the selection of the demonstration hybrid mine truck system concept, architecture and energy storage technologies. The size of the energy storage was selected based on a system benefits study. Subscale testing of representative energy storage modules and energy management algorithms has been carried out, and a subscale laboratory demonstration of the combined ESS and EMS hybrid system is in progress. The team looks forward to an exciting second project year, with the completion of the subscale demonstration, procurement of the full-power hybrid system hardware and full-power static testing.

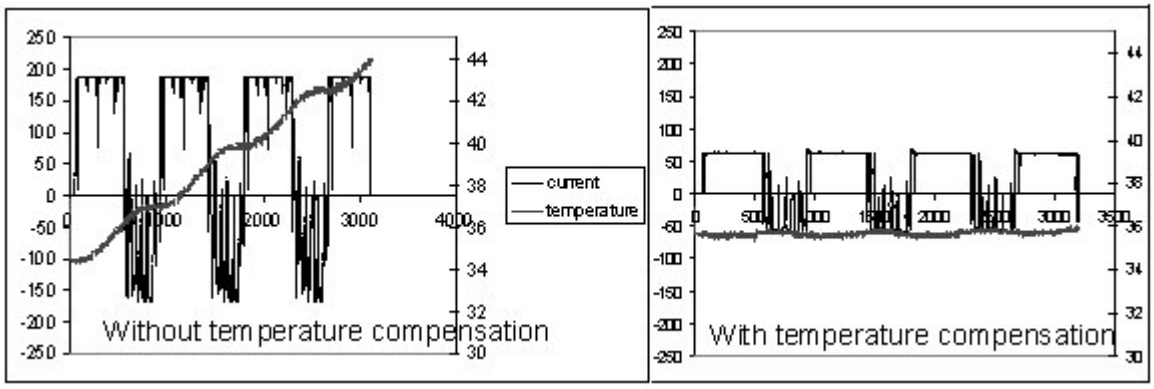

Figure 9. Battery temperature control

XII. Long-Life Oil Filtration System

Real-World Testing of an Advanced Filtration System

Principal Investigator: J.M. Cousineau
Co-Investigators: K.S. Aerts, A.J. Holmio, and E.M. Alanko
Engineered Machined Products, Inc.
2701 North 30th Street, Escanaba, MI 49829
(906) 789-7497; jason.cousineau@emp-corp.com

Technology Development Manager: Sid Diamond
(202) 586-8032; sid.diamond@ee.doe.gov
Technical Program Manager: Jules Routbort
(630) 252-5065; routbort@anl.gov

Contractor: Argonne National Laboratory
Contract No.: 2E-00341

Objective

- Test and evaluate the advanced filtration system technology and all of its components in order to obtain enough design, bench testing, and field evaluation experience to get the technology prepared for commercialization.
- Realize the true benefits of this technology in real-world applications.

Approach

- Individual system components will undergo performance and reliability testing.
- Full system development prototypes will be designed and fabricated.
- Prototypes will undergo performance and reliability testing.
- Development prototypes will be installed in test vehicles for real-world field testing.
- The test vehicles' useful oil life will be measured by pulling oil samples weekly.
- The useful oil life will be compared to a baseline oil life to determine the performance of the filtration technology.

Accomplishments

- System components have been performance and reliability tested.
- The development prototypes have been designed and fabricated, as well as performance tested.
- Baseline oil analysis studies on two test vehicles have been completed.
- Two full-system development prototypes have been installed on the two test vehicles and the field testing has begun.

Future Direction

- Continue to pull oil samples and monitor the system prototype performance on the test vehicles.
- Complete field testing and determine the overall performance of the filtration technology.

- Install and field test systems on other applications, such as new engines equipped with EGR technology.
- Develop and put strategy in place to commercialize the technology.

Introduction

Current oil filtration technology has been around since the late 1950s. This technology is the full-flow, spin-on, filter. The full-flow filter is typically located after the oil pump on the engine. Therefore, 100% of the engine's oil flow passes through the filter. The filter is then designed to remove only the large particles from the oil because the filter must not restrict the oil flow. In turn the filtering effectiveness is extremely limited. Current full-flow filters are only efficient in controlling particles 20 microns and larger. 95% of the contamination generated within the engine is below 10 microns. This current filtration technology leads to short oil change intervals. Frequent oil changes are expensive, time consuming, and generate a tremendous amount of waste from the disposal of oil and oil filters. Fleet owners and operators are pushing the limits on extending these oil change intervals to reduce operating costs. Oil levels and oil additives can get dangerously low causing excessive engine wear.

The industry's solution to the inadequate oil filtration thus far has been the advent of bypass filters. Bypass filters are being installed on engines in parallel to the full-full filter. These filters continuously divert a side stream of 10–15% of the engine oil flow, filter it more efficiently through the use of finer filtration, and then return it back to the oil pan. Tests have proven that the addition of bypass filters will extend the useful oil life and lengthen full-flow filter life. However, bypass filters do have limitations. Bypass filters typically have shorter change intervals than the full-flow filters due to their smaller size and finer filtering capability. Even though the oil change interval is being extended, filters are still being changed frequently leading to little if any reduction in filter change and disposal costs as well as no reduction in waste. With more soot being deposited in the oil due to EGR, this problem will be even more evident. Another problem associated with by-pass filters, is the introduction of oil pressure parasitic losses. Because bypass filters divert approximately 10% of an engines total oil stream, an oil pressure parasitic loss can be introduced. Diversion of this amount of oil can lead to starvation of certain engine components of necessary lubrication.

Engineered Machined Products, Inc. (EMP) has a substantial amount of experience in oil management. EMP has spent the last several years developing an advanced filtration system (AFS) for diesel engine applications. The intent of the system is to extend oil life as well as the full-flow filter life to 100,000 miles allowing for a reduction in maintenance intervals to one per year. This will dramatically reduce the consumption of oil, as well as the generation of waste from the disposal of oil and oil filters.

Other benefits include reduced engine wear, increased fuel economy, and finally reduced emissions. These benefits of applying finer filtration to engine applications have been well documented by the Society of Automotive Engineers. It has been found that improving filtration from 40 microns to 15 microns can yield as much as 70% reduction in engine wear [1]. Studies have shown reductions in fuel consumption from 3–5% by controlling oil quality with finer filtration [2,3]. It has also been found that diesel exhaust emissions correlate to the amount of suspended solids in the engine oil [4]. Studies have shown reductions in emissions from 17–30% using finer filtration to clean the oil [5,6].

The Advanced Filtration System (AFS) is an auxiliary advanced engine filtration system consisting of an electric oil transfer pump, replaceable/recyclable filtering cartridge, a self-indexing system to continuously advance in clean filtering medium, and a housing to enclose it all. This system operates independently of an engine's main lubrication system and applies a continuous filtering method to the engine oil. The reel-to-reel configuration enables the filtration device to automatically replace used or dirty filtering medium in a controlled and continuous fashion (Figure 1). The AFS provides greatly expanded oil filtering and contaminant retention over a set service interval. As

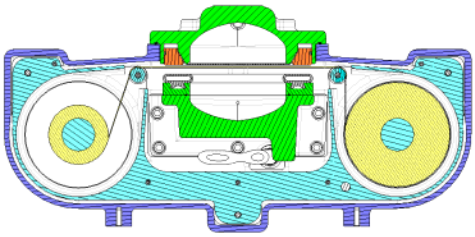

Figure 1. AFS cross-section showing the "reel-to-reel" filtering method

a result, the filtering operation can remove the large amount of soot introduced to the lube oil by exhaust gas re-circulation (EGR), a pollution-reduction technique used in many heavy-duty truck engines.

The reel-to-reel principle is based upon the monitoring of the pressure differential between the upstream side and the downstream side of the filtering medium. When a high pressure differential exists due to the build-up of particles on the filtering medium, the system sends signals to the transfer pump to cease oil flow to the filter, and to the self-indexing system to advance clean filtering medium to the oil flow from a supply reel. Simultaneously, the self-indexing system ejects the dirty filtering medium from the oil flow to a take-up reel. The transfer pump then initiates oil flow back through the filtering device. The process repeats until a desirable pressure differential is achieved. When the recommended service interval is reached, the filtering cartridge can be removed and replaced with a new cartridge.

There are two key features that distinguish the AFS from existing technology. First, it uses an electric transfer pump to take fluid from a reservoir and transfer it to the filtration device. This allows the filter system to function independently of the system it is protecting (Figure 2). In addition, the transfer pump allows for automated draining and filling of oil during servicing and provides the capability to pre- and post-lube the engine. Second, the system's unique "reel-to-reel" filtering method automatically exchanges used or plugged filtering medium for new or clean filtering medium as needed. This filtering method allows for an unlimited supply of filtering medium as well as more efficient use of the filtering medium.

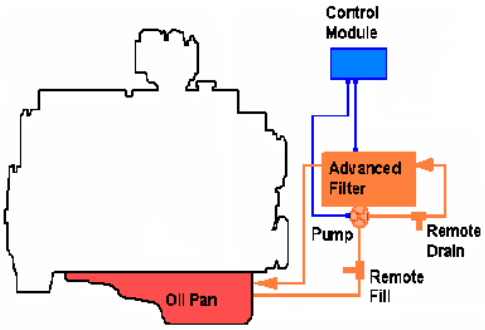

Figure 2. System diagram showing the independent arrangement in regard to the engine it is protecting

Results and Discussion

As stated, the objective of this phase II program was to determine the true real world benefits through field testing. Several tasks had to be completed before field testing of the AFS could begin. First, the development prototypes had to be designed and constructed. The design process consisted of designing an oil pump, a filter cartridge, a housing to enclose it all, and a control unit (Figures 3–6).

Figure 3. The electric oil transfer pump constructed out of aluminum 6061-T6 billet

Figure 4. The filter unit housing constructed out of aluminum 356-T6 sand castings

Figure 5. The filter cartridge constructed out of fiberglass compression molding and nylon 6/6 inner components

Figure 6. The electronic control unit to control the system, provide diagnostics and data acquisition

The next step was to put the system together in the lab for bench testing. Performance and reliability was to be tested. Also, the system algorithm needed to be debugged. Two issues arose during the bench testing of the system prototype. The first issue was with one of the filter unit components. This component was the inflatable seal device. The function of this sealing device is to ensure a positive seal between the upstream and downstream cavities. A positive seal yields very efficient filtration. Also, the seal prevents the filter housing from filling with oil. This ensures that the engines lube system retains its original capacity. When the system is first powered up the seal must be filled with oil from the transfer pump. This oil flow and pressure cause the seal to inflate axially to seal off the upstream and downstream cavities. When it is determined that the filter window is plugged, the oil pressure inside the seal is released allowing for the seal to deflate and thus the filtering media to advance through the opening. During the bench testing several seal failures were encountered. The seal would fatigue after about 200 cycles of inflation/deflation causing a tear in the seal. The solution was to fabric reinforce the seal material to increase its fatigue strength.

The second issue which was encountered during the bench testing of the system prototype was with the filtering medium. Under pressure the filtering medium would produce tears. It turns out that the tears were due to the media supports deflecting or doming into the downstream cavity when under pressure. This in turn caused the filtering medium to be stretched and eventually torn. The solution to this issue was a redesign of the media support. The original media support was simply a wire mesh. Its replacement was a waffle grid pattern extruded to a thickness to prevent any deflection due to the oil pressure.

While the system bench testing and debugging was going on, the baseline testing of the test vehicles was also happening. The test vehicles chosen were two class 8 trucks. The Kenworth trucks are equipped with 1998 Detroit Diesel Series 60 engines. Both trucks were lent to EMP from a local trucking fleet, Niagara Logistics, who deliver EMP parts around the Midwest. Both trucks have consistent routes and average about 2,500 miles a week. Pressure port sampling valves were installed on both engines. For the baseline, weekly oil samples were taken for a period of about six months. The samples were sent to an outside analysis lab. Many characteristics of the oil were measured. The characteristics measured are as follows:

- Viscosity
- Water content
- Glycol content
- Fuel content
- Soot content
- Total base number
- Wear metals
- Oxidation

The data received from the analysis lab was recorded in a spreadsheet. This allowed for trending of the data. Typically, the oil characterictics either go up or they go down with increasing oil age. The following baseline data show these trends (Figures 7 and 8). Data were collected for a period of six months or approximately 60,000 miles. The remaining data have been projected out to one year.

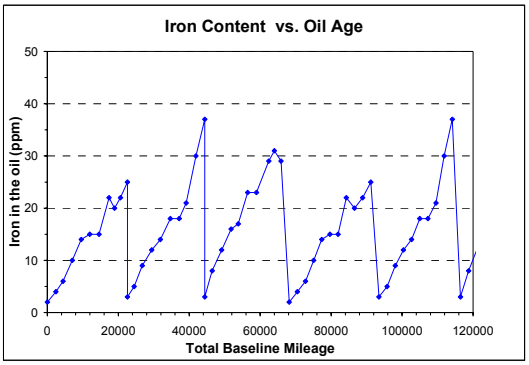

Figure 7. Trending of the iron content in one of the test vehicles. As the oil ages the iron content increases. The sharp drop in iron content represents an oil change.

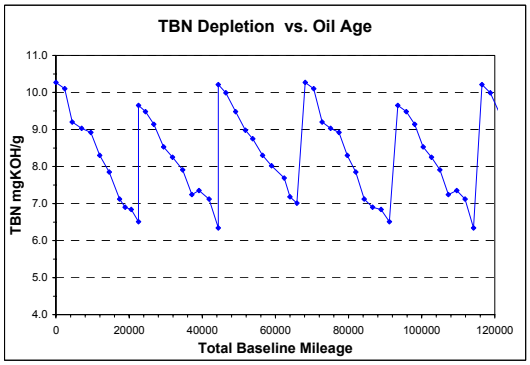

Figure 9. Expected iron content (dashed line) with AFS installed. Trend showing long gradual increase and eventually reaching a stable limit.

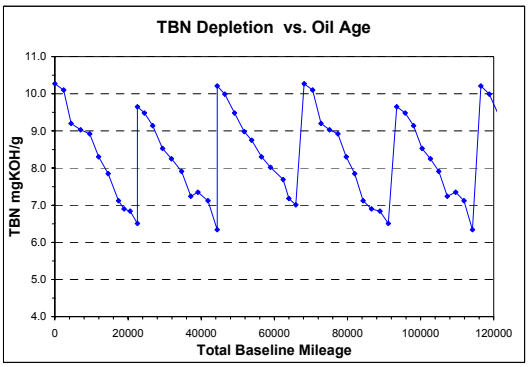

Figure 8. Trending of the Total Base Number (TBN). This number represents the ability of the oil to neutralize acids. As the oil ages the TBN decreases.

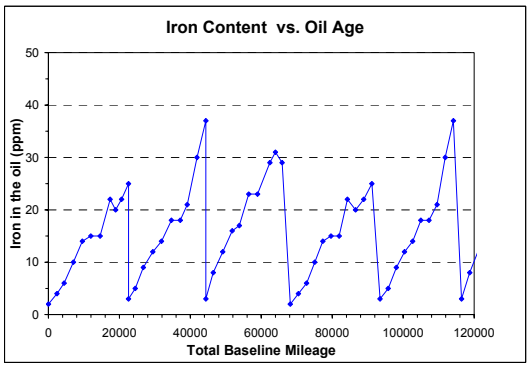

Figure 10. Expected TBN (dashed line) with AFS installed. Trend showing long gradual decrease. At some point it will reach a minimum limit at which the oil will need to be changed or additives replenished.

The results expected once the AFS is installed clearly need to reflect an extension of the oil age. This means when looking at the analysis trends that there are no saw tooth patterns. For an upward trending characteristic, the data with the AFS should reflect a long gradual increase over the 120,000 miles never exceeding the baseline maximum data points (Figure 9). For a downward trending characteristic, the data with the AFS should reflect a long gradual decrease over the 120,000 miles never exceeding the baseline minimum data points (Figure 10). Also, it should be noted that at some point the AFS should provide a stable level of contamination.

Once the vehicle baseline testing and the prototype performance testing were completed, it was time to install the prototype units into their respective vehicles. The installations took several days each as custom brackets had to be fabricated to mount the units to the trucks. Also, electrical and fluid connections had to be made. The filter units were installed under the hood on the cold side of the engine. The transfer pumps were installed along side the oil pan. This allowed for easy priming of the pump.

Once the AFS units were installed on the test vehicles (Figure 11) it took several weeks to debug the systems. There were electrical and software algorithm changes that needed to take place in order for the system to function properly. The system is initialized by the ignition of the vehicle. Once the system is powered up it waits until the oil reaches the desired temperature of 150°F. There is a thermistor placed in the oil pan to monitor the oil temperature. When the thermistor reads the value of 150, the pump is activated sending oil flow to the unit. The system then goes through a warm-up period of 4 minutes and oil is circulated through the

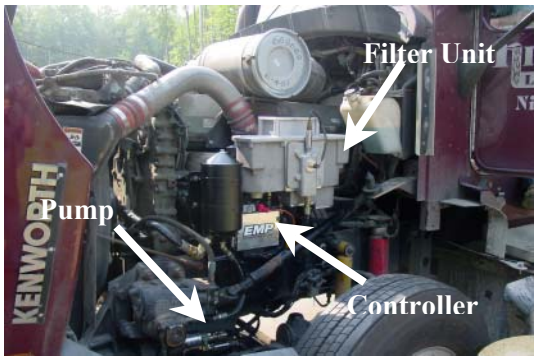

Figure 11. Installation of AFS on test vehicle. Kenworth truck equipped w/1998 DDC S60 engine.

unit to continue to warm the oil. After the warm-up cycle the seal is inflated and filtration begins. When the ignition is turned off the AFS will continue to run until 4 minutes later when it times out and the then goes into sleep mode until the ignition is on. The cycle then starts again.

To date, there has been only one issue experienced during the field testing. Again, an issue related to the inflatable seal (Figures 12 and 13). Over time as the filter medium would collect contaminants the pressure internal to the upstream cavity would increase, as expected. This pressure however was great enough to force the seal out of its retaining groove. When the pre-determined pressure differential across the filter medium was achieved, the medium could not be advanced because the seal was pinching the medium up against its support causing a binding issue. To resolve this issue, the inflatable seal was redesigned to incorporate a better means of retaining the seal.

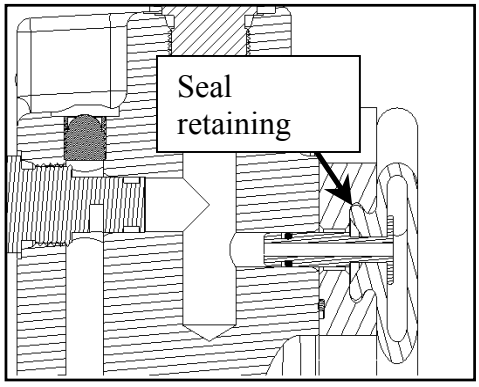

Figure 12. Shows the original seal design and its retaining feature. Internal pressure would force the seal out of its groove.

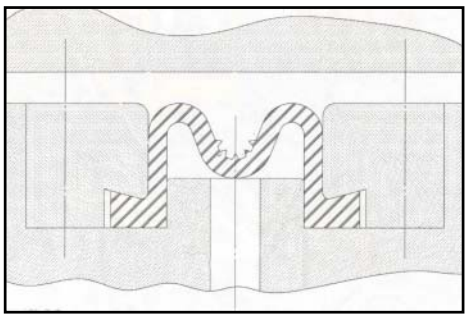

Figure 13. Shows the new seal design with its improved retaining feature

As can be seen from the figure, the new seal design allows for the seal to be physically clamped into a retainer ring. This greatly enhances it retention. This new seal design also allows for more improvements in functionality. Its mode for inflation is now more of a shape changing phenomenon versus a stretching of the material phenomenon. This will increase its fatigue strength even more. Also, there is now less material which will reduce the component cost of the seal. Finally, a valve stem is no longer needed to fill the seal with oil. The entire bottom surface of the seal is open to allow oil to enter. This will quicken the inflation and deflation times of the seal. Because of this component switch the field tests had to be started over.

Conclusions

The field testing is now successfully underway. There have been about three samples collected on each of the test vehicles. We should have a good idea on how the system is performing by the end of the year (2003). The process has also been started to install test units on other applications as well. A baseline test has begun for an off-road end loader. Many more applications will follow including engines equipped with EGR.

While the field testing is occurring, a strategy to bring this system to market is also currently being put into place. This work done in phase II has allowed us to take the next step with this technology: commercialization.

This technology will make a big impact in the trucking industry as well as other industries. With the AFS, trucks that typically average 5–6 maintenance intervals per year related to oil and filter changes (at an average cost of $180 per

service) will now require only 1–2 oil changes per year, resulting in an annual average per-truck savings of $540–900. Across the entire U.S. heavy-duty truck fleet, the savings could add up to more than 30 million gallons of lube oil per year.

References

1. David R. Staley, "Correlating Lube Oil Filtration Efficiencies with Engine Wear," SAE 881825 (1988).
2. Gordon E. Andrews, Jie Xu, M.H. Jones, James Hall, A.A. Rahman, "The Influence of an On-line Oil Recycler on Oil Quality from a Bus in Service Using Synthetic Oil," SAE 2001-01-1969 (2001).
3. Gordon E. Andrews, Hu Li, James Hall, A.A. Rahman, S. Saykali, M.H. Jones, "Improvements in Lubricating Oil Quality by an On-line Oil Recycler for a Refuse Truck Using in Service Testing," SAE 2001-01-0669 (2001).
4. Vincent D. Pellegrin, Alvin Lowi Jr, "Correlation of Smoke Levels with Engine-Lubricating-Oil Solids in Metropolitan Transit Buses," SAE 872251 (1987).
5. Gordon E. Andrews, Jie Xu, James Hall, A.A. Raham, P. Mawson, "The Influence of an On-line Oil Recycler on Emissions From a Low Emission Di Diesel Engine as a Function of Oil Age," SAE 2001-01-3617 (2001).
6. Gordon E. Andrews, Hu Li, James Hall, A.A. Rahman, S. Saykali, "The Influence of an Oil Recycler on Emissions with Oil Age for a Refuse Truck Using in Service Testing," SAE 2001-01-0623 (2001).